



HAL
open science

Selective dissolution from Zn-Al alloy coatings on steel

Thanh Nam Vu

► **To cite this version:**

Thanh Nam Vu. Selective dissolution from Zn-Al alloy coatings on steel. Material chemistry. Université Pierre et Marie Curie - Paris VI, 2012. English. NNT : 2012PAO66303 . tel-00839479

HAL Id: tel-00839479

<https://theses.hal.science/tel-00839479>

Submitted on 28 Jun 2013

HAL is a multi-disciplinary open access archive for the deposit and dissemination of scientific research documents, whether they are published or not. The documents may come from teaching and research institutions in France or abroad, or from public or private research centers.

L'archive ouverte pluridisciplinaire **HAL**, est destinée au dépôt et à la diffusion de documents scientifiques de niveau recherche, publiés ou non, émanant des établissements d'enseignement et de recherche français ou étrangers, des laboratoires publics ou privés.

**THESE DE DOCTORAT DE
L'UNIVERSITE PIERRE ET MARIE CURIE**

Spécialité

Chimie Physique et Chimie Analytique

Présentée par

VU Thanh Nam

Pour obtenir le grade de

DOCTEUR de l'UNIVERSITÉ PIERRE ET MARIE CURIE

Sujet de la thèse :

Dissolution sélective à partir des alliages Zn-Al sur l'acier

(Selective dissolution from Zn-Al alloy coatings on steel)

soutenue le 20 septembre 2012

devant le jury composé de : (préciser la qualité de chacun des membres).

M. K. OGLE	Professeur à ChimieParistech	Directeur de thèse
M. D. THIERRY	Directeur de l'Institut de la corrosion, Brest	Rapporteur
M. B. VUILLEMIN	Professeur à Université de Bourgogne	Rapporteur
Mme. P. VOLOVITCH	Maître de conférences à ChimieParistech	Examineur
M. J. STEINMETZ	Professeur à Université Henry Poincaré	Examineur
Mme. E. SUTTER	Professeur à Université Pierre et Marie Curie	Examineur
M. M. ROHWERDER	Chef de groupe "Molecular Structures and Surface Design", Max-Planck-Institut, Dusseldorf	Examineur

Selective dissolution from Zn-Al alloy coatings on steel

Zn-Al alloys are commonly used to protect steel in automobile and architectural industries. Their corrosion protection properties depend on their surface composition which may change markedly with time during application due to selective dissolution phenomenon. This phenomenon has been known for a long time, but no systematic investigation has been published due to the difficulty in distinguishing elementary dissolution of zinc and aluminum which are both active and amphoteric, and whose relative activities may be reversed under certain conditions.

The main objective of this work is to understand selective dissolution phenomena and map out the selective dissolution of Zn-Al alloys and to a lesser extent Zn-Mg-Al alloys as a function of pH and potential. This will help to build up a predictive model of galvanic coupling which is a major preoccupation of the automotive industry.

To approach the target, we utilize atomic emission spectroelectrochemistry (AESEC) technique which is a combination of electrochemical method and inductively coupled plasma atomic emission spectroscopy. This technique allows us to quantify in real time and separately dissolution rates of zinc and aluminum from Zn-Al alloys at open circuit potential and applied potential in different solutions. Selective dissolution of zinc and aluminum from Zn-Al alloys is then mapped out in the pH and potential ranges. The explanations for the selective dissolution and inhibition phenomena occurring during experiments are also given thanks to the complementary results from other surface characterization methods (XRD, SEM/EDS, IR, and XPS).

This project is financially supported by Autocorr European Research Fund for Coal and Steel (RFCS). I kindly acknowledge the RFCS project partners ArcelorMittal, France; Salzgitter AG, Germany; ThyssenKrupp, Germany, VoestAlpine, Austria and KTH, Sweden for helpful scientific discussions.

Acknowledgement

How fast time flies! Three years have been almost passed. I am coming to the end of a road. I know that I am not alone on this road, many people have been going with me and I acknowledge their help.

First of all, I would like to thank Prof. Kevin Ogle who is my PhD advisor. I have learnt a lot during the time working with him, not only my scientific knowledge but also my personal skills have been improved. I have learnt how to give a good oral presentation; how to write an industrial report; how to get over stress; how to deal with different partners in a project, etc. Those are valuable experiences that will help me in the further professional career.

Secondly, I would like to thank Asst. Prof. Polina Volovitch with whom I have worked a lot. We did not always have agreement in discussion, but beyond that I learnt many things from her. She has a broaden knowledge and a big passion for science and research.

Thirdly, I would like to thank Prof. Philippe Marcus, the director of Laboratoire de Physico-Chimie des Surfaces, who welcomed me to the lab. I also want to thank secretaries of my laboratory: Mrs. S. Gandziarski and Mrs. M-J. Michel; as well as secretaries of doctoral school: Mrs. Soobrayen Koonavadee (and Mrs. I. Duc) who helped me in administrative procedures. I kindly acknowledge Mrs. A. Nadolny, person in charge of Chimie-ParisTech's library, who is very active and help me finding quickly scientific articles/documents even some of them are not available online.

I would like to thank Prof. Inger Odnevall Wallinder from KTH Royal Institute of Technology, and Dr. Christian Allely from ArcelorMittal for scientific help. I am also grateful to Dr. W. Friedhoff and Dr. Frank Beier from Salzgitter for an industrial internship.

Many thanks to my lab-mates in LPCS: Sophie, Carole, Maria, Slava, Hao, Bing Bing, Jae Dong, Matthieu, Feng, Toni, Thomas, Catarina, Clement, Blanca, Maud, Fabien, Antoine, Arnaud, Nicolas, Elise ... and other people in the laboratory. We shared special time and scientific space in LPCS. I also want to say thank you to my Vietnamese friends Nam beo, Linh, Ly, Hai Nam, Vi, Hiep, Toan, Ha, Hoang, Trang, Thach, Hang, Lien, Hong, Dang, Giap ... With them, I "killed" my spare time outside lab ☺

Finally, I would like to thank my parents, my family, and other people that I do not specify here for their support and encouragement to me.

VU Thanh Nam

Paris, June 2012

Table of content

Résumé	6
L'histoire de cette thèse.....	6
Résumé de cette thèse	7
Conclusions	11
Chapter I. Introduction	17
1.1. Origin and objectives of the PhD study	17
1.2. Summary of the PhD dissertation.....	18
1.3. List of publications.....	21
Chapter II. Introduction to Galfan (5% Al-Zn) and Galvalume (55% Al-Zn).....	25
2.1. Zn-Al phase diagram.....	25
2.2. Galfan (5 wt% Al-Zn)	26
2.3. Galvalume (55 wt% Al-Zn).....	29
2.4. Production method - Hot-Dip galvanizing	30
2.4.1. <i>Batch Galvanizing</i>	31
2.4.2. <i>Continuous galvanizing</i>	31
2.5. Summary	32
2.6. References	32
Chapter III. Basic introduction to corrosion of Zn and Zn-Al coatings	35
3.1. Corrosion of zinc coating	35
3.2. Corrosion of Zn-Al alloy coatings - selective dissolution.....	41
3.3. Summary	42
3.4. References	43
Chapter IV. Atomic emission spectroelectrochemistry (AESEC)	47
4.1. Introduction	47
4.2. Instrumentation.....	47
4.3. ICP-OES calibration.....	52
4.4. Analysis of the AESEC data	53
4.5. Summary	59
4.6. References	60

Chapter V. Understanding corrosion via corrosion product characterization: Role of alloying element in improving the corrosion resistance of ZnMgAl coatings..... 63

5.1. Introduction	64
5.2. Experimental	66
5.2.1. <i>Sampling</i>	66
5.2.2. <i>Characterization methods</i>	67
5.3. Results	68
5.3.1. <i>Detected corrosion products: results of XRD and FTIR</i>	68
5.3.2. <i>Detected corrosion products: distribution of elements by SEM-EDS</i>	72
5.3.3. <i>Selective dissolution of Zn and Al observed by AESEC</i>	74
5.4. Discussion: Role of Mg and Al in Zn-Mg-Al coatings	75
5.4.1. <i>Initial stages of corrosion</i>	76
5.4.2. <i>Dissolution of Al and formation of new corrosion products at advanced stages of corrosion</i>	78
5.5. Conclusions	81
5.6. References	82

Chapter VI. The initial release of zinc and aluminum from non-treated Galvalume and the formation of corrosion products..... 87

6.1. Introduction	88
6.2. Experimental	89
6.2.1. <i>Material and test media</i>	89
6.2.2. <i>Flow-cell test</i>	89
6.2.3. <i>Immersion tests</i>	90
6.2.4. <i>Long-term field exposure</i>	91
6.2.5. <i>Corrosion product formation</i>	91
6.2.5.1 <i>Scanning electron microscopy / Energy dispersive x-ray analysis (SEM/EDS)</i>	92
6.2.5.2 <i>Infrared Reflection Absorption Spectroscopy (IRAS)</i>	92
6.2.5.3 <i>Grazing incident X-ray diffraction (GIXRD)</i>	92
6.2.5.4 <i>Confocal Raman microspectroscopy (CRM)</i>	92
6.2.5.5 <i>X-ray photoelectron spectroscopy/Auger Electron Spectroscopy (XPS/AES)</i> .	93
6.3. Results and Discussion.....	93
6.3.1. <i>Initial metal release in chloride containing media at aerated conditions</i>	93
6.3.2. <i>Initial formation of corrosion products in chloride containing media at aerated conditions</i>	98

6.3.3. <i>Initial metal release and corrosion product formation in chloride containing media at non-aerated OCP and at an applied anodic potential.</i>	101
6.4. Conclusions	104
6.5. References	105
Chapter VII. The effect of pH on the selective dissolution of Zn and Al from Zn-Al coatings on steel	110
7.1. Introduction	111
7.2. Experimental	113
7.2.1. <i>Materials</i>	113
7.2.2. <i>Atomic emission spectroelectrochemistry (AESEC) technique</i>	113
7.2.3. <i>Immersion test</i>	114
7.2.4. <i>X-Ray Diffraction (XRD)</i>	114
7.3. Results	115
7.3.1. <i>Spontaneous dissolution of 5%Al-Zn, 55%Al-Zn, and pure metals with AESEC measurement</i>	115
7.3.2. <i>Immersion test result of 5%Al-Zn</i>	122
7.3.3. <i>Comparison of immersion test and AESEC results</i>	123
7.4. Discussion	124
7.4.1. <i>Selective dissolution of Zn and Al from 5%Al-Zn and 55%Al-Zn</i>	124
7.4.2. <i>Oxygen effect</i>	125
7.5. Conclusion.....	127
7.6. References	128
Chapter VIII. Selective dissolution of Zn and Al from Zn-Al coatings on steel during polarization in acidic, neutral and alkaline solutions	134
8.1. Introduction	135
8.2. Experimental	136
8.2.1. <i>Materials</i>	136
8.2.2. <i>The AESEC Technique</i>	136
8.2.3. <i>Analysis of the ICP-OES data</i>	137
8.3. Results	137
8.3.1. <i>Overview of the potential – pH dependence of selective dissolution</i>	137
8.3.2. <i>Acidic solution</i>	139
8.3.3. <i>Neutral solution</i>	141
8.3.4. <i>Zn and Al dissolution rates as a function of potential in alkaline solution</i>	142

8.3.5. <i>Selective dissolution of Zn and Al in the different electrolyte during polarization</i>	143
8.4. Discussion	144
8.5. Conclusion	146
8.6. References	147
Chapter IX. The Anodic Dissolution of Zinc and Zinc Alloys in Alkaline Solution: Al and Zn partial dissolution from 5% Al-Zn coatings	150
9.1. Introduction	151
9.2. Experimental	152
9.2.1 <i>Materials</i>	152
9.2.2. <i>Scanning Electron Microscopy/Energy Dispersive Spectroscopy (SEM/EDS)</i> ...	152
9.2.3. <i>The AESEC Technique</i>	153
9.2.4. <i>Analysis of the ICP-OES data</i>	153
9.3. Results	155
9.3.1 <i>Microstructure Analysis</i>	155
9.3.2. <i>Spontaneous reaction of 5% Al-Zn alloy with alkaline solutions</i>	156
9.3.3. <i>Zn and Al dissolution in different potential domains</i>	158
9.3.4. <i>SEM / EDS analysis after applied potential</i>	160
9.3.5. <i>Kinetic parameters</i>	162
9.3.6. <i>Potentiostatic Transient Experiments</i>	164
9.3.7. <i>Steady State Polarization curve</i>	168
9.4. Discussion	170
9.5. Conclusions	172
9.6. References	173
Chapter X. Inhibition mechanism of Al dissolution during polarization of Zn-Al alloys in alkaline solution	176
10.1. Introduction	177
10.2. Experimental	178
10.2.1. <i>Materials</i>	178
10.2.2. <i>Atomic emission spectroelectrochemistry (AESEC) technique</i>	179
10.3. Results	179
10.3.1. <i>Polarization curves for pure Zn, pure Al, and bi-electrode in 0.1 M NaOH</i>	179
10.3.2. <i>Polarization curves for pure Al in 0.1 M NaOH added Zn²⁺</i>	183
10.4. Discussion	185

10.5. Conclusion.....	185
10.6. References	186
Chapter XI. Conclusions and perspectives	189
Annex.....	195
New - Verband Der Automobilindustrie (New-VDA) test	195
X-ray diffraction.....	195
Scanning electron microscope (SEM) – Energy dispersive spectroscopy (EDS).....	198
Attenuated total reflectance (ATR) infrared	200
References	201

Résumé

L'histoire de cette thèse

L'incorporation des nouveaux matériaux de revêtement, d'alliages plus légers et de nouveaux grades d'acier est devenue un objectif important de l'industrie automobile, enfin de produire des automobiles plus légères et plus économes en carburant. Toutefois, la possibilité de corrosion galvanique induite par couplage métal / métal asymétrique est un obstacle majeur pour la commercialisation des nouveaux matériaux de revêtement. En fait, le rapport du Partenariat des Matériaux automobile des États-Unis en 2005 cité la corrosion galvanique comme l'un des problèmes majeurs à surmonter dans l'évolution de la prochaine génération de l'automobile de multi-matériaux.

Un objectif à long terme de la recherche actuelle est de développer des modèles prédictifs de couplage galvanique basé sur les propriétés électrochimiques des alliages et des matériaux dans l'industrie automobile. L'objectif de ce travail est d'étudier en détail comment les propriétés électrochimiques des alliages Zn-Al (et dans une moindre mesure Zn-Mg-Al) sont influencées par des mécanismes de dissolution sélective. Les propriétés électrochimiques dépendent de la composition de surface des alliages exposés à l'électrolyte. Cette composition de la surface peut changer significativement quand l'élément le moins noble est sélectivement dissous à partir de l'alliage. Ceci est bien connu pour les matériaux de revêtement tels que Zn-Ni ou Zn-Fe où le moins noble Zn est enlevé sélectivement laissant derrière lui une couche de Ni ou de Fe poreuse. Pour ces alliages, les potentiels électrochimiques de ces deux éléments sont tout à fait différents et donc les variations sont relativement simples à prédire en utilisant le modèle cinétique le plus simple de couplage galvanique impliquant la théorie de potentiel mixte (schéma d'Evan).

Cependant, les composantes des alliages Zn-Al et Zn-Mg-Al sont beaucoup plus rapprochés dans la série galvanique et les éléments spécifiques qui sont sélectivement dissous dépendront de l'environnement chimique, notamment le pH qui peut changer significativement à la suite de réactions anodique et cathodique équilibrées se produisant dans une zone confinée (**Fig. 1**). La réaction cathodique est supposé être la réaction de réduction de l'eau (ou de l'oxygène), tandis que la réaction d'oxydation anodique comprend les vitesses de la dissolution des métaux différentes exposées à l'électrolyte. Ces vitesses élémentaires

décident de la dissolution sélective mais ne peut pas être distinguées par des procédés électrochimiques classiques.

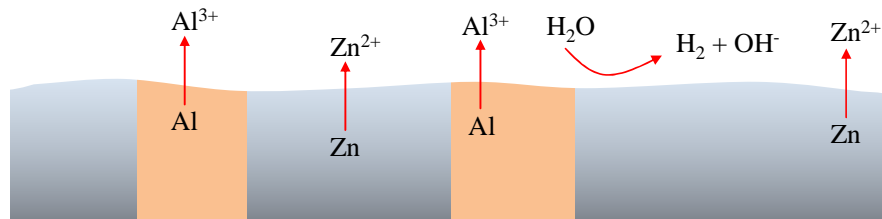


Figure 1: Schéma montrant réactions se produisant dans la zone confinée de l'alliage Zn-Al

Mon projet de thèse vise à étudier les phénomènes de dissolution sélective pour les alliages Zn-Al et dans une moindre mesure des alliages Zn-Mg-Al en fonction du pH et de potentiel. Ce projet s'inscrit dans le cadre d'un projet RFCS, qui vise à cataloguer le comportement de couplage galvanique pour différents matériaux et de développer un modèle numérique de prévision de couplage. La technique principale utilisée dans ce travail est spectroélectrochimie d'émission atomique (AESEC), une combinaison d'une méthode analytique et d'une cellule électrochimique. Cette technique est utilisée pour mesurer en temps réel les vitesses de dissolution partielle de chaque composant d'un alliage pendant l'exposition du pH différent et contenant du chlorure au potentiel de circuit ouvert et potentiels appliqués. Une compréhension des phénomènes de dissolution sélective liés à la formation des produits de corrosion a été tenté.

Résumé de cette thèse

Cette thèse est divisée en trois parties principales. La Partie I est une introduction et se compose de cinq chapitres. Le **Chapitre 1** (ce chapitre) présente l'origine et les objectifs du projet de thèse, et donne un aperçu de cette thèse. Le **Chapitre 2** discute les matériaux principaux utilisés dans ce travail (Galfan et Galvalume). Le **Chapitre 3** examine les bases de la corrosion et l'électrochimie des revêtements en alliage à base du zinc. Il convient de noter que le chapitre 2, chapitre 3, et chaque chapitre dans la partie II comprend une étude bibliographique. Le **Chapitre 4** présente la technique atomique spectroélectrochimie émission (AESEC) par laquelle la plupart des résultats de ce travail ont été obtenus. Ce chapitre fournit également des recherches originales sur les applications analytiques de cette technique cinétique impliquant la distribution spatiale des constantes de temps.

La partie II est la plus importante de mon travail et se compose de nouvelles recherches sur les mécanismes de dissolution sélective. Ces travaux sont présentés sous forme d'articles publiés ou soumis. Le **Chapitre 5** est un chapitre introductif qui illustre la complexité des phénomènes étudiés de corrosion en présentant une étude systématique de la corrosion des revêtements Zn-Mg-Al et Zn-Mg mettant en évidence la relation entre les produits de corrosion et les phénomènes de dissolution sélective mesurée par AESEC. Les résultats de dissolution / corrosion préférentielle des éléments différents d'alliages à base de Zn sont étudiés à l'échelle microscopique par la caractérisation des produits de corrosion formés sur ces alliages après les tests accélérée de corrosion. Ce travail a été réalisé en collaboration avec ArcelorMittal pour les tests de corrosion et la fourniture des matériaux de revêtement.

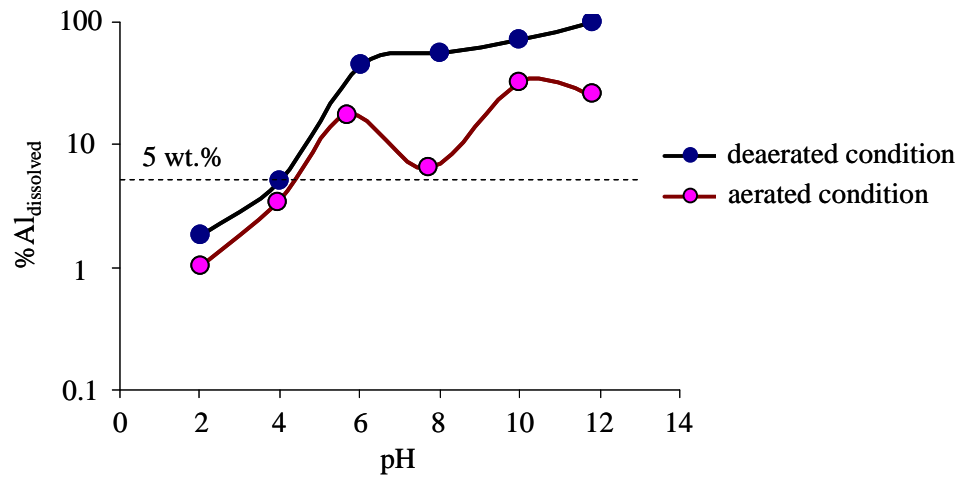
Le travail expérimental avec Zn-Mg-Al donne un aperçu des phénomènes de dissolution sélective pour un système complexe et intéressante, toutefois le reste de cette thèse est axée sur les revêtements de Zn-Al. Cela a été fait pour deux raisons: (1) Il est nécessaire de comprendre Zn-Al, avant que nous puissions espérer de comprendre le système plus complexe comme Zn-Mg-Al, et (2), il existe deux produits de Zn-Al stables et disponibles dans le commerce, Galfan (5% de Al-Zn) et Galvalume (55% de Al-Zn). En revanche, les produits de Zn-Mg-Al sont très récents et sont en cours d'élaboration en ce moment.

Le **Chapitre 6** discute de la dissolution sélective de Zn et Al de 55% Al-Zn dans l'eau de pluie et l'eau de mer synthétique (pH ayant une valeur différente et la concentration différente de chlorure) par la mesure *in situ* avec AESEC et *ex situ* avec test d'immersion pendant l'exposition à court terme. Ces résultats sont comparés avec celui de l'exposition à long terme qui a été faite par KTH Royal Institute of Technology. Ce chapitre permet une comparaison entre la technique AESEC et les expériences d'immersion plus conventionnelles et donne également une corrélation plus détaillée entre le comportement de dissolution sélective et l'analyse de surface.

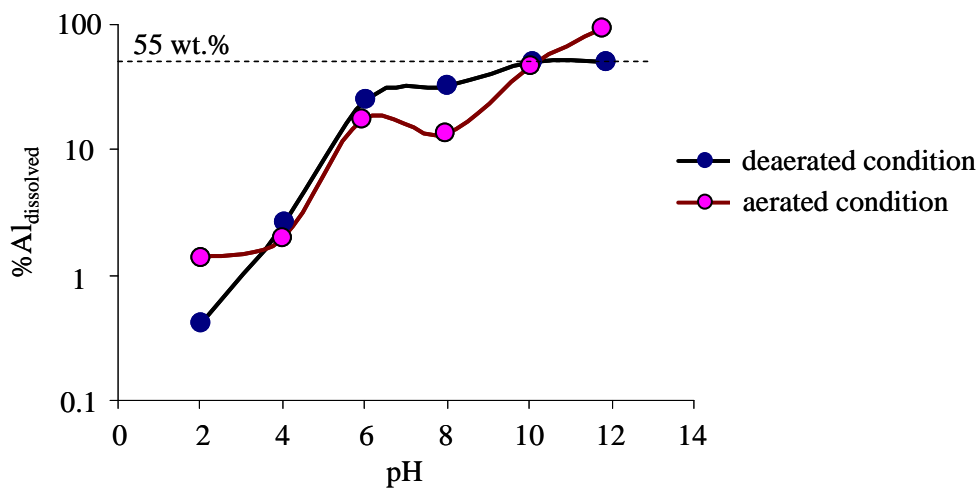
Le **Chapitre 7** présente la dissolution sélective de Zn et Al de 5% de Al-Zn et 55% d'Al-Zn en une fonction du pH dans les électrolytes simples contenant 30 mM de NaCl par mesure de la réactivité intrinsèque de Zn et Al en temps réel (**Fig. 2**). Le résultat est ensuite comparé avec le test d'immersion dans lequel une couche de produits de corrosion est formée pour comprendre comment la couche de produit influe sur le taux de dissolution de Zn et Al.

Le **Chapitre 8** présente la dissolution sélective de Zn et Al de 5% de Al-Zn et 55% de Al-Zn en fonction du potentiel de polarisation dans les électrolytes simples ayant pH différent.

Les résultats démontrent que la dissolution sélective ne dépend pas seulement du pH, mais aussi du potentiel (**Fig. 3**).



(a)



(b)

Figure 2: Fraction de Al dissous (% Al_{dissolved}) libéré de (a) 5% d'alliage Al-Zn et (b) 55% Al-Zn en fonction du pH dans solutions gazeuses et désaéré de 30 mM de NaCl. La composition d'Al dans le revêtement Al-Zn est également indiquée par la ligne pointillée (du chapitre 7).

Les **Chapitre 7** et **8** sont les chapitres principaux de cette thèse, car ils correspondent à la dissolution sélective des alliages Zn-Al en fonction du pH et du potentiel qui sont des paramètres importants de la corrosion galvanique.

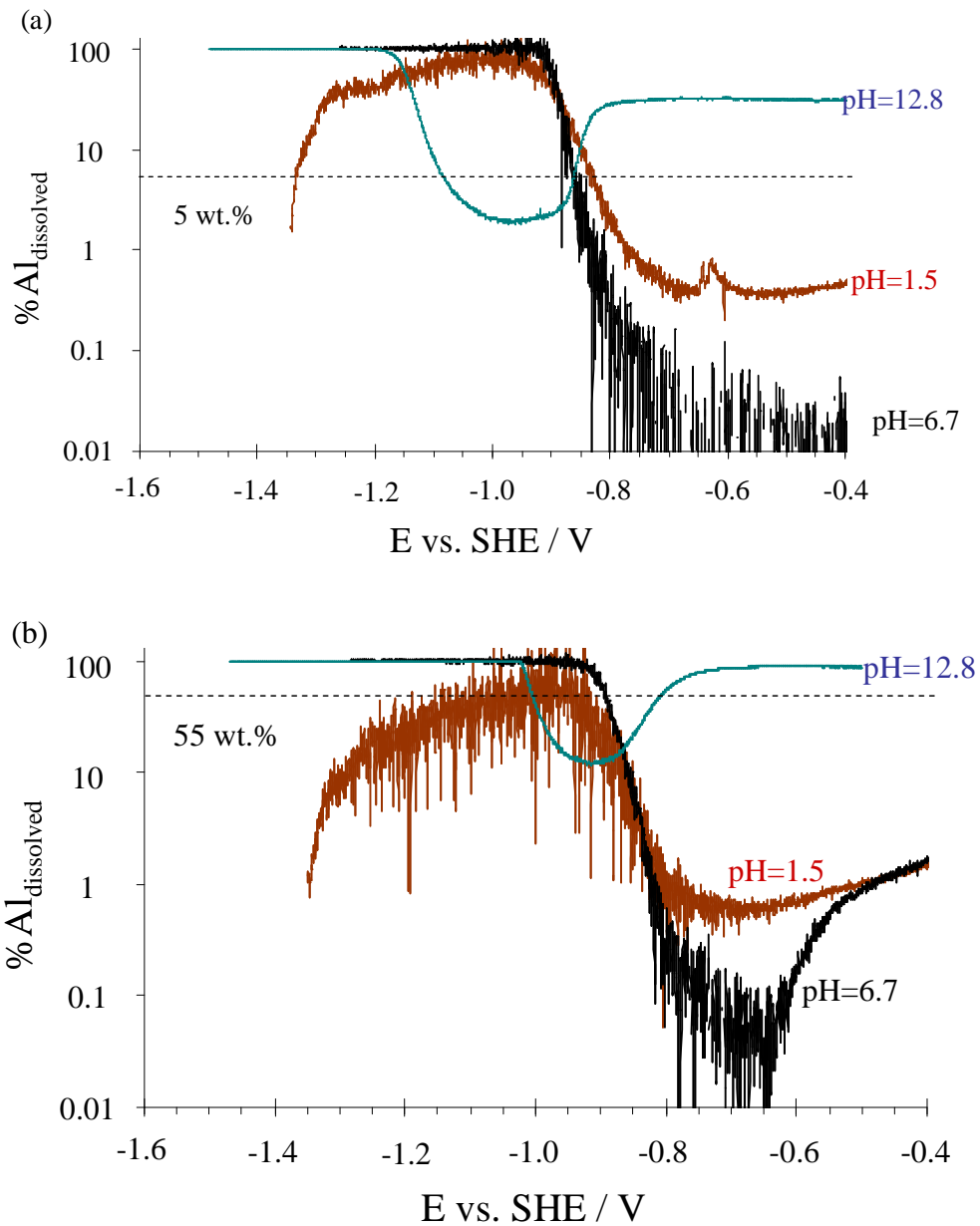


Figure 3: Fraction d'Al dissous à partir de a) Galfan) et b) Galvalume en fonction du potentiel dans les environnements différents: HCl 0,1 M, NaCl 0,1 M et 0,1 M de NaOH (du chapitre 8).

Le **Chapitre 9** compare les taux de dissolution de Zn et Al de 5% Al-Zn dans les solutions alcalines pendant la polarisation en balayage linéaire et pendant la polarisation d'état stationnaire dans laquelle les taux de dissolution élémentaires au potentiels appliqués sont mesurées. Ce chapitre indique également l'inhibition de la dissolution de l'aluminium aux potentiels actifs du zinc.

Le **Chapitre 10** précise le mécanisme d'inhibition de la dissolution de l'aluminium en étudiant séparément les différents facteurs qui peuvent contrôler la vitesse de dissolution d'Al lors de la polarisation des alliages Zn-Al en solution alcaline. Cela se fait en utilisant une bi-électrode spéciale Zn/Al. Les produits de corrosion contenant du zinc sont démontrés comme étant la raison principale.

La partie III donne les conclusions et les perspectives de ce travail (**Chapitre 11**). Pour conclure, les phénomènes de dissolution sélective de Zn-Al alliages sont systématiquement étudiés en fonction du pH et du potentiel dans les médias différents. Les comportements de dissolution de Zn et Al au cours de différentes expériences sont expliqués. Pour les perspectives, nous discutons de la possibilité d'étendre ces études à un autre alliage complexes, tels que Zn-Mg-Al.

Conclusions

Ce travail de thèse a tracé la dissolution sélective des alliages binaires Zn-Al en fonction du pH et du potentiel qui sont deux facteurs importants qui déterminent la vitesse de corrosion des matériaux au cours de leurs applications à l'extérieur. Comme nous l'avons dit, le zinc et l'aluminium ont des activités similaires et il est difficile de quantifier les taux de dissolution de chaque métal à partir des alliages Zn-Al par des méthodes électrochimiques classiques. Cette difficulté a été surmontée dans ce travail en utilisant la technique AESEC qui nous permet de mesurer *in situ* les taux de dissolution élémentaires des alliages Zn-Al tels que le Galfan (5% Al-Zn) et Galvalume (55% Al-Zn) et des alliages Zn-Mg-Al dans une moindre mesure au potentiel de circuit ouvert et au potentiel appliqué dans les environnements différents. D'autres méthodes *ex situ* telles que DRX, MEB / EDS, IR et XPS ont également été utilisées pour caractériser les produits de corrosion précipités et la composition de surface corrodée.

Ces résultats donnent une image plus complète de la cinétique de dissolution des alliages Zn-Al qui peuvent finalement être étendues pour inclure la famille d'alliages Zn-Al-Mg et d'être incorporé dans un modèle numérique. Les résultats de mon travail peuvent se résumer comme suit:

1. La dissolution sélective à partir des alliages Zn-Al en fonction du pH a été tracée

La dissolution sélective de Zn et Al des alliages Zn-Al a été étudiée en fonction du pH lorsque 5% Al-Zn et 55% Al-Zn ont été exposés à un électrolyte NaCl 30 mM (chapitre 7) et aux électrolytes plus complexes - l'eau de mer / l'eau de pluie (chapitre 6). Il est démontré que le mécanisme de dissolution changé depuis la dissolution sélective du zinc dans la gamme de pH de 2-4 (pour Galfan) et 2-8 (pour Galvalume) à la dissolution sélective d'aluminium à pH plus élevé. La présence ou l'absence d'oxygène dans l'électrolyte ne change pas le comportement de dissolution sélective, mais influence les taux de dissolution (v_{Zn} et v_{Al}) qui variaient avec le temps. L'oxygène stabilisé la couche d'oxyde en solution aérée provoquant un déplacement anodique du potentiel de circuit ouvert par rapport aux résultats obtenus en solution désaérée. Le couplage galvanique entre phases riche en Zn et Al d'alliage 5% Al-Zn a été observée dans la solution désaérée à pH = 11,8, où Al dissous rapidement, mais Zn n'a pas fait.

2. La dissolution sélective à partir des alliages Zn-Al en fonction du potentiel a été tracée

La dissolution sélective de Zn et Al de 5% Al-Zn et 55% Al-Zn a été étudié en fonction du potentiel dans HCl 0,1 M (pH = 1,5), 0,1 M de NaCl (pH = 6,7), et 0,1 M de NaOH (pH = 12,8). Au cours de la polarisation cathodique, il y avait une forte dissolution sélective de Al à partir des deux alliages dans NaOH 0,1 M et 0,1 M de NaCl, mais la dissolution sélective de Zn a été observée à partir de Galvalume dans HCl 0,1 M. Au cours de la polarisation anodique, une forte dissolution sélective de Zn a été vu dans les solutions acides et neutres. Dans les solutions alcalines, les branches anodiques de courbes de polarisation à la fois pour Galfan et Galvalume sont divisées en 2 domaines différents: le domaine de zinc actif dans lequel dissolution sélective de Zn se produit et le domaine de zinc passive dans lequel dissolution sélective d'Al se produit.

3. La dissolution d'aluminium est inhibée par la présence des ions Zn dissous

L'inhibition de la dissolution d'Al dans la présence d'ions Zn dissous a été mentionnée dans le chapitre 7 au chapitre 10. Dans l'enquête de la dissolution sélective en fonction du pH (chapitre 7), la comparaison des résultats AESEC et les résultats des tests d'immersion démontre que la formation d'une couche de produit de corrosion massive riche en Zn inhibe la

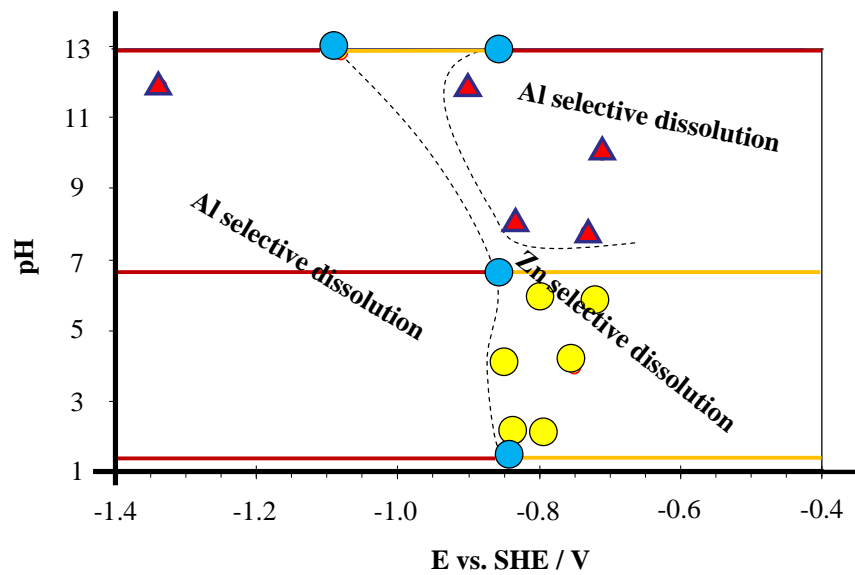
vitesse de libération d'Al. Il est démontré également la complémentarité des mesures des taux de corrosion à temps court par la technique AESEC et à temps long par le test d'immersion. Au cours d'une exposition à long terme, les réactions de corrosion élémentaires affectent le pH de l'électrolyte de sorte que le pH se rapproche de neutre. Les expériences AESEC impliquent un électrolyte sans cesse renouvelé et donc la mesure de la vitesse de la dissolution représente la réactivité «intrinsèque» du matériel avec un électrolyte. Dans l'instruction de dissolution sélective en fonction du potentiel dans une solution alcaline (chapitre 8 et 9), les expériences de polarisation AESEC indiquent l'inhibition de la dissolution d'aluminium dans le domaine de zinc actif. Le mécanisme d'inhibition de la dissolution d'Al dans la solution alcaline à des potentiels de zinc actifs a été proposé et vérifié (chapitre 10) en effectuant des expériences de polarisation sur la bi-électrode spéciale. Il est démontré que la dissolution d'Al au cours du domaine de zinc actif où Zn dissolution sélective se produit est inhibée par les produits de corrosion contenant Zn et le tamponnage du pH, qui sont attribuées à la présence de Zn^{2+} dans la zone confinée.

4. La dissolution d'aluminium n'a pas un effet significatif sur la dissolution du zinc

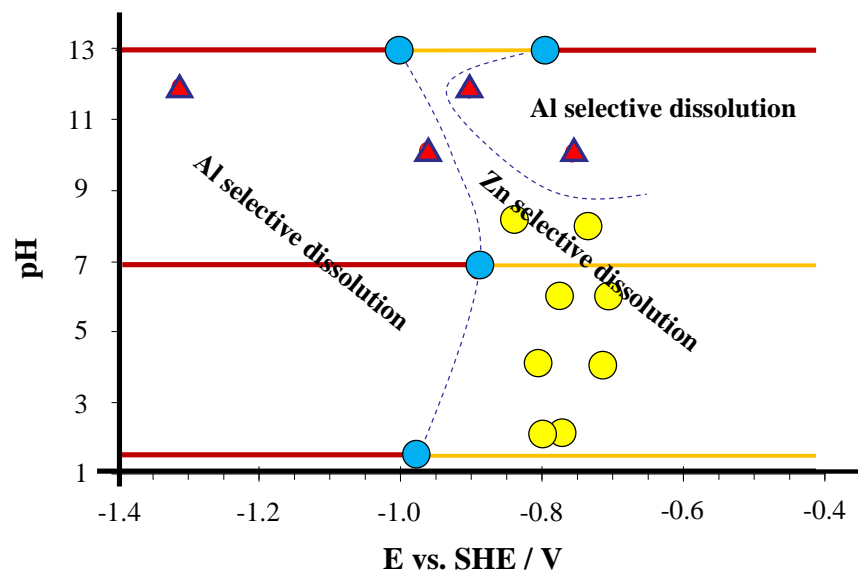
Les expériences de polarisation dans divers solutions alcalines donne une pente de Tafel d'environ 35 mV / décade pour le Zn courant de dissolution - courbe du potentiel. Cette pente de Tafel est presque indépendante de la concentration des ions hydroxyde. Cette valeur est compatible avec la dissolution de zinc pur. Cela signifie que le taux de dissolution d'Al n'a pas un effet significatif sur la cinétique de dissolution du zinc.

Afin de produire un schéma numérique basé sur les résultats de ce travail, la dissolution sélective à partir de Galfan et Galvalume a été tracée en fonction du pH et du potentiel, comme indiqué dans la **Fig. 4**. En principe, Zn dissolution sélective se produit aux potentiels anodiques et au pH faible, tandis que dissolution sélective d'Al se produit aux potentiels cathodiques ou même aux potentiels anodiques si le pH est suffisamment élevé. Le diagramme de la **Fig. 4** permet de prédire la corrosion, la dissolution sélective ou de-alliage des alliages Zn-Al aux potentiels différents et dans les environnements différents, notamment du pH. Toutefois, il convient de noter que les limites (lignes pointillées) entre les domaines différents de cette figure sont approximatives et probablement déplacer légèrement en fonction de la température d'application, la composition de l'électrolyte, etc. En outre, le pH

évolue au cours des expériences, mais sa variation est acceptable (inférieure à 0,3), et le potentiel contient probablement un potentiel de jonction en raison de la membrane qui n'a été mesurée.



(a) Galfan



(b) Galvalume

Figure 4: Schéma montrant les différents domaines où la dissolution de Zn et Al sélective se produit en fonction du pH et le potentiel à 25 °C. Les lignes en pointillés sont les limites entre ces différents domaines. Les traits pleins présenter les résultats des essais potentiodynamiques balayage dans lequel les points de bleu sont des points critiques, où la dissolution sélective des changements Al à celle de Zn et vice-versa.

5. Identification du phénomène de dissolution sélective pendant la corrosion d'alliage Zn-Mg-Al.

Les comportements de dissolution des éléments différents de Zn-Mg-Al alliages dans le mécanisme de corrosion a été identifié par la combinaison de la technique AESEC, des essais cycliques de corrosion et de caractérisation de la surface après les essais de corrosion dans milieux chlorure et sans chlorure. Le rôle importance de la phase riche en Al dans la microstructure de l'alliage Zn-Mg-Al est de servir comme cathode dans le stade initial du processus de corrosion, tandis Zn et Mg sont sélectivement dissoute à des régions anodiques. Le pH a augmenté en raison de la réaction cathodique conduit à la dissolution Al via le mécanisme de dissolution cathodique. Pour les alliages contenant du Mg, nous proposons que la résistance à la corrosion améliorée soit obtenue par une stabilisation de simonkolleite et hydroxysulfate de zinc qui sont plus protectifs par rapport à l'oxyde de zinc et de hydrozincite. À des stades ultérieurs, pour Zn-Al-Mg, la résistance à la corrosion est renforcée par la formation d'hydroxydes doubles lamellaires (LDH). Selon l'une modélisation thermodynamique, les ions Mg^{2+} lient l'excès des anions carbonate ou sulfate tamponnant le pH et empêchant la formation de produits solubles / moins protectifs. Une dissolution préférentielle de Zn et Mg dans les stades initiaux de la corrosion est confirmée par la dissolution dans l'expérience *in situ* et semble jouer un rôle important dans le processus de corrosion.

Chapter I:

Introduction

1. Introduction

1.1. Origin and objectives of the PhD study

The incorporation of new coating materials, lighter alloys and new grades of steel has become an important objective of the automotive industry in an effort to produce lighter, more fuel efficient automobiles. However, the possibility of galvanic corrosion induced by asymmetric metal/metal couplings is a major obstacle for the marketing of the new coating materials. In fact, the report of the United States Automotive Materials Partnership in 2005 [1,2] cited galvanic corrosion as one of the major problem to be surmounted in the evolution of the next generation of the multi-material automobile.

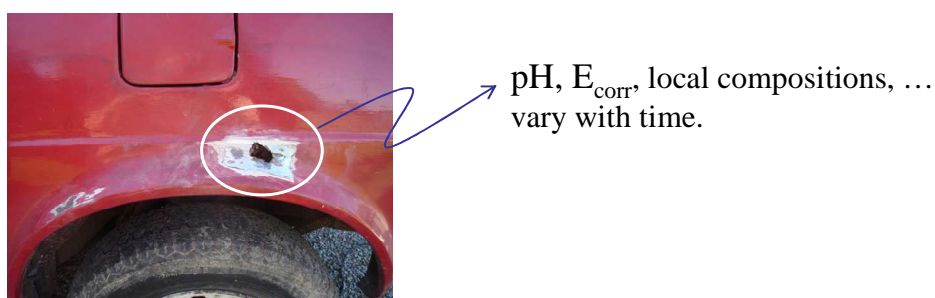


Figure 1-1: Example of galvanic corrosion of alloy coatings on steel in automobile

A long range goal of current research is to develop predictive models of galvanic coupling for materials in the automotive industry based on electrochemical properties which are defined by open circuit potential, polarization curve, composition of electrolyte. These properties depend on surface composition of the alloys exposed to the electrolyte. However, the surface composition is not constant with time (**Fig. 1-1**), it may change markedly as the less noble element is selectively dissolved from an alloy. The objective of this work is to investigate in detail how selective dissolution of alloys (such as Zn-Al or to a lesser extent Zn-Mg-Al) influences their electrochemical properties.

The selective dissolution phenomenon is well known for binary alloy coatings such as Zn-Ni or Zn-Fe where the less noble Zn is selectively removed leaving behind a porous Ni or Fe layer [3]. For these alloys, the electrochemical potentials of the two elements are quite different and therefore the variations are relatively straightforward to predict by using the

simplest kinetic model of galvanic coupling involving the mixed potential theory (Evan's diagram) [4]. However, the components of the Zn-Al and Zn-Mg-Al have similar activities and the specific elements that are selectively dissolved will depend upon the chemical environment, notably pH which may significantly change as a result of balanced anodic and cathodic reactions occurring in a confined zone (**Fig. 1-2**). The cathodic reaction is assumed to be the water (or oxygen) reduction reaction, while the anodic oxidation reaction involves elementary dissolution rates of the various metals exposed to electrolyte. These elementary dissolution rates decide the selective dissolution but are difficult to be distinguished by conventional electrochemical methods.

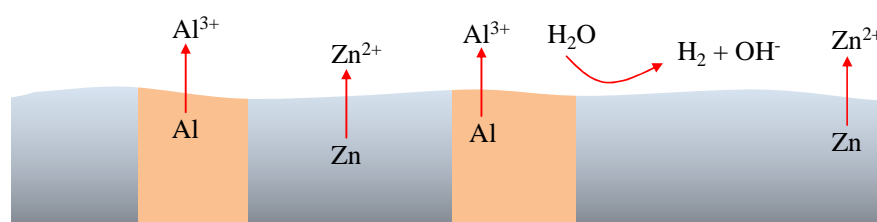


Figure 1-2: Schematic diagram showing reactions occurring in confined zone of Zn-Al alloy

My PhD project aims at overcoming this difficulty by separately quantifying the elementary dissolution rates and investigating selective dissolution phenomena for Zn-Al alloys (and to a lesser extent Zn-Mg-Al alloys) as a function of pH and potential. This project is part of Autocorr European project that is funded by Research Fund for Coal and Steel (RFCS). It seeks to catalog galvanic coupling behavior for different materials and to develop a numerical predictive model of the coupling. The primary technique used in this work is the atomic emission spectroelectrochemistry (AESEC), a combination of spectroscopic and electrochemical methods. This technique is used to measure in real time the partial dissolution rates of each component of an alloy during exposure in different pH and chloride-containing media at open circuit potential and applied potentials. An understanding selective dissolution phenomena as related to corrosion product formation has been attempted.

1.2. Summary of the PhD dissertation

This dissertation is divided into three main parts. Part I is an introductory section and consists of four chapters. **Chapter 1** (this chapter) introduces the origin and objectives of the PhD project, and gives an overview of this dissertation. **Chapter 2** introduces the main

materials used in this work (Galfan and Galvalume). **Chapter 3** reviews the basics of corrosion and electrochemistry of zinc based alloy coatings. It should be noted that in addition to **Chapter 2** and **3**, each chapter in part II includes a bibliographic study. **Chapter 4** introduces atomic emission spectroelectrochemistry (AESEC) technique by which most of the results in this work were obtained. This chapter also provides some original research into the analytical applications of this kinetic technique involving the spatial distribution of time constants.

Part II is the most important part of my work and consists of systematic research into the mechanisms of selective dissolution. Each chapter represents either a published or submitted article. **Chapter 5** is an introductory chapter that illustrates the complexity of the investigated corrosion phenomena by presenting a systematic study of the corrosion of Zn-Mg-Al and Zn-Mg coatings highlighting the relationship between corrosion products and selective dissolution phenomena measured by AESEC. The results of selective dissolution/corrosion of various elements of Zn based alloys are investigated at a microscopic scale by characterizing corrosion products formed on these alloys after accelerated corrosion tests. This work was done in collaboration with ArcelorMittal for the corrosion tests and the supply of the coating materials.

The experimental work with Zn-Mg-Al gives an overview of the selective dissolution phenomena for a complex and interesting system; however the remainder of this thesis is focused on the Zn-Al coatings. This was done for two reasons: (1) It is necessary to understand Zn-Al before we can hope to understand the more complex Zn-Mg-Al system, and (2) there exists two stable commercially available Zn-Al products, Galfan (5% Al-Zn) and Galvalume (55% Al-Zn). By contrast, Zn-Mg-Al products are very new and are under development at this time and there is no stable material supply.

Chapter 6 discusses the selective dissolution of Zn and Al from 55%Al-Zn alloy in synthetic rainwater and seawater (having different pH value and different chloride concentration) by *in situ* measurement with AESEC and *ex situ* measurement with immersion test during short term exposure. These results are compared with that from long term exposure which was made by KTH Royal Institute of Technology. This chapter permits a comparison between the AESEC technique and the more conventional immersion experiments and also gives a more detailed correlation between selective dissolution behavior and surface analysis. This chapter contributes to the investigation of the selective dissolution of Zn-Al alloy in a complex and natural electrolyte at 2 different pH values.

Chapter 7 presents a systematic study of the selective dissolution of Zn and Al from 5%Al-Zn and 55%Al-Zn at open circuit potential in a wide range of pH in 30 mM NaCl electrolytes containing by measurement of intrinsic reactivity of Zn and Al in real time. The result is then compared with immersion test in which a layer of corrosion products is formed to understand how the product layer affects Zn and Al dissolution rates and how the reactivity of the materials in short time exposure is correlated with that in longer time exposure. This chapter contributes to the investigation of the selective dissolution of Zn-Al alloy as a function of pH in a simple electrolyte.

Chapter 8 presents the selective dissolution of Zn and Al from 5%Al-Zn and 55%Al-Zn as a function of potential during linear scanning polarization in 0.1 M HCl, 0.1 M NaCl, 0.1 M NaOH electrolytes. The results demonstrate that the selective dissolution depends not only on pH but also on potential. Basically, selective dissolution of aluminum occurs at cathodic potentials and selective dissolution of zinc occurs at anodic potentials. However, in the alkaline solution, the aluminum selective dissolution can happen at the anodic potentials at which zinc is passive. This chapter contributes to the investigation of the selective dissolution of Zn-Al alloy as a function of potential in simple electrolytes.

Chapter 7 and **8** are the key chapters of this dissertation because they map out the selective dissolution of Zn-Al alloys as a function of both pH and potential which are important parameters in galvanic corrosion.

Chapter 9 compares dissolution rates of Zn and Al from 5%Al-Zn during linear scanning polarization and during steady state polarization in which the elementary dissolution rates at constant applied potentials are measured in alkaline solution. This chapter also demonstrates the existence of the inhibition of Al dissolution at zinc active potentials but the explanation has not been confirmed.

Chapter 10 clarifies the inhibition mechanism of Al dissolution by investigating separately the different factors (such as complex microstructure, interfacial pH, corrosion product) which may control the Al dissolution rate during polarization of the Zn-Al alloys in alkaline solution. This is done using a special Zn / Al bielectrode. Zinc containing corrosion products are demonstrated to be the main reason.

Part III gives conclusions and perspectives of this work (**chapter 11**). For conclusion, the selective dissolution phenomena of Zn-Al alloys are systematically investigated as a function of pH and of potential in chloride containing media. Behaviors of Zn and Al dissolution

during different experiments are explained. For perspectives, we discuss the possibility of extending these studies to another complex alloys, such as Zn-Mg-Al.

1.3. List of publications

Part II of this PhD dissertation is an array of published or submitted articles. A list of publications and the author's contribution to each one is given below. Please note that each chapter is self-contained with an introduction and experimental section. This inevitably has lead to some repetition between chapters.

Scientific articles:

1. Understanding corrosion via corrosion product characterization: II. Role of alloying elements in improving the corrosion resistance of Zn-Mg-Al coatings on steel (chapter 5)

P. Volovitch, **T. N. Vu**, C. Allely, A. Abdel Aal, K. Ogle,

Corrosion Science 53 (2011) 2437-2445.

Contribution: XRD, SEM-EDS, and IR analysis, data treatment, and part of data interpretation.

2. The initial release of zinc and aluminum from non-treated Galvalume and the formation of corrosion products in chloride containing media (chapter 6)

X. Zhang, **T. N. Vu**, P. Volovitch, C. Leygraf, K. Ogle, I. Odnevall Wallinder

Applied Surface Science 258 (2012) 4351-4359.

Contribution: AESEC measurement, AESEC data interpretation, and part of the manuscript.

3. The effect of pH on the selective dissolution of Zn and Al from Zn-Al coatings on steel (Chapter 7)

T. N. Vu, P. Volovitch, K. Ogle,

Corrosion Science (Submitted in May 2012).

Contribution: All experimental work, data treatment, data interpretation, and the entire manuscript.

4. Selective dissolution of Zn and Al from Zn-Al coatings on steel during polarization in acidic, neutral, and alkaline solutions (chapter 8)

T. N. Vu, P. Volovitch, K. Ogle,

Contribution: All experimental work, data treatment, data interpretation, and the entire manuscript.

5. The anodic dissolution of zinc and zinc alloys in alkaline solution. II. Al and Zn partial dissolution from 5%Al-Zn coating (chapter 9)

T. N. Vu, M. Mokaddem, P. Volovitch, K. Ogle

Electrochimica Acta 74 (2012) 130-138.

Contribution: SEM-EDS analysis, part of AESEC measurement, data treatment, part of data interpretation.

Conference proceedings:

1. New approach for measuring reactivity and degradation of complex surfaces: a review of recent results

P. Volovitch, L. Jiang, **T. N. Vu**, K. Ogle

Book of abstracts of Coatings Science International 2011 (COSI-2011), Noordwijk, The Netherlands, June 2011, pp. 47-50

2. Selective dissolution of Zn and Al from Zn-Al alloy coatings on steel

T. N. Vu, K. Ogle, P. Volovitch

Book of abstracts of the European corrosion congress (EUROCORR2011), Stockholm, Sweden, Sept. 2011, p. 31

3. Comparative study of corrosion mechanisms for Zn, ZnMg, and ZnMgAl coatings on steel

P. Volovitch, C. Allely, **T. N. Vu**, L. Diaz, K.Ogle

Book of abstracts of the European corrosion congress (EUROCORR 2011), Stockholm, Sweden, Sept. 2011, p. 29

Conference / meeting participation:

1. Oral presentation at the European corrosion congress (Eurocorr2011) in Stockholm, Sweden (September 2011).

2. Oral presentations at Autocorr European RFCS meeting in Linz, Austria (April 2010); Dortmund, Germany (November 2010); Stockholm, Sweden (May 2011); and Paris, France (December 2011).

References

¹ RFCS 2008 Call – AutoCorr submission, 2008.

² Richard T. Barrett, Fastener design manual, NASA reference publication 1228, 1990.

³ A. Besseyrias, F. Dalard, J. J. Rameau, H. Baudin, Corros. Sci. 121 (1997) 1883.

⁴ C. Wagner, W. Traud, Z. Electrochem. 44 (1938) 391.

Chapter II:

Introduction to Galfan and Galvalume

2. Introduction to Galfan (5% Al-Zn) and Galvalume (55% Al-Zn)

In this chapter, we will introduce the phase diagram of the Zn-Al system and the associated microstructure. An overview of the history and industrial processing of commercial 5% Al-Zn (GalfanTM) and 55% Al-Zn (GalvalumeTM) coatings which are the main materials of this work is also given. Understanding the microstructures of the materials is important for the interpretation their dissolution behavior.

2.1. Zn-Al phase diagram

Aluminum is added to the zinc bath to improve corrosion resistance of Zn based coatings by either inhibiting the formation of Fe-Zn phases (therefore allowing the formation of a dominant zinc overlay which has a good galvanic protection to steel) or introducing multiphase microstructures in the overlay coating. However, different phases in the microstructure of the coating contribute differently to its corrosion resistance. An examination of the Zn-Al equilibrium phase diagram (**Fig. 2-1**) will help us to predict the different phase which may be formed in the coating structure [1]. The solid phases present in the Zn-Al system include β' , β , and η . β' and β are the Al rich and Zn rich portions respectively. η is the Zn terminal solid solution, and (Al) is the Zn-in-Al solid solution (β' is therefore special case of (Al)). The transformations involving these phases are given in **Table 2-1**.

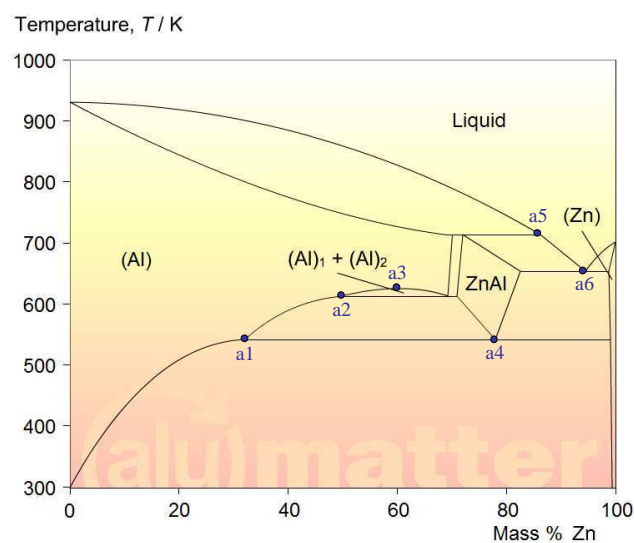


Figure 2-1: Zn-Al phase diagram [2,3]

Table 2-1: Phase transformation in the Zn-Al system

Point	Phase transformation	Zn composition (wt%)	Temperature (K)	Transformation type
A1	$(Al) \rightarrow (Al) + \eta$	32	542	
A2	$(Al) \rightarrow (Al) + \beta$	50	613	
A3	$(Al) \rightarrow \beta' + \beta$	61	627	critical
A4	$\beta \rightarrow \beta' + \eta$	78	542	eutectoid
A5	$L \rightarrow L + \beta$	86	714	
A6	$L \rightarrow \beta + \eta$	94	654	Eutectic

2.2. Galfan (5 wt% Al-Zn)

Galfan coated steel was developed and patented by Unites States Inland Steel Company in 1977. The subsequent development of Galfan coated steel continued in 1979 in a research sponsored by The International Lead Zinc Research Organization (ILZO) at the Center de Recherché Metallurgiques (CRM) in Liege, Belgium. Galfan coated steel was first commercialized production in 1982 in Ohio, United States [4]. Galfan is a zinc alloy coating that offers performance advantages as compared to conventional hot-dip galvanizing. Consisting of 95 wt.% zinc and 5 wt.% aluminum-mischmetal, the Galfan alloy coating provides a superior corrosion protection, extraordinary ability to form and draw; excellent ability to paint, and good ability to weld. The ductility and strong anti-corrosion properties of Galfan make it a coating highly suited for deep-drawn parts and parts requiring a high level of corrosion protection. It is ideal for sheet steel, wire, and tubes [5]. Galfan coatings are typically 7-23 μm thick (**Table 2-2**). In certain applications, a 10 micron Galfan coating can replace a 20 micron galvanized coating, providing better weldability, drawability, and corrosion resistance. Galfan can thus reduce costs, simplifying secondary processes and eliminating the need of post-treatment [6].

Galfan coatings have a better anti-corrosion property than pure zinc coatings with the same thickness in severe marine environments. In moderate marine, industrial, and rural environments, however, these coatings perform no better than pure zinc [7]. They can be used to replace thick galvanized coating and post-galvanizing treatments.

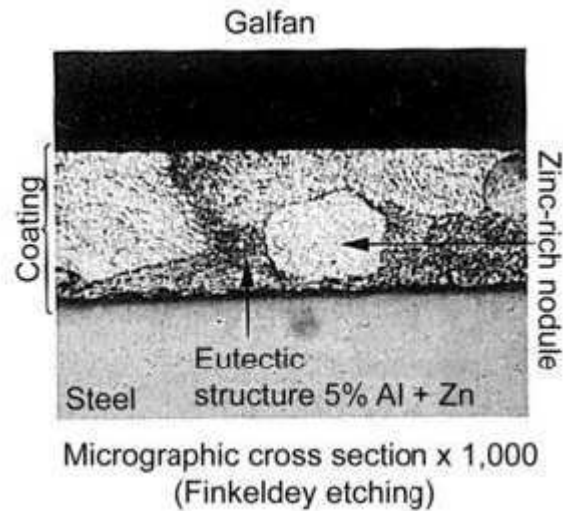
Table 2-2: The standard Galfan coating values and corresponding thicknesses [6]

EN 10327 standard	μm per side	Minimum nominal g/m^2 double side
ZA095	7	95
ZA130	10	130
ZA200	15	200
ZA255	20	255
ZA300	23	300

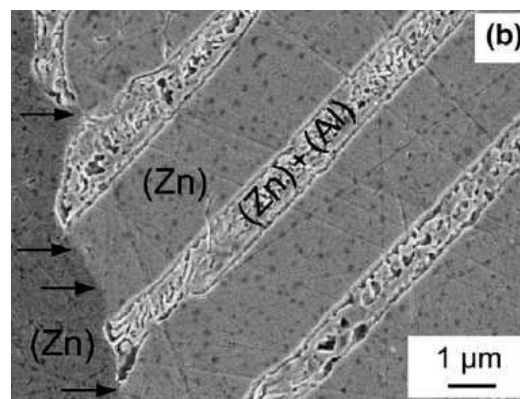
Microstructure of Galfan

The microstructure of Galfan coating is characterized by a matrix of eutectic phase, which consists of zinc-rich and aluminum-rich lamellae, and scattered regions of primary zinc (**Fig. 2-2**). The fineness of the structure increases with increasing cooling rates, and the structure is completely eutectic when fast-cooled. It is also oriented in the direction of cooling. One characteristic of the Galfan microstructure is the absence of a brittle intermetallic phase between the steel and the coating which is not preferably formed at a low temperature and a high aluminum content of the bath [7]. The absence of this brittle phase is directly responsible for the high formability of Galfan-coated steel [8,9].

The as-galvanized Galfan coatings are typically characterized by the appearance of spangles, which often show a strong (0001) basal texturing [10]. Also, the surface of fresh galvanized coating is readily oxidized in air to form a very thin oxide film. The surface oxide film on Galfan is usually enriched with aluminum due to the high affinity between aluminum and oxygen [11].



(a) Cross sectional view



(b) eutectic phase

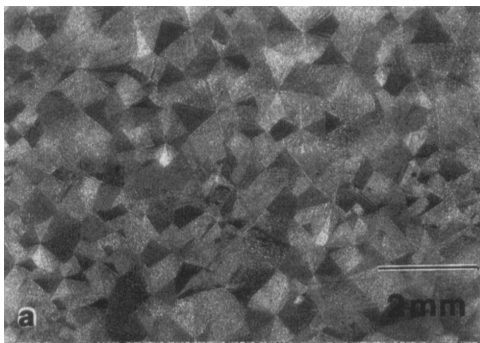
Figure 2-2. Microstructure of Galfan [3,6]

Galfan is obtained by continuous hot-dip coating in a molten bath made up of approximately 95 % zinc and 5 % aluminum. Al is added to the bath to prevent the formation of a thick, continuous layer of Zn-Fe intermetallic that could lead to poor coating adhesion during forming [12,13]. Galfan Zn-5 wt.%Al coating also contains about 0.1 wt.% mischmetal (cerium and lanthanum) to increase wettability of the bath and reduce the incidence of bare spots. About 0.1 wt.% magnesium is sometimes added to counteract the adverse effects of lead and tin impurities on intergranular corrosion and paint adhesion [7].

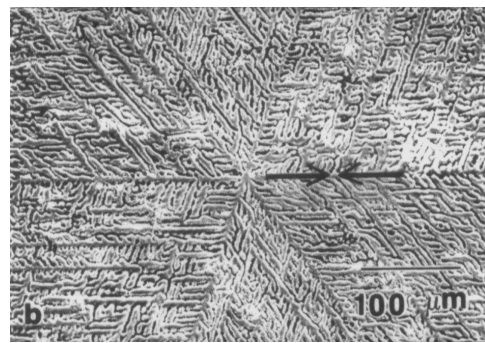
2.3. Galvalume (55 wt% Al-Zn)

Galvalume was first prepared in 1962 and patented by Bethlehem International Engineering Corporation. Its first commercial production was started in 1972 [14]. The Galvalume coating is comprised of approximately 55% aluminum, 43.5% zinc, and 1.5% silicon. In the construction application, Galvalume is known as an excellent product for long-life roofing sheets, especially low-slope roofing on industrial buildings. For low-slope roofing, the product is applied mostly as a bare (unpainted) roofing sheet exposing directly to the atmosphere. Galvalume steel sheet is also used as a prepainted sheet when a more decorative finish is desired. When used for low-slope roofing, Galvalume has been shown to perform well for over 20 years and in many cases over 25 years without failure [14].

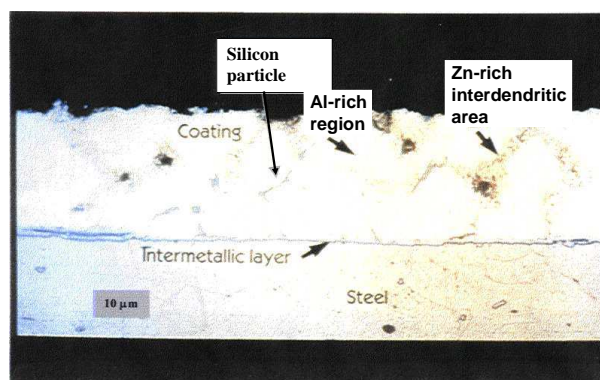
Microstructure of Galvalume



(a) Spangle finish [10]



(b) Dendrite arm spacing [10]



(c) Cross sectional view [15]

Figure 2-3. Microstructure of Galvalume

The microstructure of the 55Al-Zn coating is shown in the photograph below (**Fig. 2-3**). The coating has two principal phases in its microstructure. One phase is the primary aluminum-rich dendritic phase that begins to grow initially during solidification. The other is an interdendritic zinc-rich region that forms when the zinc concentration in the solidifying liquid reaches high level. The origin of these phases is explained by the aluminum-zinc phase diagram. Other phases in the microstructure of the coating layer include small discrete particles of elemental silicon, and probably an iron-rich phase which results from dissolved iron in the bath during production process [15].

Silicon is added into the bath to promote its adherent property and to prevent the excessive growth of an intermetallic alloy layer at the steel/coating interface [16,17]. It participates in the solidification process of Galvalume to produce Al-Si eutectic at temperature from 520°C to 480°C which is mainly responsible for the observed silicon distributions in the interdendritic region (flowery pattern on the surface) and to form Al-Zn-Si eutectic product at temperature of 381°C distributing in zinc-rich network (needle-like morphology) [18].

2.4. Production method - Hot-Dip galvanizing

Hot-dip galvanizing [8] is a method used to produce a zinc based coating on steel by immersing it in a bath of molten zinc (as well as some other additives if necessary). This is the oldest and the most popular process for producing zinc based coatings. In general, an article to be galvanized is cleaned, pickled and fluxed in a batch process or heat-treated in a reducing atmosphere to remove surface oxide. It is then immersed in a bath of molten zinc and aluminum mixture for a sufficient time, after which it is withdrawn and cooled. Any of these stages can affect coating quality.

The portions of different phases of a Zn based coating on steel depend on the diffusion rate [19]. The main diffusion process is diffusion of Zn through the galvanized layer toward the iron interface. The diffusion of the iron moving outward occurs at a much lower rate.

Hot-dip galvanizing can be divided into two main processes: batch galvanizing and continuous galvanizing. The latter is commonly used to produce Galfan and Galvalume.

2.4.1. Batch Galvanizing

In the batch hot-dip galvanizing [8], the articles need to be galvanized are first degreased and then pickled to remove rust from steel parts. Each of the degreasing and pickling steps is followed by a water rinse. The most common degreasing process uses heated (65 - 82°C) alkaline solution. Aqueous solutions of 3-14 wt.% sulfuric acid or 5-15 wt.% hydrochloric acid are generally used in pickling. To avoid over pickling, inhibitors are often used.

The molten zinc bath generally operates in a temperature range of 445 – 454°C. The bath temperature affects the fluidity of the molten zinc, the rate of formation of oxides on the bath surface, the rate of coating solidification, the coating thickness, and the amount and structure of the coating layer. The immersion time is usually in the range of 3 – 6 min. The speed of immersion and withdrawal influence the coating uniformity, particularly with large articles.

2.4.2. Continuous galvanizing

In the continuous hot-dip coating process [8], coils of steel are welded end to end and are coated at speeds of up to 200 m/min. In general, there are “hot” and “cold” continuous hot-dipping processes. The major different between the “hot” and “cold” processes is in the preparation of the steel surface. In the “hot” process the steel sheet enters an alkaline bath that removes oils, dirt, and residual iron fines from the rolling process. This is followed by a further cleaning stage with mechanical brushing and electrolytic alkaline cleaning. The sheet then passes into a radiant tube furnace containing a mixture of hydrogen and nitrogen that reduces surface iron oxides. The steel sheet is also heated up to a temperature of re-crystallization. The steel is then cooled to near bath temperature before entering the zinc bath. In the “cold” process, the steel sheet is cleaned, pickled, and fluxed in-line with no heating but required to be dried from aqueous flux solution of ammonium chloride and zinc chloride before entering the zinc bath.

After the steel strip exits the bath, a layer of molten zinc is coated on the surface. The thickness of the layer is controlled by passing the strip between wiping dies to remove excess metal with a stream of gas. Forced-air cooling is used to reduce the sheet temperature.

2.5. Summary

Galvalume (55% Al-Zn) and Galfan (5% Al-Zn) have been commercially produced for several decades. Both of them have complex microstructures: Galfan consists of a zinc-rich phase (η) and a eutectic phase in which zinc-rich lamellae (η) are surrounded by aluminum-rich lamellae (β); Galvalume has two principle phases which are aluminum-rich dendritic and zinc-rich interdendritic (with a minor phase of silicon particles). From these phases, Zn and Al dissolution behaviors are probably different. Industrial production methods of Galfan and Galvalume which may affect their microstructures are also introduced in this chapter. Understanding the microstructure of Zn-Al alloys should help us to understand their corrosion.

2.6. References

- ¹ A.R. Marder, The metallurgy of zinc coated steel, *Prog. Mater. Sci.* 45 (2000) 191-271.
- ² <http://aluminium.matter.org.uk/content/html/ENG/default.asp?catid=79&pageid=-297682400>
- ³ G.A. Lopez, E.J. Mittemeijer, B.B. Straumal, Grain boundary wetting by a solid phase: microstructural development in a Zn-5 wt% Al alloy, *Acta. Mater.* 52 (2004) 4537-4545.
- ⁴ Rare-earth Information Center News. Energy and mineral resources research institute Iowa state university, 1985.
- ⁵ http://www.expert-steel.com/en/products_1.html
- ⁶ Steel coated with Galfan zinc-aluminum alloys, The product catalogue - European edition, ArcelorMittal, 2008.
- ⁷ R. Baboian, Corrosion tests and standards: application and interpretation, 2nd edition, 2005, pp. 621-623.
- ⁸ X. G. Zhang, Electrochemistry and Corrosion of Zinc, first ed., Springer, 1996.
- ⁹ R. F. Lynch, Hot-dip galvanizing alloys, *J. Met.* 39 (1987) 39-41.
- ¹⁰ A. R. Marder, Microstructural characterization of zinc coatings, in Zinc-Based Coating Systems: Metallurgy and Performance, G. Krauss and D.K. Matlock (eds.), the Minerals, Metals and Materials Society, Warrendale, Pennsylvania, 1990, pp. 55-82.

-
- ¹¹ V. Leovy, B. Schmitz, Surface chemistry of Zn and Zn/Al hot-dipped steels: Influence of some processing parameters, *Scand. J. Metall.* 17 (1988) 17-23.
- ¹² H. E. Townsend, Continuous hot dip coatings, *ASM Metals Handbook* (vol. 5), American Society for Metals, Materials Park, Ohio, 1994, pp. 339-348.
- ¹³ S. Feliu Jr., V. Barranco, XPS study of the surface chemistry of conventional hot-dip galvanised pure Zn, galvanneal and Zn–Al alloy coatings on steel, *Acta. Mater.* 51 (2003) 5413–5424.
- ¹⁴ J. Yoon, Galvanizing revamping proposal for continuous galvalume line, 2006.
- ¹⁵ Galvalume coated steel sheet, GalvInfo Center, 2003.
- ¹⁶ J. H. Selverian, A. R. Marder, M. R. Notis, the effect of silicon on the reaction between solid iron and liquid 55 wt pct Al-Zn baths, *Metall. Mater. Trans. A* 20 (1989) 543-555.
- ¹⁷ J. H. Selverian, A. R. Marder, M. R. Notis, Preparation of cross sections of thin-coated sheet steel for analytical electron microscopy observation, *J. Electron Micr. Tech.* 5 (1987) 223-226.
- ¹⁸ R. Y. Chen, D. J. Willis, The behavior of silicon in the solidification of Zn-55Al-1.6Si coating on steel, *Metall. Mater. Trans. A* 36 (2005) 117-128.
- ¹⁹ J. Mackowiak, N. R. Short, Metallurgy of galvanized coatings, *Int. Mater. Rev.* 1 (1979) 237-263.

Chapter III:

Basic introduction to corrosion of Zn and Zn-Al coatings

3. Basic introduction to corrosion of Zn and Zn-Al coatings

Zinc based alloys have been used as anti-corrosion coatings since 1742 [1] to improve the aqueous corrosion of steel. They function by at least three mechanisms: barrier protection, galvanic protection, and the formation of inhibiting corrosion products. In the barrier mechanism, the coating serves to isolate the underlying metal from the corrosive environment and will first corrode. The barrier mechanism is effective as long as the coating is continuously intact. Continuity is particularly important with noble coatings so that localized pitting due to galvanic attack is avoided. Barrier coatings must also have a lower corrosion rate than the substrate. In the galvanic mechanism, the zinc based coating is less noble than the underlying steel substrate, so that it corrodes preferentially and provides galvanic protection to the substrate that may be exposed at pores, cut edges, or scratches in the coating to electrolyte. In the inhibition mechanism, corrosion products from the sacrificial zinc containing coating act as a barrier to further corrosion.

In this chapter, we will present the corrosion behavior of pure Zn as a function of pH, the sequences of corrosion products formed on pure Zn, and the corrosion mechanism of pure Zn in confined zones. These are well understood. After that, the selective dissolution problem with binary Zn-Al alloys will be discussed. Note that this chapter does not provide an entire bibliography of selective dissolution phenomenon of Zn-Al alloys.

3.1. Corrosion of zinc coating

The corrosion of zinc coating has been investigated extensively and as early as 1932, Roetheli *et al.* [2] demonstrated that the corrosion rate of pure Zn as a function of pH in aerated aqueous solutions depends upon the nature of the corrosion product films. They demonstrated that zinc was rapidly corroded in aerated solutions with pH less than 6 or greater than 12.5 where the corrosion products have high solubility and hydrogen ions, hydroxyl ions, or oxygen can reach the metal surface. In solutions having pH values from 6 to 12.5, the low corrosion rates were attributed to the presence of dense and adherent protective corrosion product films. They also indicated a significant diminution of the oxygen solubility as the pH increased in NaOH solution having concentration higher than 1 M. The corrosion

rates which are proportional to the oxygen concentration would be higher than observed if there was not the oxygen solubility diminution.

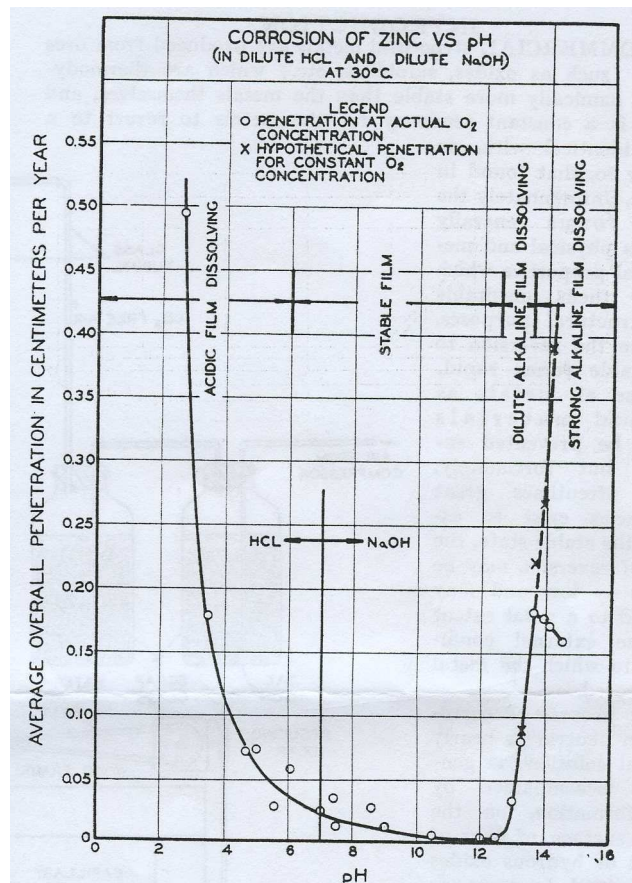


Figure 3-1: Corrosion rate of zinc as a function of pH in an immersion test at 30°C showing 4 different regions: (1) acidic film dissolving; (2) stable film; (3) dilute alkaline film dissolving; (4) strongly alkaline film dissolving. Solutions were prepared from HCl and NaOH. The pH was determined two times per day [2].

To understand the formation and growth of corrosion products during the atmospheric corrosion of zinc, Odnevall Wallinder *et al.* showed the corrosion product sequence formed on zinc coating when it was exposed in different environments (**Fig. 3-2**). $\text{NaZn}_4\text{Cl}(\text{OH})_6\text{SO}_4 \cdot 6\text{H}_2\text{O}$ was demonstrated to be formed in the marine atmosphere [3,4]; $\text{Zn}_4\text{SO}_4(\text{OH})_6 \cdot n\text{H}_2\text{O}$ was formed in the rural atmosphere [5-8], $\text{Zn}_4\text{Cl}_2(\text{OH})_4\text{SO}_4 \cdot 5\text{H}_2\text{O}$ appeared after the urban and industrial exposures [3,9,10], $\text{Zn}_5(\text{OH})_8\text{Cl}_2 \cdot \text{H}_2\text{O}$ and $\text{Zn}_5(\text{CO}_3)_2(\text{OH})_6$ were present in most corrosive environments [5,11-15].

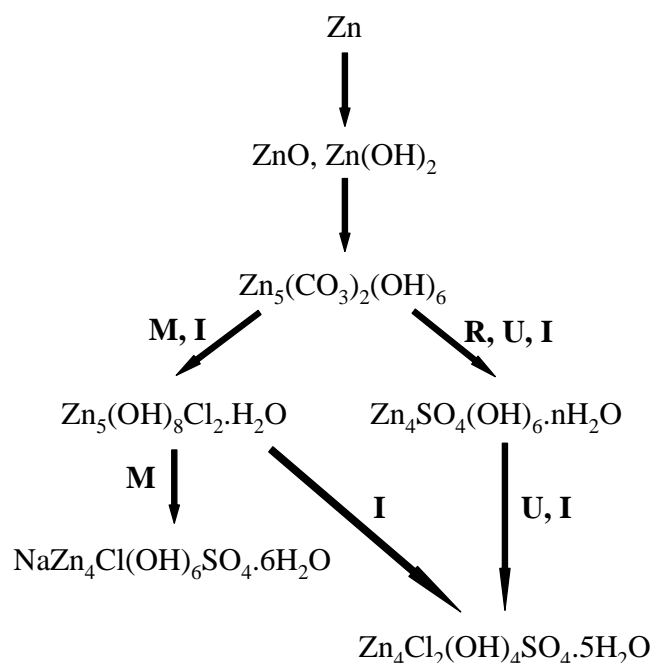
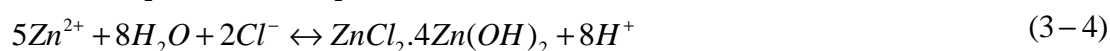
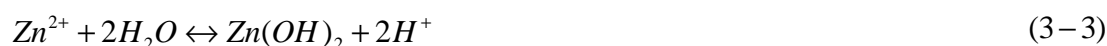


Figure 3-2: Reaction sequences in the marine (M), the industrial (I), the rural (R), and the urban (U) atmospheres (after ref. [3-10]).

The time dependence of the corrosion of zinc coated steel was investigated by Yadav *et al.* [16]. They showed that the corrosion of a zinc coating on steel in a simulated marine atmospheric environment under the cyclic wet-dry condition progressed through three well-defined stages (**Fig. 3-3**). In the first stage, zinc dissolved as Zn^{2+} which diffused outward through pores of the corrosion products. The layer of corrosion products, which were mainly $\text{ZnCl}_2 \cdot 4\text{Zn(OH)}_2$, seem not to act as a barrier for the mass transports of O_2 and dissolved Zn^{2+} in this stage. Consequently, the oxygen reduction reaction (**Eqn. 3-1**) was considered to take place at the almost same rate on the entire surface (including active and inactive sites). The higher anodic dissolution rate (**Eqn. 3-2**) at the Zn active sites than at the Zn inactive sites made the pH of solution in the vicinity of the inactive area increase slightly, and therefore stabilized Zn(OH)_2 (**Eqn. 3-3**) and $\text{ZnCl}_2 \cdot 4\text{Zn(OH)}_2$ (**Eqn. 3-4**) at the inactive area increased. This lead to a higher anodic dissolution rate at the active sites than at the inactive sites.



In the second stage, the corrosion reached the Zn-Fe intermetallic layer (which is formed on a conventional galvanized steel without aluminum used in their work). Once the intermetallic layer was exposed to the electrolyte, it would serve as a cathode due to its more positive potential than the pure zinc layer while the anodic dissolution reaction occurred on the remaining Zn surface. This galvanic protection of the steel substrate was effective only when the surface was sufficiently wet. The coating may lose its ability as sacrificial anode when the surface was covered by a thin electrolyte layer in each dry period. This led to the commencement of underlying steel corrosion. In the third stage, the corrosion of steel really starts with the presence of red rust consisting primarily of FeOOH.

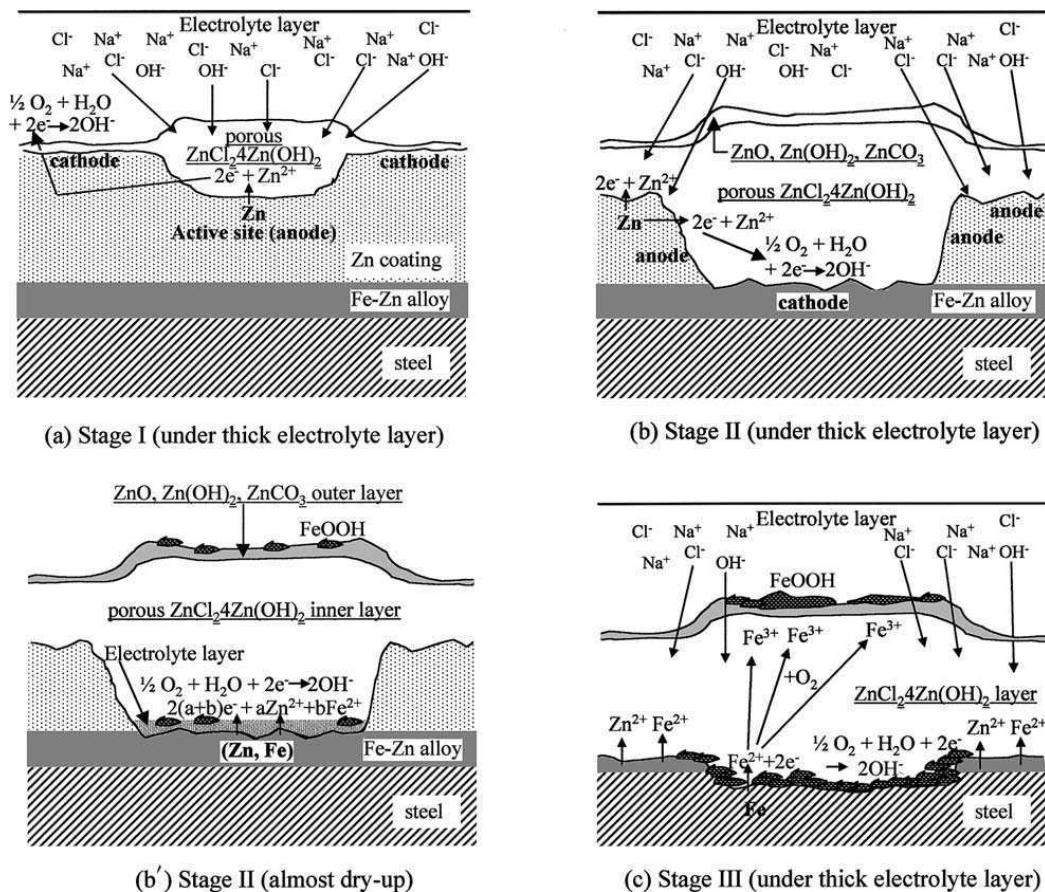


Figure 3-3: Illustration of corrosion mechanism of galvanized steel in a simulated marine atmosphere under the cyclic wet-dry condition [16].

In aluminum containing galvanized steel coatings, the Fe-Zn intermetallic layer is replaced by the Fe_2Al_5 layer [17,18]. However, the electrochemical potential of this layer is much higher than that of the zinc coating and a similar mechanism may be proposed.

Miyoshi and Ito [19] have proposed a four stage progression mechanism to describe the progression of coated steel corrosion in the hem flange environment. This behavior is illustrated by the hypothetical data of **Fig. 3-4** in which the progression of steel corrosion is shown as a function of exposure time. The first curve is that of cold rolled steel (CRS) and the second is that of electrogalvanized steel (E-Zn). The slope of the progression with time gives the rate of steel corrosion.

The corrosion of uncoated CRS progresses in a linear fashion with time. By contrast, the progression of electrogalvanized steel occurs through three time periods (4 stages) characterized by different corrosion rates:

- Stage 1 (t_1): barrier stage during which the zinc coating is intact and serves as a barrier for the steel.
- Stage 2 (t_1): sacrificial stage during which the zinc coating is absent in certain areas and the steel substrate is exposed. However as long as the confined zone is wet, the steel will be protected by galvanic coupling with zinc.
- Stage 3 (t_2) or inhibition stage: the zinc coating is entirely dissolved but the corrosion rate of steel is less than the rate obtained for cold rolled steel. The inhibition is due to zinc corrosion products that may serve as barrier layers on the steel or may buffer the pH in the confined zone preventing the acidification coupled with an accelerated corrosion rate.
- Stage 4 (t_3) or uninhibited steel corrosion: in the final stage, the corrosion rate of steel is equal to the rate of CRS. This stage is reached after the zinc corrosion products have been washed out of the flange environment.

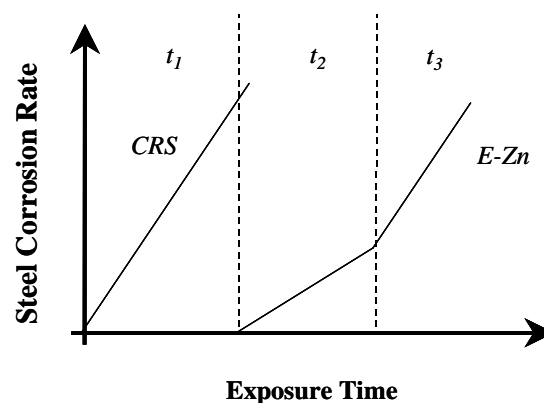
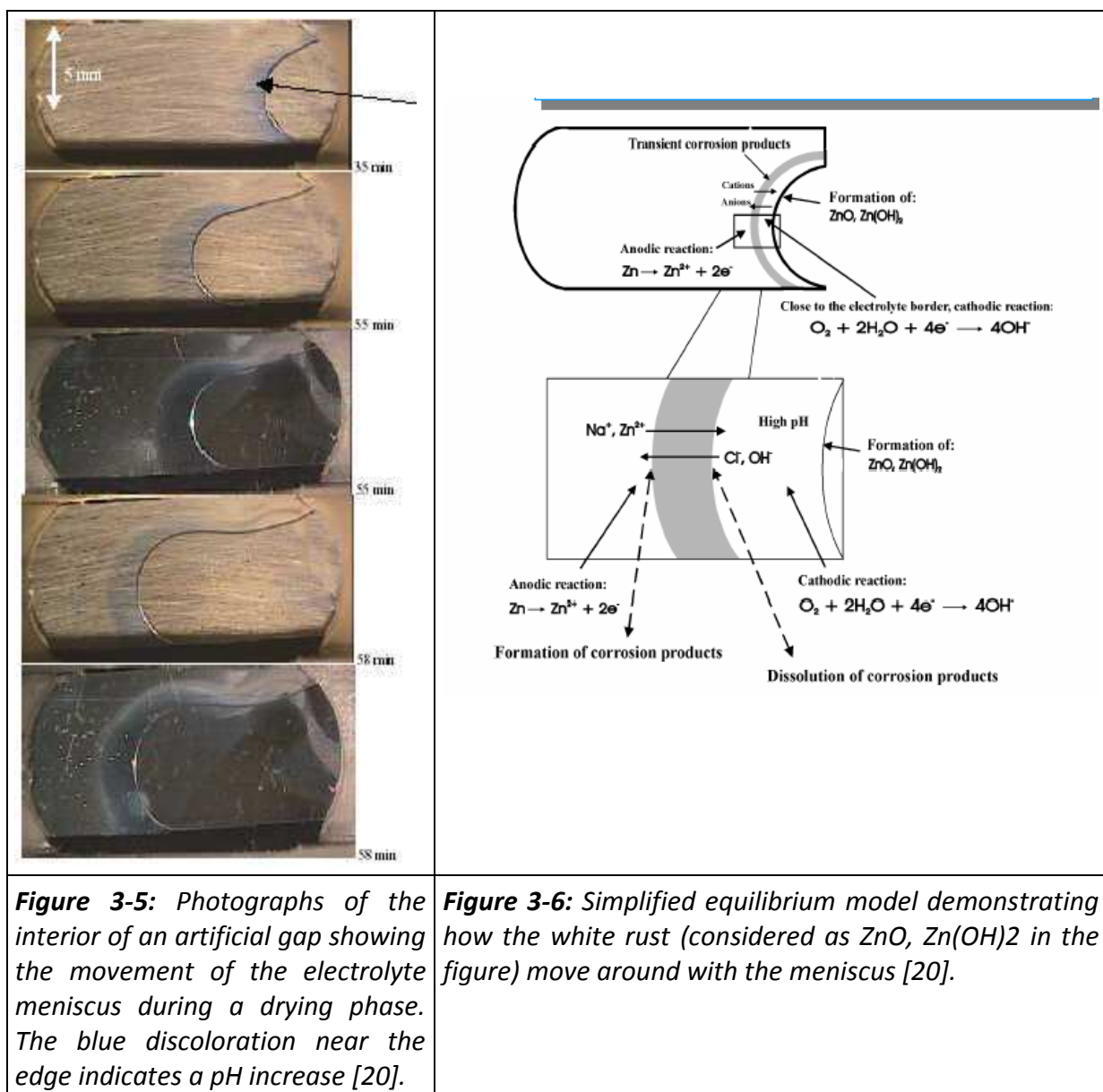


Figure 3-4: Hypothetical curves showing the progression of steel corrosion in the flange environment. Three different time periods indicated as t_1 , t_2 , and t_3 .

It is clear that no coating will alter the rate of steel corrosion in stage 4. Therefore, the effect of the coating can be understood as being due to three unique mechanisms:

1. Reduction of the intrinsic corrosion rate of the coating thereby leading to an increase in the duration of stage 1 and 2.
2. Decreasing the solubility of the corrosion products of the coating, thereby leading to an increase in stage 3.
3. Increasing the protective nature of the corrosion products of the coating (barrier effects, pH buffering, ion exchange properties ...), thereby decreasing the rate of corrosion in stage 1, 2 and 3.



The work of Miyoshi and Ito considered the evolution of the system over periods of years without talking into account the details of the wet/dry cycles that occur on a much more rapid time scale. D. Persson *et al.* [20] demonstrated the corrosion mechanism of confined zinc surface during the drying process of a zinc crevice in immersion-drying cycles in 1% NaCl. They showed that there was an area of precipitated zinc-containing corrosion products located next to the electrolyte border (**Fig. 3-5 and 3-6**); another area with high pH was seen between the electrolyte border and the corrosion product zone. This high pH was caused by the oxygen reduction reaction occurring in the higher concentration zone, i.e. the border of the electrolyte. The border would move within the confined zone during the wet / dry cycles.

3.2. Corrosion of Zn-Al alloy coatings - selective dissolution

Unlike Zn coatings, the binary Zn-Al coatings do not shown a uniform-thinning corrosion process. Their electrochemical corrosion properties depend on the surface composition which may change significantly due to selective dissolution phenomena in which one component is dissolved faster than the other. It has been demonstrated that the corrosion resistance of Zn-Al alloys increases when the Al composition increases from 5% to 23% [21].

Many researches concerning the selective dissolution have been done. E. Palma *et al.* [22] demonstrated that during the early stages of atmospheric exposure of the 55% Al-Zn life, zinc-rich areas are preferentially corroded first, while aluminum-rich phases stay fairly much unaffected. In a sense, the zinc-rich areas provide galvanic protection while the aluminum-rich areas perform like a barrier coating. D. Persson *et al.* [23] also indicated that during the exposure of 55% Al-Zn to a marine environment the zinc-rich interdendritic areas were sensitive to corrosion while the aluminum-rich dendritic areas are more resistant to corrosion attack. In addition, in an investigation of the metal release in the outermost surface layer of 55% Al-Zn exposed to a marine environment, Qiu *et al.* [24] demonstrated that the mass fraction $Zn/(Zn+Al)$ was between 0.01 and 0.32 (i.e. Al was enriched in the surface and Zn was selectively dissolved) during first two weeks; between 0.55 and 0.8 (i.e. Al was selectively dissolved) after 4 weeks and 26 weeks of the exposure. These results are consistent with the corrosion potential measurement of 55% Al-Zn of J. C. Zoccola *et al.* [25] in which the corrosion potential of pure zinc was observed at the initial stage, followed by an increase to the potential of aluminum due to the depletion of the zinc-rich phase.

Selective dissolution of Zn-Al alloys has been investigated during atmospheric exposure and selective dissolution of Zn was observed at the initial stage of the exposure while that of Al was at the later stage. However, in different environments, the zinc-rich and aluminum-rich phases probably behave differently. I. Odnevall Wallinder *et al.* [26] observed the visual appearance of 55 wt.% Al-Zn samples exposed to deionized water with different pH after 40 < days of exposure in sealed bags. The sample exposed to pH = 1 had a white layer of corrosion products (referring to Zn containing products) with black stains on top of this layer. The sample exposed at pH = 13 however was completely covered by a black layer which was found to contain Al(OH)₃. These results imply a preferential formation of Zn and Al containing products on 55 wt.% Al-Zn at pH 1 and 13 respectively. Unfortunately, a systematic study of the selective dissolution of Zn-Al alloys at these different pH values has not been done and very little information about the dissolution kinetics and mechanism has been clearly established.

One of the major difficulties in investigating the selective dissolution of Zn-Al alloys is how to distinguish zinc and aluminum dissolution rates which contribute to the total dissolution rate of the alloys. For simple binary alloys of noble metals, the combination of electrochemical techniques and Auger electron spectroscopy, X-ray diffraction, X-ray photoelectron spectroscopy have been used to quantify the selective dissolution of CuPd [27], Cu₁₃Au, Cu₁₈Au [28], Cu₃Au [29], and AgPd [30]. However, these methods require disconnecting the sample from the electrolyte and are only suitable for the alloys consisting of noble metals. To quantify the selective dissolution of the Zn-Al alloys, these methods do not work because both Zn and Al are both active. Their surface after being taken out from solution would differ from that in the solution.

3.3. Summary

This chapter has introduced the corrosion of Zn and Zn-Al coatings, as well as noted some specific features of corrosion process occurring in confined zone. The corrosion of the Zn coatings occurs through a uniform-thinning process. That of the Zn-Al coatings is much more complex due to selective dissolution phenomenon. It is not easy to study this phenomenon for binary alloys containing two active elements like the Al-Zn alloys. Therefore, a special technique called atomic emission spectroelectrochemistry (AESEC) will be introduced in next chapter to allow us to solve this issue.

3.4. References

- ¹ J. R. Partington, A history of chemistry, St. Martin's press, New York, 1962.
- ² B. E. Roetheli, G. L. Cox, W. B. Literal, Effect of pH on the corrosion products and corrosion rate of zinc in oxygenated aqueous solutions, *Met. Alloy.* 3 (1932) 73-76.
- ³ I. Odnevall, Atmospheric corrosion of field exposed zinc, A multianalytical characterization from initial films to fully developed layers, Royal Institute of Technology, ISBN 91-7170-866-9, 1994.
- ⁴ I. Odnevall, C. Leygraf, The formation of $\text{NaZn}_4\text{Cl}(\text{OH})_6 \cdot 6\text{H}_2\text{O}$ in a marine atmosphere, *Corros. Sci.* 34 (1993) 1213-1229.
- ⁵ S. Koizumi, S. Shima, Y. Matsushima, A development of black chromate-oxide finished by baking process for galvanized steel, International conference on zinc and zinc alloy coated steel sheet – Galvatech, 1989, 246-253.
- ⁶ T. Biestek, M. Drys, N. Sokolov, D. Knotkova, R. Ramishvili, V. Kozhukharov, M. Zeidel, Atmospheric corrosion of metallic systems. V. Identification of the chemical compounds in the corrosion products of zinc, *Protec. Metals.* 19 (1984) 612-615.
- ⁷ I. Odnevall, C. Leygraf, A comparison between analytical methods for zinc specimens exposed in a rural atmosphere, *J. Electrochem. Soc.* 138 (1991) 1923.
- ⁸ I. Odnevall, C. Leygraf, The formation of $\text{Zn}_4\text{SO}_4(\text{OH})_6 \cdot 4\text{H}_2\text{O}$ in a rural atmosphere, *Corros. Sci.* 36 (1994) 1077-1087.
- ⁹ R. S. Jayasree, V. P. Mahadevan Pillai, V. U. Nayar, I. Odnevall, G. Keresztury, Raman and infrared spectral analysis of corrosion products on zinc $\text{NaZn}_4\text{Cl}(\text{OH})_6\text{SO}_4 \cdot 6\text{H}_2\text{O}$ and $\text{Zn}_4\text{Cl}_2(\text{OH})_4\text{SO}_4 \cdot 5\text{H}_2\text{O}$, *Mater. Chem. Phys.* 99 (2006) 474-478.
- ¹⁰ I. Odnevall, C. Leygraf, The formation of $\text{Zn}_4\text{Cl}_2(\text{OH})_4\text{SO}_4 \cdot 5\text{H}_2\text{O}$ in an urban and an industrial atmosphere, *Corros. Sci.* 36 (1994) 1551-1559.
- ¹¹ J. J. Friel, Atmospheric corrosion products on Al, Zn, and AlZn metallic coatings, *Corros.* 42 (1986) 422-426.
- ¹² E. Johansson, J. Gullman, Corrosion study of carbon steel and zinc comparison between field exposure and accelerated tests, ASTM special technical publication 1239 (1995) 240-256.

-
- ¹³ M. Carbucicchio, R. Ciprian, F. Ospitali, G. Palombarini, Morphology and phase composition of corrosion products formed at the zinc-iron interface of a galvanized steel. *Corros. Sci.* 50 (2008) 2605-2613.
- ¹⁴ D. de la Fuente, J.G. Castano, M. Morcillo. Long-term atmospheric corrosion of zinc. *Corros. Sci.* 49 (2007) 1420-1436.
- ¹⁵ L. Veleva, M. Acosta, E. Meraz, Atmospheric corrosion of zinc induced by runoff. *Corros. Sci.* 51 (2009) 2055-2062.
- ¹⁶ A.P. Yadav, A. Nishikata, T. Tsuru, Degradation mechanism of galvanized steel in wet-dry cyclic environment containing chloride ions, *Corros. Sci.* 46, 361-376 (2004).
- ¹⁷ K.-K. Wang, L. Chang, D. Gan, H.-P. Wang, Heteroepitaxial growth of Fe_2Al_5 inhibition layer in hot-dip galvanizing of an interstitial-free steel, *Thin Solid Films* 518 (2010) 1935-1942.
- ¹⁸ M. Yousaf, J. Iqbal, M. Ajmal, Variables affecting growth and morphology of the intermetallic layer (Fe_2Al_5), *Mater. Charact.* 62 (2011) 517-525.
- ¹⁹ Y. Miyoshi, Y. Ito, Corrosion protection functions of zinc coating on steel sheet, as revealed by the investigation of field cars and laboratory test, *Galvatech'92*, 528.
- ²⁰ D. Persson, A. Mikhailov, D. Thierry, In situ studies of the corrosion during drying of confined zinc surfaces, *Mater. Corros.* 58 (2007) 452-462.
- ²¹ N.-Y. Tang, Y. Liu, Corrosion performance of aluminum-containing zinc coatings, *ISIJ International* 50 (2010) 455-462.
- ²² E. Palma, J. M. Puente, M. Morcillo, The atmospheric corrosion mechanism of 55%Al-Zn coating on steel, *Corros. Sci.* 40 (1998) 61-68.
- ²³ D. Persson, D. Thierry, N. LeBozec, Corrosion product formation on Zn55Al coated steel upon exposure in a marine atmosphere, *Corros. Sci.* 53 (2011) 720-726.
- ²⁴ P. Qui, Quantified in situ analysis of initial atmospheric corrosion, Doctoral thesis in corrosion science, KTH, Stockholm, Sweden, 2011.
- ²⁵ J. C. Zoccola, H.E. Townsend, A.R. Borzillo and J. B. Horton in: S.K. Coburn (Eds), *ASTM STP 646*, American Society for Testing Materials, Philadelphia, 1978, pp 165-184.
- ²⁶ I. Odnevall Wallinder, W. He, P. Augustsson, C. Leygraf, Characterization of black rust staining of unpassivated 55% Al-Zn alloy coatings. Effect of temperature, pH and wet storage, *Corros. Sci.* 41 (1999) 2229-2249.

- ²⁷ J. Gniewek, J. Pezy, J. O'M. Bockris, The effect of noble metals additions upon the corrosion of copper: an Auger spectroscopy study, *J. Electrochem. Soc.* 125 (1978) 17-23.
- ²⁸ H. W. Pickering, Volume diffusion during anodic dissolution of a binary alloy, *J. Electrochem. Soc.* 115 (1968) 143-147.
- ²⁹ A. Pareek, S. Borodin, A. Bashir, G. N. Anka, P. Keil, G. A. Eckstein, M. Rohwerder, M. Stratmann, Y. Grunder, F. U. Renner, Initiation and inhibition of dealloying of single crystalline Cu₃Au (111) surfaces, *J. Am. Chem. Soc.* 133 (2011) 18264-18271.
- ³⁰ J. Laurent, D. Landolt, Anodic dissolution of binary single phase alloys at subcritical potential, *Electrochim. Acta.* 36 (1991) 49-58.

Chapter IV:

Atomic emission spectroelectrochemistry (AESEC)

4. Atomic emission spectroelectrochemistry (AESEC)

4.1. Introduction

In this work, atomic emission spectroelectrochemistry (AESEC) technique is applied to evaluate in real time the dissolution rates of the elemental components of Zn-Al alloys and Zn-Mg-Al alloys coatings in different environments, notably pH, at open circuit potential or applied potential. This technique allows us to measure directly and independently the elementary dissolution rates of zinc and aluminum from the samples during their exposure to the electrolyte. It is particularly suitable for kinetic measurements of leaching and de-alloying (selective dissolution), and it has proved to be a powerful technique in studying the selective dissolution of Fe-Cr alloys during polarization and applying potential in sulfuric acid [1,2], of conversion coating in NaOH [3], the enrichment of Cu on 304 stainless steel surface after linear scanning polarization [4], the selective dissolution of Al from 2024 Al alloy at cathodic potential domain [5], along with other applications [6,7].

4.2. Instrumentation

The AESEC technique consists of an inductively coupled optical emission spectrometer (ICP-OES) coupled to an electrochemical flow cell. The instrumentation may be divided into 3 modules (**Fig. 4-1**): (A) an electrochemical flow cell where a flat solid material is exposed to a flowing electrolyte; (B) a downstream ICP-OES spectrometer that is used to analyze the elemental composition of the electrolyte leaving the flow cell; and (C) a special electronic system that is used to collect the emission intensities and electrochemical data as a function of time.

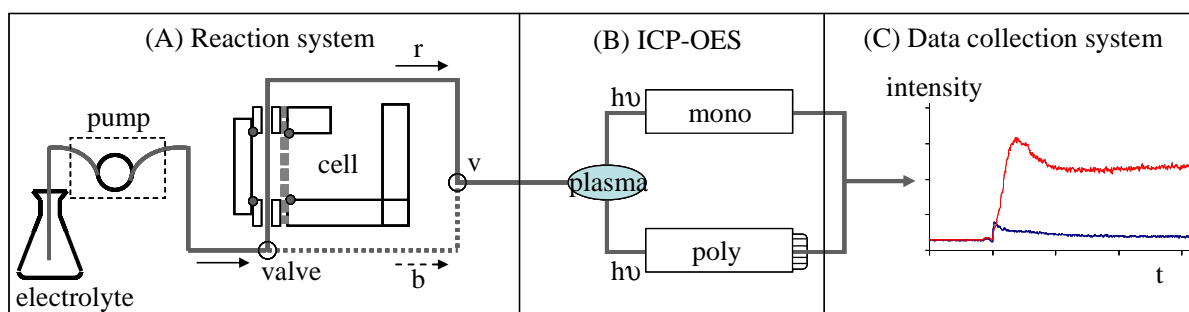


Figure 4-1: Schematic block diagram of the atomic emission spectroelectrochemistry technique: (A) Reaction cell with electrolyte container and peristaltic pump. Arrows indicate direction of electrolyte flow during (b) background experiment with cell bypass and (r) reaction experiment. The valve (v) is used to switch between a background and a reaction measurement. (B) ICP-OES spectrometer: photon ($h\nu$) emitted from the plasma are collected either in a monochromator (mono) or in a polychromator (poly) unit. (C) fast electronics allows real time monitoring the emission intensity of up to 31 wavelengths, 30 from the polychromator + 1 from the monochromator as well as 2 analog signals for electrochemical measurements.

Electrochemical cell

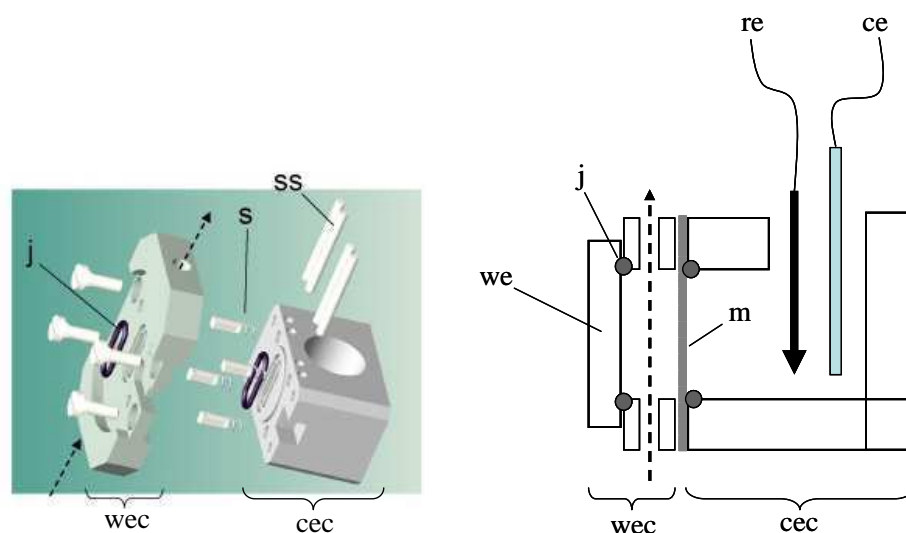


Figure 4-2: A computer image and functional diagram of the electrochemical cell: j = o-ring; s = spring; ss = spring support; wec = working electrode compartment; cec = counter electrode compartment; m = membrane; we = working electrode; ce = counter electrode; re = reference electrode. Dashed line arrows indicate the direction of solution flow.

A flow cell with two compartments and three electrodes constructed from Teflon was illustrated in **Fig. 4-2**. The surface of working electrode is brought in contact with the flowing electrolyte in a small volume compartment (≈ 0.2 ml), separated from a counter electrode compartment by a porous membrane allowing passage of ionic currents while preventing bulk mixing of the two electrolytes.

The geometrical surface area exposed to the electrolyte was measured by dissolving a $5 \mu\text{m}$ zinc coating from an electrogalvanized steel sample and measuring the area of the exposed steel. The value was found to be $0.53 \pm 0.02 \text{ cm}^2$ [8]. The flow rate in the electrochemical cell was adjusted at approximately $0.05 \text{ cm}^3 \text{ s}^{-1}$ and measured for each series of experiments.

The potentiostat was an EG&G Princeton Applied Electronics M273A functioning in the potentiostatic mode. The potentiostat is controlled manually from the front panel with the output analogue current and potential signals being routed into the measuring circuit of the ICP-OES spectrometer. In this project, a counter electrode of Pt wire and a reference electrode of saturation calomel electrode (SCE), or Hg/HgO, or Ag/AgCl were used.

Inductively coupled plasma - optical (atomic) emission spectroscopy (ICP – OES)

Atomic emission spectroscopy is an analytical method deriving analytical information from atomic spectra in the optical region of the electromagnetic spectrum. Atomic emission spectrometry is often referred to as “optical emission spectroscopy” (OES), in particular because the acronym “AES” also refers to Auger electron spectroscopy [9]. Inductively coupled plasma (ICP) is an excitation source, used for the optical emission spectroscopy by 1971 [10], to produce excited atoms and ions that emitted electromagnetic radiation at a wavelength characteristic of a particular element. The emitted radiation can be easily detected when it is in the vacuum ultraviolet (VUV, 120–185 nm), ultraviolet (UV, 185–400 nm), visible (VIS, 400–700 nm), and near infrared regions (NIR, 700–850 nm) [11]. The intensity of this emission is indicative of the concentration of the elements within the sample.

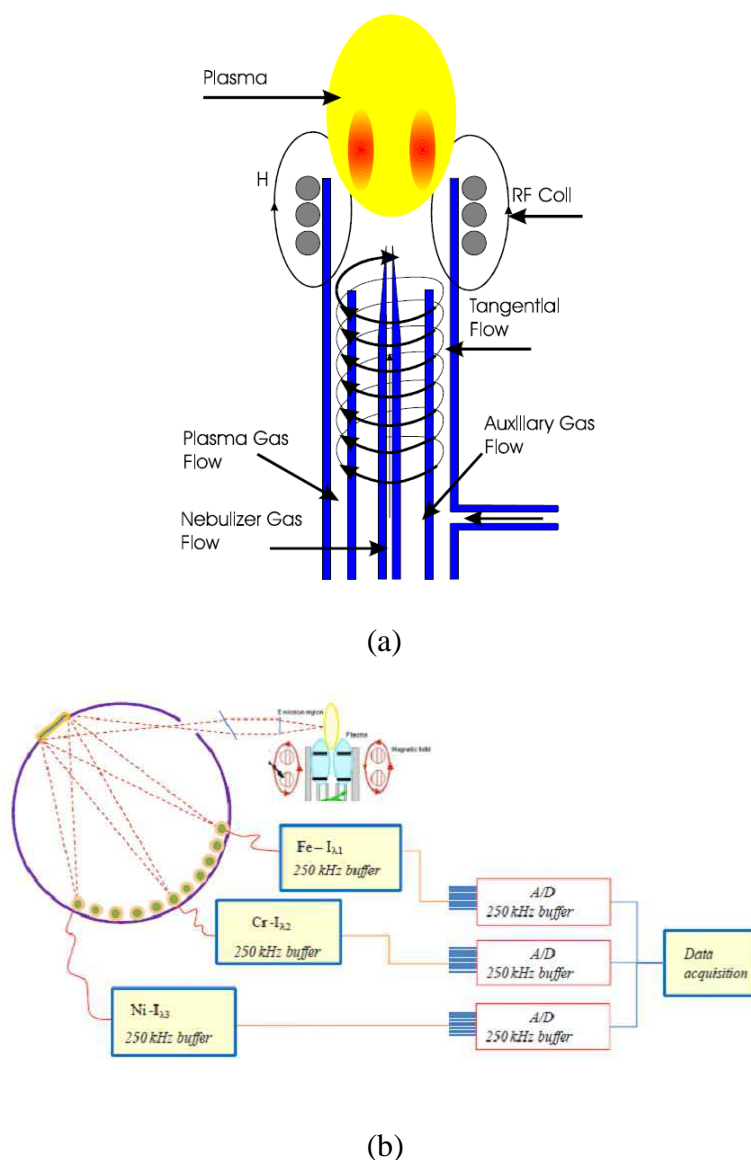


Figure 4-3: (a) A schematic diagram of an ICP torch; (b) Simplified schematic of the data acquisition system from optical system with simultaneous measurement by three 16-bit A/D converters [12,13].

In this work, the ICP-OES spectrometer was used to measure the composition of the electrolyte downstream from the working electrode compartment of the electrochemical cell permitting a qualitative identification of the soluble reaction products and a quantitative measure of the simultaneous dissolution rates of the products. A commercial ICP-OES from HORIBA Jobin Yvon (Ultima 2CTM) was used in this work. It utilizes radiofrequency-(40 MHz, 1 kW) inductively coupled Ar plasma, which is an electrically neutral, highly ionized gas that consists of ions, electrons, and atoms, as the atomization and excitation source. **Fig 4-**

3a gives a schematic diagram of an ICP torch. The circular quartz tube (12–30 mm OD) has three separate gas inlets. The only gas routinely used is argon as it has a high ionisation energy (15.6 eV) and a good capacity to atomise, ionise and excite most of the elements [14]. The gas enters the plasma through the outer channel with a tangential flow pattern at a rate of 8 – 20 L min⁻¹. The auxiliary gas, which travels up the centre channel, also has a tangential flow (0.5 – 3 l min⁻¹) pattern. The nebulizer gas has a laminar flow pattern (0.1 to 1.0 l min⁻¹) and injects the sample into the plasma. The analytical zone is approximately 1 cm above the coils and offers the best optical viewing area for maximum sensitivity [15]. The plasma temperature in the analytical zone ranges from 5000–8000 K (the temperature varies with power, flow rate, etc.). The high temperature assures that most samples are completely atomized.

The signals from the phototubes (mono and poly) were monitored in real time using the QuantumTM software and data acquisition package developed by HORIBA Jobin Yvon, SAS for use with glow discharge spectroscopy. Radiation emitted from the plasma (hν) was collected in the radial direction and collected by a polychromator for the simultaneous detection of 30 predetermined wavelengths and a monochromator that could be used for the detection of an adjustable wavelength. The polychromator used a Paschen–Runge configuration with a 0.5 M focal plane and was equipped with a holographic grating of 3600 grooves/mm. The theoretical resolution of the polychromator was 0.025 nm in the first order and 0.015 nm in the second order covering a spectral range from 165 to 408 nm. The monochromator used Czerny–Turner configuration with a 1.0 m focal plane and was equipped with a holographic grating of 2400 grooves / mm with practical resolution of 0.005 nm in a spectral range from 120 to 320 nm and a resolution of 0.010 nm in a range from 320 to 800 nm. Three 16-bit A/D converters operating at a frequency of 250 kHz are used to continuously monitor the output of the 31 photomultiplier tubes (**Fig 4-3b**). Both polychromator and monochromator were nitrogen purged [16].

The electrolyte was continuously feed into the plasma using a peristaltic pump. The pump served to transfer the electrolyte from the electrochemical flow cell into a concentric glass nebulizer and a cyclonic spray chamber. The hydraulic system was specially optimized to give the best temporal resolution without undue lowering of the detection limits. The nebulizer used in this work was Meinhard nebulizer (Model TR-30-K3) which has a bigger inner diameter than Conikal nebulizer and optimistically operates at a higher flow rate (2.9 ml min⁻¹ vs. 1.0 ml min⁻¹). A higher flow rate yields a better temporal resolution but lowers the

sensitivity due to dilution of the dissolving species into a larger volume per second of electrolyte. However, with the bigger inner diameter, Meinhard nebulizer has a higher ability of preventing itself from blocking by insoluble particles which are formed easily in certain conditions, for example during dissolution of metals in neutral pH.

4.3. ICP-OES calibration

Fig. 4-4 shows a calibration curve on a log-log scale for Zn, Al, and Mg emission intensities covering four orders of magnitude of concentration using standard solutions (Titrosol™). The intensity values are in arbitrary units and the curve demonstrates an excellent linear relationship. Concentrations higher than 10 ppm were not used in this work so as to avoid contaminating the nebulisation system, however linearity is normally maintained to concentrations above 100 ppm [17].

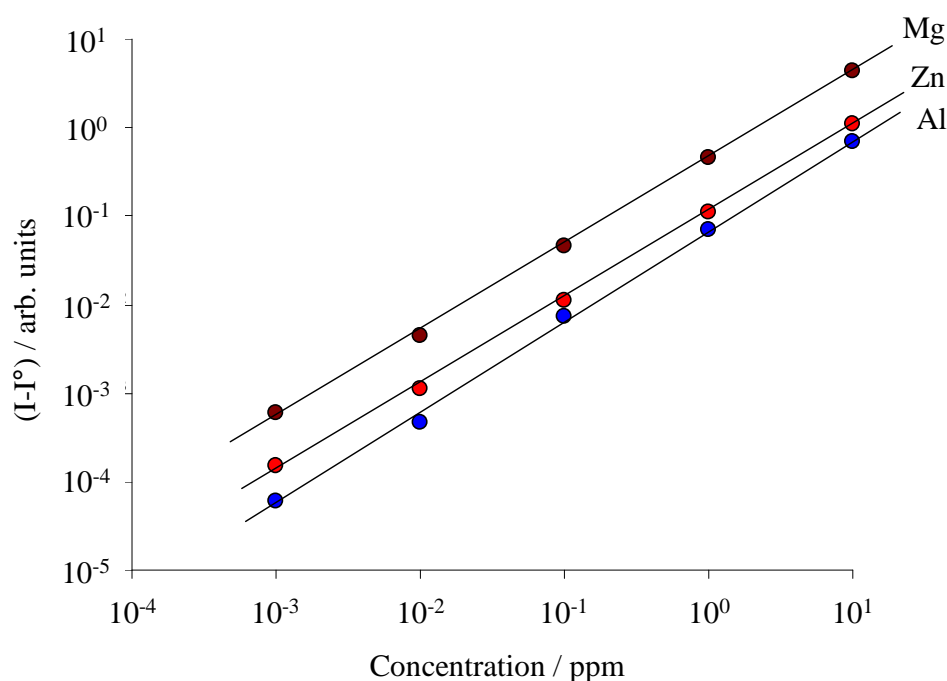


Figure 4-4: Calibration curves on a log-log axis showing the atomic emission intensity as a function of Mg, Zn, and Al concentration at the characteristic wavelengths of 279.553, 213.856, and 167.081 nm respectively.

4.4. Analysis of the AESEC data

The basic quantification principle of ICP - OES is that the emission intensity of a given element in the plasma at its characteristic wavelength is proportional to its concentration in the electrolyte stream (see **Fig. 4-4**). In addition, because the output current and potential signals from the potentiostat are routed into the measuring circuit of the ICP-OES spectrometer, their intensities from the spectrometer are also indicative of the current and potential magnitude.

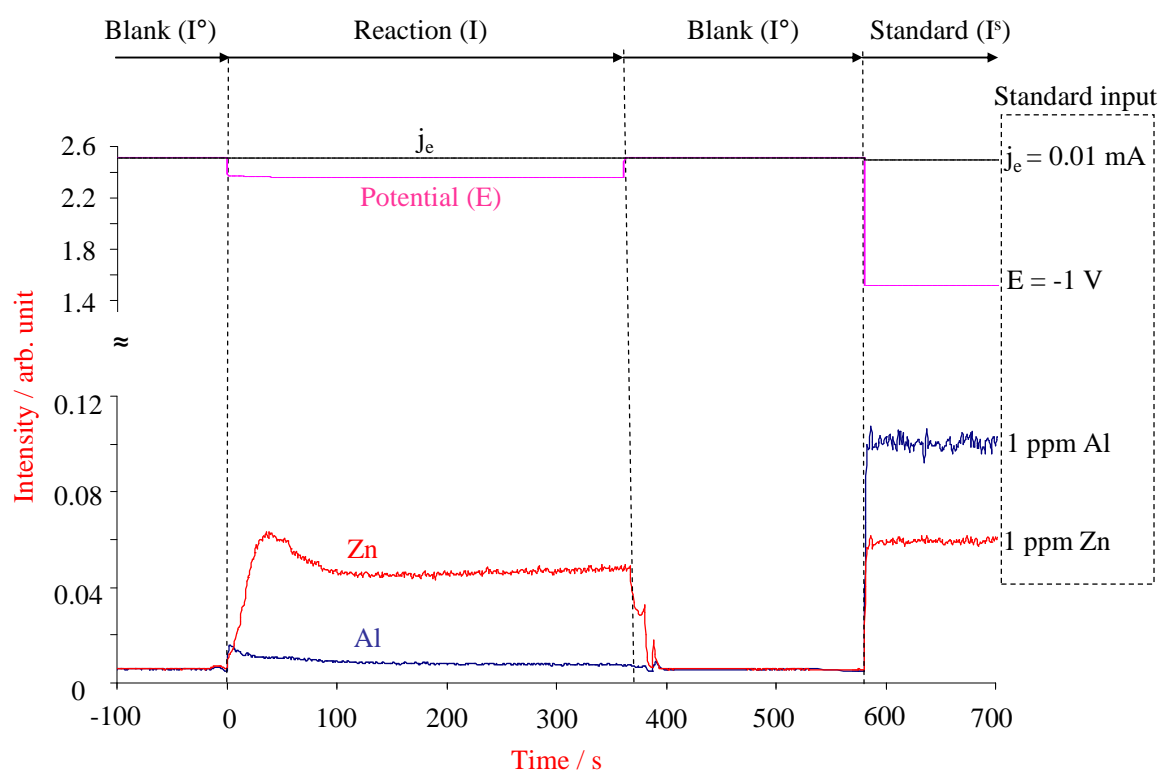


Figure 4-5: An example of the output data obtained by the AESEC technique: spontaneous dissolution of Zn-5%Al alloy in 30 mM NaCl at pH 2, in which the “standard” input k equals to 0.01 mA, -1 V, 1 ppm, and 1 ppm for the electric current, potential, Al and Zn concentration respectively.

Fig. 4-5 shows a typical output data of the AESEC technique with the emission intensity of elements (i.e. Zn & Al) and the electrochemical (i.e. current & potential) signal intensities as a function of time. The elemental concentration (C_M) and the electrochemical parameter can be calculated as:

$$C_M (\text{or } j_e, E) = k \frac{I - I^\circ}{I^s - I^\circ} \quad (4-1)$$

Where j_e is the electrical current, E is the potential, I° is the background intensity, I is the intensity during the reaction period, I^s is the intensity during the “standard” period, and k is the “standard” input (**Fig. 4-5** is shown as an example).

From the elemental concentration (C_M , ppm), the elemental dissolution rate of component M (v_M , $\mu\text{g s}^{-1}\text{cm}^{-2}$) or the elemental dissolution current density (j_M , mA cm^{-2}) of the sample can be also calculated using Faraday equation:

$$v_M = \frac{fC_M}{A} \quad (4-2)$$

$$j_M = \frac{nFfC_M}{1000AM_M} \quad (4-3)$$

In which f is the flow rate of the electrolyte through the cell ($\text{cm}^3 \text{s}^{-1}$), A is the surface area of the sample (all surface reaction rates are normalized to the geometrical surface of the sample exposed to the electrolyte (0.52 cm^2)). This is done for convenience and is not meant to imply that the specific reaction is actually uniform on the surface), F is the Faraday constant (96485 C mol^{-1}), n is the number of electrons transferred in the oxidation step of the component M , M_M is the molar mass of M (g mol^{-1}).

The total current is the sum of the anodic and cathodic partial currents, $i_e = i_a + i_c$. Note that in this work we can use the current density and total current interchangeably since the current density is defined as $j = i/A$, such that we can also write $j_e = j_a + j_c$. The anodic current may in turn be divided into soluble component for each element and an insoluble component, j_{ins} . The soluble components are measured by the ICP-OES (**Eqn. 4-3**). We assume that the insoluble component remains on the surface of the sample (or within the porosity) in the form of a corrosion product or oxide film. Therefore, if the concentration and electrical transients have the same time resolution, the total current may be written as:

$$j_e = j_{\text{ins}} + \sum j_M + j_c \quad (4-4)$$

where j_c is the cathodic partial current and j_{ins} is the partial current corresponding to the instantaneous rate of formation of “insoluble” components of the anodic reaction. (Note that both Zn and Al dissolution pass through oxide/hydroxide intermediates. Although we use the term “insoluble”, in fact this only means that at a given time, the formation of solid intermediates is more rapid than their dissolution leading to an oxide growth on the surface). Under conditions in which $j_c = 0$, both Zn and Al dissolve from the alloy and j_{ins} may be determined by:

$$j_{ins} = j_e - j_{Zn} - j_{Al} \quad (4-5)$$

Under transient conditions, **Eqn. 4-5** cannot be applied directly because of the temporal resolution difference between the electrochemical measurements (fast) and the spectrochemical measurements that are broadened by diffusion and mixing in the hydraulic system. This may be corrected by performing a numerical convolution of j_e and $h(t)$ [17] such that:

$$j^*(t) = \int_0^t j_e(\tau) * h(t-\tau) d\tau \quad (4-6)$$

where $h(t)$ is the time constant distribution for the hydraulic system and τ is simply a variable of integration. Following this operation, the electrochemical data will be on the same time resolution as the concentration data. More precisely, **eqn. 4-5** should be written as:

$$j_{ins} = j_e^* - j_{Zn} - j_{Al} \quad (4-7)$$

Determining the time constants

The time constant distribution was determined by measuring the concentration – time response as follows: A copper electrode was placed in contact with the flowing 1 M HCl for 5 minutes at the open circuit potential, followed by a 0.5 s potentiostatic pulse at 0.1 V vs. Ag/AgCl, and then a return to the open circuit potential. The transitory emission intensities were measured with a time resolution of 0.5 s. A typical result is shown in **Fig. 4-6**. A 0.5 s pulse is considered to be sufficiently short on the time scale of these experiments. The pulsed anodic dissolution of copper gives rise to an asymmetric peak, which increases quickly to a maximum and then returns slowly to the background signal (I°). The time between the

potentiostatic pulse and the first point of Cu intensity which rises above the background, t° , is associated with the time necessary for the copper ions to travel between the electrochemical cell and the nebulization system.

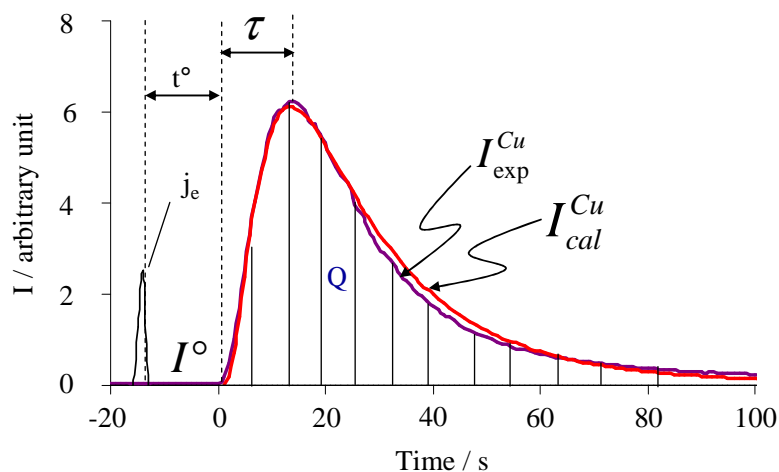


Figure 4-6: ICP intensity – time response of the electrochemical flow cell: A 0.1 V potentiostatic pulse was applied to pure copper in 1 M HCl and then the electrical current and Cu emission intensities were measured. t° is defined as the time between the initial pulse and the first point at which the Cu signal rises above the background (I°). τ is the time between t° and the peak maximum.

The obtained Cu intensity – time curve was then simulated by an empirical function in the form of a log-normal distribution $h(t)$:

$$h(t) = \frac{I^{Cu} - I^\circ}{Q} = \sqrt{\frac{\beta}{\pi\tau^2}} e^{\frac{-1}{4\beta}} e^{-\beta \ln^2(\frac{t}{\tau})} \quad (4-8)$$

where I^{Cu} is the Cu emission intensity, I° is the background of Cu intensity, Q is the integral of the transient in arbitrary units, β and τ are the characteristic time constants for the log-normal distribution, and t is the experimental time scale.

Eqn. 4-8 can be rewritten as:

$$I^{Cu} = Q \sqrt{\frac{\beta}{\pi\tau^2}} e^{\frac{-1}{4\beta}} e^{-\beta \ln^2(\frac{t}{\tau})} + I^\circ \quad (4-9)$$

Using the curve fitting option in the MATLAB software version 7.11.0, the time constants β and τ were determined to be equal to 0.95 and 13.5 respectively.

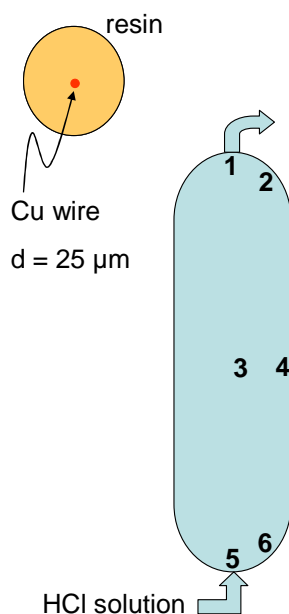


Figure 4-7: Schematic image showing the Cu wire – resin sample and the different points in the electrochemical cell which were tested in the local time constant determining experiment.

The concentration – time response is associated with diffusion from the sample surface to the flowing electrolyte stream, mixing in the channel flow cell. In addition, the electrochemical flow cell is not ideal and the diffusion distances probably differ from the edge to the centre of the sample and from top to bottom of the flow cell. Therefore, the time constants at the different points in the cell may be different. In this chapter, their values are also determined as follows: a copper wire with a diameter of 25 μm was placed in non-conductive and transparent epoxy resin. The Cu wire was perpendicular to the testing resin surface which was polished by metallographic paper up to 1 μm grain. The resin sample was then placed in contact with the flowing electrolyte in such a way as the Cu wire locating at the positions 1, 2, 3, 3, 4, 5, and 6 as shown in **Fig. 4-7**. After that, the time constant determining experiment was performed as described as above.

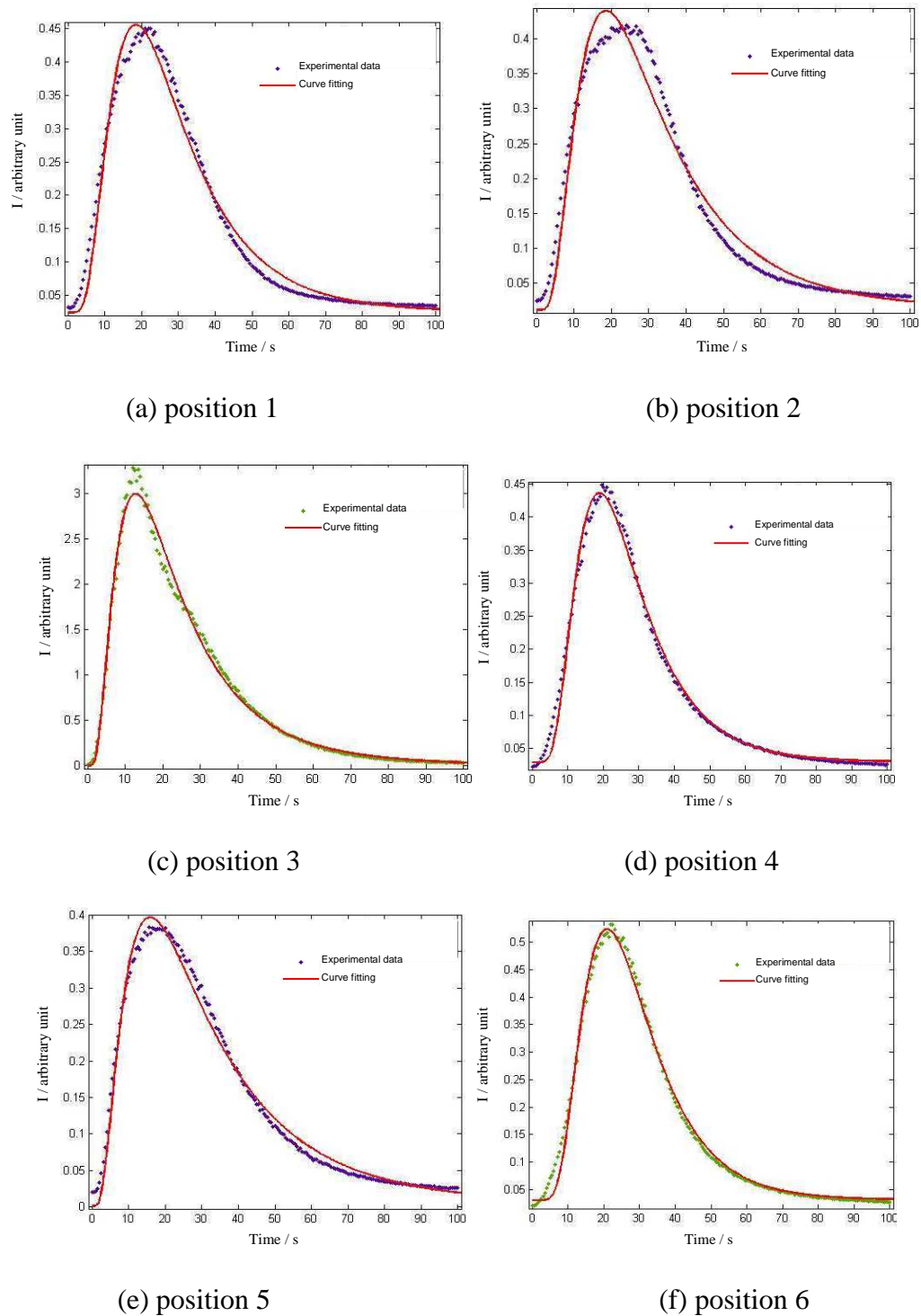


Figure 4-8: Experimental data of Cu emission intensity as a function of time in the local time constant determining experiment on the Cu wire locating at the different positions described in Fig. 4-7 and fitting curves obtained by MATLAB software using the log-normal distribution function

The local time constants of the log-normal distribution, β and τ , were found for the different points in **Fig. 4-7** using the **Eqn. 4-9** and the MATLAB software. The resulting curve fitting in **Fig. 4-8** shows that the time constant distributions at the different locations in the flow cell have the different shapes and do not always fit well with the log-normal distribution, especially in case of position 1 and 2 where they are on the top of the electrochemical flow cell. The physical processes at these positions in the flow cell are more complex than the other ones due to the cell design as it is filled by electrolyte progressively from bottom to top and sometimes leaving a very small unfilled space at the top of the cell which can be seen through the transparent resin sample.

The local time constants are given in **Table 4-1** and show the different values for the different positions, demonstrating that the physical processes, such as diffusion and mixing in the flow cell, differ from one point to another. In this chapter, the experiments were done on conductive samples big enough to cover the flow cell, so that the time constants obtained for the entire Cu surface (0.95 and 13.5 for β and τ respectively) were used in further calculation.

Table 4-1: Local time constants β and τ obtained for the different positions in **Fig. 4-7**

position	β	τ
1	1.55	18.4
2	1.25	18.5
3	0.93	12.7
4	1.99	18.8
5	0.90	15.8
6	1.75	20.9

4.5. Summary

In this chapter, the instrumentation and the principle treatment of the AESEC data have been introduced. The AESEC is the main technique used in this work due to its advantage in investigation of the selective dissolution. The numerical convolution of the AESEC data is

performed depending on the specific measurements, for example the dissolution current, j_M , and the electric current, j_e , in chapter 9.

4.6. References

- ¹ D. Hamm, K. Ogle, C.-O.A. Olsson, S. Weber, D. Landolt, Passivation of Fe-Cr alloys studied with ICP-AES and EQCM, *Corros. Sci.* 44 (2002) 1443-1456.
- ² K. Ogle, M. Mokaddem, P. Volovitch, Atomic emission spectroelectrochemistry applied to dealloying phenomena II. Selective dissolution of iron and chromium during active-passive cycles of an austenitic stainless steel, *Electrochim. Acta.* 55 (2010) 913-921.
- ³ K. Ogle, A. Tomandl, N. Meddahi, M. Wolpers, The alkaline stability of phosphate coatings I: ICP atomic emission spectroelectrochemistry, *Corros. Sci.* 46 (2004) 979-995.
- ⁴ K. Ogle, J. Bayens, J. Swiatowska, P. Volovitch, Atomic emission spectroelectrochemistry applied to dealloying phenomena: I. The formation and dissolution of residual copper films on stainless steel, *Electrochim. Acta.* 54 (2009) 5163.
- ⁵ M. Mokaddem, P. Volovitch, F. Rechou, R. Oltra, K. Ogle, The anodic and cathodic dissolution of Al and Al-Cu-Mg alloy, *Electrochim. Acta.* 55 (2010) 3779-3786.
- ⁶ P. Volovitch, L. Jiang, T. N. Vu, K. Ogle, New approach for measuring reactivity and degradation of complex surfaces: a review of recent results, *Book of abstracts of Coatings Science International 2011 (COSI-2011)*, Noordwijk, The Netherlands, June 2011, p. 47-50.
- ⁷ K. Ogle, Atomic emission spectroelectrochemistry: A new look at the corrosion dissolution and passivation of complex materials, invited plenary lecture, EuroCorr 2011, Stockholm, Sweden, Sept. 2011.
- ⁸ K. Ogle, S. Weber, Anodic dissolution of 304 stainless steel using atomic emission spectroelectrochemistry, *J. Electrochem. Soc.* 147 (2000) 1770-1780.
- ⁹ P. W. J. M. Boumans (ed.), *Inductively coupled plasma emission spectroscopy Part I: Methodology, Instrumentation, and Performance*, A Wiley-interscience publication, New York (1987) p 2.
- ¹⁰ P. W. J. M. Boumans (ed.), *Inductively coupled plasma emission spectroscopy Part I: Methodology, Instrumentation, and Performance*, A Wiley-interscience publication, New York (1987) p 70.

-
- ¹¹ T. J. Manning, W. R. Grow, Inductively coupled plasma – atomic emission spectrometry, *The Chemical Educator*, Springer-Verlag NEW YORK, INC. 2 (1997) 1-19.
- ¹² K. Ogle, A. Tomandl, N. Meddahi, In situ monitoring of dissolution-precipitation mechanisms using coupled quartz crystal microbalance / atomic emission spectroelectrochemistry, *EFC 54 - Innovative pre-treatment techniques to prevent corrosion of metallic surfaces* (2007) edited by L. Fedrizzi, H. Terryn and A. Simões , p 158.
- ¹³ K. Ogle, Atomic Emission Spectroelectrochemistry: A new look at the corrosion, dissolution and passivation of complex materials, *Proceedings of EuroCorr*, Stockholm (2012).
- ¹⁴ R.X.Xin, Plasma emission spectrometry, Chemical Industry Press, (2006).
- ¹⁵ P. W. J. M. Boumans (ed.), Inductively coupled plasma emission spectroscopy Part I: Methodology, Instrumentation, and Performance, A Wiley-interscience publication, New York (1987) p 73.
- ¹⁶ L. Jiang, Application of atomic emission spectroelectrochemistry to the formation and degradation of conversion coatings on galvanized steel (Zn and Zn-Mg-Al), PhD dissertation (2012) p 34.
- ¹⁷ K. Ogle, J. Baeyens, J. Swiatowska, P. Volovitch, Atomic emission spectroelectrochemistry applied to dealloying phenomena: I. The formation and dissolution of residual copper film on stainless steel, *Electrochim. Acta.* 54 (2009) 5163-5170.

Chapter V:

Understanding corrosion via corrosion product characterization:

Role of alloying element in improving the corrosion resistance of Zn-Mg-Al coatings

P. Volovitch, **T. N. Vu**, C. Allely, A. Abdel Aal, K. Ogle,
Corrosion Science 53 (2011) 2437-2445.

5. Understanding corrosion via corrosion product characterization: Role of alloying element in improving the corrosion resistance of ZnMgAl coatings

Abstract. Corrosion products are identified on Zn, ZnMg and ZnMgAl coatings in cyclic corrosion tests with NaCl or Na₂SO₄ containing atmospheres. For Mg-containing alloys the improved corrosion resistance is achieved by stabilization of protective simonkolleite and zinc hydroxysulfate. At later stages, the formation of layered double hydroxides (LDH) is observed for ZnMgAl. According to thermodynamic modeling, Mg²⁺ ions bind the excess of carbonate or sulfate anions preventing the formation of soluble or less-protective products. A preferential dissolution of Zn and Mg at initial stages of corrosion is confirmed by in-situ dissolution experiment. The physicochemical properties of different corrosion products are compared.

Keywords: Metal coatings, zinc, aluminum, magnesium, atmospheric corrosion, de-alloying.

5.1. Introduction

Combined zinc-aluminum-magnesium coatings on steel developed during the last decades have shown markedly superior corrosion resistance than conventional hot dip and electrogalvanized coatings [1-3]. In general zinc based coatings corrode on the order of 100 times slower than cold rolled steel and zinc-aluminum-magnesium coatings are another order of magnitude slower [4-14]. An enhanced self-healing effect for Zn-Mg and Zn-Mg-Al coatings was also previously reported [3, 8, 13, 15-18]. The understanding of the nature of the products formed during corrosion for different coating compositions under different exposure conditions can be the key to the formulation of better barrier protective coatings.

Table 5-1: Equivalence between the name of corrosion product, its composition and its designation

Name	Abbreviation	Chemical formula
layered double hydroxide	LDH	$M(II)_xM(III)_y(A^-)_m(OH)_n \cdot nH_2O$ $M(II)=Zn^{2+}$, Mg^{2+} , $M(III)=Al^{3+}$ $A^- = CO_3^{2-}$, Cl^- , SO_4^{2-}
zinc hydroxysulphate	ZHS	$Zn_4SO_4(OH)_6 \cdot nH_2O$, $n=3-5$
zincite	Z	ZnO
smithonite	S	$ZnCO_3$
mixture of magnesium carbonates	MC	$MgCO_3$, $MgCO_3 \cdot 3H_2O$, $Mg_5(CO_3)_4(OH)_2 \cdot 4H_2O$
hydrozincite	HZ	$Zn_5(CO_3)_2(OH)_6$
simonkolleite	ZHC	$Zn_5(OH)_8Cl_2 \cdot H_2O$

Previous studies of the inhibitive properties of zinc corrosion products on galvanized steel in natural exposure have demonstrated that basic zinc salts (like simonkolleite (ZHC): $Zn_5(OH)_8Cl_2 \cdot H_2O$, hydrozincite (HZ): $Zn_5(CO_3)_2(OH)_6$ or zinc hydroxysulfate (ZHS): $Zn_4SO_4(OH)_6 \cdot nH_2O$) improve significantly the short term [19-20] and long-term corrosion resistance [14]. The designations of corrosion products named in this work are presented in **table 5-1**. The stability of the protecting layer, however, compared to the other investigated

metals is restricted to a rather small pH-range [21-22]. The presence of high sulfur dioxide, carbonate or chloride concentrations causes the dissolution of the protective layer and leads to the formation of highly soluble products [24, 12] with practically no decline in the corrosion rate with time [23].

The influence of ions in solution on the precipitation of different Zn corrosion products was studied by several authors [25-27]. The formation of basic zinc chloride in detriment of zinc oxide was observed in the presence of Al(III) and Fe(II), whereas ZnO was formed in presence of Fe(III) and Mg (II) under identical conditions (pH adjusted at 9.2). In contrast, preferential simonkolleite formation in the presence of Mg^{2+} was observed for technical samples of zinc coatings on carbon steel [25, 28].

The presence of Al and Mg can also result in the formation of new corrosion products. Possible Mg-based corrosion products were discussed by Prosek et al [29], but the presence and nature of this product were never completely confirmed. For ZnAl and ZnMgAl the formation of ZnAl products with layered double hydroxide structure (ZnMg-CO₃ LDH) with stoichiometry close to $Zn_6Al_2CO_3(OH)_{16}4H_2O$ was communicated [30-31]. Interestingly, this compound was first detected during seawater exposure of Zn-Al coatings [30] in a mixture with hydrotalcite $Mg_6Al_2CO_3(OH)_{16}4H_2O$. LDH are usually known by mineralogists as the sjögrenite-hydrotalcite group [32]. They have closely related structures and the general formula $[M^{II}_{1-x}M^{III}_x(OH)_2]^{x+}[A^{n-}]_{x/n} \cdot yH_2O$. The basic structure of an LDH may be derived by substitution of a fraction of the Mg^{2+} in a brucite lattice by trivalent cations like Al^{3+} such that the layers acquire a positive charge, which is balanced by intercalation of anions (and, usually, water) between the layers. These compounds are known to exchange both cations and anions [33-34] thereby varying the identity and relative proportions of the divalent and trivalent cations as well as the identity of the interlayer ions. These compounds are known to improve significantly the corrosion behavior of Mg-Al alloys [35-37] and one of the possible mechanisms of their action is the anion-exchange between carbonate-anion and aggressive species [37-38] which may become trapped in the interlayer, blocking their access to the substrate.

In our previous publication [28] we attribute the improved corrosion resistance of Zn-Mg coatings to the enhanced stability of simonkolleite versus ageing by carbon dioxide containing atmosphere in presence of magnesium cations. In the present work, the corrosion products formed on Zn, ZnMg and ZnMgAl coatings with different composition in different exposure conditions are identified. The results are compared with thermodynamic modeling

and in-situ atomic emission spectroelectrochemistry (AESEC) and possible mechanisms are discussed by which the alloying elements (Al and Mg) may influence the formation of specific corrosion products.

5.2. Experimental

5.2.1. Sampling

Steel samples with Zn, ZnMg and ZnMgAl coatings were prepared and supplied by ArcelorMittal. The reference samples used in this work were commercial hot-dip galvanized (GI) steel sheets with a total thickness between 0,7 mm and 0,8 mm and a coating thickness of 10 μm with a composition typical of use in the automotive industry (Zn, Al less than 0.3 wt%). ZnMg coatings of 9 μm thickness were obtained by the Physical Vapor Deposition (PVD) process, The final composition of the coating was Mg 16.0 wt%, Zn – 84.0 wt%, predominantly composed of the intermetallic phase Zn_2Mg . The ZnMgAl coatings were prepared in laboratory by the hot-dip process with composition 3 wt%-4 wt% of Al and 3 wt%-4 wt% of Mg and thicknesses of 8 μm and 10 μm were tested.

Table 5-2: List of conditions for which the corrosion product was analyzed after corrosion test. Each column corresponds for one standard test, testing time in number of cycles is shown. The note “SRR” means that this number of cycles corresponds with the start of red rust formation, “5%” means the formation of 5% red rust, * indicates that the test was made in confined zone with flange assembly.

Coating type	Test type and number of cycles (c)				
	CCT1 (5%RR)	KWT-DC*	VDA	VDA*	VDA-SO ₄
GI	6 c	4 c SRR	<1 c (SRR) 2 c (5%RR)	5 c (SRR)	10 c
ZnMg	Not tested	10 c SRR	6 c (SRR) 15 c (5%)	17 c (SRR)	20 c
ZnMgAl	80 c	6 c	15 c (5%RR)	2, 6 c (SRR) 15 c (5%RR)	20 c

The technical samples were exposed in different corrosion tests for different exposure times as specified in **Table 5-2**. The test conditions are described in **Table 5-3**. Samples were exposed as is (open panel), in a 120 μm confined zone configuration prepared with a metal/glass flange assembly (confined zone, indicated with * in **Table 5-2**), or for the salt spray test were painted and scratched in order to evaluate the corrosion product in artificial defect.

Table 5-3: Description of on cycle conditions for corrosion tests applied for studied samples

	Cycle time (hours)	Salt Spray Phase (35°C)			Humid phase			Dry phase		
		% duration (of time)	pH	Electrolyte composition	% duration (of time)	R.H (%)	T (°C)	% duration (of time)	R.H (%)	T (°C)
CCT1	8	50	7	NaCl 50g/l	25	95	50	25	<30	60
VDA	168	14	7	NaCl 50g/l	19	99	40	67	<75	23
VDA-SO ₄	168	14	7	Na ₂ SO ₄ 50g/l	19	99	40	67	<75	23
KWT-DC	168	~5	7	NaCl 10g/l	~62	80 to 95	23 to 50	~33	50 to 75	28 to 50

5.2.2. Characterization methods

After visual inspection and optical micrograph observations, the corroded samples were cut into 2 cm x 2 cm squares and deposited onto a carbon ribbon and observed by scanning electron microscopy (SEM) and energy dispersive spectroscopy (EDS). The majority of work was performed using Gemini 1530 microscope with FEG-source (Scottky-type) and EDS for elemental analysis with Si(Li) detector and QUANTAX evaluation software (Bruker AXS). Additional work was performed using other SEM instruments. For several samples the corrosion product layer was removed with a surgeon's scalpel and analyzed by microscopy from the side close to the substrate. The residual surface of substrate was also observed.

ATR infrared spectroscopy was performed directly on the corroded samples using a Bruker Tensor 27, $\lambda_{\text{laser}} = 15799.76 \text{ \AA}$ and treatment with OPUS 6.5. software. The results were compared with reference spectra taken from the literature [25, 29, 39, 40] and from the RRUFFTM spectral database for minerals.

For X-ray diffraction studies, 3 types of spectra were studied. Firstly, the diffraction experiments were performed directly on the corroded surface, on the powder obtained when

the corrosion products were removed from the surface, collected and triturated, and on the surface after removal of corrosion product (in order to identify the most adherent product). The powders were deposited on the glass support with a thin Vaseline™ layer for fixation and analyzed by X-ray diffraction using the Cu(K α) radiation in a Siemens D5000 diffractometer. The XRD were collected with the angular resolution 0.02°. The phase identification has been carried out by referencing the software PCPDFWIN version 2.02 containing the JCPDS (ICDD) database files.

Selective leaching in 5 wt% Na₂SO₄ solution was studied by in-situ atomic emission spectroelectrochemistry (AESEC) method for ZnMgAl coating. The AESEC technique permits a direct measurement of the partial elemental dissolution rates from metals and alloys by measuring the elemental composition of the electrolyte as a function of time downstream from an electrochemical flow cell using inductively coupled plasma optical emission spectrometry (ICP-OES). A detailed description of the flow cell and the analytical parameters can be found in previous publications [41-43].

5.3. Results

5.3.1. Detected corrosion products: results of XRD and FTIR

Visual inspection of corroded samples confirmed the better corrosion resistance of ZnMg and ZnMgAl coatings as compared with GI (**Fig. 5-1**). The list of corrosion products which were identified on different types of coatings is summarized in **Table 5-4** not including the iron corrosion products. For the analysis presented in this table, the XRD peaks which were present on the substrate before the beginning of the test (natural Zn and Al oxides) were not taken into account. Interestingly, the aluminum oxides and hydroxides expected from previous knowledge of corrosion products on Al-Mg alloys were not developed during corrosion of ZnMgAl alloys.

It may be noted from **Table 5-4** that for unalloyed galvanized steel, amorphous hydrozincite and ZnO are present in all test conditions, simonkolleite and smithonite (zinc carbonate) are also often detected. In alloyed coatings major Zn-rich products are simonkolleite (in chloride tests) or zinc hydroxysulfate (in sulfate tests), hydrozincite is often present but smithonite was never observed and ZnO rarely detected and then only in a rather small fraction. Al and Mg containing products are present as layered double hydroxides (LDH) and magnesium carbonates are also detected. Interestingly, no pure Al or Mg oxide-

hydroxide species (brucite, MgO, corundum etc.) were detected. The latest is consistent with high stability of LDH.

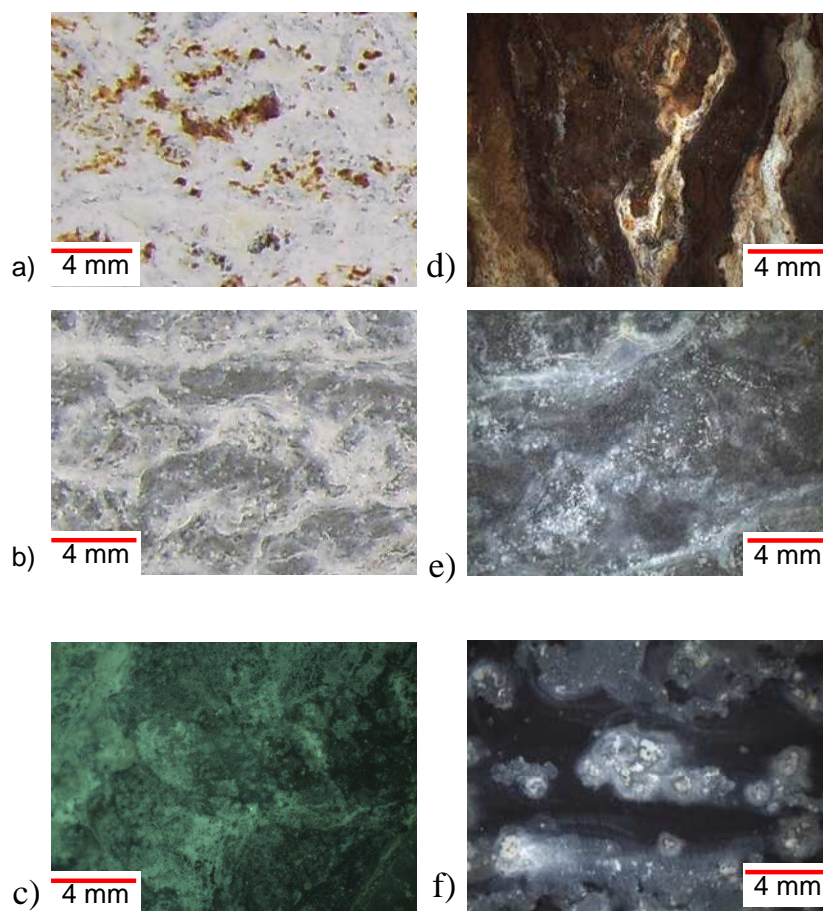


Figure 5-1: General view of samples after cyclic corrosion test:

a) GI, 2 cycles VDA;

b) Zn-Al_{2-4%}Mg_{2-4%}, 20 cycles VDA;

c) ZnMg, 17 cycles VDA;

d) GI, 10 cycles VDA – SO₄;

e) Zn-Al_{2-4%}Mg_{2-4%}, 20 cycles VDA – SO₄;

f) ZnMg, 20 cycles VDA – SO₄.

The identification of LDH in corrosion products by XRD is sometimes difficult because of the variation of crystallographic parameters with the nature and varying ratios between different cations or anions caused by easy ion exchange. In the present work several LDH structures were clearly determined, including layered zinc aluminum hydroxychloride (ZnAlCl-LDH, Zn₂AlCl(OH)₆·xH₂O), layered zinc aluminum hydroxycarbonate (ZnAlCO₃-LDH, Zn₄Al₂(CO₃)(OH)₁₂·3H₂O) and hydrotalcite (HT, MgAlCO₃-LDH, Mg₆Al₂CO₃(OH)₁₆·4H₂O). For some cases the peak positions differ slightly from the theoretical value for the

stoichiometry presented and move with cycling, indicating the change of the product microstructure. The variation of interlayer distance related to the ion exchange with progress of corrosion supposed from the variation of (003) XRD peak position is consistent with crystallographic data [38] showing the variation of the interlayer distance with the nature of anions and cations and the ratio of the different species.

Table 5-4: Summary of corrosion products observed by XRD and or FTIR on different samples. The note “SRR” means that this number of cycles corresponds with the start of red rust formation, “5%RR” means the formation of 5% red rust. See **Table 5-2 and 5-3** for detailed test conditions. * indicates that the test was made in confined zone with flange assembly. Indicates (a) refers for amorphous hydrozincite which was not detected by XRD but by FTIR.

Coating type	Test type and corrosion stage						
	CCT1 (5%RR)	KWT-DC* (SRR)	VDA		VDA*		VDA2
			SRR	5%RR	SRR	5%RR	
GI	ZHC, Z, HZ (a)	ZHC, Z, HZ (a)	ZHC, Z, HZ (a)	Z>ZHC, S	ZHC, Z	Z>ZHC, HZ	Z, HZ
ZnMg	Not tested	ZHC, HZ	ZHC>HZ (a)	ZHC, MC, HZ (a)	ZHC	Not tested	ZHS
ZnMgAl	ZHC, LDH>>Z	ZHC, LDH	ZHC	ZHC, LDH, HZ	ZHC	ZHC,LDH	ZHS, LDH

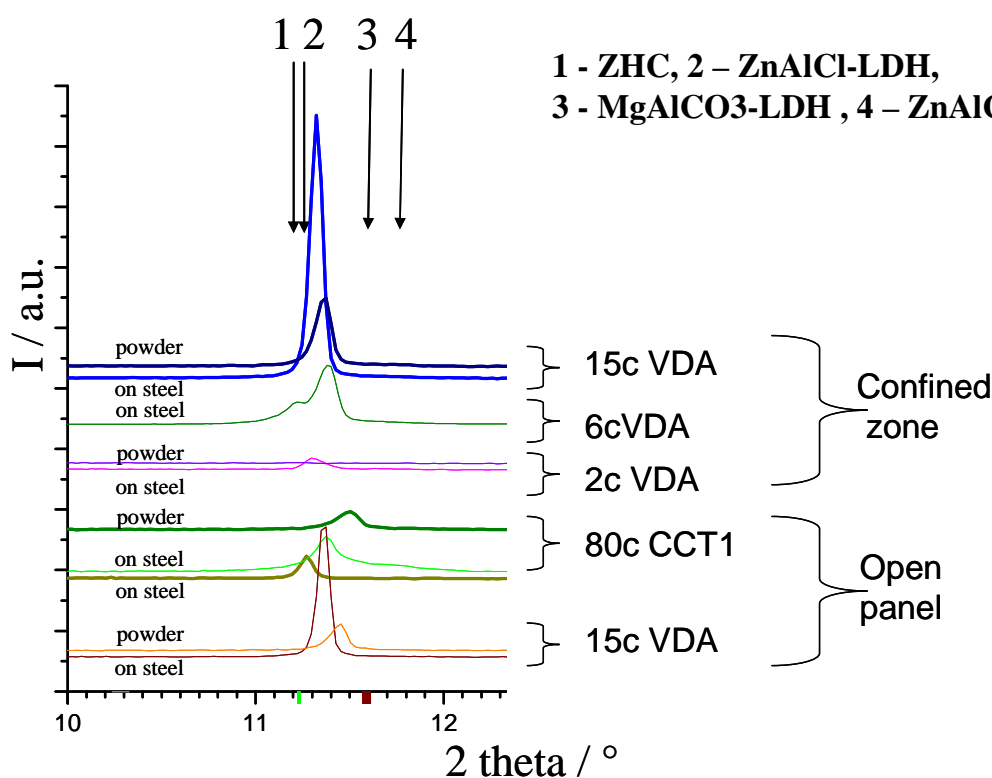


Figure 5-2: Evolution of the peak position in the low angle region of XRD of corrosion product on ZnMgAl after advanced stages of corrosion. Theoretical positions (1, 2, 3, and 4) of the characteristic peaks of several products are also given.

Fig. 5-2 shows an example of the evolution of layered corrosion product during the corrosion of ZnMgAl exposed to a chloride containing cyclic corrosion test in (i) a confined zone (upper) and (ii) open panels (lower). For each sample the upper curve corresponds to the powder removed from the surface and the lower curve corresponds to the product which stays on the substrate. The arrows indicate the theoretical position of the characteristic peak (corresponding with minimal interlayer distance) for layered structures: 1 - ZHC, 2 – ZnAlCl-LDH, 3 - MgAlCO₃-LDH , 4 – ZnAlCO₃-LDH. It can be seen that with progress of corrosion the displacement of peak 003 in LDH corresponds to the evolution of interlayer distance probably related to progressive incorporation of carbonate, exchange of Mg with Zn as well as the increase of Al content. This shift is more pronounced in the powder than in the layer of adherent product close to the substrate. Interestingly, simonkolleite and ZnAlCl LDH seems to be more adherent products because they were systematically found on the substrate but not in the powder.

An interesting observation was also made concerning the grey areas at which LDH was detected on the substrate after 15 cycles of VDA test in confined zone, the signal of metallic aluminum was still present in this zones but not the signal of Zn-Mg intermetallics. This suggests that the layer of the LDH is thin enough to access the uncorroded substrate and that under the layer of LDH the matrix is depleted in Zn and Mg. It can be noted from fig.2 that simonkolleite is formed in case of high Cl content and lower pH (CCT1 test). It was also formed in the first stages of VDA test, but disappears with time in the VDA test. The later result can be related to the high pH at these stages which is enough for intensive dissolution of Al and the formation of ZnAlCl - LDH. This compound is more stable than simonkolleite at high Al content as suggested by Ishikawa et al. [26] concerning the preferential formation of ZHC or ZnAlCl - LDH during precipitation from aqueous solution as function of Al³⁺ to Zn²⁺ ratio.

The FTIR analysis of the same samples revealed that amorphous hydrozincite on the opened panels increases with cycling.

For unalloyed samples in VDA-sulfate test (last column in **Table 5-4**), only ZnO and HZ were detected. In contrast, for both ZnMg and ZnMgAl samples under identical conditions the major product was ZHS. For ZnMgAl coatings, ZnAlCO₃ - LDH was also identified.

5.3.2. Detected corrosion products: distribution of elements by SEM-EDS

SEM analysis has identified Al-containing corrosion products on the top of the surface for samples showing the formation of red rust (advanced stage of corrosion). No Al-containing product was detected in the powder and on the top layer of corrosion product on ZnMgAl panels after 20 cycles of VDA which is coherent with presented in previous section XRD results showing the formation of LDH only at more advanced stages of corrosion. This implies that Al is not reactive during initial stages of corrosion. It is of interest to note that the distribution of Al in corrosion product is not uniform.

SEM-EDS analysis of samples after VDA-sulfate test revealed that the sulfur-rich product was more or less uniformly distributed in the corrosion product on both Mg and AlMg alloyed coating. On unalloyed coating only trace quantities of S were detected near the substrate and no S was present in the thickness of the corrosion product layer (**Fig. 5-3**). This is consistent with the fact that zinc hydroxysulfate was detected only in corrosion products on

alloyed coatings. The typical morphologies of S-rich phases observed in ZnMg and ZnMgAl samples are presented in **Fig. 5-4**.

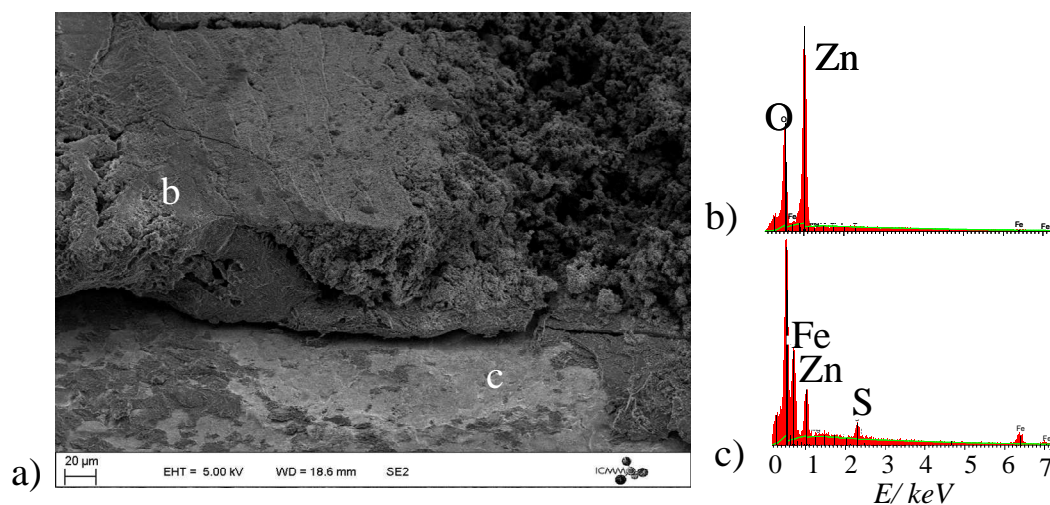


Figure 5-3: a) SEM image of corrosion product on the surface of GI after 10 cycles of the VDA- SO_4 test (view from the scratch) and (b, c) EDS spectra of two zones as indicated. Sulfur is found only at some places in very thin layer on substrate.

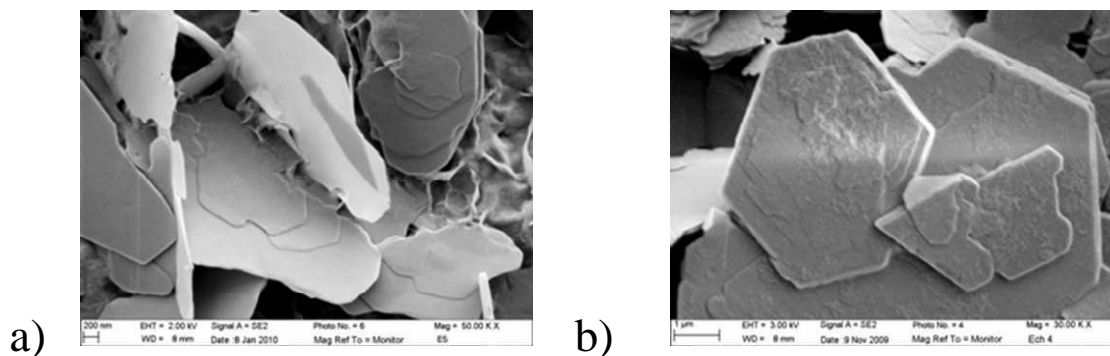


Figure 5-4: Typical morphology of S-rich product (supposed as zinc hydroxysulfate) a) on ZnMg and b) on ZnMgAl coated steels after 20 cycles of the VDA- SO_4 test.

The distribution of chemical elements in corrosion product on ZnMgAl after VDA-sulfate test observed by SEM is shown in **Fig. 5-5**. Several observations can be made from this figure. First of all, the uniform layer containing Zn, O and S covers the surface. The Al rich corrosion product (shown with straight oval) is depleted in Zn and Mg. In contrast the metallic phase in the close contact with corroded zone (shown with dashed oval) seems to be

depleted in Al and Mg. Such a distribution strongly suggests the local selective dissolution of Al and Mg.

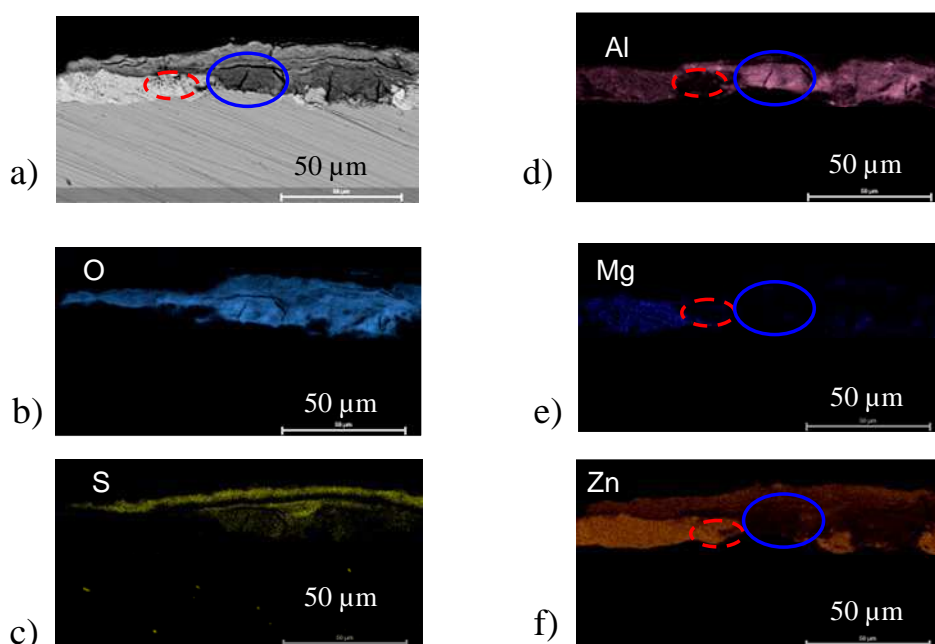


Figure 5-5: (a) SEM backscattered electron (BSE) image and (b-f) elemental X-rays maps of corroded layer on Zn-Mg-Al after 20 cycles of the VDA - sulfate test. The corroded areas are darker than the uncorroded areas in BSE image. The presence of continued layer of corrosion product containing Zn, S and O can be marked. The Zn-rich uncorroded area depleted in Al and Mg is shown by dashed oval, the oxidized Al corrosion product depleted in Zn and Mg is shown by straight line oval.

5.3.3. Selective dissolution of Zn and Al observed by AESEC

A typical reactivity measurement of ZnMgAl coating in 5 wt% Na_2SO_4 aqueous solution is shown in **Fig. 5-6**. The curve shows the Al, Zn and Mg dissolution rate (expressed as a current density by application of Faraday's law) as well as measured electrical current. Prior to t_0 a blank solution was fed into the plasma spectrometer using a bypass of the electrochemical cell. This measurement is used to define the zero of emission intensity for the calculation of concentration. At $t = t_0$ the electrolyte comes into contact with the surface and the dissolution rate of spontaneous reaction is measured as a function of time. In - situ observation of dissolution of ZnMgAl alloy by ICP-OES demonstrated that in neutral solution at open circuit potential only Zn and Mg are dissolved in 5 wt% Na_2SO_4 (**Fig. 5-6**). At $t = t_1$ the polarization starts and the dissolution rate under potentiodynamic polarization is measured

as a function of time. At anodic polarization (positive electrochemical current) until the potential of Al dissolution is not achieved the selective dissolution of Zn and Mg continues. In contrast, Al dissolution occurs at high cathodic polarization (negative electrochemical current) which increases the surface pH which is in accordance with our previously published results for Al alloys [42]. Similar results were obtained in NaCl electrolyte. Finally, these results imply that at initial stages of corrosion the anodic areas release Zn and Mg and the cathodic areas release Al.

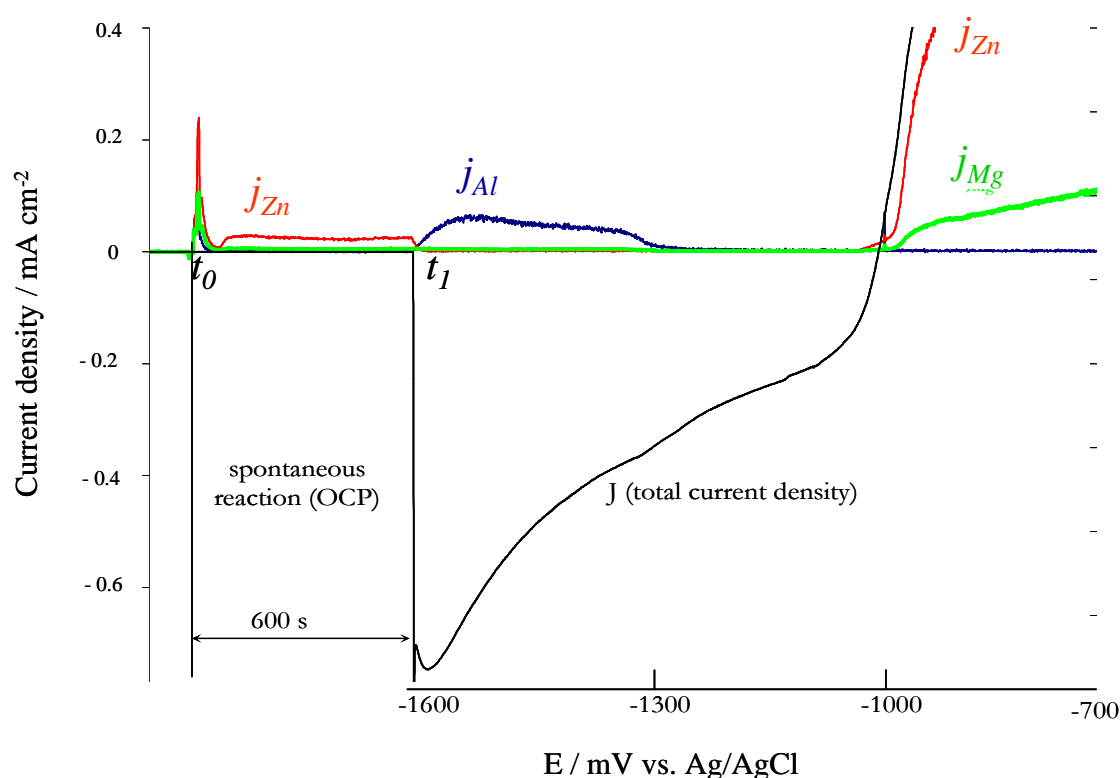


Figure 5-6: Selective dissolution of Zn and Mg at anodic potentials and selective dissolution of Al at very cathodic potentials during polarization of Zn-Mg-Al in 5% Na₂SO₄ observed by AESEC with a scan rate of 0.5 mV s⁻¹.

5.4. Discussion: Role of Mg and Al in Zn-Mg-Al coatings

The mechanism of corrosion of Zn-Mg-Al coating can be understood if the dissolution and the precipitation stages are taken into account. We will discuss it in two steps, for the initial stages of corrosion at near neutral pH when the coating potential is determined by the more active metals Zn and Mg, and then for the advanced stages when significant oxidation of

Al becomes possible either because of high local pH or due to the surface potential increase after dissolution of the zinc-rich phases.

5.4.1. Initial stages of corrosion

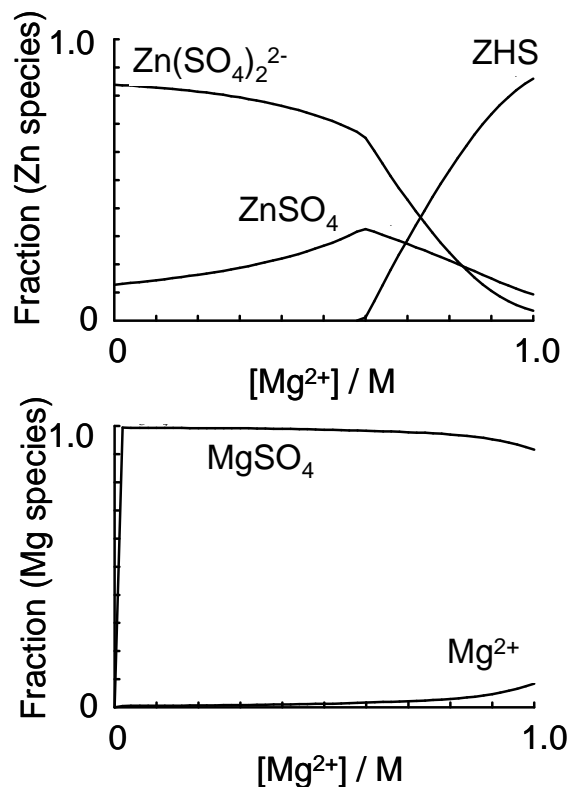


Figure 5-7: Example of thermodynamic modeling showing the influence of Mg on the ratio between soluble complexes of Zn in sulfate solution and precipitation of zinc hydroxysulfates.

If we accept that during initial stages of corrosion the coating potential is maintained by more active metals Zn and Mg and the surface stays at near neutral pH, only Zn and Mg are dissolved selectively from the coating. Even if some Al^{3+} is formed at cathodic areas, its solubility in neutral pH is so small that it can't diffuse and remains in the form of the non-protective intact oxide on the coating surface. This is in accordance with the absence of Al-rich corrosion product (except the initial natural oxide) after 2 and 6 cycles of VDA test as well as with the morphology of corrosion product presented in **Fig. 5-5**. At this stage the action of Zn-Mg-Al is identical with that of Zn-Mg and is determined by the presence of Mg. Previously [28] we proposed for ZnMg alloys in Cl-containing atmosphere that the role of Mg is the stabilization of the crystalline forms of simonkolleite against transformation into

smithonite ($S = \text{ZnCO}_3$), amorphous hydrozincite (HZ, a) and zincite ($Z = \text{ZnO}$) during ageing cycles in the presence of CO_2 . In this work we have further demonstrated the increased fraction of basic zinc salts (ZHC in chloride tests and ZHS in sulfate test) compared with ZnO and HZ. We propose that at initial stages of corrosion the role of Mg is correlated with the stabilization of the crystalline forms of basic zinc salts (simonkolleite, zinhydroxysulfate etc.) against their transformation into soluble sulfate complexes in sulfate containing media or into ZnCO_3 , amorphous HZ and ZnO during ageing. Results of thermodynamic modeling demonstrate that this stabilization is achieved by the presence of Mg^{2+} ions which bind the excess of carbonate or sulfate anions (**Fig. 5-7 and 5-8**). The calculation is made for an aqueous solutions of Zn^{2+} , Mg^{2+} , Cl^- , SO_4^{2-} and CO_3^{2-} at 25 °C using the Hydra-Medusa© software [44]. This software includes a dedicated database of equilibrium constants including most known zinc corrosion products. The results clearly demonstrate that Mg^{2+} ions will preferentially precipitate with carbonate or sulfate (**Fig. 5-8**), thereby lowering the carbonate or sulfate ion concentration and stabilizing the protective simonkolleite or zinhydroxysulfate phase.

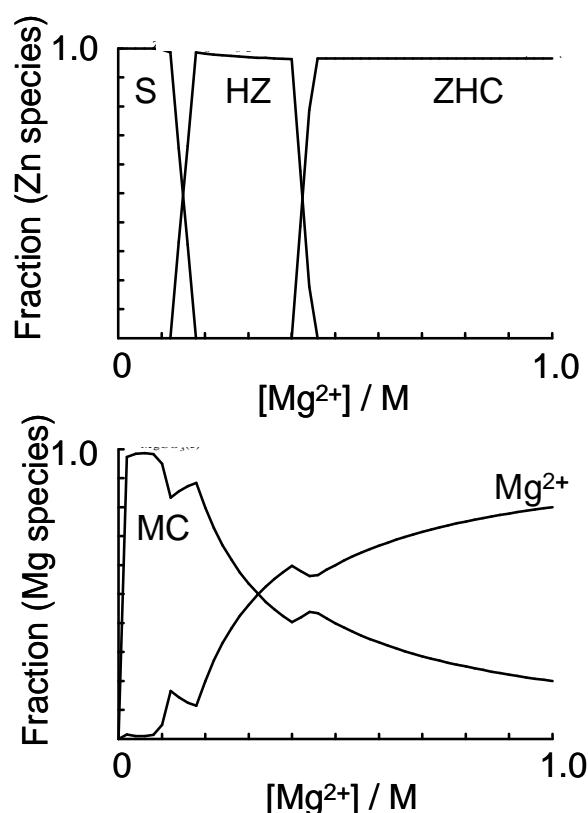


Figure 5-8: Example of thermodynamic modeling showing the influence of Mg on the ratio between simonkolleite, hydrozincite and zinc carbonate.

5.4.2. Dissolution of Al and formation of new corrosion products at advanced stages of corrosion

Once the corrosion process progresses the dissolution of Al can start in neutral or alkaline conditions:

- 1) in neutral conditions when zinc-rich phases are sufficiently consumed to allow an increase of the coating electrochemical potential,
- 2) if the pH of the surface increases either uniformly by the progress of corrosion or on cathodic areas.

The presence of Al^{3+} in solution can influence 2 phenomena:

- a) At low concentrations, Al^{3+} , as demonstrated by [26] influences the crystallization of zinc oxides and enhances the formation of simonkolleite in place of ZnO even at higher solution pH.
- b) Once the concentration of Al^{3+} is sufficient, Zn-Al (and/or Mg-Al) LDH are formed.

The mechanism of formation of corrosion products at the initial stages of corrosion can be illustrated in **Fig. 5-9**. The formation of areas depleted in Mg and Zn can be attributed to selective dissolution of Zn and Mg from anodic areas at which Al stays intact or in form of natural oxide (step Ia). The presence of this oxidized Al phase does not protect Mg and Zn from dissolution because the entire coating thickness seems to have been consumed. The formation of a region depleted in Al near this anodic area can be related to an increase of local pH on cathodic areas and the selective dissolution of Al and Mg from AlMg intermetallics (step Ib). The dissolution is significant in the border region because the cathodic current is higher in zones close to the anodic region. At the same time, because of the very low solubility of Al^{3+} , it precipitates forming a local Al-rich product more or less instantly (step II). The concentration of Zn^{2+} in solution continues to increase because of its higher solubility. As a result the precipitation of zinc corrosion products (zinc hydroxysulfate ZHS in this case) starts later and continues slowly forming a more uniform layer (dashed line) which covers all (cathodic, anodic or intact) areas (step III). The formation of such a layer can offer barrier protection.

Ib. Cathodic dissolution

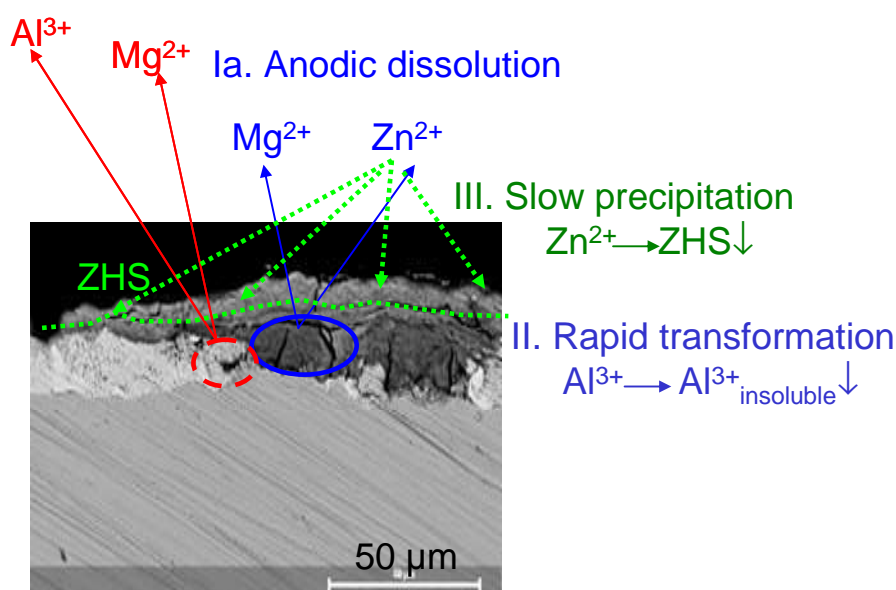


Figure 5-9: Schematic illustration of possible mechanism of formation of corrosion product on cathodic and anodic areas of ZnMgAl alloy for the area presented in **Fig. 5-5**.

Ia. Dealloying of Mg and Zn from anodic areas at which Al stays intact or in form of natural oxide. The presence of this oxidized Al phase do not protect Mg and Zn from following dissolution because all coating thickness seems to be consumed.

Ib. With increases of local pH on cathodic areas the dissolution of Al (and Mg from intermetallics) becomes significant and because cathodic current should be higher in zones close to anodic region, the dissolution is significant in the border region between cathodic and anodic zones (dashed oval);

II. Because of the very low solubility of Al^{3+} , it precipitates forming a local Al-rich product more or less instantly;

III. The concentration of Zn^{2+} in solution should increase more and require higher pH, as a result the precipitation of zinc corrosion products (zinc hydroxysulfate ZHS in this case) starts later and continue slowly forming more uniform layer (dashed line) which covers all (cathodic, anodic or intact) areas.

In order to evaluate the barrier properties of different corrosion products, the comparison of selected physicochemical properties of different products is presented in **Table 5-5**. The data for this table are taken from references [45-54] as marked and from SEM

observations made during our work. It seems from the data presented in the table that the plate-like morphology which may be agglomerated [46-47], the low electron density, and the layered structure with difficult ion-transfer through the layer are the common origins of the protective nature of simonkolleite, ZHS and LDH (**Table 5-5**). Cation and anion exchange may also contribute to the improved adherence of the product to the base metal and can improve the barrier properties by creating traps for aggressive species [37-38].

Table 5-5: Some properties of selected corrosion products

LDH - $Mg_6Al_2CO_3(OH)_{16} \cdot 4H_2O$ and related structures, ZHS – zinc hydroxysulphate,

HZ – hydrozincite, ZHC –simonkolleite. If not specified, data are taken from [53, 54].

Phase	LDH	ZnO	ZHS	HZ	ZHC
Density ρ (g/cm ³)	2.06 (MgAl)	5.56	2.0	3.5	3.2
Hardness H (Mohs)	2 (MgAl)	4-5	2-2.7	2-2.5	1.5
Electron density (gm/cc)	2.13 (MgAl)	5.28		3.37	3.08
Cristallinity (this work)	C	C	C	Amorphous	C
Aspect (this work)	Platelets	Granular or eagles	Platelets	Platelets, fibers or aggregates	Platelets
pH range for solubility (calculation with [44])	Strong acid	Acid or base		Acid or strong base	Acid or strong base
pKs	~25.4 (MgAl) ~20.8 (ZnAl) [38, 45]	~17 [49]	~16.6 [50]	~14.6 [51]	~13.7 [51]
Permeability for air $\times 10^3$, torr/s, [46, 52]	0.3 -30 (the smallest value for ZnMgAl)	93		about 10	about 10

The role of Mg is not limited to the initial stages of corrosion. The presence of Mg^{2+} can influence the formation of LDH-like structures. The solubility constant of MgAl - LDH is 5 orders of magnitude higher than that that of ZnAl - LDH [45] that means that in presence of

Mg^{2+} the formation of LDH should start earlier. In light of the high ion-exchange capacity of Mg^{2+} in LDH structures, its replacement by Zn^{2+} can be expected, suggesting that ZnAl - LDH is formed by ion exchange. Moreover, the higher solubility constant can be related to the higher number of initial nucleation sites for precipitation and results in the smaller nanosized crystal structure which should have the better barrier properties. Indeed, according to Ishikawa et al. [45], between ZnAl, ZnMg and ZnMgAl - LDH structures the Mg containing structures are better barriers to oxygen diffusion. That means that the presence of Mg in LDH is beneficial for corrosion protection. On the basis of this bibliographical data we suggest that the ratio between Al and Mg can be important and an excess of Al can result in formation of aluminum oxides and hydroxides in place of LDH as observed for Al-Mg alloys.

Finally, we find that the actions of Al and Mg are complementary and complex. The ratio between these two elements can influence the nature and hence the barrier effect of the corrosion product formed. Further studies are in progress to understand the mechanism of corrosion protection offered by each corrosion product separately.

5.5. Conclusions

1. The better corrosion resistance of ZnMgAl coated steel as compared to galvanized steel for different corrosion test conditions in chloride-rich and chloride – free (sulfate) atmosphere was observed.
2. Qualitative analyses of the corrosion products indicate that simonkolleite and zinc hydroxysulfate are stabilized on the ZnMg and ZnMgAl coating throughout the cyclic corrosion test exposure in different atmospheres while they are not observed on galvanized steel at advanced stages of corrosion.
3. We propose on the basis of thermodynamic modeling that these compounds are stabilized in the presence of Mg^{2+} by the reaction of Mg^{2+} with anions forming soluble or low protective complexes with Zn (CO_3^{2-} and excess SO_4^{2-}).
4. As demonstrated by SEM, XRD and *in-situ* atomic emission spectroelectrochemical experiments, in the early stages of corrosion Al remains on the coating in an insoluble form and a strong preferential dissolution of Zn and Mg occurs.
5. Al dissolution and formation of Zn-Al and/or Zn-Mg layered double hydroxides was confirmed for more advanced stages of corrosion when the surface pH or the surface potential increases sufficiently.

6. On the basis of the SEM observations and literature analysis, the barrier properties of LDH and simonkolleite are explained by the compact morphology, the low electron density and the layered structure with difficult ion-transfer through the layers.

7. On the basis of the experimental observations and thermodynamic modeling we suggest that Mg and Al have a synergic effect for corrosion protection of ZnMgAl coatings on steel a) in the early stages of corrosion stabilizing simonkolleite and b) in the advanced stages of corrosion by the formation of layered double hydroxides.

Acknowledgements

Authors are grateful for Dr. Gilles Walles for discussions concerning crystallography of layered structures. We would like to thank the RFCS (Research Fund for Coal and Steel) for partial support of this work.

5.6. References

- [1] T. Koll, K. Ullrich, J. Faderl, J. Hagler and A. Spalek, Proc. of Galvatech '04, Association for Iron & Steel Technology, Chicago, IL, United States, 2004, 803.
- [2] C. Schwerdt, M. Riemer, S. Koehler, B. Schuhmacher, M. Steinhorst and A. Zwick, Proc. of Galvatech '04, Association for Iron & Steel Technology, Chicago, IL, United States, 2004, 783.
- [3] C. Hosking, M.A. Ström, P.H. Shipway, C.D. Rudd, Corros. Sci. 49 (2007) 3669-3695.
- [4] I. Odnevall I, C. Leygraf, in W. W. Kirk and Herbert H. Lawson (Eds.), Atmospheric Corrosion, ASTM STP 1239, American Society for Testing and Materials, Philadelphia, 1994.
- [5] I. Odnevall, Atmospheric Corrosion of Field Exposed Zinc. A Multianalytical Characterization from Initial Films to Fully Developed Layers, doctoral thesis, Royal Institute of Technology, Stockholm, Sweden, ISBN 91-7170-866-9, 1994.
- [6] Y. Miyoshi, Y. Ito, Proc. of Galvatech '92, Verlag Stahleisen, Amsterdam, The Netherlands, 1992, p.528.
- [7] S. Kurokawa, M. Uchida, K. Mochizuki, Kawasaki Steel Ges. 27 (1995) 33.

-
- [8] Y. Morimoto, K. Honda, K. Nishimura, S. Tanaka, A. Takahashi, H. Shindo, M. Kurosaki, Nippon Steel Technical Report No. 87 (2003) 24.
- [9] S. Takeshi, Y. Fukio, M. Yasushi, A. Atsushi, Tetsu to Hagane 89 (2003) 166-173.
- [10] Q. Qing, C. Yan, Y. Wan, C. Cao, Corros. Sci. 44 (2002) 2789-2803.
- [11] K. Ogle, V. Baudu, L. Garrigues, X. Philippe, J. Electrochem. Soc. 147 (2000) 3654-3660.
- [12] K. Ogle, S. Morel, D. Jacquet, J. Electrochem. Soc. 153 (2006) B1-B5.
- [13] F. Thébault, B. Vuillemin, R. Oltra, C. Allely, L. Dosdat., K. Ogle, Electrochim. Acta 53 (2008) 5226-5234.
- [14] D. de la Fuente, J.G. Castano and M. Morcillo, Corros. Sci. 49 (2007) 1420-1436.
- [15] M. Stratmann, R. Hausbrand and M. Rohwerder, Steel Research International 74 (2003) 453-458.
- [16] M. Stratmann, R. Hausbrand and M. Rohwerder, Proceedings of 13th Asian-Pacific Corrosion Control Conference Osaka University, Japan, November, 2003 Japan Society of Corrosion Engineering Paper No.PL- 5.
- [17] K. Ishizuka, K. Nishimura, M. Kurosaki, K. Hayashi, H. Shindo. Nippon Steel Technical report No. 88 (2003) 44.
- [18] T. Tsuru, K.-I. Tamiya, A. Nishikata, Electrochim. Acta 49 (2004) 2709-2715.
- [19] W. Wiederholt, Korrosionsverhalten von Zink, Band 3: Verhalten von Zink gegen Chemikalien, Zinkberatung e.V., D-40000 Dusseldorf, 1976.
- [20] I. Odnevall and C. Leygraf, Corros. Sci. 16 (1994) 1551-1559.
- [21] T.E. Graedel, J. Electrochem. Soc. 136 (1989) 193C-203C.
- [22] U. Niirnberger, Otto Graf Journal, FMPA 2 (1991) 244-277.
- [23] B.G. Callaghan, Atmospheric corrosion testing in Southern Africa. In: W.H. Ailor, Editor, Atmospheric Corrosion, John Wiley and Sons, New York (1982), 893–921.
- [24] D. Knotkova and K. Barton, Atmos. Envir., 26A (1992) 3169-3180.
- [25] T. Prosek, D. Thierry, C. Taxen, J. Maixner, Corros. Sci. 49 (2007) 2676-2693.
- [26] T. Ishikawa, K. Matsumoto, A. Yasukawa, K. Kandori, T. Nakayama, T. Tsubota, Corros. Sci. 46 (2004) 329-342.

- [27] T. Ishikawa, M. Murai, K. Kandori, T. Nakayama, *Corros. Sci.* 48 (2006) 3172-3185.
- [28] P. Volovitch, C. Allely, K. Ogle, *Corros. Sci.* 51 (2009) 1251-1262.
- [29] T. Prosek, A. Nazarov, U. Bexell, D. Thierry, J. Serak, *Corros. Sci.*, 50 (2008) 2216-2231.
- [30] Y. Li, *Corros. Sci.* 43 (2001) 1793-1800.
- [31] S. Schürz, G.H. Luckeneder, M. Fleischanderl, P. Mack, H. Gsaller, A.C. Kneiss, G. Mori, *Corros. Sci.* 52 (2010) 3271-3279.
- [32] R.V. Gaines, H.C.W. Skinner, E.E. Foord, B. Mason, A. Rosenzweig, *Dana's New Mineralogy*, 1997, 8th edn. Wiley, New York.
- [33] D. G. Evans, R. C. T. Slade, *Struct Bond* 119 (2006) 1-87.
- [35] J.K. Lin, J.Y. Uan, *Corros. Sci.* 51 (2009) 1181-1188.
- [36] J. Wanga, D. Li, X. Yu, X. Jing, M. Zhang, Z. Jiang, *J. Alloys and Comp.* 494 (2010) 271-280.
- [37] J.K. Lin, C.L. Hsia, J.Y. Uan, *Scripta Mater.* 56 (2007) 927-930.
- [38] F. Cavani, F. Trifirb, A. Vaccari, *Catalisys Today* 11 (1991) 173-187.
- [39] T. H. Muster, I. S. Cole, *Corros. Sci.* 46 (2004) 2319-2335.
- [40] B. Lefez, S. Jouen, J. Kasperek, B. Hannoyer, *Appl. Spectroscopy* 55 (2001) 935-938.
- [41] K. Ogle, J. Baeyens, J. Swiatowska, P. Volovitch, *Electrochim. Acta* 54 (2009) 5163-5170.
- [42] M. Mokaddem, P. Volovitch, F. Rechou, R. Oltra, K. Ogle, *Electrochim. Acta* 55 (2010) 3779-3786.
- [43] K. Ogle, M. Mokaddem, P. Volovitch, *Electrochim. Acta* 55 (2010) 913-921.
- [44] I. Puigdomenech, *Hydra/Medusa Chemical Equilibrium Database and Plotting Software* KTH Royal Institute of Technology, 2004.
- [45] C.A. Johnson, F.E. Glasser, *Clays and Clay Miner.* 51 (2003) 1-8.
- [46] T. Ishikawa, M. Ueda, K. Kandori, T. Nakayama, *Corros. Sci.* 49 (2007) 2547-2556.
- [47] L. Xue, X. Mei, W. Zhang, L. Yuan, X. Hu, Y. Huang, K. Yanagisawa, *Sensors and Actuators B147* (2010) 495-501.

- [48] W.X. Zhang, K. Yanagisawa, *Chem. Mater.* 19 (2007) 2329-2334.
- [49] C. Merlin, These de doctorat de l'université Henri Poincaré, Nancy I, 1999.
- [50] R. Grauer, *Werkstoffe und corrosion* 31 (1980), 837-850.
- [51] H. Tolosa, These de doctorat de l'université des Sciences et technique de Languedoc, Montpellier II, 1992.
- [52] H. Tanaka, A. Fujioka, A. Futoyu, K. Kandori, T. Ishikawa *J. Sol. State Chem.* 180 (2007) 2061-2066.
- [53] J. W. Anthony, R. A. Bideaux, K. W. Bladh, M. C. Nichols, *Handbook of Mineralogy: Borates, Carbonates, Sulfates*, vol. V, 2003, Mineral Data Publishing, 791.
- [54] J. W. Anthony, R. A. Bideaux, K. W. Bladh, M. C. Nichols, *Handbook of Mineralogy: Halides, Hydroxides, Oxides*, vol. III, 1997, Mineral Data Publishing, 628.

Chapter VI:

The initial release of zinc and aluminum from non-treated Galvalume and the formation of corrosion products in chloride containing media

X. Zhang, **T. N. Vu**, P. Volovitch, C. Leygraf, K. Ogle, I. Odnevall Wallinder
Applied Surface Science 258 (2012) 4351-4359.

6. The initial release of zinc and aluminum from non-treated Galvalume and the formation of corrosion products

ABSTRACT: The main aim of this study was to explore the initial release of zinc and aluminium from non-treated Galvalume and the parallel formation of corrosion products when exposed to synthetic rain water of different chloride content and synthetic seawater, all at aerated conditions. Comparisons were also made with long-term exposures of Galvalume in a non-sheltered marine outdoor environment. The observed release rates from short-term conditions agree qualitatively with long-term exposure in the marine environment with a selective release of zinc over aluminium during all types of exposures. The release and corrosion processes are intertwined through the formation of corrosion products with properties that influence the long-term release of Galvalume. Prior to exposure, Al_2O_3 dominates the entire Galvalume surface, and is subject to local destruction upon interaction with chloride ions. As a consequence Al_2O_3 is gradually replaced and covered by zinc-rich corrosion products primarily in the interdendritic parts, most likely non-crystalline basic zinc chlorides and/or sulfates, during the first year of marine exposure. This is followed by the formation and integration of aluminium-rich corrosion products at exposure times between one and five years. The change in composition of corrosion products is reflected in a parallel increase in zinc release rate during the first year, followed by a decrease during the subsequent four years. The importance of the Al_2O_3 layer is also seen during exposure in deaerated synthetic rainwater or seawater, where the formation of Al_2O_3 was presumably hindered. In synthetic rain water this resulted in a ratio between released aluminium and zinc that was higher than in aerated conditions, while in deaerated synthetic seawater at an applied potential the aluminium release dominated over the zinc release.

Keywords: Galvalume, metal release, corrosion products, chlorides

6.1. Introduction

Galvalume (other trade names e.g. Zinalume, Aluzink, Aluzinc) is a commercial aluminium/zinc coating (55%Al-43.4%Zn-1.6%Si by weight [1]) applied on steel for galvanic protection, also at cut-edges. From a corrosion perspective, the barrier capacity of Galvalume on steel is enhanced compared with galvanized steel (at equivalent thicknesses) in marine and industrial atmospheres [2]. Galvalume and other zinc-aluminium alloys are widely used in many applications such as electric motor housings, door plates, window drive rails, electronics boxes, roofs, air-conditioning equipment, appliances, and automotive under-body parts or high temperature applications[3-4]. Several investigations have described the spangled microstructure of Galvalume dominated by Al-rich dendritic areas (70.3%Al- 29.7% Zn-0.2%Si) and interdendritic Zn-rich regions (42.5%Al-57.5%Zn-0.7% Si) containing Si [1, 5] in which corrosion products initially form and evolve [1, 6-10]. The corrosion process results also in selective release of alloy components [11]. These processes involve typically the selective release of the less noble element leaving a surface enriched in the nobler element. As Zn and Al are both very active metals, the local environment will possibly determine whether Al or Zn is the active element. The material will also change as corrosion products evolve on the surface and selective release leads to an enrichment of one or more alloy components in the underlying alloy phase [12-16].

The objectives of this paper are to *i*) study the initial release of zinc and aluminum from non-treated Galvalume and the formation of corrosion products when exposed to synthetic rain water of different chloride content and seawater at aerated laboratory conditions (two different set-ups), and their relevance for long-term atmospheric outdoor conditions, and *ii*) investigate differences at non-aerated conditions at open circuit conditions and at an applied potential from a corrosion product and metal release perspective, effects possibly taking place in oxygen depleted zones such as crevices, and in scratches not able to re-passivate. Two different experimental approaches to monitor metal release (chemical and electrochemical processes) have been applied: *i*) *in situ* analysis of zinc and aluminum released from Galvalume held under electrochemical control (OCP and -400 mV vs. NHE) in freshly flowing media by means of inductively coupled plasma optical emission spectroscopy (AESEC), *ii*) *Ex situ* analysis of released zinc and aluminum by means of graphite furnace atomic absorption spectroscopy (GF-AAS) at specific time periods and solution volumes of the test media at controlled conditions (temperature, agitation).

6.2. Experimental

6.2.1. Material and test media

Galvalume, an Al-Zn coating (55%Al-43.4%Zn-1.6%Si by weight) with a thickness of 25 μm on steel was subject for investigation.

Metal release studies were conducted in three different test media including synthetic rain water (pH 4.4.) [17] with modified chloride content (0.01 and 0.3 mM) and synthetic seawater (pH 8.1) [18]. The chemical composition of each media is given in **Tables 6-1 and 6-2**. These acid- and chloride containing media were selected to enable comparison with atmospheric field data, and be of relevance for automotive applications. All media were prepared from analytical grade chemicals and ultra-pure water (18.2 M Ω cm). The pH of the test media was controlled prior to sample exposure and kept at 4.35 \pm 0.05 (if necessary adjusted by the addition of 70-80 μL of 5% NaOH) and at 8.1 \pm 0.05 (no pH adjustment needed) for rainwater and seawater, respectively. All laboratory vessels used for solution preparation were acid cleaned in 10% HNO₃ for 24 hours, rinsed four times in ultra-pure water and dried at ambient laboratory conditions.

Table 6-1: Chemical composition [mg L^{-1}] of synthetic rainwater [17] of different chloride content

Synthetic rainwater	NH ₄ NO ₃	Na ₂ SO ₄	K ₂ SO ₄	MgSO ₄ ·7H ₂ O	CaCl ₂ ·2H ₂ O	95% H ₂ SO ₄	NaCl
[Cl ⁻]=0.01 mM	0.64	0.712	0.270	1.229	0.735	11.7 μL	
[Cl ⁻]=0.3 mM	0.64	0.712	0.270	1.229	0.735	11.7 μL	16.948

Table 6-2: Chemical composition [mg L^{-1}] of synthetic seawater ASTM D1141-98 [18]

Synthetic seawater	NaCl	MgCl ₂	Na ₂ SO ₄	CaCl ₂	KCl	NaHCO ₃	KBr	H ₃ BO ₃	SrCl ₂	NaF
[Cl ⁻]=560 mM	24.5	5.20	4.09	1.16	0.695	0.201	0.101	0.027	0.025	0.003

6.2.2. Flow-cell test

The AESEC (Atomic emission spectroelectrochemistry) technique was employed for real-time measurements of released metals as a function of time downstream from an electrochemical flow cell using inductively coupled plasma optical emission spectrometry (ICP-OES) – detection limits within measurement are 5.1 $\mu\text{g L}^{-1}$ (at 213.856 nm) and 4.2

$\mu\text{g L}^{-1}$ (at 167.081 nm) for zinc and aluminum, respectively. The AESEC technique is described in detail elsewhere [15]. A sample area of 0.5 cm^2 was exposed to the test media flowing with a rate of approximately 3.0 mL min^{-1} . The time duration of exposures was set to 3000 s (50 min). The solutions were deaerated by nitrogen flow, or aerated by air bubbles at ambient temperature for 10 minutes prior to the experiment. Applied potential measurements were conducted using a potentiostat (EG&G Princeton Applied Electronics M273A) functioning in potentiostatic mode combined with ICP-OES. The potentiostat is controlled manually from the front panel with the output analog current and potential signals being routed into the measuring circuit of the ICP-OES spectrometer. Measurements of the release of metals at open-circuit potential (OCP) and at an applied anodic potential (-400 mV vs. NHE) were performed using the AESEC technique. The release rates of metals downstream from the electrochemical flow cell were calculated based on the measured metal concentrations, C_m , times the flow rate per surface area.

6.2.3. Immersion tests

Samples for immersion tests were cut to a dimension of $4 \times 0.5 \text{ cm}^2$. The reverse side and the edges of the samples were sealed with a transparent non-metal containing lacquer three times to receive a defined exposed geometric surface area of 2 cm^2 . This lacquer has previously been shown to act as an efficient barrier at similar immersion conditions [19]. Triplicate samples were exposed in the different test media for the different exposure periods. Prior to exposure, the samples were cleaned with ethanol and ultra-pure water (MilliQ, $18.2 \text{ M}\Omega \text{ cm}$).

Each sample was mounted with double sided tape in a centered position at the bottom of polypropylene boxes ($29 \times 6 \times 5 \text{ cm}^3$) used as exposure vessels. Four boxes in total, triplicate samples and one blank (no sample), were exposed in parallel using a bi-linear shaking table providing a gentle agitation that moved the solution over the sample surface (set at an angle of 12° and 30 cycles/minute in order to simulate the flow-cell test conditions to some extent). Similar exposure time periods as investigated in the flow cell test were selected for the immersion experiments. Three short time periods were therefore selected, 600 s (10 min), 1800 s (30 min) and 3000 s (50 min). The specific solution volumes were based on the flow rate of solution electrolyte, the exposure time and the surface area of the sample used in the flow cell experiments. For example, in the flow cell test, 10 min of exposure would correspond to 30 mL of solution passing over the sample area of 0.5 cm^2 . Translated to the

immersion experiments, this would correspond to specific solution volumes of 120 mL (10 min), 360 mL (30 min) and 600 mL (50 min). Prior to exposure, the specific solution volume was transferred into the box and covered with parafilm.

After exposure, the solution was transferred to a storage flask and acidified to a pH less than 2 using Suprapur 65% HNO₃ (120 µL-rainwater; 150 µL-seawater). This is a standard procedure prior to total metal analysis and it serves to preserve the solution and to completely dissociate metal complexes and avoid any metal adsorption onto the inner walls of the storage vessel. The exposed samples were rinsed in ultrapure water and dried in ambient air before packed in Kleenex™ tissue wipes and stored for surface characterization.

Total concentrations of released zinc and aluminum in rainwater samples were analyzed by means of graphite furnace atomic absorption spectroscopy (GF-AAS) at standard operational conditions. Three replicate readings were made for each sample and control samples were run consecutively during the analysis (every 10th sample). The limits of detection (defined as three times the standard deviation between replicate readings of blank samples) were 2.5/2 µg L⁻¹ for aluminum and 1/1.5 µg L⁻¹ for zinc in the rain waters of chloride concentrations 0.01/0.3 mM, respectively. The limit of detection for aluminum in artificial sea water was 1 µg L⁻¹. Analysis of released zinc in seawater samples was conducted using the flame mode with a limit of detection of 1.5 µg L⁻¹. Selected samples were validated by analyses also by means of GF-AAS.

6.2.4. Long-term field exposure

Laboratory findings were compared with long-term field data generated for non-treated Galvalume exposed at unsheltered conditions at 45° from the horizontal facing south in the marine site of Brest, France for 5 years (SO₂ < 3 µg m⁻³, 450 mm y⁻¹), in agreement to the ISO 9226 standardized exposure condition for corrosion rate measurements [20]. All samples were exposed 5-10 m from the waterline [21]. Detailed information of the test site is given elsewhere [21-22].

6.2.5. Corrosion product formation

A multitude of highly surface sensitive and nondestructive analytical methods were adopted for detailed analysis of corrosion product formation. The approach includes Scanning Electron Microscopy (SEM) for morphological investigations, Infrared (IRAS) and Confocal

Raman Microspectroscopy (CRM) for information of functional surface groups and possibly their lateral distribution, surface sensitive Grazing Incidence X-ray Diffraction (GIXRD) for detection of crystalline phases, and X-ray photoelectron spectroscopy (XPS) and Auger Electron Spectroscopy (AES) for elemental compositional and chemical state information within the first few nanometers of the surface.

6.2.5.1 Scanning electron microscopy / Energy dispersive x-ray analysis (SEM/EDS)

Galvalume surfaces morphology and composition analysis were obtained using a table-top SEM (Hitachi TM-1000) with an accelerating voltage of 15 kV, equipped with Hitachi EDS facility.

6.2.5.2 Infrared Reflection Absorption Spectroscopy (IRAS)

The IRAS spectra were carried out by using a commercial Digilab 4.0 Pro FTIR spectrometer with 1024 scans at a resolution of 4 cm^{-1} in absorbance units ($-\log(R/R_0)$), where R is the reflectance of the exposed sample and R_0 the reflectance of unexposed sample [23].

6.2.5.3 Grazing incident X-ray diffraction (GIXRD)

GIXRD was performed in X'pert PRO PANALYTICAL system, equipped with an x-ray mirror ($CuK\alpha$ radiation) and a 0.27° parallel plate collimator on the diffracted side. Scanning was generated on $1 \times 1\text{ cm}$ surface area at a grazing angle of 88° versus the surface.

6.2.5.4 Confocal Raman microspectroscopy (CRM)

The confocal Raman measurements were carried out with a WITec alpha 300 system, equipped with a laser source of wavelength 532 nm. The integration time per Raman spectrum was in the order of 50 ms. Measurements were obtained with a Nikon objective, Nikon NA0.9 NGC, together with a pinhole with 100 μm diameter. The Raman spectra were produced in the scanning area with a lateral resolution around 300 nm and a vertical resolution around 2 μm .

6.2.5.5 X-ray photoelectron spectroscopy/Auger Electron Spectroscopy (XPS/AES)

Analysis of chemical composition of the outermost surface layer was performed with a XPS (Kratos AXIS HS) system combined with an Auger unit. Wide scans and detailed scans (pass energy 20 eV) of Al 2p, Zn 2p, ZnLMM, Cl 2p, S 2p, O 1s and C 1s were accomplished using a monochromatic Al K α X-ray source (1486.6 eV) operated at 300 W (15 kV/20 mA). Measurements were conducted at two different areas of analysis, each approximately sized 0.4 mm². AES mapping were performed using an acceleration voltage of 10 kV and a beam current of 300 nA.

6.3. Results and Discussion

6.3.1. Initial metal release in chloride containing media at aerated conditions

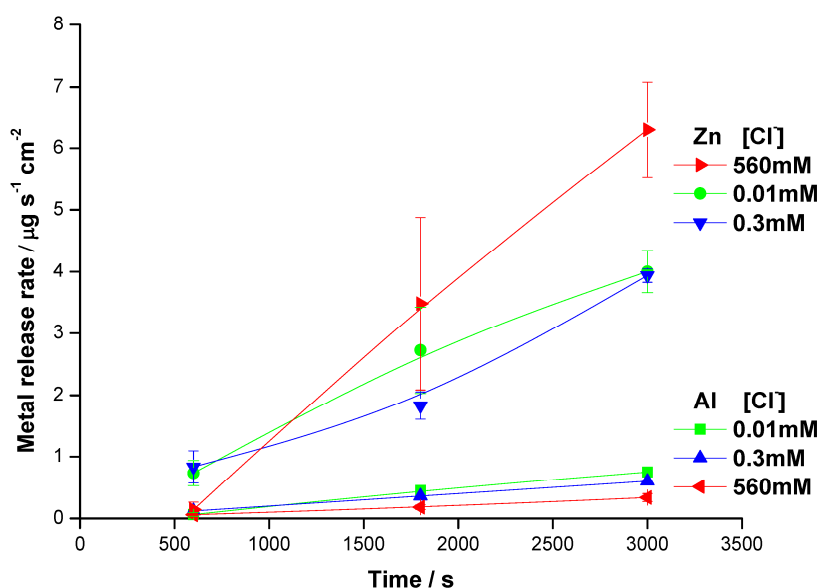


Figure 6-1: Release rates of zinc and aluminum from Galvalume exposed in synthetic rainwater (0.01 mM, 0.3 mM Cl⁻) and artificial sea water (560 mM Cl⁻) during immersion testing. Each marker corresponds to the mean value of three replicate samples. (Solid lines are only used as guides)

Results from the immersion tests are presented in **Fig. 6-1**. All media revealed significantly higher release rates of zinc compared to aluminum and increasing release rates of zinc with time. No significant effect of chloride content on the release rate of either zinc or

aluminum was evident for the synthetic rain media of constant pH. In seawater of significantly higher chloride content but more alkaline pH compared with the rainwater media, small differences were evident after the two first time periods but significant (factor of two) after 3000s of exposure. These results imply that chloride ions in seawater after a certain time period locally destroy the protective ability of aluminum oxide at a faster rate compared to rainwater exposure. The released concentrations of aluminum were however for most cases very low, below or close to the limit of detection (the marker corresponds to the limit of detection value, no error bars displayed). Measurable amounts of aluminum were only observed after the two longer time periods in seawater and after the short time period in rain water (0.01 mM Cl⁻). Similar to findings in the slightly acidic (pH 4.4) rainwater of low chloride content, very low amounts of aluminum (<5.5%) were released compared to zinc even after 3000 s in seawater (pH 8.1). Preferential release of zinc was hence evident in both synthetic rainwater and seawater and not pH-dependent at these conditions. At higher pH (> 10), previous findings have shown aluminum to be preferentially released compared to zinc [14, 16].

Real-time measurements of released metals using the AESEC flow cell test at aerated OCP conditions are presented in **Fig. 6-2**. Release rates for were calculated from the average equivalent concentration using Faradays law (conversion from $j_{Zn} + j_{Al}$), see experimental. The open circuit potential (E_{oc}) is also given as a function of time. Similar to the immersion test findings, very low release rates of aluminum and a dominance of released zinc were observed, independent on test media. Despite very different chloride concentrations in the three test media, the total release currents were very similar. One explanation may be that the corrosion rate is determined by the cathodic reaction. However, the distribution of the total current between the alloy components will be determined by the material.

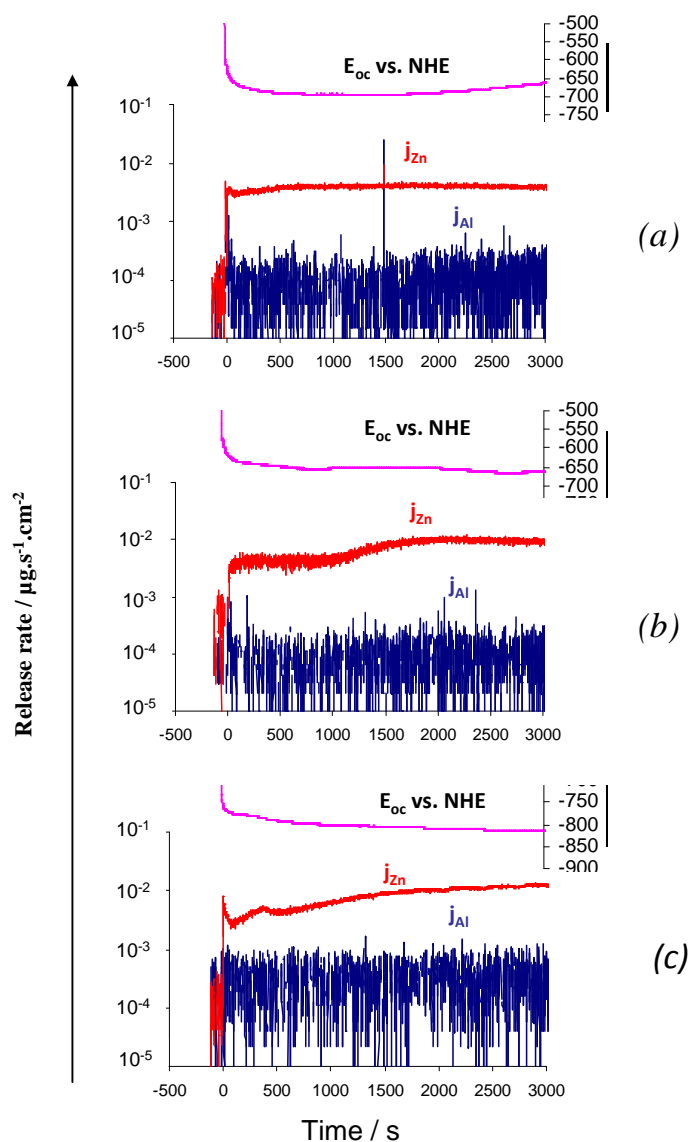


Figure 6-2: Release rates of zinc and aluminum for Galvalume exposed to aerated a) synthetic rain water (0.01 mM Cl⁻), b) synthetic rain water (0.3 mM Cl⁻), and c) synthetic seawater (560 mM Cl⁻) at open circuit potential (OCP).

Total release rates determined using the two different experimental set-ups are compiled in **Table 6-3** together with the corresponding relation between released aluminum and zinc (Al/(Al+Zn)) for the different exposure conditions. The results clearly show a dominance of zinc release compared to aluminum for both experimental set-ups. Quantitatively, the immersion test resulted in significantly lower total release rates compared with the flow cell test, in particular pronounced for seawater and the high chloride containing rainwater media. The reason is believed to be associated to the different exposure conditions

with constantly fresh media flowing over the surface in the flow cell test and hence the continuous removal of released metals from the media in contact with the surface, totally in contrast with the immersion test with no renewal of the media within the exposure period. No large differences in total release rates were observed between the immersion tests despite large differences in chloride content of the test media. Observed release rates during the flow cell tests were approximately twice as high in rainwater of high chloride content and in seawater compared with rainwater of low chloride content. These findings were however not reflected by measured E_{oc} values during the flow cell test showing Galvalume in both rain water media to be more active (-650 mV vs. NHE) compared to seawater conditions (-820 mV vs. NHE). This clearly illustrates that metal release rates cannot be predicted from corrosion resistance measurements.

Table 6-3: Total release of zinc and aluminum for Galvalume after exposure (3000 s) at aerated conditions in synthetic rainwater (pH 4.4) of different chloride content and in synthetic sea water (pH 8.1,) and corresponding Al/(Al+Zn) release ratios.

Electrolyte	Total Al+Zn		Al/(Al+Zn) release ratio	
	Immersion tests (μgcm^{-2})	Flow-cell tests (μgcm^{-2})	Immersion tests	Flow-cell tests
Synthetic rainwater (0.01 mM Cl ⁻)	4.00	11.9	Below LOD	0.018
Synthetic rainwater (0.3 mM Cl ⁻)	4.01	21.5	0.019	0.005
Synthetic seawater (560 mM Cl ⁻)	6.64	25.0	0.053	0.012

Generated data at aerated conditions were in concordance with field data where the release of zinc and aluminum were continuously monitored for Galvalume surfaces exposed at non-sheltered conditions in a marine environment during five years [24]. Significantly more zinc was released compared with aluminum throughout the exposure period with an annual Al/(Al+Zn) release ratio typically varying between 0.04 ± 0.01 for individual years of exposure, **Fig. 6-3**. Similar to laboratory findings, field data at the marine site (deposition rates of chloride: $7 - 8757 \text{ mg m}^{-2} \text{ day}^{-1}$) showed initially increasing release rates of zinc during the first year of exposure as a consequence of rapid formation of zinc-rich corrosion products in primarily zinc-rich interdendritic areas. This was followed by decreasing rates due to the gradual formation and integration of aluminum-rich corrosion products also in

interdendritic areas [24]. Exposures at urban field conditions [25] with low deposition rates of chlorides ($< 2 \text{ mg Cl}^- \text{ m}^{-2} \text{ day}^{-1}$), did not show any initially increased release rates of zinc with time but rather gradually reduced rates with time during a ten-year exposure period, **Fig. 6-3**. This may be related to undisturbed aluminum oxides gradually hindering the release of zinc from zinc-rich corrosion products formed in the interdendritic areas. The formation of corrosion products at laboratory conditions is discussed in the next paragraph.

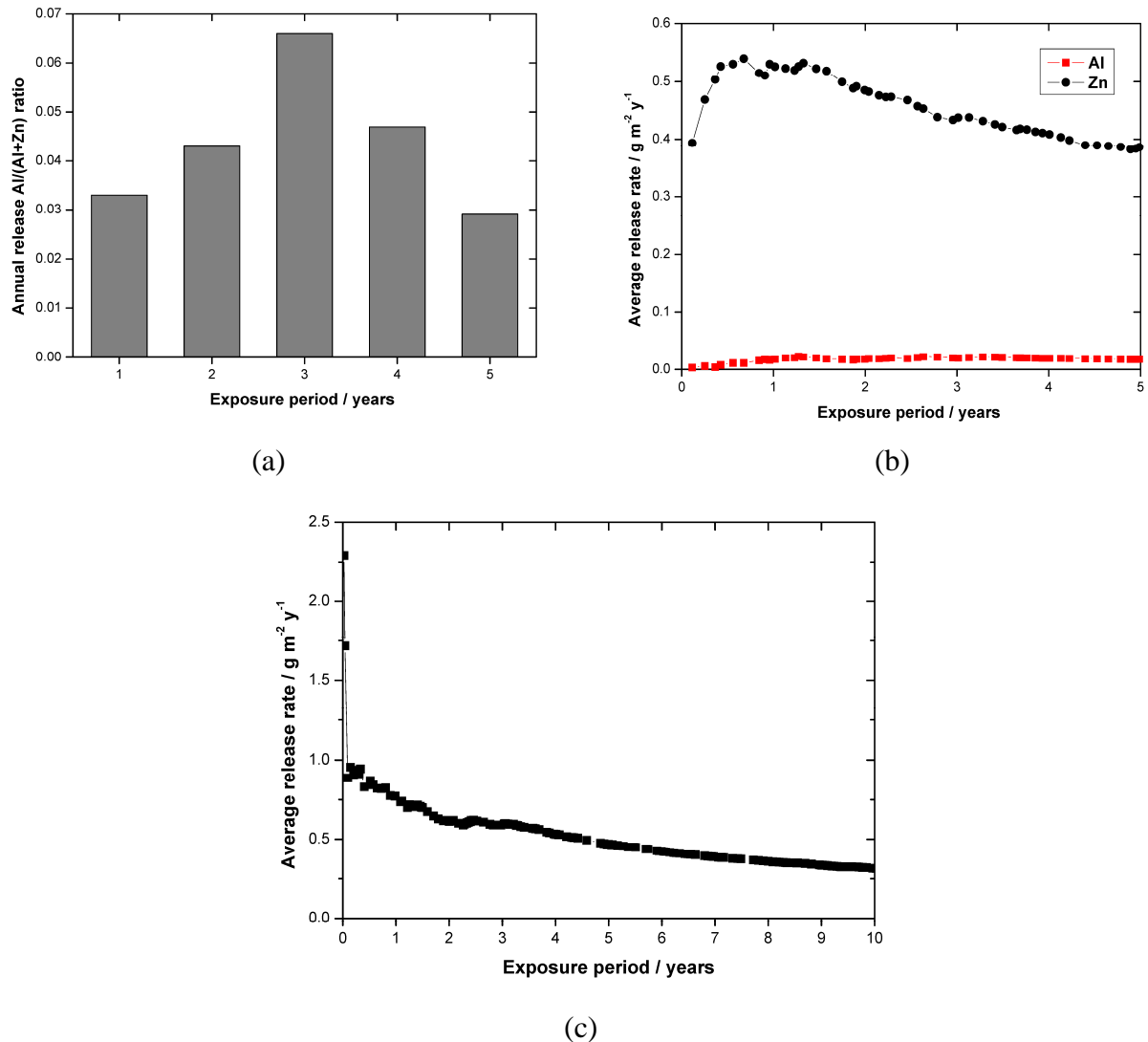


Figure 6-3: (a) Average release rates of zinc and aluminum and (b) corresponding annual release Al/(Al+Zn) ratio for each year of exposure for Galvalume exposed to non-sheltered conditions at marine site of Brest, France for five years, and (c) average release rates of zinc during 10 years of urban non-sheltered conditions.

6.3.2. Initial formation of corrosion products in chloride containing media at aerated conditions

Relatively similar surface morphology observations were made by means of SEM for Galvalume exposed to E_{oc} conditions at both flow cell and immersion conditions, **Fig. 6-4**. In agreement with literature findings [6-8], the SEM investigation concluded preferential formation of corrosion products in zinc-rich interdendritic areas, mostly pronounced after the seawater exposure. No significant differences were observed during the SEM investigation between samples exposed to rainwater media of different chloride content showing only slight and local corrosion. None of the exposure conditions resulted in the identification of any crystalline corrosion products by means of GIXRD, except for Al_2O_3 , present in all cases. According to literature findings, crystalline Al_2O_3 is favoured by the presence of chlorides [26-27]. The lack of crystalline zinc-containing corrosion products may be related to the presence of amorphous phases only, or to very small amounts and/or presence of crystalline corrosion products within interdendritic areas impossible to detect with GIXRD.

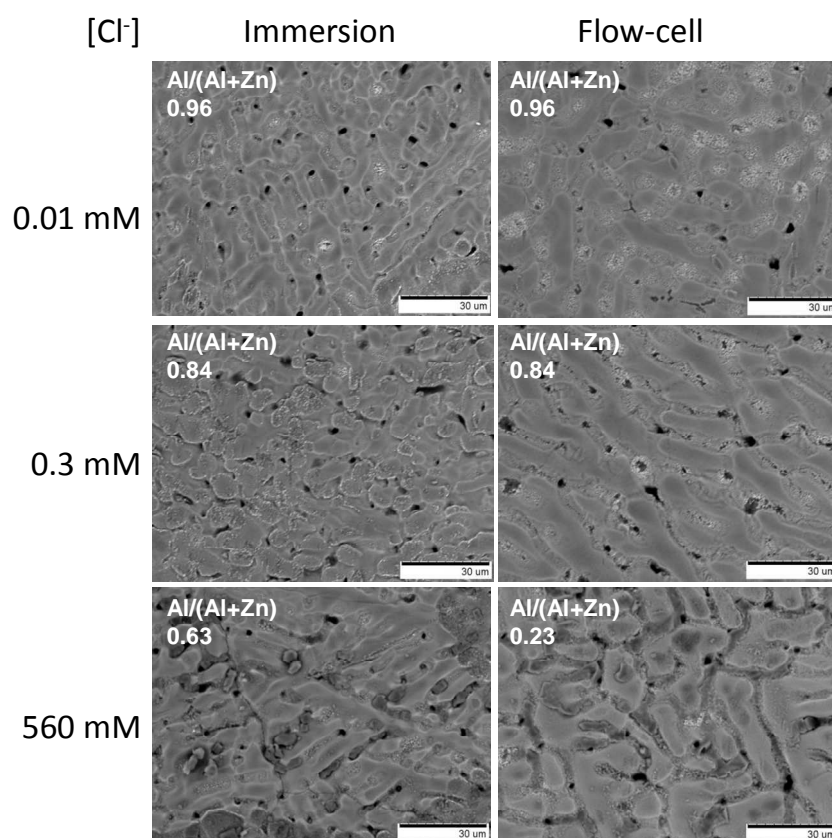


Figure 6-4: SEM images of Galvalume exposed for 3000s to artificial rain water 0.01 mM, 0.3 mM Cl^- and artificial sea water (560 mM Cl^-) via immersion experiments (left) and flow-cell tests (right). The average mass ratio $Al/(Al+Zn)$ refers to XPS compositional measurements of two separate areas (each sized 0.4 mm^2).

Analysis by means of XPS clearly demonstrated the dominance of aluminum-rich phases in the outermost surface layer of the non-exposed bare surface of Galvalume, **Fig. 6-5**. The Al/(Al+Zn) surface mass fraction varied between 0.85 and 0.99 over the surface, a ratio very different from the bulk composition (0.55) and reported mass ratios of 0.7 and 0.2 for aluminum-rich dendritic areas and zinc-rich interdendritic areas, respectively[24]. The exposure in artificial rain water of low chloride content (0.01 mM) did not result in any significant changes of this fraction with an average Al/(Al+Zn) mass ratio of 0.96 (0.92-0.99) for both experimental conditions. Only small changes were observed at the high chloride concentration (0.3 mM) of rainwater with no differences between two experimental set-ups (mean 0.84 (0.82-0.86)). For these surfaces, both metallic (Al 2p_{3/2}: 72.2±0.2 eV) and oxidized aluminum peaks (74.5±0.2 eV) were observed, suggesting the presence of Al₂O₃ with an estimated thickness of 4-6 nm [28]. Calculations of the Auger parameters [29] suggested the presence of ZnO [30] (2011.10.3 eV) and possibly Zn(OH)₂ (2008.3±0.3 eV) [24, 30] on surfaces exposed to the synthetic rain waters. The exposure to seawater resulted in significant changes of the surface distribution of aluminum-rich and zinc-rich corrosion products. The mean Al/(Al+Zn) surface mass fraction was for these surfaces reduced to 0.63 (0.58-0.68) in the case of the immersion study, and to 0.23 in the case of the flow-rate study. The metallic aluminum signal was still observed for samples exposed in the immersion study, but not present for the flow-cell exposure indicative of a growth also of the aluminum oxide. Calculated Auger parameters suggested the presence of ZnO, Zn(OH)₂ and zinc in another oxidized phase not possible to assign (2009.5±0.5 eV). In both cases, even though more pronounced in the flow rate study, the seawater exposure promoted the formation of zinc-rich corrosion products in the interdendritic areas as evident from the SEM investigation, **Fig. 6-4**.

These findings are in concordance with the metal release data with increasing release rates of zinc with time, and at faster rates in seawater after the longest immersion period investigated (3000 s) for both experimental conditions. This can presumably be explained by a faster interaction and local destruction of the aluminum oxide (formed at high temperatures during alloy production), present in both zinc-rich and on aluminum-rich areas, by the high chloride content in seawater compared to the artificial rainwaters of significantly lower chloride concentration. A larger XPS surface fraction of zinc-rich corrosion products was however expected, **Fig. 6-4**, for the flow cell test in rainwater of higher chloride concentration since the calculated total release rate in this case was as high as for the seawater exposure, **Table 6-3**. This cannot be explained but may be related to a non-uniform formation of zinc-rich corrosion products in interdendritic areas. No chlorides were identified by means of XPS

on the surfaces exposed to any of the rainwater media, whereas both sulfate and chloride were observed on Galvalume exposed to seawater conditions. Previous findings at atmospheric conditions have shown these species to be correlated to the local formation of basic zinc sulfates and / or chlorides in zinc-rich interdendritic areas [1, 6-10].

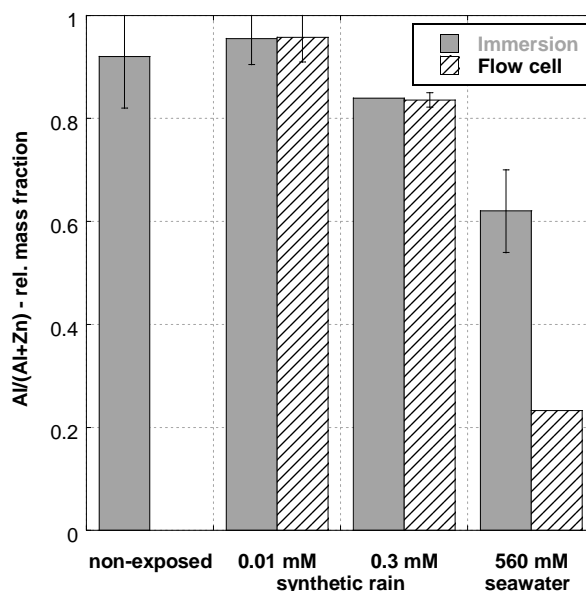


Figure 6-5: Average mass ratio $Al/(Al+Zn)$ based on XPS compositional measurements of two separate areas (each 0.4 mm^2) after 3000s exposure in artificial rainwater and seawater

The formation and presence of Al_2O_3 suggested by XPS findings were supported by IRAS observations with a band centered at approximately 775 cm^{-1} , assigned as crystalline Al_2O_3 [31], and consistent with GIXRD findings. The band at 555 cm^{-1} suggested the presence of ZnO [32], already indicated via XPS findings. This phase was also supported by Raman measurements showing a band around 570 cm^{-1} and a broad peak at approximately 400 cm^{-1} , indicative of amorphous ZnO [33]. IRAS spectra generated for surfaces exposed to seawater showed in addition a strong band centered at approximately 3445 cm^{-1} , assigned to OH^- , and a band centered at 1124 cm^{-1} that may be assigned to SO_4^{2-} and/or OH^- . These observations were supported by XPS confirming the presence of sulfate, and sulfur by means of EDS. These findings combined with the unidentified oxidized zinc compound suggested by the Auger parameter calculation of XPS findings, suggest possibly the presence of an amorphous basic zinc sulfate. As also chlorides were identified, amorphous basic zinc chlorides and/or sulfates cannot be excluded. IRAS bands were furthermore identified at approximately 1599 and 1467 cm^{-1} , possibly assigned to CO_3^{2-} [6]. However, no peaks

correlated to basic zinc carbonates (strong peaks at 1060-1070 cm^{-1}) [34] were identified by means of Raman measurements.

6.3.3. Initial metal release and corrosion product formation in chloride containing media at non-aerated OCP and at an applied anodic potential.

At non-aerated conditions, possibly simulating situations in oxygen-depletion zones, measured E_{oc} values revealed less active surfaces (-850 mV vs. NHE) in the rainwater media compared to aerated conditions (-650 mV vs. NHE), whereas no differences were observed between aerated and non-aerated conditions in seawater (-850 mV vs. NHE). Contradictory to findings at aerated conditions, the higher concentrations of chlorides in the rainwater and in seawater did not result in higher released amounts of metals compared with rainwater of low chloride content, **Table 6-4**. Similar to aerated conditions, zinc was predominantly released compared to aluminum in all media although with a higher proportion of released aluminum compared to zinc.

Table 6-4: Total release of zinc and aluminum (conversion from $j_{Zn} + j_{Al}$) for Galvalume after flow cell exposure (3000 s) at aerated and non-aerated OCP conditions, and at non-aerated conditions and an applied potential (-400 mV vs. NHE) in synthetic rainwater (pH 4.4) of different chloride content and in synthetic sea water (pH 8.1), and corresponding Al/(Al+Zn) release ratios.

Test media	Total release (Al+Zn)			Al/(Al+Zn) ratio		
	Flow-cell tests (aeration OCP) ($\mu\text{g}\cdot\text{cm}^{-2}$)	Flow-cell tests (deaeration OCP) ($\mu\text{g}\cdot\text{cm}^{-2}$)	Flow-cell tests (deaeration -400 mV vs. NHE) ($\mu\text{g}\cdot\text{cm}^{-2}$)	Flow-cell tests (aeration OCP)	Flow-cell tests (de-aeration OCP)	Flow-cell tests (deaeration, -400 mV vs. NHE)
Synthetic rainwater (0.01 mM Cl ⁻)	11.9	9.30	63.4	0.018	0.043	~0
Synthetic rainwater (0.3 mM Cl ⁻)	21.5	8.42	130	0.005	0.040	~0
Synthetic seawater (560 mM Cl ⁻)	25.0	4.04	4129	0.012	0.087	0.56

An applied anodic potential (-400 mV vs. NHE) at deaerated conditions resulted as expected in significantly higher total metal release rates, **Table 6-4** and **Fig. 6-6 (left)**, conditions that may occur in confined zones where re-passivation is disabled. Zinc was predominantly released in the case of rainwater exposure with non-significant released amounts of aluminum. In seawater, the situation was the opposite with aluminum released to a very large extent, almost 56% of the total amount of zinc and aluminum. A heavily corroded surface also with significantly corroded aluminum-rich dendritic areas were observed by means of SEM at these conditions, **Fig. 6-6 (right)**, effects not seen at E_{oc} conditions, *c.f.* **Fig. 6-4**.

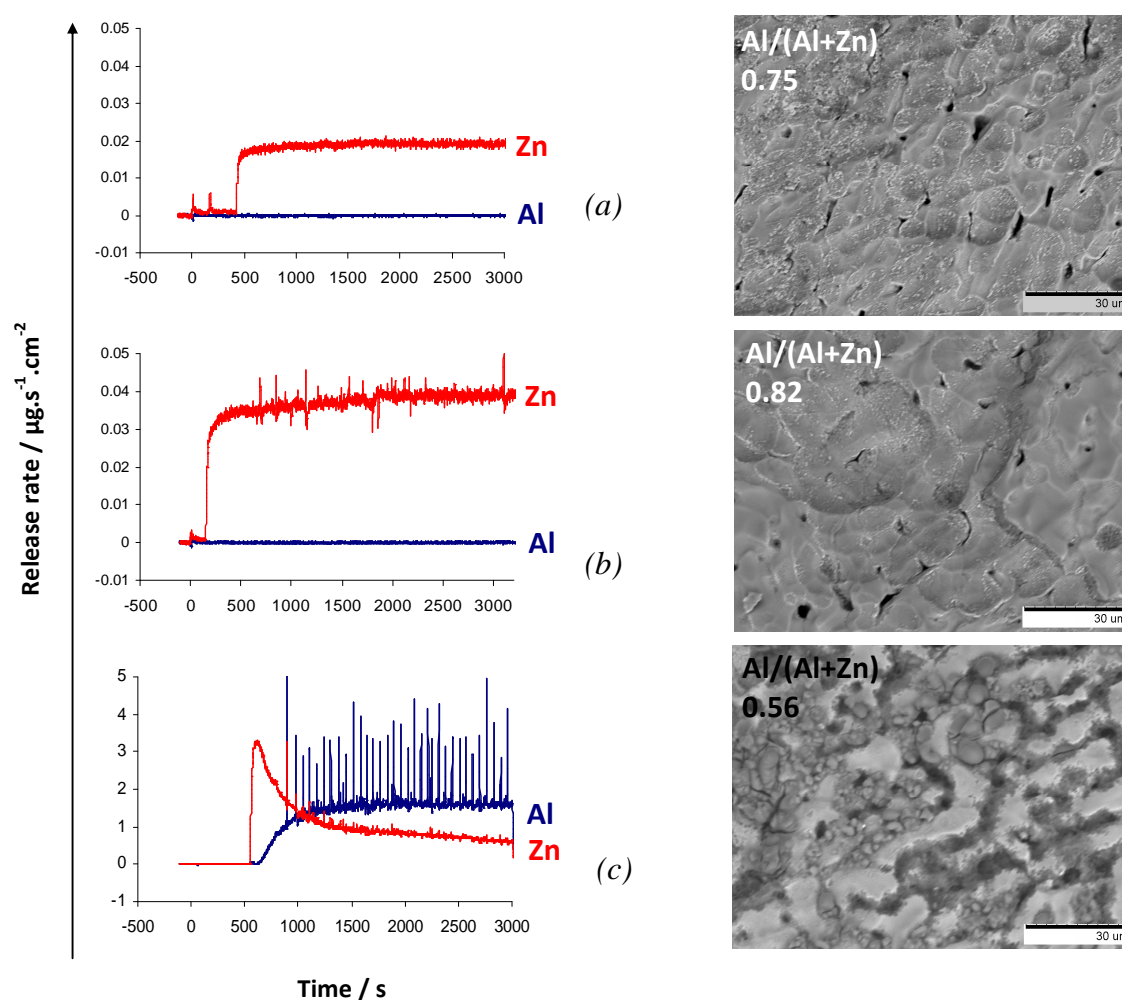


Figure 6-6: Release rates (left) and SEM images (right) of Galvalume exposed for 3000s to artificial rain water 0.01 mM, 0.3 mM Cl⁻ and artificial sea water (560 mM Cl⁻) at non-aerated flow-cell at an applied potential of -400 mV vs. NHE (right). The average mass ratio Al/(Al+Zn) inserted in the SEM images refers to XPS compositional measurements of two separate areas (each 0.4 mm²).

According to XPS, the mass distribution of aluminum- and zinc-rich corrosion products (Al/Al+Zn) on the surface changed from 0.75 (0.57-0.93) to 0.82 (0.77-0.87) to 0.56 (0.47-0.65) for Galvalume exposed to non-aerated E_{oc} conditions in rainwater of low and high chloride content and seawater, respectively. Similar phases, Al_2O_3 and ZnO were suggested by XPS to be present at both conditions. At sea-water conditions, an additional aluminum peak was observed at higher bindings at 75.5 eV (Al $2p^{3/2}$), possibly assigned as AlOOH or $Al(OH)_3$ [35], in agreement with findings of IRAS showing a broad band between 770 and 1000 cm^{-1} suggesting the additional presence of amorphous Al_2O_3 , and/or AlOOH [9]. XPS and EDS identified sulfur as sulfate, chlorine as chloride and sodium on the surface. According to AES mapping, these elements were predominantly present in platelet-like phases formed locally in interdendritic areas as evidenced from XPS and AES mapping, **Fig. 6-7**. These observations are in concordance with findings for Galvalume exposed at non-sheltered conditions at a marine site for five years where ZnO, $Zn_5(CO_3)_2(OH)_6$, non-assigned corrosion products rich in SO_4^{2-} and $(OH)Cl^-$ (possibly $NaZn_4Cl(OH)_6SO_4 \cdot 6H_2O$ [36]) and $Al(OH)_3 \cdot 1/2H_2O$ were identified [24]. Similar zinc-rich corrosion products have been identified on bare zinc sheet exposed in parallel at the marine site [33].

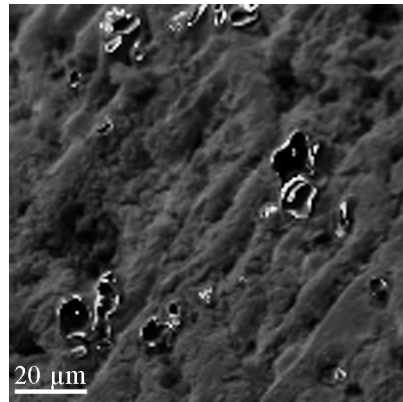


Figure 6-7: Locally occurring corrosion products rich in S and Cl (white areas) from AES mapping ($100 \times 100\ \mu\text{m}$) of Galvalume after 3000 s exposure at non-aerated activated (-400 mV vs. NHE) conditions in synthetic seawater.

The results clearly demonstrate that the mechanisms of zinc and aluminum release may change radically depending upon environmental conditions. These results could have important consequences for confined zone corrosion since the gap electrolyte may readily pass from aerobic to anaerobic conditions.

6.4. Conclusions

This multi-analytical study of non-treated Galvalume exposed to short-term aerated synthetic rain or seawater of different chloride content and to a long-term natural marine outdoor environment permits the following conclusions to be drawn:

- All investigated synthetic rainwater media revealed significantly higher release rates of zinc compared to aluminum and also increasing release rates of zinc with time.

- Release rates were compared in two short-term exposure conditions, stagnant immersion test and flow cell test. A selective release of zinc was always observed, but the immersion test resulted in significantly lower total release rates compared with the flow cell test.

- During immersion conditions the total release of zinc and aluminium was similar in all media, whereas under flowing conditions the total release rate increased with chloride content.

- Results from aerated short-term conditions agree qualitatively with long-term non-sheltered exposure in the marine environment: a selective release of zinc was observed throughout the five-year exposure period with the annual $Al/(Al+Zn)$ release ratio typically in the range 0.04 ± 0.01 , also an initial increase in zinc release rate during the first year followed by a decreasing zinc release rate.

- This time-dependence is a consequence of the gradual build-up of zinc-rich corrosion products during the first year, particularly in interdendritic areas, followed by the formation and integration of aluminum-rich corrosion products at exposure times longer than one year.

- The only crystalline corrosion product detected was Al_2O_3 . This phase dominates the entire Galvalume surface before exposure, and is subject to local destruction upon interaction with chloride ions. As a consequence Al_2O_3 is gradually replaced and covered by zinc-rich corrosion products in the interdendritic parts, most likely non-crystalline basic zinc chlorides and/or sulfates, during the first year of marine exposure.

- Also in deaerated synthetic rainwater, zinc was selectively released, although the ratio between released aluminum and zinc was higher than in aerated conditions. However, in deaerated synthetic seawater and at an applied potential, aluminum release dominated over zinc release, presumably because of the hindrance of the formation of a protective Al_2O_3 layer.

- In all, this study is another confirmation of the different mechanisms that govern metal corrosion and metal release, two processes that are intertwined through the

formation of corrosion products with properties that influence the long-term release of Galvalume.

Acknowledgement

Financial support from the Chinese Scholarship Council (CSC) is gratefully acknowledged. The authors are grateful for the financial support of the field exposure provided by Nordic Galvanizers Association, Sweden; Rheinzink, Germany; Saferoad, Norway and SSAB, Sweden and to the RFCS project “Autocorr” with partners Arcelor Mittal, France, Salzgitter AG, Germany, ThyssenKrupp, Germany and Voestalpine, Austria.

Instrumental grants from Knut and Alice Wallenberg foundation (XPS) and from Nils and Dorthi Troëdsson Foundation (combined confocal Raman and AFM) are gratefully acknowledged.

The French Corrosion Institute, Brest, France, is highly acknowledged for their invaluable help in collecting runoff water at the marine site.

Valuable discussions from Dr. Ping Qiu and Dr. Klara Midander are highly appreciated.

We also thank Dr. Gunilla Herting and MSc David Lindström for all field exposure AAS analytical efforts.

6.5. References

- [1] A.R. Moreira, Z. Panossian, P.L. Camargo, M.F. Moreira, I.C.d. Silva, J.E.R. de Carvalho, Zn/55Al coating microstructure and corrosion mechanism, *Corros. Sci.*, 48 (2006) 564-576.
- [2] E. Palma, J.M. Puente, M. Morcillo, The atmospheric corrosion mechanism of 55% Al-Zn coating on steel, *Corros. Sci.*, 40 (1998) 61-68.
- [3] W.-B. Chen, P. Chen, H.Y. Chen, J. Wu, W.-T. Tsai, Development of Al-containing zinc-rich paints for corrosion resistance, *Appl. Surf. Sci.*, 187 (2002) 154-164.
- [4] GALVALUME sheet steel, in: U.S.S.T. Bulletin (Ed.), Construction, 2005.
- [5] J.H. Selverian, M.R. Notis, A.R. Marder, The microstructure of 55 w/o Al-Zn-Si (Galvalume) hot dip coatings, *Mat. Engin.*, 9 (1987) 133-140.
- [6] A.K. Neufeld, I.S. Cole, Use of FTIR to study surface changes on metals in the early stages of degradation, in: 13th International Corrosion Congress, Melbourne, Australia, 2006, pp. Paper 046.

-
- [7] J.J. Friel, Atmospheric corrosion products on Al, Zn and AlZn metallic coatings, *Corros.*, 42 (1986) 5.
- [8] E. Palma, M. Morcillo, A laboratory study of the cathodic protection afforded by 55-percent Al-Zn coating in comparison with a galvanized coating, *Plating and Surface Finishing*, 85 (1998) 106-109.
- [9] I.O. Wallinder, C. Leygraf, Characterization of corrosion products formed on rain sheltered Aluzink TM and aluminum in a rural and an urban atmosphere, in: *Proc. 13th Int. Corr. Congr.*, , Australia, 1996, pp. 1-8.
- [10] I. Odnevall Wallinder, W. He, P.E. Augustsson, C. Leygraf, Characterisation of black rust staining of unpassivated 55% Al-Zn alloy coatings. Effect of temperature, pH and wet storage., *Corros. Sci.*, 41 (1999) 2229-2249.
- [11] M. Mokaddem, P. Volovitch, K. Ogle, The anodic dissolution of zinc and zinc alloys in alkaline solution. I. Oxide formation on electrogalvanized steel, *Electrochim. Acta*, 55 (2010) 7867-7875.
- [12] K. Ogle, A. Tomandl, N. Meddahi, M. Wolpers, The alkaline stability of phosphate coatings I: ICP atomic emission spectroelectrochemistry, *Corros. Sci.*, 46 (2004) 979-995.
- [13] K. Ogle, M. Mokaddem, P. Volovitch, Atomic emission spectroelectrochemistry applied to dealloying phenomena II. Selective dissolution of iron and chromium during active-passive cycles of an austenitic stainless steel, *Electrochim. Acta*, 55 (2010) 913-921.
- [14] M. Mokaddem, P. Volovitch, F. Rechou, R. Oltra, K. Ogle, The anodic and cathodic dissolution of Al and Al-Cu-Mg alloy, *Electrochim. Acta*, 55 (2010) 3779-3786.
- [15] K. Ogle, J. Baeyens, J. Swiatowska, P. Volovitch, Atomic emission spectroelectrochemistry applied to dealloying phenomena: I. The formation and dissolution of residual copper films on stainless steel, *Electrochim. Acta*, 54 (2009) 5163-5170.
- [16] K. Ogle, M. Serdechnova, M. Mokaddem, P. Volovitch, The cathodic dissolution of Al, Al₂Cu, and Al alloys, *Electrochim. Acta*, 56 (2011) 1711-1718.
- [17] G. Herting, I. Odnevall Wallinder, C. Leygraf, A comparison of release rates of Cr, Ni and Fe from stainless steel alloys and the pure metals exposed to simulated rain events, *J. Electrochem. Soc.*, 152 (2005) B23-29.
- [18] A.s. D1141-98, Standard Practice for the Preparation of Substitute Ocean Water, in, 2003.

- [19] G. Herting, I. Odnevall Wallinder, C. Leygraf, Corrosion-induced release of chromium and iron from ferritic stainless steel grade AISI 430 in simulated food contact, *Journal of Food Engineering*, 87 (2008) 291-300.
- [20] ISO, ISO standard 9226, Corrosion of metals and alloys -- Corrosivity of atmospheres -- Determination of corrosion rate of standard specimens for the evaluation of corrosivity, in, 1992.
- [21] J. Sandberg, I.O. Wallinder, C. Leygraf, N. Le Bozec, Corrosion-induced zinc runoff from construction materials in a marine environment, *J. Electrochem. Soc.*, 154 (2007) C120-C131.
- [22] D. Lindström, I. Odnevall Wallinder, Long-term use of galvanized steel in external applications. Aspects of patina formation, zinc runoff, barrier properties of surface treatments, and coatings and environmental fate, *Environ. Monit. Assess.*, 173 (2011) 139-153.
- [23] T. Aastrup, C. Leygraf, Simultaneous infrared reflection absorption spectroscopy and quartz crystal microbalance measurements for *in situ* studies of the metal/atmosphere interface, *J. Electrochem. Soc.*, 144 (1997) 2986-2990.
- [24] P. Qiu, C. Leygraf, I.O. Wallinder, Evolution of corrosion products and metal release from Galvalume coating during short and long-term atmospheric exposures, manuscript, in: *Mater. Chem. Phys.*, 2011.
- [25] S. Bertling, I. Odnevall Wallinder, C. Leygraf, D. Berggren Kleja, Occurrence and fate of corrosion-induced zinc in runoff water from external structures, *Sci. Total Environ.*, 367 (2006) 908-923.
- [26] C.L. McBee, J. Kruger, Nature of passive films on iron-chromium alloys, *Electrochim. Acta*, 17 (1972) 1337-1341.
- [27] T.P. Hoar, On corrosion-resistant materials, *J. Electrochem. Soc.*, 117 (1970) 17C-22C.
- [28] B.R. Strohmeier, An ESCA method for determining the oxide thickness on aluminum alloys, *Surf. Interface Anal.*, 15 (1990) 51-56.
- [29] C.D. Wagner, The Auger parameter, its utility and advantages: a review, *J. Electron. Spectr. Relat. Phenom.*, 47 (1988) 283-313.
- [30] A.K. Chandra, R. Mukhopadhyay, J. Konar, T.B. Ghosh, A.K. Bhowmick, X-ray photoelectron spectroscopy and Auger electron spectroscopy of the influence of cations and anions of organometallic adhesion promoters on the interface between steel cord and rubber skim compounds, *J. Mater. Sci.*, 31 (1996) 2667-2676.

-
- [31] P. Brüesch, R. Kötz, H. Neff, L. Pietronero, Vibrational properties of Al₂O₃ films on gold, aluminum, and silicon, *Phys. Rev. B*, 29 (1984) 4691.
- [32] F. Zhu, X. Zhang, D. Persson, D. Thierry, *In Situ* Infrared Reflection Absorption Spectroscopy Studies of Confined Zinc Surfaces Exposed under Periodic Wet-Dry Conditions, *Electrochem. Solid-State Lett.*, 4 (2001) B19-B22.
- [33] J. Hedberg, N. Le Bozec, I. Odnevall Wallinder, Spatial distribution and formation of corrosion products in relation to zinc release for zinc sheet and coated pre-weathered zinc at urban and a marine atmospheric conditions, submitted, *Corros. Sci.*, (2011).
- [34] M.C. Hales, R.L. Frost, Synthesis and vibrational spectroscopic characterisation of synthetic hydrozincite and smithsonite. , *Polyhedron*, 26 (2007).
- [35] Y. Zhang, Characterization of as-received hydrophobic treated AlN powder using XPS, *J. Mater. Sci. Lett.*, 21 (2002) 1603-1605.
- [36] I. Odnevall, C. Leygraf, Formation of NaZn₄Cl(OH)₆SO₄ · 6H₂O in a marine atmosphere, *Corros. Sci.*, 34 (1993) 1213-1229.

Chapter VII:

The effect of pH on the selective dissolution of Zn and Al from Zn-Al coatings on steel

T. N. Vu, P. Volovitch, K. Ogle,

Corrosion Science (Submitted in May 2012).

7. The effect of pH on the selective dissolution of Zn and Al from Zn-Al coatings on steel

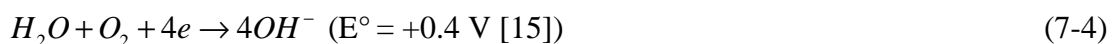
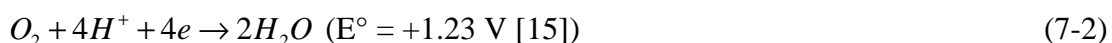
ABSTRACT: Selective dissolution of Al and Zn from 5 wt% Al-Zn (Galfan) and 55 wt% Al-Zn (Galvalume) galvanized steel coatings was investigated by comparing Zn and Al dissolution rates in 30 mM NaCl at pH from 2 to 12 using in situ kinetic analysis (atomic emission spectroelectrochemistry, AESEC) and in a 5 day immersion test. The selective dissolution of Zn occurred at low pH and selective dissolution of Al at high pH. Results from AESEC and from the immersion test were compared and interpreted in terms of the inhibiting and passivating effect of corrosion product films.

Keywords: Selective dissolution; Zn-Al alloy; pH; atomic emission spectroelectrochemistry (AESEC); aeration and de-aeration.

7.1. Introduction

The corrosion behavior of pure Zn and Zn coated steel has been investigated in considerable detail and reviewed in [1,2]. In previous work [3], we demonstrated the combined use of the atomic emission spectroelectrochemical (AESEC) method and immersion testing to investigate the mechanisms of selective dissolution of 55 wt% Al-Zn galvanized steel (Galvalume™). In this work, we use two common commercial Al-Zn alloys, 5% Al-Zn (Galfan™) and 55% Al-Zn (Galvalume™) [4-9] to address the question of how the selective dissolution rate of either Zn or Al will vary with pH. This variation is of particular interest for galvanized steel exposed in confined zones (such as in car bodies) where significant localized pH changes may occur [10].

During aqueous electrochemical corrosion processes on zinc alloys, the following cathodic reactions may occur [11-14]:



In the pH range 4-11, oxygen reduction is the major cathodic reaction for Zn [14], and it can be inhibited by the protective corrosion product layer which forms on the alloy surface and blocks oxygen diffusion. The anodic dissolution rate (**Eqn. 7-5**) depends on the stability of zinc and/or aluminum containing corrosion product in **Eqn. 7-6**.



Classic studies have demonstrated that both the corrosion rate of pure Zn [16] and of pure Al [17,18] follow U-shaped curves as a function of pH with significant corrosion rates in both acidic and alkaline solutions. It is generally agreed that the specific rate of the reaction is determined by the nature and stability of the corrosion product films that form on the surface of the material. In neutral NaCl solutions, $Zn(OH)_2$ / $ZnCl_2 \cdot 4Zn(OH)_4$ [19] or $Zn(OH)Cl$ [20]

are formed on Zn and Al_2O_3 on Al [21]. As the pH rises, ZnO and/or $\text{Zn}(\text{OH})_2$ are thermodynamically favored on Zn [22] ultimately becoming soluble as $\text{Zn}(\text{OH})_3^-$ and $\text{Zn}(\text{OH})_4^-$. For Al in alkaline solution, the native Al_2O_3 and $\text{Al}(\text{OH})_3$ films are less stable than their Zn counter parts and the dominant species is $\text{Al}(\text{OH})_4^-$ [21,23]. Therefore the rate of Al dissolution in alkaline solution is much higher than that of Zn at an equivalent pH. In acidic solution, no stable oxide exists for either metal [24].

Preferential corrosion of Zn from 55 wt.% Al – Zn alloy during the early stage of field exposure was demonstrated qualitatively by surface analysis [25,26]. In other works [27,28], selective dissolution of Zn from Al-Zn alloys in slightly acidic and neutral solutions was quantified by comparing aluminum-to-zinc concentration ratio in the solution with the same ratio in the 5%Al-Zn and 15%Al-Zn alloys.

During outdoor exposure, the environment changes continuously, and Zn-Al alloy coatings may suffer acidic attack from air pollution and acid rain [29], or local alkaline attack due to oxygen reduction [12]. I. Odnevall Wallinder et al. [30] observed the visual appearance of 55 wt.% Al-Zn samples exposed to deionized water with different pH after 40 days of exposure in sealed bags. The sample exposed to $\text{pH} = 1$ had a white layer of corrosion products (i.e. Zn containing products) with black stains on top of this layer. The sample exposed at $\text{pH} = 13$ however was completely covered by a black layer which was found to contain $\text{Al}(\text{OH})_3$. These results imply a preferential formation of Zn and Al containing products on 55 wt.% Al-Zn at pH 1 and 13 respectively. This can be considered as an indirect observation of Zn and Al selective dissolution.

In this article, for the first time, the Zn and Al selective dissolution from 5%Al-Zn and 55%Al-Zn coatings was systematically studied as a function of pH from 2.0 to 11.8 by measuring directly and in real time the elementary dissolution rates of Zn and Al using atomic emission spectroelectrochemistry (AESEC) [31]. In order to minimize the effect of Cl^- [32,33], a diluted NaCl solution (30 mM) was used. The influence of oxygen in the electrolyte on Zn and Al dissolution rates is also taken into account by performing experiment in N_2 de-aerated and aerated conditions. The reactivity under anaerobic conditions is important because either a confined zone may itself become depleted in oxygen or the presence of a corrosion product layer which blocks oxygen diffusion may lead to anaerobic conditions at the alloy surface. In addition, 5 day immersion test is performed to compare results between long time exposure and short time exposure.

7.2. Experimental

7.2.1. Materials

Commercial hot dipped galvanized steels with 7 μm thick 5% Al-Zn and 25 μm thick 55% Al-Zn coatings (supplied by ArcelorMittal) were used. The samples (2 cm x 5 cm) were degreased by n-heptane but were not polished. 99.99% Zn (supplied by Goodfellow) and 99.99% Al (AA1199) were polished with metallographic paper up to 1 μm grain. All samples were then cleaned by ethanol in an ultrasonic bath for 10 minutes, followed by drying in flowing nitrogen.

Reagent grade NaCl and deionized water (specific resistivity of 18.2 $\text{M}\Omega\text{ cm}$) purified with a MilliporeTM system were used for 30 mM Cl^- solution preparation. The pH was preliminarily adjusted by adding HCl or NaOH. For pH 2, the NaCl amount was reduced to ensure that the chloride concentration was constant at 30 mM. The solutions were either de-aerated by nitrogen bubbles or aerated with an air pump for 10 – 15 minutes prior to experiments. The pH was again adjusted if necessary after the aeration or the de-aeration.

7.2.2. Atomic emission spectroelectrochemistry (AESEC) technique

The technique consists of an inductively coupled optical emission spectrometer (ICP-OES) coupled to an electrochemical flow cell. The system described in detail in previous reference [31] is from HORIBA Jobin Yvon (Ultima 2CTM). The emission intensity of Zn and Al in the plasma was monitored at 213.856 nm and 167.081 nm respectively, using a polychromator system purged by flowing nitrogen with oxygen concentration lower than 3 ppm for UV region application. The potentiostat was an EG&G Princeton Applied Electronics M273A functioning in the potentiostatic mode. The potentiostat is controlled manually from the front panel with the output analog signals current and potential signals being routed into the measuring circuit of the ICP-OES spectrometer. The flow rate in the electrochemical cell was adjusted to approximately $0.048\text{ cm}^3\text{ s}^{-1}$ and measured for each series of experiments. The detection limits in this work (defined as 3 * standard deviation of the blank, each point of the blank is the average value of 10 s) were determined to be 1.8×10^{-4} and $8.5 \times 10^{-5}\text{ }\mu\text{g s}^{-1}\text{ cm}^{-2}$ in the aerated condition; 1.3×10^{-4} and $1.1 \times 10^{-4}\text{ }\mu\text{g s}^{-1}\text{ cm}^{-2}$ in the de-aerated condition for Zn and Al respectively.

7.2.3. Immersion test

A cleaned specimen of 5%Al-Zn coated steel was positioned as the bottom of a cylindrical plexiglass cell with surface area of 10.2 cm² being determined by the diameter of an o-ring. Each cell contained 50 ml of 30 mM NaCl solution with adjusted pH of 2.0, 4.0, 6.1, 8.0, 10.0, or 11.9 respectively. This test was performed at room temperature. After 5 days, the pH was re-measured, the solution was filtered and analyzed by ICP-OES to determine the ion concentration, $C_M(sol)$ with $M = Zn$ and Al . The release rates of Zn and Al, $v_{Zn}(sol)$ and $v_{Al}(sol)$, were then calculated:

$$v_M(sol) = \frac{C_M(sol)}{A\Delta t} \quad (7-7)$$

where A is the sample surface (10.2 cm²) and Δt is the immersion time duration (5 days).

Precipitated corrosion products were filtered from the solution and removed from either the dried sample surface or the cell wall by a razor-blade. They were collected together, and characterized by X-ray diffraction. After that, the total precipitated products were dissolved in 100 ml (V) of 10 wt.% HNO₃ solution and then the Zn and Al ion concentrations, $C_M(ins)$, were measured by ICP-OES. The contribution of the insoluble components, $v_M(ins)$, to the total metal release rate was calculated as follows:

$$v_M(ins) = \frac{C_M(ins)V}{A\Delta t} \quad (7-8)$$

7.2.4. X-Ray Diffraction (XRD)

The XRD characterization was carried out by X'Pert PRO PANalytical system using Cu K_α radiation. The dried corrosion product was ground to powder, placed on a silicon plate by vaseline, and scanned from 5° to 70° (2theta) with a step size of 0.04°. Product identification was made using X'Pert HighScore software supporting multiple reference databases including the international centre for diffraction data (ICDD) version 2011.

7.3. Results

7.3.1. Spontaneous dissolution of 5%Al-Zn, 55%Al-Zn, and pure metals with AESEC measurement

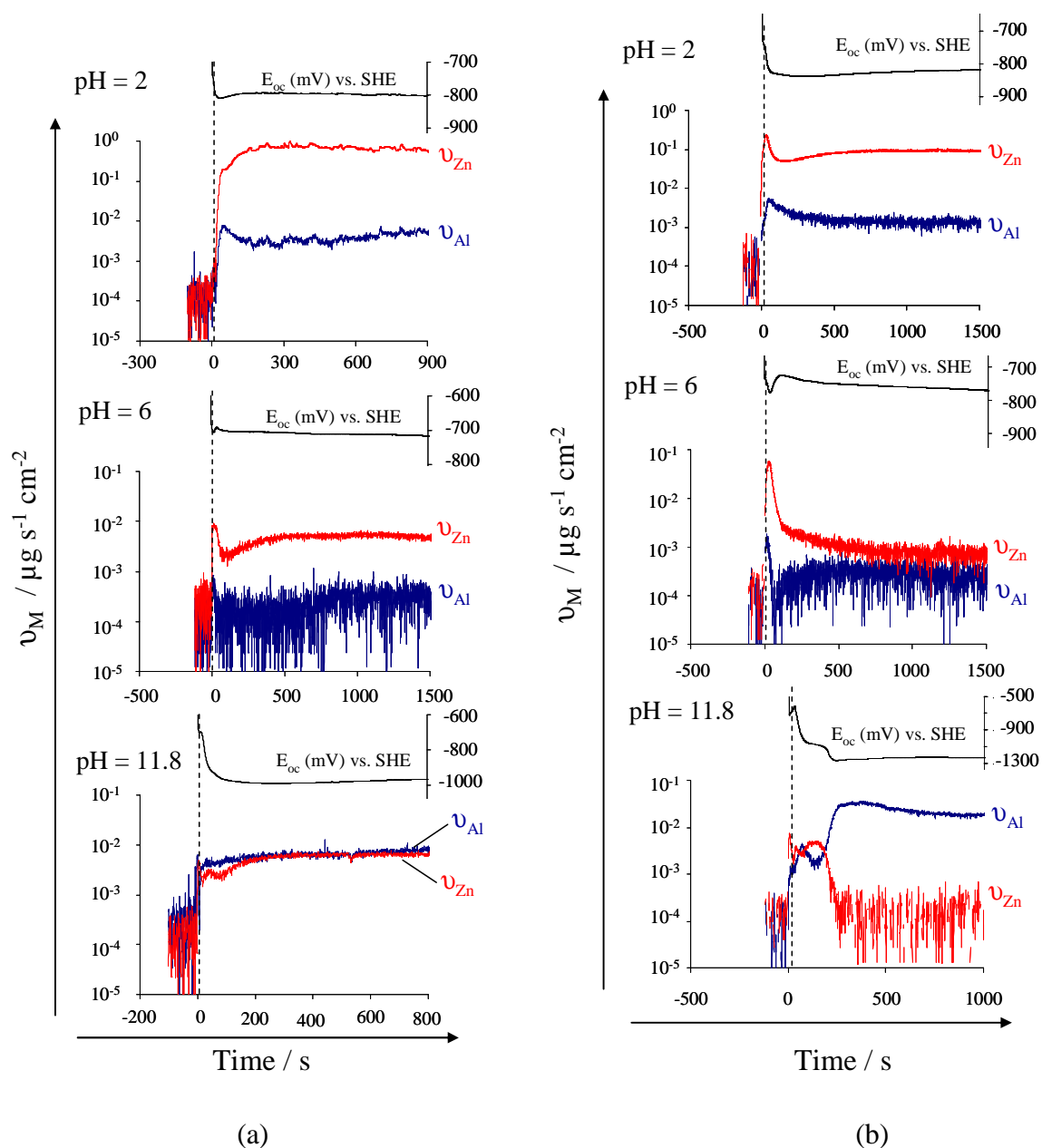


Figure 7-1: Open circuit potential (E_{oc}) and elemental dissolution rates (v_{Zn} and v_{Al}) from 5% Al-Zn as a function of time in (a) aerated 30 mM NaCl and (b) de-aerated 30 mM NaCl solutions at pH = 2.0, pH = 6.0, and pH = 11.8 during short time exposure experiment with AESEC technique. The dashed lines indicate the time when samples contact the solutions.

Fig. 7-1 shows the typical variation of the spontaneous elementary dissolution rates (v_{Al} and v_{Zn}) and the open circuit potential (E_{oc}) of 5% Al-Zn as a function of time when the sample was in contact with the aerated and deaerated 30 mM NaCl at different initial pH. The figure only shows the results at three typical pH values for acidic, neutral, and alkaline solutions. During the experiment, only 5% volume of the solution downstream is aspirated into the plasma of the ICP-OES, the remainder was collected and the pH measured (final pH). The difference between the initial and final pH was less than 0.3 pH units in all cases. The dashed line indicates the time when the sample contacts the electrolyte. In the aerated solution (**Fig. 7-1a**), a near steady state for v_{Al} , v_{Zn} and E_{oc} is observed after 300 s in all experiments. E_{oc} at pH = 2.0 and especially at pH = 11.8 are more negative than that at other pH values.

In the deaerated solution (**Fig. 7-1b**), a sharp peak of v_{Al} and v_{Zn} is observed during the first few seconds after the sample contacts the electrolyte, followed by a near steady state dissolution. E_{oc} of 5% Al-Zn at pH from 2.0 to 8.0 oscillates around -800 mV vs. SHE. At pH 11.8, Al dissolution rate suddenly changes from a transitory period in which $v_{\text{Al}} \approx v_{\text{Zn}} \approx 0.005 \mu\text{g s}^{-1} \text{cm}^{-2}$ to another where v_{Al} is 10 times higher ($0.05 \mu\text{g s}^{-1} \text{cm}^{-2}$), while v_{Zn} is almost zero. Correspondingly, E_{oc} jumps from -1030 mV to -1250 mV vs. SHE.

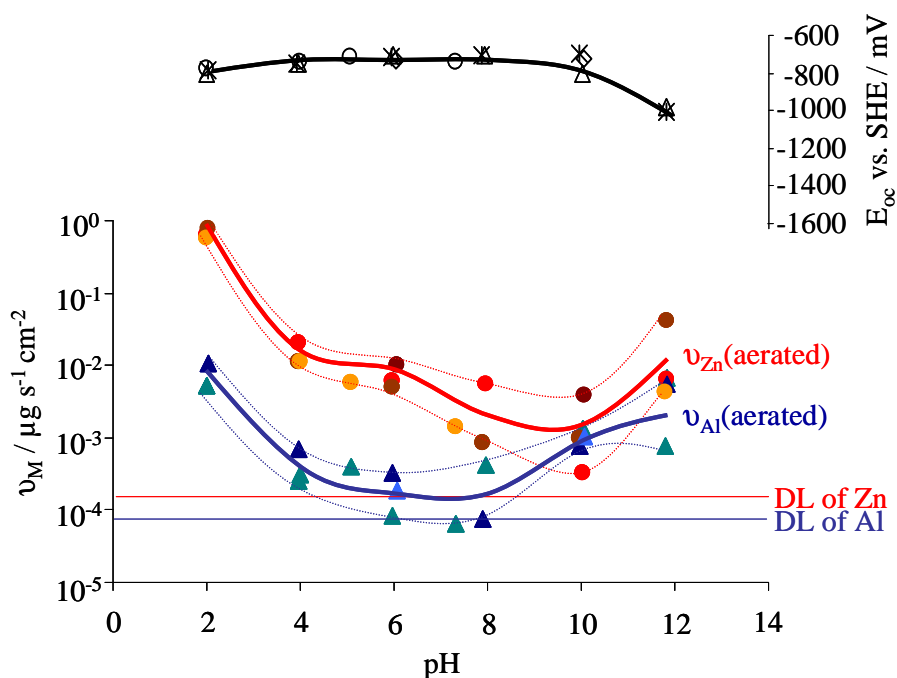
In **Fig. 7-2**, the average v_{Zn} , v_{Al} , and E_{oc} of Galfan in 30 mM NaCl were determined during the last 200 s of the near steady state regions of experiments similar to **Fig. 7-1**. The results are presented as a function of pH. At each pH value, the measurement was repeated from 3 to 5 times. The round and triangular points present the mean values of the Zn and Al dissolution rates respectively and the dashed line indicates the deviation of the data. The results demonstrate that v_{Zn} and v_{Al} depend not only on pH but also on the aeration or de-aeration. At pH = 2, $v_{\text{M}}(\text{aerated})$ (with M = Zn and Al) is approximately 10 times greater than $v_{\text{M}}(\text{de-aerated})$: the order of magnitude is 10^0 vs. $10^{-1} \mu\text{g s}^{-1} \text{cm}^{-2}$ for v_{Zn} , and 10^{-2} vs. $10^{-3} \mu\text{g s}^{-1} \text{cm}^{-2}$ for v_{Al} respectively. At pH = 11.8 in the de-aerated solution (**Fig. 7-1b**), v_{Zn} is much lower than v_{Al} and close to the detection limit, though Galfan contains 94.5 wt.% Zn. The $v_{\text{Al}}/v_{\text{Zn}}$ ratios for the different pH values in both solutions are shown in **Table 7-1**.

To compare the Zn and Al dissolution rates from Galfan with those from pure metals, similar experiments were also made on pure Zn and pure Al. **Fig. 7-3** presents their dissolution rates as a function of pH with the corresponding E_{oc} in the de-aerated 30 mM NaCl. E_{oc} of pure Zn at the different pH values is rather stable at about -800 mV vs. SHE. However, E_{oc} of pure Al is cathodically shifted from -710 mV vs. SHE at pH = 2 to -1620 mV

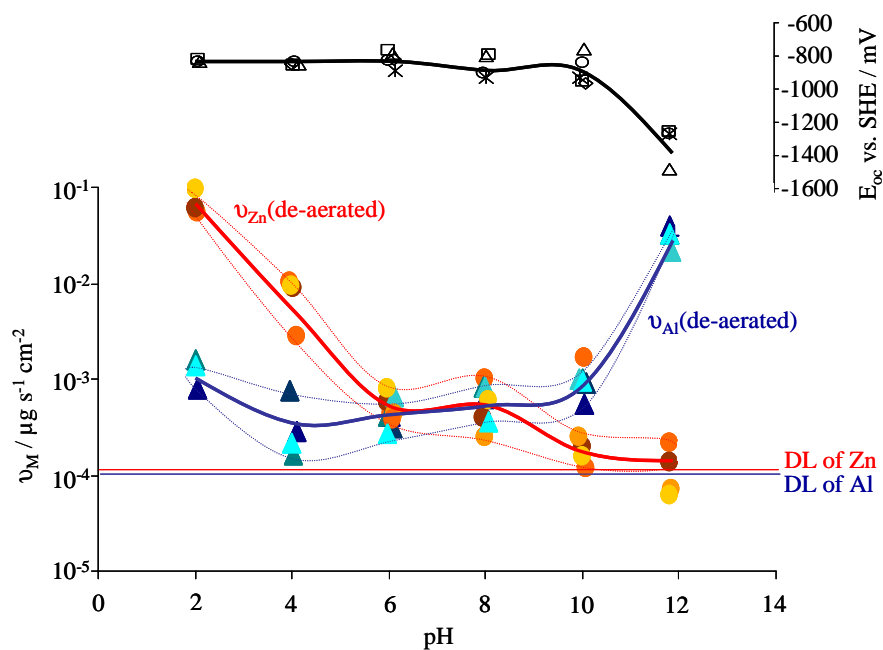
vs. SHE at pH = 11.8 corresponding to the active state of Al. The variation of Zn and Al dissolution rates with pH shows a U-like curve, similar to the result obtained during immersion [1,24]. The Zn dissolution rate in the acidic solution is higher than in alkaline solution, while the Al dissolution rate shows the opposite behavior. In addition, E_{oc} of pure Zn is slightly more negative than E_{oc} of pure Al at low pH, but at high pH E_{oc} of pure Al is much more negative. Comparison of the results in **Fig. 7-2** and **7-3** indicates that the variation of $v_M(\text{aerated})$ ($M = \text{Zn, Al}$) from 5% Al-Zn with pH has the similar behavior (U-like curve) to v_M from pure Zn and pure Al in the de-aerated solution.

Table 7-1: Average Al/Zn ratio of 5%Al-Zn in aerated and de-aerated 30 mM NaCl solutions (calculated from data in **Fig. 7-2**)

Solution	pH=2.0	pH=4.0	pH=6.0	pH=8.0	pH=10.0	pH=11.8
Aerated	0.01	0.03	0.04	0.07	0.37	0.25
De-aerated	0.02	0.04	0.78	1.17	1.79	260.83



(a)



(b)

Figure 7-2: Average dissolution rates of Zn and Al (v_{Zn} and v_{Al}) and open circuit potential (E_{oc}) of 5%Al-Zn as a function of pH (pH did not change significantly after measurement) in (a) aerated 30 mM NaCl and (b) de-aerated 30 mM NaCl. The dashed line shows the deviation of data (measurement at each pH was repeated 3 to 5 times), and the solid line shows the mean data curve. Detection limit lines of Zn and Al are also given.

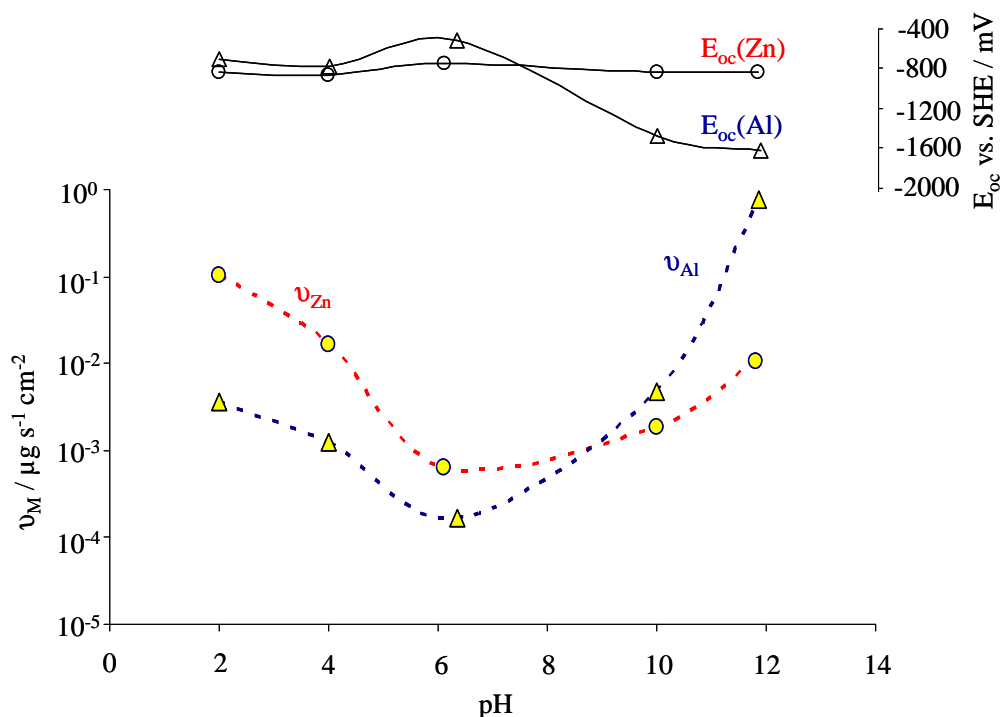
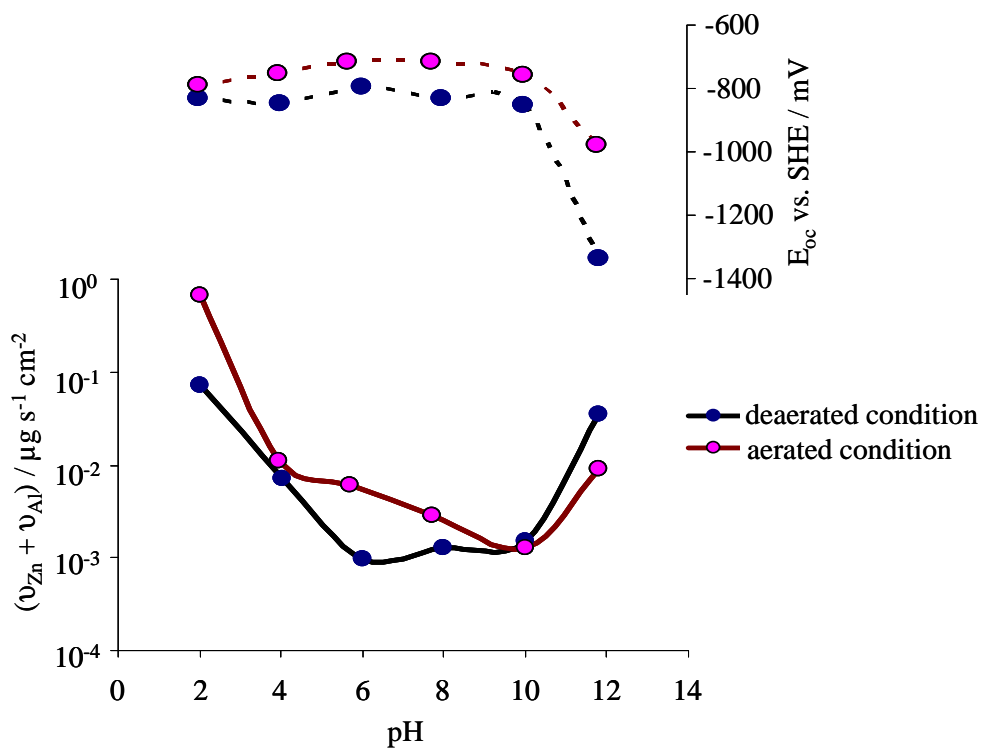
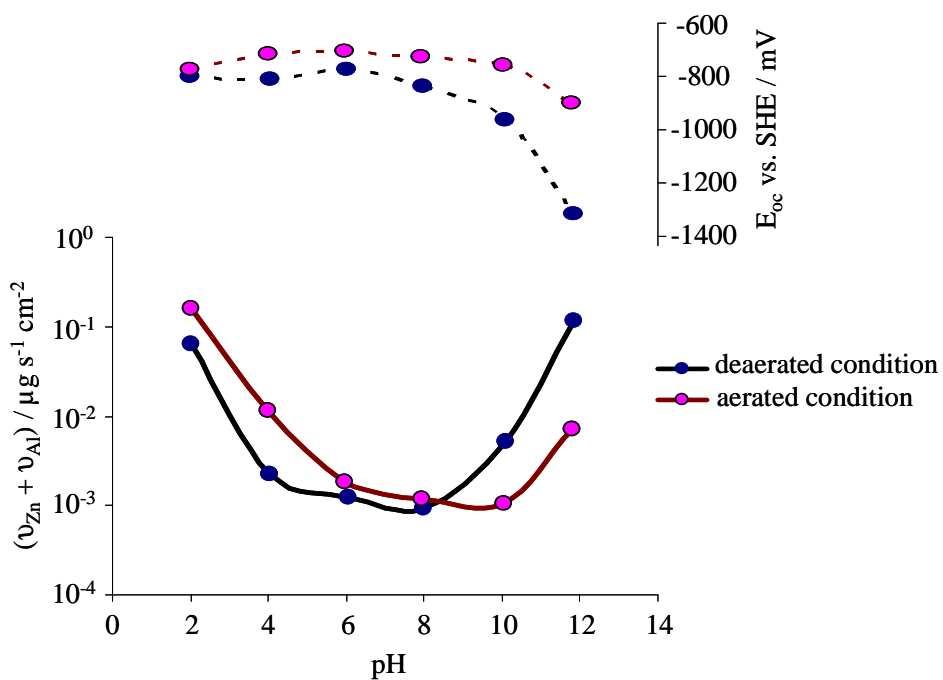


Figure 7-3: Average dissolution rates (v_{Zn} and v_{Al}) and open circuit potential (E_{oc}) of pure Zn and pure Al as a function of pH (pH did not change significantly after measurement) in de-aerated 30 mM NaCl solution.

The total dissolution rates of 5% Al-Zn coating calculated as $v_{\text{Zn}} + v_{\text{Al}}$ and the open circuit potential E_{oc} in both aerated and de-aerated solutions are plotted as a function of pH in **Fig. 7-4a**. The result for 55% Al-Zn coating with a higher Al composition is also shown in **Fig. 7-4b**. Both figures show the U-like curves as seen with pure Zn and pure Al (**Fig. 7-3**), even though contributions of Zn and Al to the total dissolution rate are different in the different solutions (aerated or de-aerated) at the different pH values. At every pH, the Zn-Al alloy coatings present a more negative E_{oc} in the de-aerated than in the aerated solution: for example, E_{oc} of 5% Al-Zn is around -820 mV vs. SHE compared to -750 mV vs. SHE at pH 2-10; and -1350 mV compared to -950 mV at pH = 11.8.

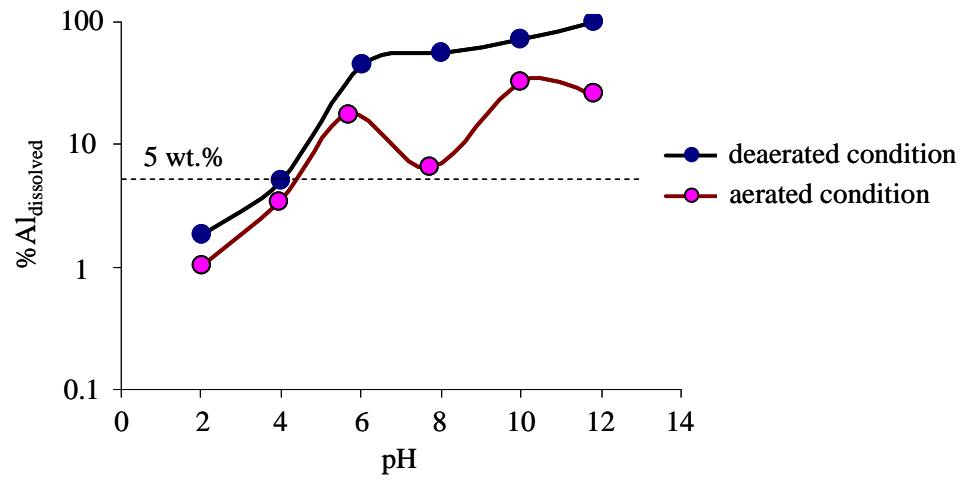


(a)

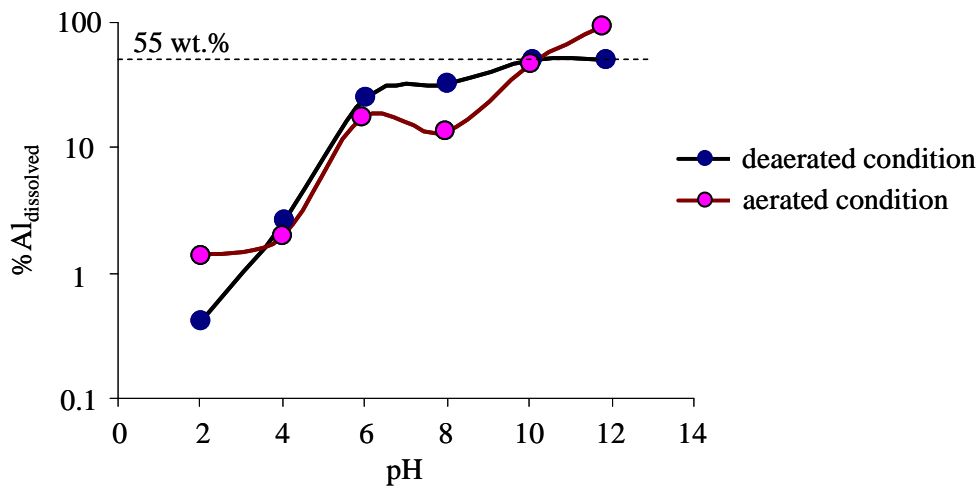


(b)

Figure 7-4: Total dissolution rate $(v_{Zn} + v_{Al})$ and open circuit potential (E_{oc}) of (a) 5%Al-Zn and (b) 55%Al-Zn in aerated and de-aerated 30 mM NaCl solutions as a function of pH.



(a)



(b)

Figure 7-5: Dissolved Al fraction ($\%Al_{dissolved}$) released from (a) 5%Al-Zn and (b) 55%Al-Zn in aerated and de-aerated 30 mM NaCl solutions as a function of pH. The Al composition in the Al-Zn coatings is also indicated by the dashed line.

Fig. 7-5 presents the dissolved Al fraction (**Eqn. 7-9**) released from 5%Al-Zn and 55% Al-Zn at different pH values based on the dissolution rates of Zn and Al in **Fig. 7-2**.

$$\% Al_{dissolved} = \frac{v_{Al}}{v_{Al} + v_{Zn}} 100\% \quad (7-9)$$

In all cases, Zn selective dissolution is observed in the more acidic electrolytes. As the pH becomes more alkaline however, the relative rate of Al dissolution increases until at high pH Al selective dissolution is observed. The transition occurs around pH= 4 for 5% Al-Zn and pH = 10 for 55% Al- Zn. For Galvalume under anaerobic conditions, the selective dissolution of Al is not observed in the pH range investigated here; rather Al and Zn dissolve simultaneously at the higher pH values.

7.3.2. Immersion test result of 5%Al-Zn

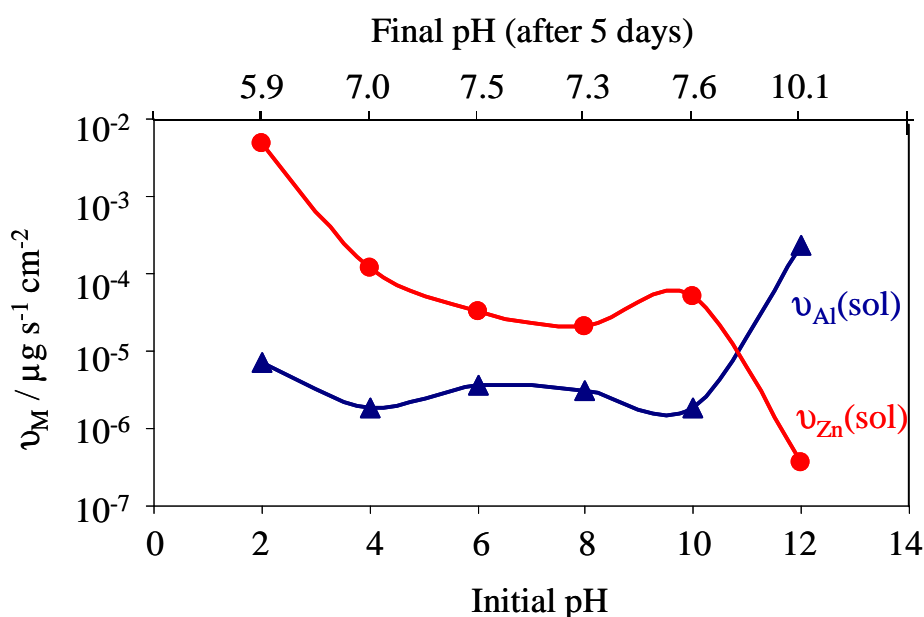


Figure 7-6: Release rates of Zn and Al due to soluble components ($v_{Zn(sol)}$ and $v_{Al(sol)}$) from 5%Al-Zn as a function of initial and final pH in immersion test.

Fig. 7-6 shows the mean release rates of Zn and Al due to soluble components, $v_{Zn(sol)}$ and $v_{Al(sol)}$, from 5%Al-Zn after 5 days of immersion test in the unit of $\text{g cm}^{-2} \text{s}^{-1}$ (**eqn. 7-7**), as a function of initial pH. At pH = 2.0, $v_{Zn(sol)} > v_{Al(sol)}$, while at pH = 11.9 $v_{Zn(sol)} < v_{Al(sol)}$. At pH from 4.0 to 10.0, $v_{Zn(sol)}$ and $v_{Al(sol)}$ do not change significantly. After the immersion test, the pH approaches the neutral values (indicated by the upper X axis of **Fig. 7-6**) because of H^+/OH^- consumption during the immersing period. The different corrosion products detected by XRD after the exposure of samples to the solutions are shown in **Table. 7-2**: ZnO was found at the initial pH = 2.0, 4.0, and 6.1, while $\text{Zn}_5(\text{OH})_8\text{Cl}_2 \cdot \text{H}_2\text{O}$ (simonkolleite) was found at the initial pH = 8.0, 10.0, and 11.9. Layered double hydroxide

$Zn_{0.61}Al_{0.39}(OH)_2(CO_3)_{0.167} \cdot nH_2O$ ($ZnAlCO_3$ -LDH) was present in almost all samples. The presence of CO_3^{2-} is probably due to the air contact during the drying process.

Table 7-2: Summary of corrosion products formed on 5%Al-Zn after the 5 day immersion in 30 mM NaCl at different initial pH (number of “+” symbol indicates the relative amount of the products)

Products	pH=2.0	pH=4.0	pH=6.1	pH=8.0	pH=10.0	pH=11.9
ZnO	++	+++	+++	-	-	-
$Zn_5(OH)_8Cl_2 \cdot H_2O$	-	-	-	+	+	+++
$Zn_{0.61}Al_{0.39}(OH)_2(CO_3)_{0.167} \cdot nH_2O$	++	+	+	+	+	-

7.3.3. Comparison of immersion test and AESEC results

The total ion release rate, $v_M(\text{immersion})$, from 5%Al-Zn after 5 day immersion is calculated as a total contribution from both soluble and insoluble components which were described by **eqn. 7-7 and 7-8**.

$$v_M(\text{immersion}) = v_M(\text{sol}) + v_M(\text{ins}) \quad (7-10)$$

$$(M = Zn \text{ and Al})$$

$v_M(\text{immersion})$ is then compared with $v_M(\text{aerated})$ and $v_M(\text{de-aerated})$ at the different initial pH values (**Fig. 7-7**): the Zn dissolution rates from 5%Al-Zn during short time exposure with AESEC and during long time exposure with the immersion test are close to each other except at two extreme (initial) pH values which varied significantly in the case of the 5 day immersion. However, the Al dissolution rate during the long time exposure ($v_{Al}(\text{immersion})$) is much lower than that during short time exposure ($v_{Al}(\text{aerated})$ and $v_{Al}(\text{de-aerated})$).

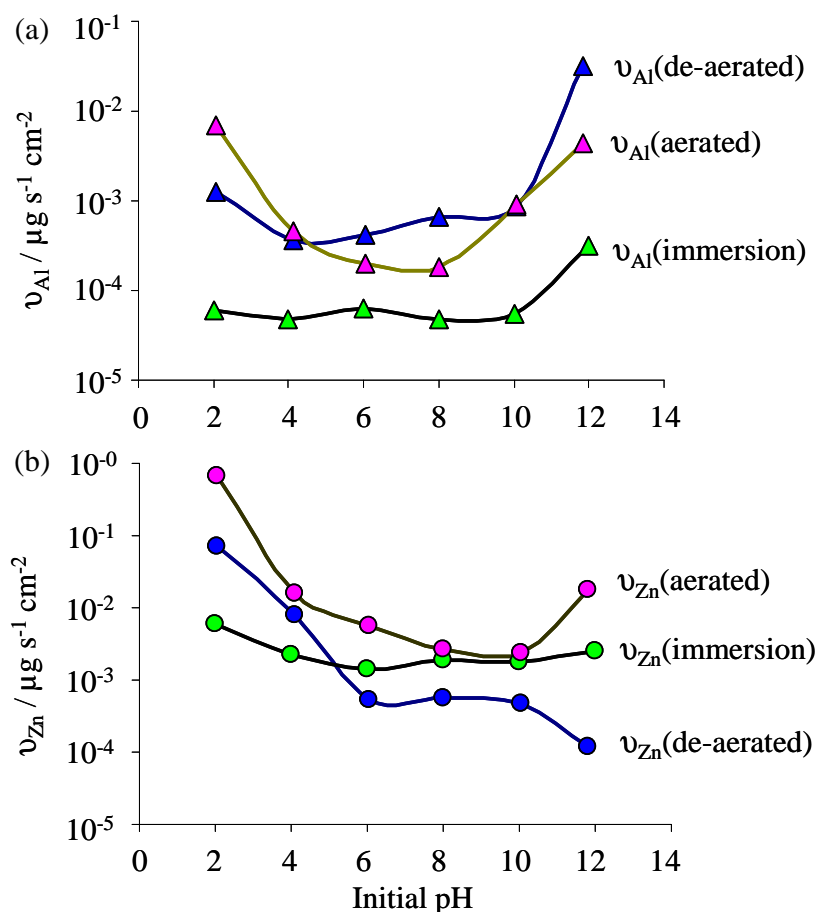


Figure 7-7: Comparing average Zn and Al release rates from 5%Al-Zn during long time exposure by immersion test ($(v_M(\text{immersion}))$) with short time exposure by AESEC technique ($(v_M(\text{aerated})$ and $v_M(\text{de-aerated})$ in which $M = \text{Zn, Al}$).

7.4. Discussion

7.4.1. Selective dissolution of Zn and Al from 5%Al-Zn and 55%Al-Zn

The selective dissolution of Zn or Al from Zn-Al alloys is evaluated by comparing the dissolved Al fraction with the Al composition in the alloys (**Fig. 7-5**). It is demonstrated that the Zn selective dissolution from 5%Al-Zn and 55%Al-Zn occurs in the pH range of 2-4 and 2-8 respectively. At higher pH, Al selective dissolution occurs. **Fig. 7-3** indicates that E_{oc} of pure Zn is more negative than E_{oc} of pure Al at low pH, and vice versa at high pH. However, E_{oc} of the Zn-Al alloys (**Fig. 7-4**) is always between E_{oc} of pure Zn and pure Al in the same solutions (except at pH = 6). Interestingly, it is closer to E_{oc} of Zn at pH 2-4 where the Zn selective dissolution occurs and to E_{oc} of Al at pH 11.8 where the Al selective dissolution occurs. This correlation is not clear for pH = 6-8 at which both Zn and Al have very low

activities, and for pH = 10 which is a sensitive point of changing zinc's and aluminum's activities with pH [24].

According to the result presented in **Fig. 7-5**, the dissolved fraction of Al from 5% Al-Zn and 55% Al-Zn coatings generally increases with pH, but the Al dissolution rate remains below that of Zn dissolution (%Al_{dissolved} is lower than 50 wt.%), except at pH from 8.0 to 11.8 in the de-aerated solutions for 5% Al-Zn (**Fig. 7-5a**) and pH 11.8 for 55% Al-Zn (**Fig. 7-5b**). This is consistent with the observation of the Zn-dominating corrosion products during the atmospheric exposure of Zn-Al alloys [12,25,26,34].

7.4.2. Oxygen effect

With the presence of oxygen, the total dissolution rates of 5% Al-Zn and 55% Al-Zn at low pH are higher in the aerated solution than in the de-aerated solution (**Fig. 7-4a and 7-4b**). In the acidic solution, two cathodic reactions may occur as mentioned in the introduction (**Eqn. 7-1 and 7-2**) with the oxidation reduction potential of 0 V and +1.23 V respectively. As a consequence, because of the stronger oxidizing agent presence, the dissolution rate in the aerated solution will be accelerated.

In neutral and slightly acidic or alkaline solutions, there is a stable oxide layer separating the alloy and the electrolyte. This layer inhibits oxygen reduction [14,35], therefore oxygen influences insignificantly on the dissolution rates of the Al-Zn alloys in the aerated and de-aerated solutions.

The dissolution profiles and the open circuit potential evolution of 5% Al-Zn obtained in the de-aerated alkaline solution (**Fig. 7-1b**) suggest that the dissolution of this coating may occur in two main kinetic periods: (1) the dissolution of the native oxide layer, followed by (2) the dissolution of the exposed metal. These two periods correspond to the near steady states having the E_{oc} of -1030 mV and -1250 mV vs. SHE. An estimation of the oxide layer thickness dissolved in the first period is possible by integrating v_{Zn} and v_{Al} from 0 s to 200 s at pH = 11.8 in **Fig. 7-1b**. It yields an amount of Zn and Al dissolution of 7.3×10^{-7} and 4.6×10^{-7} g cm⁻² respectively. Assuming the oxide layer consists of ZnO and Al₂O₃ with the densities of 5.6 g cm⁻³ and 4.0 g cm⁻³ respectively [36], it would have a thickness of 3.8 nm. This value is in accordance with the measured oxide thickness on Galfan [1]. During the second kinetic period, v_{Al} jumps up to a very high value while v_{Zn} simultaneously drops to

almost zero which can be interpreted as evidence for galvanic coupling between Al-rich and Zn-rich phases.

In the aerated condition (**Fig. 7-1a**), we did not see the two kinetic periods at pH = 11.8. The open circuit potential is quite stable during the whole experiment, and close to the E_{oc} of the first period in the de-aerated solution (-985 mV vs. -1030 mV) at which the native oxides are dissolved. It suggests that with the presence of oxygen, the (hydro)oxide formation rate is high enough to renew the (hydro)oxide layer between the alloy and the electrolyte, which is dissolved continuously during the experiment.

In addition, the presence of oxygen in the solution increased the dissolved Al fraction of 5%Al-Zn (**Fig. 7-5a**) but showed no measurable effect on the dissolution of 55%Al-Zn (**Fig. 7-5b**).

7.4.3. Correlation between in-situ and ex situ measurements

$v_{Zn}(sol)$ and $v_{Al}(sol)$ for 5 day exposure obtained from immersion test (**Fig. 7-6**) shows a very similar trend as observed from the AESEC measurement in de-aerated solutions (**Fig. 7-2b**) for short time exposure. This is because the initial oxygen dissolved in the solution near the sample surface is depleted and not renewed during the immersion test resulting in a de-aerated-like media at the sample/electrolyte interface. A thick corrosion product layer formed during the immersion test could also contribute to the decrease of oxygen diffusion [37].

$v_{Zn}(immersion)$ does not differ much from $v_{Zn}(aerated)$ and $v_{Zn}(de-aerated)$ at the same initial pH as shown in **Fig. 7-7b**, except at pH = 2, a very low $v_{Zn}(immersion)$ obtained is due to the pH approaching the neutral values during the immersion test. However, v_{Al} from immersion test ($v_{Al}(immersion)$) (**Fig. 7-7a**) is much lower than v_{Al} from AESEC ($v_{Al}(aerated)$ and $v_{Al}(de-aerated)$). This implies the inhibition of Al dissolution which could be due to either a low mass and/or charge transferring through the Zn-containing corrosion product layer formed during the long time exposure [3,26] or pH buffering at near neutral values caused by the precipitation of corrosion products as similar to the mechanism in Mg-Al alloys [38]. The XRD results (shown in **Table 7-2**) indicate that the corrosion products are different on the different samples. It is not easy to give an exact explanation of how each product was formed because the precipitating environments were changing with time. They could be formed either during the immersing process (at initial and/or final pH) or during the

drying process. However, the Zn-containing products are always dominant in the crystalline corrosion product layer of every sample, and hence may decrease the Al release rate. T. Ishikawa et al. [39,40] empirically demonstrated that, in chloride solution at pH = 9, if the Al/Zn atomic ratio was lower than 0.05, ZnO was formed; if it was equal to or higher than 0.05, ZnO would be transformed into $Zn_5(OH)_8Cl_2 \cdot H_2O$ (simonkolleite or ZHC). This conclusion probably explains the formation of ZnO and ZHC on the different samples during our immersion test. The NaCl solutions used in the immersion test were not buffered and the pH changed significantly after 5 days, therefore v_{Zn} and v_{Al} in **Fig. 7-6** are not suitable to calculate the Al/Zn ratio for predicting the ZnO/ZHC formation. However, the Al/Zn ratio from the short time exposure (**Table 7-1**) can be used as a reference and it agrees with Ishikawa's observation since ZnO is seen for Al/Zn < 0.05 and ZHC for Al/Zn > 0.05. The final pH values of the immersing solutions (**Fig. 7-6**) are preferential for both ZnO and ZHC precipitation [41]. The presence of ZnAlCO₃-LDH in all samples at pH from 2 to 10 probably results from a reaction taking place in contact with dissolved CO₂ in the solutions or CO₂ in the air during the drying process in which zinc hydroxide and aluminum hydroxide were co-precipitated (from dissolved Zn and Al components) and transformed into the ZnAlCO₃-LDH [26]. Chloride anion was also present but ZnAlCl-LDH was not found probably because it is much less stable than ZnAlCO₃-LDH [42]. No ZnAlCO₃-LDH was detected on the sample exposed at initial pH = 11.9 due to either the low concentration of dissolved Zn (**Fig. 7-6**) or the low stability of ZnAl-LDH at high pH [43].

7.5. Conclusion

This work has demonstrated that the selective dissolution of Zn and Al is strongly affected by pH. When 5% Al-Zn and 55% Al-Zn were exposed to the 30 mM NaCl electrolyte, the selective dissolution changed from zinc in the pH range of 2-4 and 2-8 to aluminum at the higher pH values. The presence or absence of oxygen in the electrolyte did not change the selective dissolution behavior but influenced the dissolution rates (v_{Zn} and v_{Al}) which varied with time. Oxygen stabilized the oxide layer in aerated solution causing an anodic shift of the open circuit potential as compared to the result in de-aerated solution. The galvanic coupling between Zn-rich and Al-rich phases of 5%Al-Zn was observed in the de-aerated solution at pH = 11.8 at which Al dissolved quickly but Zn did not. Finally, during the 5 day exposure in the immersion test, the pH approached near neutral values independently of the initial values

due to the precipitation process. The formation of a massive corrosion product layer of primarily Zn-containing products inhibited the Al release rate.

This work also demonstrates the complementarity of the short time AESEC corrosion rate measurements and the long term immersion exposures. During a long term exposures the elementary corrosion reactions affect the pH of the electrolyte such that the pH approaches neutral. The AESEC experiments involve a constantly renewed electrolyte and thus the rate measurement represents the "intrinsic" reactivity of the material with an electrolyte.

Acknowledgement

We would like to thank ArcelorMittal, France for furnishing samples for this work and the Autocorr European RFCS project for partial financial support. We kindly acknowledge the RFCS project partners ArcelorMittal, France; Salzgitter AG, Germany; ThyssenKrupp, Germany, VoestAlpine, Austria and KTH, Sweden for helpful scientific discussions.

7.6. References

-
- ¹ X. G. Zhang, *Electrochemistry and Corrosion of Zinc*, first ed., Springer, 1996.
 - ² C. Leygraf, T. Graedel, *Atmospheric Corrosion*, Wiley Interscience, 2000, pp. 329 – 340.
 - ³ X. Zhang, T.-N. Vu, P. Volovitch, C. Leygraf, K. Ogle, I. Odnevall Wallinder, The initial release of zinc and aluminum from non-treated Galvalume and the formation of corrosion products in chloride containing media, *Appl. Surf. Sci.* 258 (2012) 4351–4359.
 - ⁴ A.R. Marder, The metallurgy of zinc coated steel, *Prog. Mater. Sci.* 45 (2000) 191-271.
 - ⁵ Steel coated with Galfan zinc-aluminum alloy, *The product catalogue – European edition*, ArcelorMittal (2008).
 - ⁶ R. P. Edavan, R. Kopinski, Corrosion resistance of painted zinc alloy coated steels, *Corros. Sci.* 51 (2009) 2429-2442.
 - ⁷ H. C. Shih, J. W. Hsu, C. N. Sun, S. C. Chung, The lifetime assessment of hot-dip 5% Al-Zn coatings in chloride environments, *Surf. Coat. Tech.* 150 (2002) 70-75.

-
- ⁸ J. Elvins, J. A. Spittle, D. A. Worsley, Microstructural changes in zinc aluminium alloy galvanizing as a function of processing parameters and their influence on corrosion, *Corros. Sci.* 47 (2005) 2740-2759.
- ⁹ W-B Chen, P. Chen, H. Y. Chen, J. Wu, W-T. Tsai, Development of Al-containing zinc-rich paints for corrosion resistance, *Appl. Surf. Sci.* 187 (2002) 154-164.
- ¹⁰ F. M. Androsch, K. Kostners, K.-H. Stellnberger, Beschleunigte Korrosionsprüfung von Korrosionsschutzsystemen auf Stahlblechen für die Automobilindustrie, *Stahl und Eisen* 121 (2001) 37.
- ¹¹ F. Rosalbino, E. Angelini, D. Maccio, A. Saccone, S. Delfino, Influence of rare earths addition on the corrosion behaviours of Zn-5%Al (Galfan) alloy in neutral aerated sodium sulphate solution, *Electrochim. Acta.* 52 (2007) 7107-7114.
- ¹² H. Dafydd, D. A. Worsley, H. N. McMurray, The kinetics and mechanism of cathodic oxygen on zinc and zinc-aluminum alloy galvanized coatings, *Corros. Sci.* 47 (2005) 3006-3018.
- ¹³ Zs. Pilbath, L. Sziraki, The electrochemical reduction of oxygen on zinc corrosion film in alkaline solution, *Electrochim. Acta* 53 (2008) 3218-3230.
- ¹⁴ A. P. Yadav, A. Nishikata, T. Tsuru, Oxydation reduction mechanism on corroded zinc, *J. Electroanal. Chem.* 585 (2005) 142-149.
- ¹⁵ David R. Lide, *Handbook of Chemistry and Physics*, 88th Ed., Chemical Rubber Company, 2007.
- ¹⁶ B. E. Roetheli, G. L. Cox, W. B. Literal, Effect of pH on the corrosion products and corrosion rate of zinc in oxygenated aqueous solutions, *Metals and Alloys* 3 (1932) 73.
- ¹⁷ M. Pourbaix, *Atlas d'équilibres électrochimiques*, Gauthier-Villars & Cie, Paris, 1963, p173.
- ¹⁸ V. Vujičić, B. Lovreček, A Study of the influence of pH on the corrosion rate of aluminium, *Surf. Tech.* 25 (1985) 49-57
- ¹⁹ A. P. Yadav, A. Nishikata, T. Tsuru, Degradation mechanism of galvanized steel in wet-dry cyclic environment containing chloride ions, *Corros. Sci.* 46 (2004) 361-376.

-
- ²⁰ W. Miao, I. S. Cole, A. K. Neufeld, and S. Furman, Pitting Corrosion of Zn and Zn-Al Coated Steels in pH 2 to 12 NaCl Solution, *J. Electrochem. Soc.* 154 (2007) C7-C15.
- ²¹ S.-M. Moon, S.-I. Pyun, The corrosion of pure aluminium during cathodic polarization in aqueous solutions, *Corros. Sci.* 39 (1997) 399-408.
- ²² S. Feliu Jr., V. Barranco, XPS study of the surface chemistry of conventional hot-dip galvanized pure Zn, galvanneal and Zn-Al alloy coatings on steel, *Acta. Mater.* 51 (2003) 5413-5424.
- ²³ K. Ogle, M. Serdechnova, M. Mokaddem, P. Volovitch, The cathodic dissolution of Al, Al₂Cu, and Al alloys, *Electrochim. Acta.* 56 (2011) 1711-1718.
- ²⁴ M. Pourbaix, Atlas d'équilibres électrochimiques, Gauthier- Villars, 1963.
- ²⁵ D. Persson, D. Thierry, N. LeBozec, Corrosion product formation on Zn55Al coated steel upon exposure in a marine atmosphere, *Corros. Sci.* 53 (2011) 720-726.
- ²⁶ E. Palma, J. M. Puente, M. Morcillo, The atmospheric corrosion mechanism of 55%Al-Zn coating on steel, *Corros. Sci.* 40 (1998) 61-68.
- ²⁷ V. I. Pokhmurs'kyi, M. S. Khoma, V. I. Kopylets', S. A. Kornii, Investigation of the initial stage of selective dissolution of zinc-aluminum alloys in chloride-containing media, *Mater. Sci.* 39 (2003) 394-399.
- ²⁸ Yu. Ya. Andreev, S. V. Samarichev, M. E. Goncharov, Selective anodic dissolution of aluminum-zinc alloys in neutral solution, *Russ. J. Electrochem.* 30 (1994) 1216-1221.
- ²⁹ E. Bernardi, C. Chiavari, B. Lenza, C. Martini, L. Morselli, F. Ospitali, L. Robbiola, The atmospheric corrosion of quaternary bronzes: The leaching action of acid rain, *Corros. Sci.* 51 (2009) 159-170.
- ³⁰ I. Odnevall Wallinder, W. He, P. Augustsson, C. Leygraf, Characterization of black rust staining of unpassivated 55% Al-Zn alloy coatings. Effect of temperature, pH and wet storage, *Corros. Sci.* 41 (1999) 2229-2249.
- ³¹ K. Ogle, J. Baeyens, J. Swiatowska, P. Volovitch, Atomic emission spectroelectrochemistry applied to dealloying phenomena: I. The formation and dissolution of residual copper films on stainless steel, *Electrochim. Acta*, 54 (2009) 5163-5170.

- ³² I. Murgulescu, O. Radovici, M. Borda, Studies of the mechanism of anodic dissolution of Al-Zn binary alloys in alkaline solutions by potentiodynamic and potentiostatic pulse methods, *Corros. Sci.* 5 (1965) 613-622.
- ³³ E. E. Abd El Aal, Effect of Cl⁻ anions on zinc passivity in borate solution, *Corros. Sci.* 42 (2000) 1-16.
- ³⁴ L. Veleva, M. Acosta, E. Meraz, Atmospheric corrosion of zinc induced by runoff, *Corros. Sci.* 51 (2009) 2055-2062.
- ³⁵ H. S. Wroblowa, S. B. Qaderi, The mechanism of oxygen reduction on zinc, *J. Electroanal. Chem.* 295 (1990) 153-161.
- ³⁶ P. Patnaik, *Handbook of inorganic chemical compounds*, first ed., McGraw-Hill Professional, 2002.
- ³⁷ M. S. Venkatraman, I. S. Cole, B. Emmanuel, Corrosion under a porous layer : A porous electrode model and its implication for self-repair, *Electrochim. Acta.* 56 (2011) 8192-8203.
- ³⁸ P. Volovitch, M. Serdechnova, K. Ogle, Aqueous corrosion of Mg-Al binary alloys: roles of Al and Mg, *Corrosion* in press (2012).
- ³⁹ T. Ishikawa, K. Matsumoto, A. Yasukawa, K. Kandori, T. Nakayama, T. Tsubota, Influence of metal ions on the formation of artificial zinc rusts, *Corros. Sci.* 46 (2004) 329-342.
- ⁴⁰ T. Ishikawa, K. Matsumoto, K. Kandori, T. Nakayama, Synthesis of layered zinc hydroxide chlorides in the presence of Al(III), *J. Solid. State. Chem.* 179 (2006) 1110-1118.
- ⁴¹ M. Mouanga, P. Bercot, J. Y. Rauch, Comparison of corrosion behaviour of zinc in NaCl and in NaOH solutions. Part I: Corrosion layer characterization, *Corros. Sci.* 52 (2010) 3984-3992.
- ⁴² D. G. Costa, A. B. Rocha, W. F. Souza, S. S. X. Chiaro, A. A. Leitao, Comparative structural, thermodynamic and electronic analyses of Zn-Al-Aⁿ⁺ hydrotalcite-like compounds (Aⁿ⁺ = Cl⁻, F⁻, Br⁻, OH⁻, CO₃²⁻, or NO₃⁻): An ab initio study, *Appl. Clay. Sci.* 56 (2012) 16-22.
- ⁴³ C. A. Johnson, F. P. Glasser, Hydrotalcite-like minerals (M₂Al(OH)₆(CO₃)_{0.5}.xH₂O, where M = Mg, Zn, Co, Ni) in the environment: synthesis, characterization and thermodynamic stability, *Clay. Clay. Miner.* 51 (2003) 1-8.

Chapter VIII:

**Selective dissolution of Zn and Al from Zn-Al coatings on steel
during polarization in acidic, neutral and alkaline solutions**

8. Selective dissolution of Zn and Al from Zn-Al coatings on steel during polarization in acidic, neutral and alkaline solutions

ABSTRACT: Selective dissolution of Zn and Al from 5% Al-Zn and 55% Al-Zn during potential scanning was investigated using atomic emission spectroelectrochemistry (AESEC). The results showed a strong cathodic selective dissolution of Al from both alloys in 0.1 M NaOH and 0.1 M NaCl. In the anodic domain, a strong selective dissolution of Zn was seen in 0.1 M HCl and 0.1 M NaCl. In 0.1 M NaOH solution, the anodic branch of the polarization curves for Galfan and Galvalume was divided into 2 different domains: zinc active domain in which Zn selective dissolution occurred and zinc passive domain in which Al selective dissolution occurred.

Keywords: Selective dissolution; galfan; galvalume; polarization; AESEC.

8.1. Introduction

In some applications such as automobile bodies, galvanized steel may be exposed within confined zones. The pH and ionic composition of the electrolyte in the confined zone environment will depend upon the elementary corrosion reactions and the detailed history of the atmospheric cycles. The galvanized steel may also find themselves in electrical contact with other materials and the potential of the galvanized steel will depend on the material to which it is coupled. Therefore, to predict the behavior of these materials in complex situations such as this, it is essential to understand the dissolution/corrosion of the galvanized steel alloy as a function of potential at various pH values.

The reactivity of pure zinc as a function of potential and pH is fairly well understood [1], however the more complex alloys used in galvanization such as Zn-Al and Zn-Mg-Al are not well understood. One of the complicating factors is the selective dissolution of the elemental components. In certain potential domains, the less noble element of the binary alloy may dissolve faster and cause an enrichment of the more noble element on the alloy surface. Numerous examples of such complications have been reported for binary alloys of very noble elements [2-7]. Using Auger electron spectroscopy (AES), Gniewek et al. [8] determined the surface palladium enrichment involved in the selective dissolution of copper from a binary CuPd alloy in a sulfate electrolyte. Using X-ray diffraction, H. W. Pickering [9] indicated that the porous layer formed on Cu₁₃Au and Cu₁₈Cu surfaces presented a new phase enriched in gold when these alloys were polarized at above the critical potential in sulfate solution. Using a combined AES/X-ray photoelectron spectroscopy (XPS), J. Laurent and D. Landolt [10] demonstrated that both noble metal surface concentration and surface excess of CuAu and AgPd alloys increased due to selective dissolution of the less noble component after a potentiostatic polarization.

Very little is known about the selective dissolution of binary alloys containing two active metals, such as GalfanTM (5% Al-Zn) and GalvalumeTM (55% Al-Zn) during polarization. One of the major experimental difficulties is that both Zn and Al are very active, and their surface composition of the alloy will change if the sample removed from the electrolyte for ex situ characterization. Moreover, the electrochemical activity of zinc and aluminum depend strongly on the pH of the electrolyte [11,12]. In previous work [13], we introduced atomic emission spectroelectrochemistry (AESEC) as a method of analyzing selective dissolution kinetics. This technique allows monitoring in real time the elementary dissolution rates of the different components from these materials. This technique is

particularly suitable for kinetic measurements of leaching and de-alloying, and has proven to be a powerful technique in studying selective dissolution [14-18].

In a recent work, we investigated the polarization behavior of Galfan in alkaline solution [19] and the corrosion behavior of Galfan / Galvalume at various pH values [20]. In this article, in order to map out the general behavior of the Zn-Al system in different potential ranges and in different media, we have quantified the selective dissolution of Zn and Al from Galfan and Galvalume during polarization in 0.1 M HCl (pH=1.5), 0.1 M NaCl (pH=6.7), and 0.1 M NaOH (pH=12.8) using the AESEC technique. The choice of these pH values follows the now classic article of Roetheli, et al. [21] which makes the original description of the three domains of zinc dissolution mechanism: acid film dissolving at low pH, passive at neutral pH, and alkaline film dissolving at high pH. This work follows the logic of our previous study [20] however we have used both higher and lower pH values to observe a stronger selective dissolution effect.

8.2. Experimental

8.2.1. Materials

Commercial hot dipped galvanized steel with 7.0 μm thick Galfan (5%Al - 94.5%Zn - 0.5% mischmetal [22]) and 25 μm thick Galvalume (55%Al - 43.5%Zn - 1.5%Si [23]) coatings identical to the materials used in our previous article [20] were used. These materials were used as received after being degreased by n-heptane, followed by ultrasonic cleaning for 10 minutes in reagent grade ethanol and drying in flowing nitrogen. Electrolytes were prepared from analytical grade NaOH (provided by Prolabo, S.A.) and deionized water (18.2 M Ω cm) prepared with a Millipore™ system. All solutions were deaerated for 10-15 minutes with flowing nitrogen prior to experiments to avoid the effect of cathodic oxygen reduction [24]. All experiments were performed at 25°C and ambient pressure.

8.2.2. The AESEC Technique

Atomic emission spectroelectrochemistry (AESEC) consists of an inductively coupled optical emission spectrometer (ICP-OES) coupled to an electrochemical flow cell. It has been described in detail in a previous article [17]. Briefly, the ICP-OES spectrometer was manufactured by HORIBA Jobin Yvon (Ultima 2C™) and consists of a polychromator and a monochromator for the simultaneous detection of 31 different wavelengths. The spectrometer is equipped with a fast time resolved data acquisition system developed in collaboration with

the manufacturer for this application. The emission intensity of Zn and Al in the plasma was monitored at 213.856 nm and 167.081 nm respectively.

The electrochemical experiments were conducted in the AESEC electrochemical flow cell with a three electrode system. Two reference electrodes, saturated calomel electrode (SCE, 3 M KCl, +244 mV vs. a standard hydrogen electrode (SHE)) and Hg/HgO (1M KOH, +129 mV vs. a SHE), were used in this work. In the result section, potential is standardized to SHE for an easier comparison. The potentiostat was an EG&G Princeton Applied Electronics M273A functioning in the potentiostatic mode. It was controlled manually from the front panel and the analog current and potential signals were routed into the measuring circuit of the ICP-OES spectrometer to ensure that spectrometer and electrochemical data were on the same time scale. The flow rate in the electrochemical cell was approximately 3.0 ml min⁻¹ and was measured for each series of experiments.

8.2.3. Analysis of the ICP-OES data

The total current density measured by the electrometer of the potentiostat is referred to as j_e , where e indicates the electrical nature. The partial elementary dissolution current density for element, M, j_M , is calculated from the downstream concentration of the element, C_M :

$$j_M = nF f C_M / A \quad (8-1)$$

where f is flow rate of electrolyte through the cell, F is the Faraday constant, A is the surface area, and n is the number of electrons transferred in the oxidation step ($n = 2$ for Zn and $n = 3$ for Al). Note that all surface reaction rates are normalized to the geometrical surface of the sample exposed to the electrolyte (0.5 cm²). This is done for convenience and is not meant to imply that the specific reaction is actually uniform on the surface.

8.3. Results

8.3.1. Overview of the potential – pH dependence of selective dissolution

In this section we review the general features of the open circuit and polarization behaviour of the two alloys. Table 1 gives the open circuit dissolution rates of Al and Zn for the two alloys at different pH values as well as the open circuit potentials. These results demonstrate a clear change from selective Zn dissolution at low pH to selective Al dissolution at high pH. This change is reflected in the open circuit potential that varies from around -0.8

V vs. SHE in acid and neutral solution, typical of active Zn, to around -1.4 to -1.5 V vs. SHE in alkaline solution, typical of active Al.

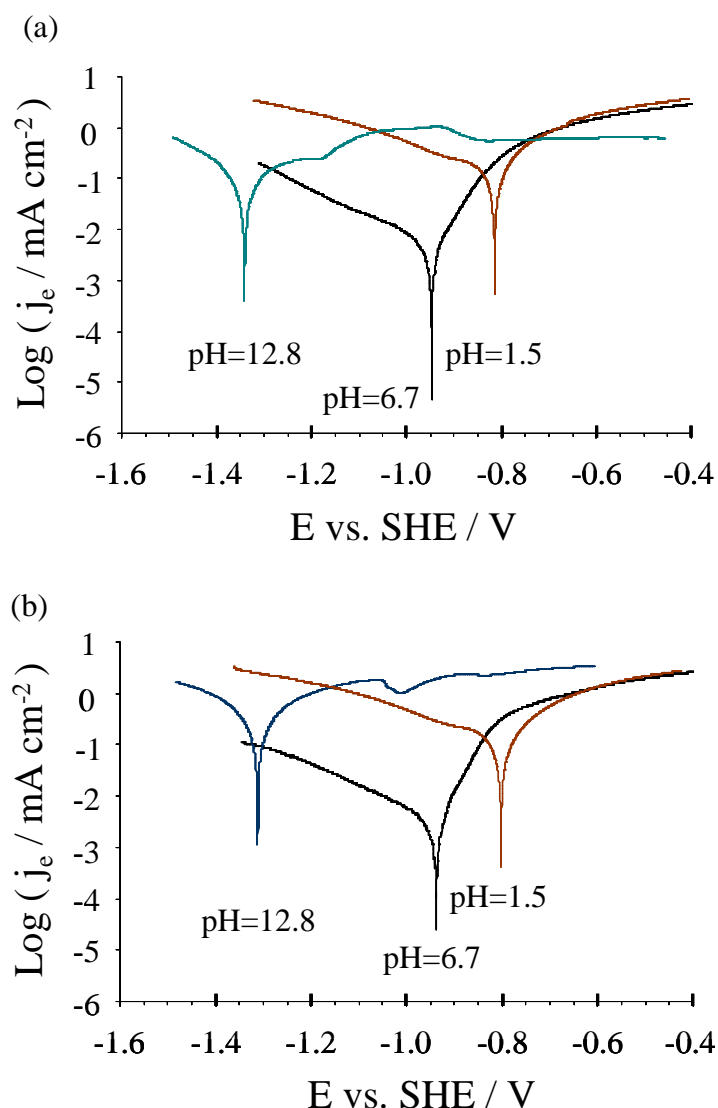


Figure 8-1: Polarization curves for a(a) 5% Al-Zn and (b) 55% Al-Zn in HCl (pH 1.5), NaCl (pH 6.7), and NaOH (pH 12.8) with scan rate of 0.5 mV s^{-1} and surface area of 0.5 cm^2

Fig. 8-1 presents the polarization curves for 5% and 55% Al-Zn in three different environments scanned in the cathodic direction at 0.5 mV s^{-1} . It is of interest to compare the zero-current potential (E_{zc}) values determined from these curves to E_{oc} obtained immediately before the polarization experiment. These values are also tabulated in Table 1. The difference in the two values reveals changes induced in the material activity by the cathodic sweep. The trend is identical for E_{zc} and E_{oc} which shift from a very negative to a less negative potential when solution pH decreases. For example, $E_{zc} \approx -1.35$ V in NaOH, -0.95 V in NaCl, and -0.8

V in HCl - and were similar for both Galfan and Galvalume. However, the current densities were not identical in the same solutions, especially in case of NaOH. In this solution, Galfan reveals lower cathodic and anodic current densities compared to Galvalume, which is due to high activity of Al in the alkaline solution and the different Al composition between Galfan and Galvalume.

Table 8-1: Open circuit potential (E_{oc}) and dissolution currents of zinc and aluminum (j_{zn} and j_{Al}) of Galfan and Galvalume in 0.1 M HCl (pH = 1.5), 0.1 M NaCl (pH = 6.7), and 0.1 M NaOH (pH = 12.8).

pH	Alloy %Al	E_{oc} V vs. SHE	E_{zc} V vs. SHE	j_{Al} $\mu A cm^{-2}$	j_{zn} $\mu A cm^{-2}$	j_{Al} / j_{zn}
1.5	5% Al	-0.82	-0.81	30	490	0.061
	55% Al	-0.80	-0.79	10	230	0.043
6.7	5% Al	-0.77	-0.95	1.5	2.0	0.75
	55% Al	-0.78	-0.93	3.3	4.5	0.73
12.8	5% Al	-1.48	-1.33	420	≈ 0.75	560
	55% Al	-1.40	-1.29	1970	< 0.50	> 4000

The open circuit corrosion potential (E_{oc}) and dissolution rates are given in **Table 8-1**. It is of interest to compare E_{oc} with the potential of zero current (E_{zc}) observed from the polarization curve in Fig. 1 as the difference in the two values reveals information on the effect of the cathodic sweep. Galfan and Galvalume in 0.1 M NaCl in this table are much more positive than in **Fig. 8-1** demonstrating that the cathodic treatment activated the Al in the alloy. However, the E_{oc} values in 0.1 M NaOH are more negative than in **Fig. 8-1** probably due to the depletion of Al after the selective dissolution of Al at the cathodic domain [19].

8.3.2. Acidic solution

In **Fig. 8-2**, the elemental dissolution rates (j_{zn} and j_{Al}) and electrical current density (j_e) are presented as a function of potential when Galfan and Galvalume were polarized with a scan rate of $0.5 mV s^{-1}$ in 0.1 M HCl. In the cathodic branch, j_{zn} is below the detection limit while j_{Al} rises only slightly ($j_{Al} = 14 \mu A cm^{-2}$ for Galfan and $6 \mu A cm^{-2}$ for Galvalume. Note

that j_{Al} is multiplied by a factor of 10 in **Fig. 8-2a**). During the anodic branch, j_e , j_{Zn} and j_{Al} increase steadily with applied potential. The spikes appearing in **Fig. 8-2a** (around -0.6 V vs. SHE) are probably caused by corrosion product detachment. Repeated experiments (not shown here) also showed similar spikes but at different potentials. At this stage, the electrical current, j_e , is smaller than the total dissolution current, $j_e < j_{Zn} + j_{Al}$ for the 5% Al-Zn alloy. This would suggest that the cathodic current (i.e. hydrogen reduction) makes a significant contribution to the total electrical current. However, for 55% Al-Zn (**Fig. 8-2b**), j_e is nearly identical to the total dissolution current: $j_e \approx j_{Zn} + j_{Al}$. Even at very anodic potentials where j_{Zn} starts decreasing and j_{Al} starts increasing, the sum still approximates the electrical current.

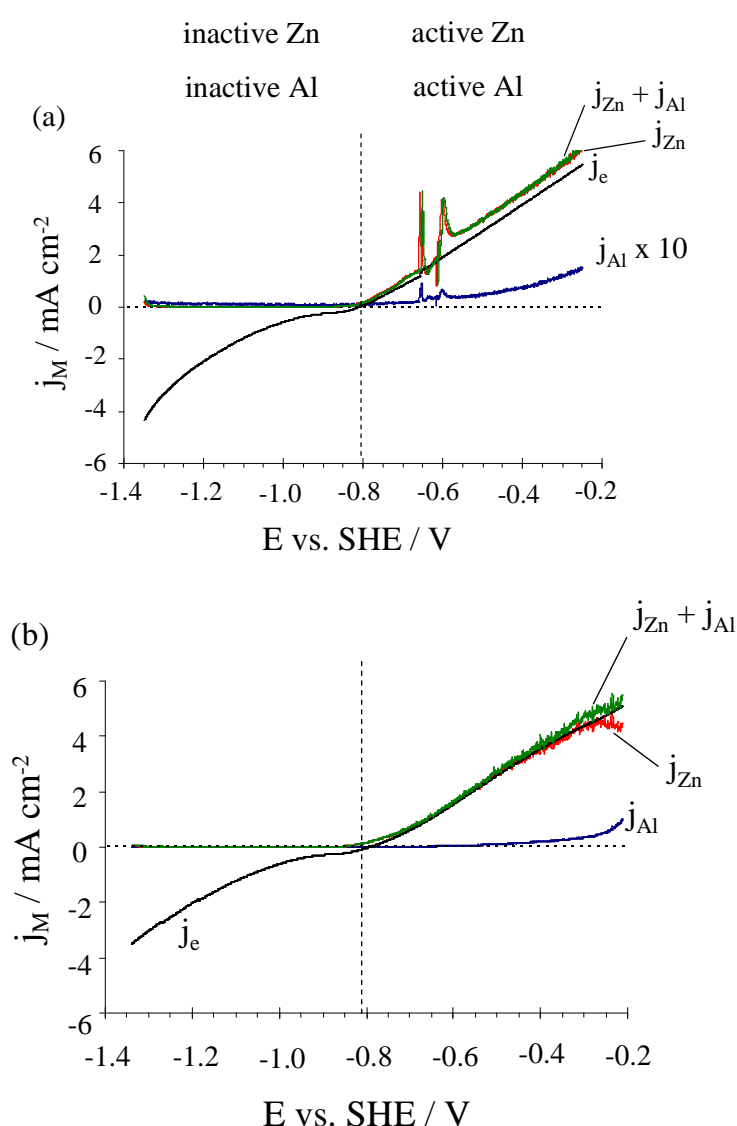


Figure 8-2: AESEC polarization experiment showing the total electrical current density (j_e) and elemental dissolution rates (j_{Zn} and j_{Al}) as a function of potential when (a) 5% Al-Zn and (b) 55% Al-Zn were polarized with a scan rate of 0.5 mV s^{-1} in 0.1 M HCl ($\text{pH} = 1.5$) solution.

8.3.3. Neutral solution

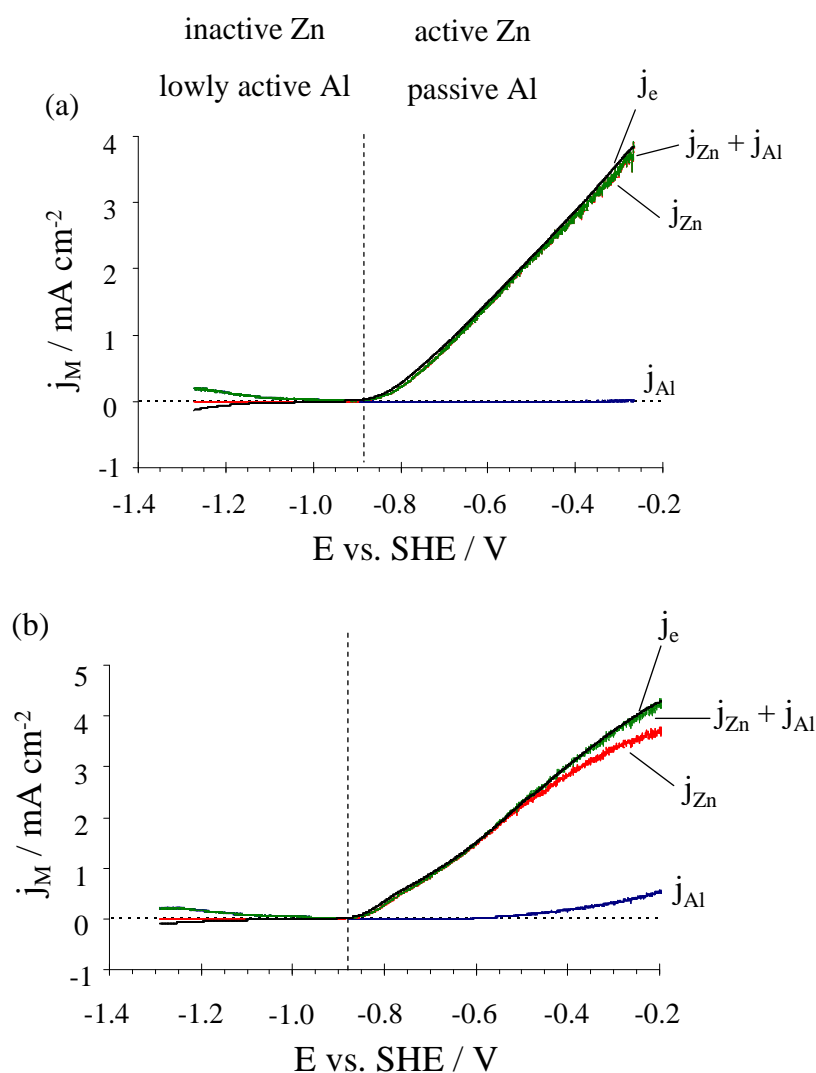


Figure 8-3: AESEC polarization experiment showing the total electrical current density (j_e) and elemental dissolution rates (j_{Zn} and j_{Al}) as a function of potential when (a) 5% Al-Zn and (b) 55% Al-Zn were polarized with a scan rate of 0.5 mV s^{-1} in 0.1 M NaCl ($\text{pH} = 6.7$) solution.

Fig. 8-3 shows the AESEC polarization curves of 5% and 55% Al-Zn when they were polarized in 0.1 M NaCl with a scan rate of 0.5 mV s^{-1} . At potentials more negative than -0.9 V vs. SHE , Zn dissolution is not detected, while Al is slightly active. The Al dissolution rates are 0.14 mA cm^{-2} and 0.17 mA cm^{-2} for 5% and 55% Al-Zn (at -1.2 V vs. SHE) respectively. In the anodic potential range, the Zn dissolution rate increases quickly, while Al is almost passive and only starts increasing gradually from -0.3 V for 5% Al-Zn and -0.65 V for 55% Al-Zn. During the entire anodic domain, the total dissolution rate always follows the electrical current: $j_e \approx j_{Zn} + j_{Al}$, indicating a negligible cathodic current. The Zn dissolution rates from Galfan and Galvalume are nearly the same (1.49 mA cm^{-2} vs. 1.50 mA cm^{-2} at -0.6 V , and

2.87 mA cm⁻² vs. 2.97 mA cm⁻² at -0.4 V), even though the bulk composition of zinc in two alloys are very different (94.5 wt.% vs. 43.5 wt.%). However, at more anodic potentials, a larger difference in j_{Zn} between Galfan and Galvalume is observed. For example, at -0.3 V vs. SHE, j_{Zn} equals to 3.5 mA cm⁻² for Galfan and 3.2 mA cm⁻² for Galvalume reflecting the different composition of the alloys.

8.3.4. Zn and Al dissolution rates as a function of potential in alkaline solution

Fig. 8-4 showed electrical current density (j_e) and elemental dissolution rates (j_{Zn} & j_{Al}) as a function of potential (a) 5% Al-Zn and (b) 55% Al-Zn polarized in 0.1 M NaOH with a scan rate of 0.5 mV s⁻¹. The AESEC polarization curve for Galfan (**Fig. 8-4a**) was discussed previously in [19].

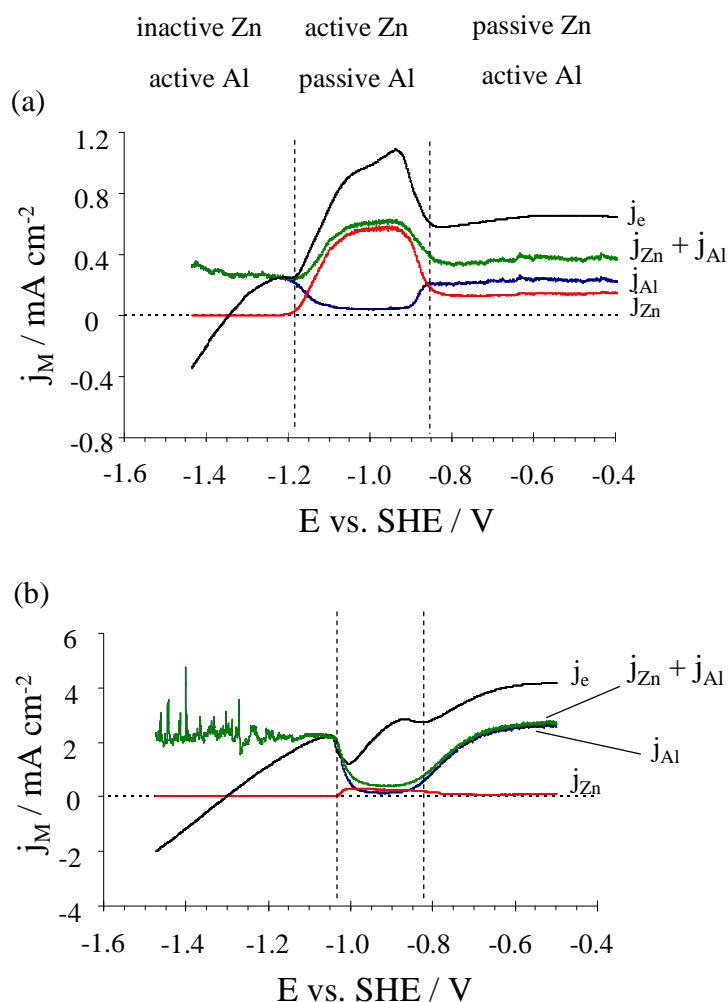


Figure 8-4: AESEC polarization experiment showing the total electrical current density (j_e) and elemental dissolution rates (j_{Zn} and j_{Al}) as a function of potential when (a) 5% Al-Zn and (b) 55% Al-Zn were polarized with a scan rate of 0.5 mV s⁻¹ in 0.1 M NaOH (pH = 12.8) solution.

The AESEC polarization curve for 55% Al-Zn (**Fig. 8-4b**) is very similar to that of 5% Al-Zn, with the notable difference that the Al dissolution current and the cathodic current are increased by about a factor of five. The Zn dissolution curve is similar. The AESEC polarization curve of 55% Al-Zn may be divided into three kinetic domains:

(1) the Zn cathodic domain, where the interfacial kinetics is characterized by the selective aluminum dissolution without any detection of Zn dissolution. The Al dissolution rate was essentially constant despite a very high cathodic current. In fact, Al dissolution did not seem to depend upon the applied potential at all. As compared with j_{Al} of 5% Al-Zn, j_{Al} of 55% Al-Zn as expected based upon the elemental composition of the alloys. Narrow spikes appear in the Al dissolution transient at the very cathodic potentials due to hydrogen evolution.

(2) The Zn active domain, where j_{Zn} begins to increase and passes through a maximum. The j_{Zn} of 55% Al-Zn starts increasing at a more positive potential than j_{Zn} of 5% Al-Zn (-1.05 V compared to -1.2 V vs. NHE) although the maximum values for j_{Zn} are 0.59 and 0.44 mA cm⁻² respectively while Al dissolution is inhibited by 84% and 89% based on a comparison of j_{Al} during and prior to the Zn active domain. The large

(3) The passive domain was followed by a rapid decrease of j_c and j_{Zn} while j_{Al} increased to a steady state potential independent rate very similar to that observed in the Zn cathodic domain.

8.3.5. Selective dissolution of Zn and Al in the different electrolyte during polarization

The dissolved Al fraction from a) 5% Al-Zn and (b) 55% Al-Zn polarized in 0.1 M HCl, 0.1 M NaCl, and 0.1 M NaOH were calculated based on the results given in **Fig. 8-2, 8-3, and 8-4** and plotted as a function of potential in **Fig. 8-5**. It is shown that the dissolved Al fractions are not proportional to their Al compositions in the coating (5 wt% and 55 wt% respectively shown by the dashed lines in **Fig. 8-5a** and **8-5b**). In 0.1 M HCl solution, the dissolved Al percent from Galfan (5 wt.% Al) is even higher than that from 55 wt.% Al-Zn at the anodic potentials. In 0.1 M NaCl, the selective dissolution suddenly changes from that of aluminum to that of zinc at -0.9 V vs. SHE for both alloys. However, at the anodic potential, %Al_{dissolved} from Galvalume is higher than from Galfan. In NaOH, the Zn active domain of Galfan starts at more negative potential (at -1.2 V vs. SHE) than that of Galvalume (-1.05 V vs. SHE) and lasts for a longer time. The higher dissolved Al from Galvalume during the entire polarization is consistent with the higher Al composition in the coating.

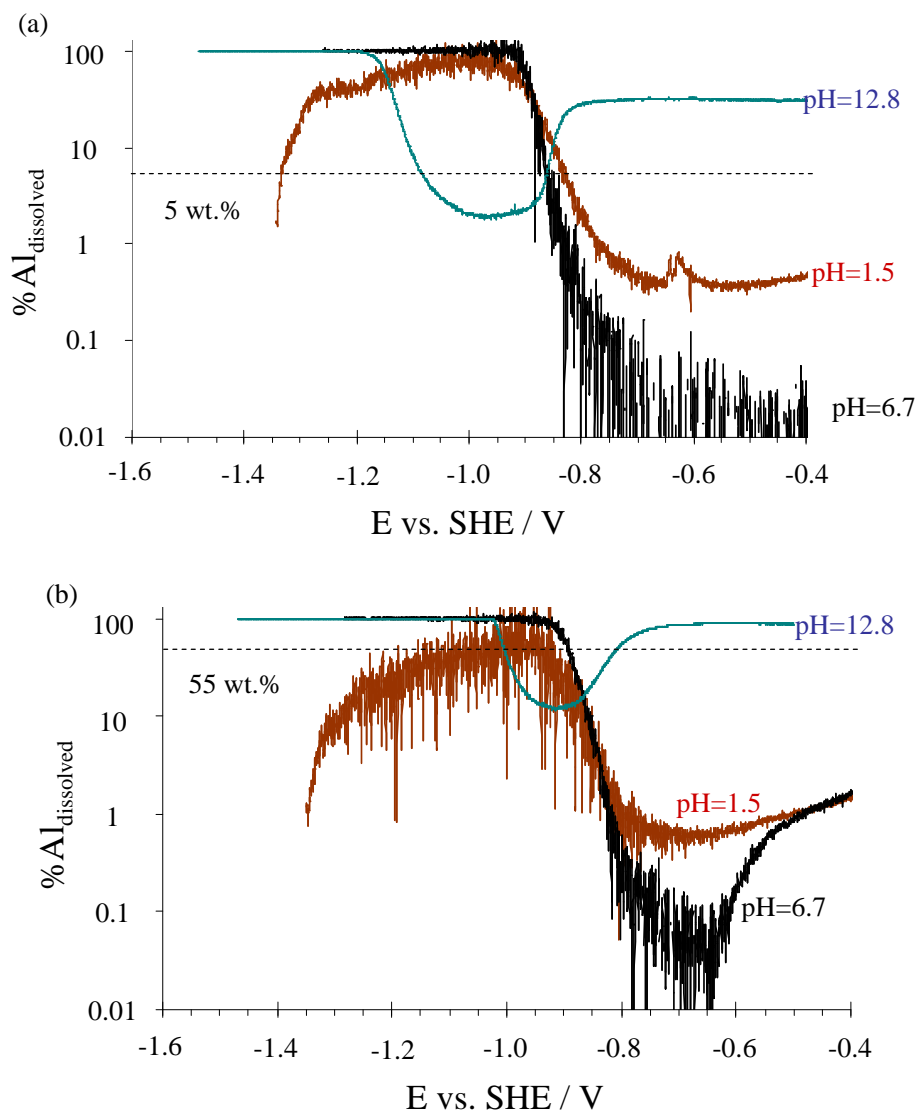


Figure 8-5: Fraction of dissolved Al from a) 5% Al-Zn and (b) 55% Al-Zn as a function of potential in the different environments: 0.1 M HCl, 0.1 M NaCl, and 0.1 M NaOH.

8.4. Discussion

The dissolution currents of zinc and aluminum at open circuit potential mentioned in **Table 8-1** demonstrated that the dissolutions of zinc and aluminum are preferential at pH = 1.5 and 12.8 respectively. The electrochemical polarization curves (**Fig. 8-1**) shows an anodic shift of E_{zc} and E_{oc} when the electrolytes are changed from alkaline to acidic. According to the mixed potential diagram (Evan's diagram) of Wagner and Traud [25], E_{zc} and E_{oc} of a Zn-Al alloy should lie between the values of uncoupled Al and Zn. The observed shift in acid is consistent with the results in [20] which demonstrated that Al was more active than Zn in the alkaline solution, while Zn was more active than Al in the acidic solution.

Cathodic polarization:

When Zn-Al alloys were polarized at very negative potentials, the reduction of water to hydroxide ions (i.e., $2\text{H}_2\text{O} + 2\text{e} \rightarrow \text{H}_2 + 2\text{OH}^-$) causes the pH of the metal/electrolyte interface to increase. This pH may be high enough to destabilize the Al passive film [26]. In 0.1 M NaCl (pH = 6.7) (**Fig. 8-3**), the very high cathodic current density leads to an increase in the interfacial pH and a significant increase in j_{Al} on the cathodic branch due to the cathodic dissolution mechanism [27]. However, in the case of 0.1 M HCl (**Fig. 8-2**) the dissolution rate of Al is insignificant because H^+ ions from the bulk solution neutralize the hydroxide before it can react with the aluminum oxides. The j_{Al} at the cathodic potentials in 0.1 M NaOH (**Fig. 8-4**) is much higher than in other electrolytes because it already contains hydroxide ions. However, in this electrolyte, j_{Al} from 55% Al-Zn is about 8 times higher than from 5% Al-Zn. This is explained by a strong dependence of j_{Al} on the Al composition of the coating in the alkaline environment where Al is very active. This explanation is consistent with the spikes observed on j_{Al} curve in **Fig. 8-4b** which correspond to hydrogen gas evolution.

As compared with the Al dissolution rate in the cathodic domain, the Zn dissolution rate is much smaller in the same electrolyte. In 0.1 M NaCl and 0.1 M NaOH, zinc dissolution was below the detection limit. Therefore, a strong selective dissolution of aluminum in the cathodic domain was observed in **Fig. 8-5**. Although Zn was not active at the cathodic potentials, a small j_{Zn} (about $3 \times 10^{-3} \text{ mA cm}^{-2}$ for both Galfan and Galvalume) was still detected in the case of 0.1 M HCl (pH = 1.5) because of its high reactivity with hydrogen ions. As mentioned above, an insignificant j_{Al} was also detected, but both of them were small. Dissolved Al fractions calculated from j_{Zn} and j_{Al} in this electrolyte for Galfan and Galvalume are not very different. Therefore, selective dissolution behavior which is based on comparison between the dissolved Al fraction and coating composition is different for these coatings: Al selective dissolution occurs for Galfan and Zn selective dissolution occurs for Galvalume (**Fig. 8-5**).

Anodic polarization

When Zn-Al alloys were polarized at anodic potentials in 0.1 M HCl, the hydrogen reduction reaction (i.e., $2\text{H}^+ + 2\text{e} \rightarrow \text{H}_2$) also occurred at the same time as the oxidation reactions of metals especially of zinc (i.e., $\text{Zn} \rightarrow \text{Zn}^{2+} + 2\text{e}$) because zinc is much more active than aluminum in acidic media though both of them are amphoteric [20]. This causes the total electrical current, j_{e} , to be lower than the total dissolution current, $j_{\text{Zn}} + j_{\text{Al}}$, especially in the case of Galfan (**Fig. 8-2a**) which has much higher bulk composition of zinc than Galvalume.

This is consistent with the observation of spikes appearing at about -0.65 V vs. SHE which attributed to gas bubble evolution. In other cases (**Fig. 8-2b, 8-3a, and 8-3b**), $j_e \approx j_{Zn} + j_{Al}$ implying that the cathodic reaction contribution is negligible. However, during anodic polarization in 0.1 M NaOH, $j_e > j_{Zn} + j_{Al}$ due to the contribution of insoluble components.

In acidic and neutral solutions, j_{Zn} is much higher than j_{Al} , therefore Zn selective dissolution occurs during the entire anodic polarization (**Fig. 8-5**). However, in alkaline solution, anodic branches for Galfan and Galvalume are divided into two different domains which depend on Zn and Al activities: zinc active domain in which aluminum dissolution is inhibited, and zinc passive domain. The inhibition of aluminum dissolution involves the dissolution/precipitation mechanism of zinc cations on the aluminum-rich surface [19], and the inhibition degree which is assessed by a decreased percentage of j_{Al} (84% and 89% for Galfan and Galvalume respectively) seems not to depend on Al composition in the coatings. The dissolved Al fraction in **Fig. 8-5** demonstrates that Zn selective dissolution from both coatings occurs in the Zn active domain, and Al selective dissolution occurs in the Zn passive domain.

8.5. Conclusion

In this work, we have mapped out Zn and Al selective dissolution from Galfan and Galvalume as a function of potential in three different electrolytes. During cathodic polarization, there was a strong selective dissolution of Al from both alloys in 0.1 M NaOH and 0.1 M NaCl, but a selective dissolution of Zn from Galvalume in 0.1 M HCl in which Zn dissolution was detected even though Zn was normally not active in the cathodic potential domain. During anodic polarization, a strong selective dissolution of Zn was seen in the acidic and neutral solutions. In the alkaline solutions, anodic branches of polarization curves for both Galfan and Galvalume are divided into 2 different domains: zinc active domain in which Zn selective dissolution occurs and zinc passive domain in which Al selective dissolution occurs.

Acknowledgement

We would like to thank ArcelorMittal, France for furnishing samples for this work and the Autocorr European RFCS project for financial support. We kindly acknowledge the RFCS project partners ArcelorMittal, France; Salzgitter AG, Germany; ThyssenKrupp, Germany, VoestAlpine, Austria and KTH, Sweden for helpful scientific discussions.

8.6. References

- ¹ X. G. Zhang, *Electrochemistry and corrosion of zinc*, Springer, 1996.
- ² H. W. Pickering, Characteristic features of alloy polarization curves, *Corros. Sci.* 23 (1983) 1107-1120.
- ³ M. Seo, G. Hultquist, C. Laygraf, N. Sato, The influence of minor alloying elements (Nb, Ti and Cu) on the corrosion resistivity of ferritic stainless steel in sulfuric acid solution, *Corros. Sci.* 26 (1986) 949-960.
- ⁴ S. Rambert, D. Landolt, Anodic dissolution of binary single phase alloys – II. Behavior of CuPd, NiPd and AgAu in LiCl, *Electrochim. Acta.* 31 (1986) 1433-1441.
- ⁵ B. G. Ateya, H. W. Pickering, The effects of potential and kinetic parameters on the formation of passivating noble metal rich surface layers during the selective dissolution of binary alloys, *Corros. Sci.* 38 (1996) 1245-1267.
- ⁶ M. A. Fawzy, G. H. Sedahmed, A. A. Mohamed, Corrosion of Pb-Sn alloys in alkaline solutions, *Surf. Tech.* 15 (1982) 147-152.
- ⁷ A. T. Kuhn, Anodic dissolution, oxygen reduction and corrosion of gold alloys, *Surf. Tech.* 13 (1981) 17-31.
- ⁸ J. Gniewek, J. Pezy, J. O'M. Bockris, The effect of noble metals additions upon the corrosion of copper: an Auger spectroscopy study, *J. Electrochem. Soc.* 125 (1978) 17-23.
- ⁹ H. W. Pickering, Volume diffusion during anodic dissolution of a binary alloy, *J. Electrochem. Soc.* 115 (1968) 143-147.
- ¹⁰ J. Laurent, D. Landolt, Anodic dissolution of binary single phase alloys at subcritical potential, *Electrochim. Acta.* 36 (1991) 49-58.
- ¹¹ B. E. Roetheli, G. L. Cox, W. B. Literal, Effect of pH on the corrosion products and corrosion rate of zinc in oxygenated aqueous solutions, *Metal. Alloy.* 3 (1932) 73-76.
- ¹² V. Vujičić, B. Lovreček, A study of the influence of pH on the corrosion rate of aluminium, *Surf. Tech.* 25 (1985) 49-57
- ¹³ K. Ogle, S. Weber, Anodic dissolution of 304 stainless steel using atomic emission spectroelectrochemistry, *J. Electrochem. Soc.* 147 (2000) 1770-1780.
- ¹⁴ D. Hamm, K. Ogle, C.-O.A. Olsson, S. Weber, D. Landolt, Passivation of Fe-Cr alloys studied with ICP-AES and EQCM, *Corros. Sci.* 44 (2002) 1443-1456.
- ¹⁵ K. Ogle, M. Mokaddem, P. Volovitch, Atomic emission spectroelectrochemistry applied to dealloying phenomena II. Selective dissolution of iron and chromium during active–passive cycles of an austenitic stainless steel, *Electrochim. Acta.* 55 (2010) 913–921.

-
- ¹⁶ K. Ogle, A. Tomandl, N. Meddahi, M. Wolpers, The alkaline stability of phosphate coatings I: ICP atomic emission spectroelectrochemistry, *Corros. Sci.* 46 (2004) 979-995.
- ¹⁷ K. Ogle, J. Bayens, J. Swiatowska, P. Volovitch, Atomic emission spectroelectrochemistry applied to dealloying phenomena: I. The formation and dissolution of residual copper films on stainless steel, *Electrochim. Acta.* 54 (2009) 5163.
- ¹⁸ M. Mokaddem, P. Volovitch, F. Rechou, R. Oltra, K. Ogle, The anodic and cathodic dissolution of Al and Al–Cu–Mg alloy, *Electrochim. Acta.* 55 (2010) 3779-3786.
- ¹⁹ T. N. Vu, M. Mokaddem, P. Volovitch, K. Ogle, The anodic dissolution of zinc and zinc alloys in alkaline solution. II. Al and Zn partial dissolution from 5%Al-Zn coating, *Electrochim. Acta.* 74 (2012) 130-138.
- ²⁰ T. N. Vu, P. Volovitch, K. Ogle, Selective dissolution of Zn and Al from Zn-Al coatings on steel: Measurement in situ with AESEC and ex situ with immersion test, *Corros. Sci.* submitted (2012).
- ²¹ B. E. Roetheli, G. L. Cox, W. B. Literal, Effect of pH on the corrosion products and corrosion rate of zinc in oxygenated aqueous solutions, *Met. Alloy*, 3(1932)73-76.
- ²² A.R. Marder, The metallurgy of zinc coated steel, *Prog. Mater. Sci.* 45 (2000) 191-271.
- ²³ Galvalume coated steel sheet, GalvInfo Center, 2003.
- ²⁴ H. Dafydd, D.A. Worsley, H.N. McMurray, The kinetics and mechanism of cathodic oxygen reduction on zinc and zinc-aluminum alloys galvanized coatings, *Corros. Sci.* 47 (2005) 3006-3018.
- ²⁵ C. W. Wagner, W. Traud, Über die deutung von korrosionsvorgängen durch überlagerung von electrochemischen teilvorgängen und über die potentialbildung an mischelektroden, *Z. Electrochem.* 44 (1938) 391-402.
- ²⁶ M. Pourbaix, Atlas d'équilibres électrochimiques, Gauthier-Villars & Cie, Paris, 1963
- ²⁷ K. Ogle, M. Serdechnova, M. Mokaddem, P. Volovitch, The cathodic dissolution of Al, Al₂Cu, and Al alloys, *Electrochim. Acta.* 56 (2011) 1711-1718.

Chapter IX:

The Anodic Dissolution of Zinc and Zinc Alloys in Alkaline Solution: Al and Zn partial dissolution from 5% Al-Zn coatings

T. N. Vu, M. Mokaddem, P. Volovitch, K. Ogle

Electrochimica Acta 74 (2012) 130-138.

9. The Anodic Dissolution of Zinc and Zinc Alloys in Alkaline Solution: Al and Zn partial dissolution from 5% Al-Zn coatings

ABSTRACT: The polarization behavior of a 5 wt.% Al- Zn steel coating (Galfan™) has been investigated in alkaline solution using atomic emission spectroelectrochemistry (AESEC). The instantaneous Zn and Al dissolution rates were measured as a function of time during a linear scan and potential step transients. The formation rate of insoluble oxides was determined from the difference between the convoluted total current and the sum of the elemental dissolution currents. It was found that, over a wide potential range, the zinc and aluminum partial currents behaved in a similar way to pure zinc and pure aluminum independently. However, during the period in which zinc was active, aluminum dissolution was inhibited. This is attributed to the inhibitive effect of the first and/or the second states of zinc oxide that are formed during the active potential domain. The third form of zinc oxide, observed at higher potential and responsible for the passivation of zinc dissolution, does not have a measurable effect on the Al dissolution rate.

Keyword: Galfan, partial elemental current, linear scan and steady state polarization, alkaline solution, AESEC.

9.1. Introduction

In Part I of this article [1], the anodic dissolution of Zn (electrogalvanized steel) in alkaline solution was investigated as a function of applied potential. By using atomic emission spectroelectrochemistry (AESEC) [1-6], we were able to measure the contribution of oxide formation and zinc dissolution to the total oxidation current. For this relatively simple material we were able to identify, as a function of potential, three different solid zinc oxidation products as intermediates in zinc dissolution and their passivating effect on the zinc dissolution reaction.

In this work, we apply the AESEC technique to observe the polarization behavior of a significantly more complex alloy coating with the trade name GalfanTM. This material is a dual phase binary alloy coating of Zn and about 5 wt% Al with rare earth elements Ce and La added as mesh metals [7-10]. The 5 wt% Al composition is near the eutectic point in the Al-Zn phase diagram (6 wt% Al) [11]. During solidification, two phases are formed; a zinc-rich η - phase surrounded by a eutectic phase consisting of β -Al and η - Zn lamellae [10-11]. The alloy is applied to steel through the continuous hot dip galvanization process and is frequently used in unpainted outdoor applications.

The specific goal of this work is to enquire into the interactions between zinc and aluminum dissolution in different potential domains. The complication for the Zn-Al system is that the anodic reaction may be divided into Zn and Al dissolution both of which, in alkaline solution, proceed via the intermediary of a solid hydroxide / oxide species [12-14]. If we use the simple $M(OH)_z$ to represent the stoichiometry of the oxide/ hydroxide intermediate, the anodic dissolution mechanism may be written as :



Indeed, in our previous work we demonstrated that Zn dissolution occurs by way of three forms of solid zinc oxidation products that were distinguished based on their effect on the

zinc dissolution reaction. Type I occurs during the early active period. It has a slight inhibiting effect on zinc dissolution and results in the occurrence of a plateau in the anodic dissolution peak. Type II oxide forms along the top of this plateau and apparently has little to no effect on zinc dissolution. Finally, a third type of oxide forms at higher potential creating a passive film which reduces the zinc dissolution rate. The different types of oxides were observed directly by the difference between the total current and the dissolution current and indirectly by the apparent effect of the oxide on the zinc dissolution reaction.

In this article, oxide formation will also be measured in a similar way for the Al-Zn alloy system. Specifically we seek to observe and quantify the effect of polarization on both Al and Zn dissolution. In the first section, we investigate the effect in a qualitative fashion using linear scan voltammetry to map out the general behavior of the system in different potential ranges. In the second part, we investigate the same phenomena using potential step transients providing more quantitative kinetic information.

9.2. Experimental

9.2.1 Materials

A commercial hot dipped galvanized steel product with a 7.0 μm thick Galfan coating was used. The samples were used as received or polished directly with 1 μm metallographic paper, following ultrasonic cleaning for 10 minutes in reagent grade ethanol and drying in flowing nitrogen. Electrolytes were prepared from analytical grade NaOH (provided by Prolabo, S.A.) and deionized water (18.2 M Ω cm) prepared with a Millipore™ system. All solutions were deaerated for 10-15 minutes with flowing nitrogen prior to experiments to avoid the effect of cathodic oxygen reduction [15]. All experiments were performed at ambient temperature and pressure.

9.2.2. Scanning Electron Microscopy/Energy Dispersive Spectroscopy (SEM/EDS)

Surfaces characterization were performed by scanning electron microscopy (SEM) coupled with energy dispersive spectroscopy (EDS), using a Gemini 1530 microscope with field emission gun (FEG) source at 15 kV, Si(Li) detector for EDS and QUANTAX software (Bruker AXS).

9.2.3. The AESEC Technique

Atomic emission spectroelectrochemistry (AESEC) consists of an inductively coupled optical emission spectrometer (ICP-OES) coupled to an electrochemical flow cell. It has been described in detail in a previous article [4]. Briefly, the ICP-OES spectrometer was manufactured by HORIBA Jobin Yvon (Ultima 2CTM) and consists of a polychromator and a monochromator for the simultaneous detection of 31 different wavelengths. The spectrometer is equipped with a fast time resolved data acquisition system developed in collaboration with the manufacturer for this application. The emission intensity of Zn and Al in the plasma was monitored at 213.856 nm and 167.081 nm respectively. The detection limits were determined to be 2.2 ppb Zn and 3.0 ppb Al, under the conditions of these experiments.

The electrochemical experiments were conducted in the AESEC electrochemical flow cell with a Ag/AgCl reference electrode (3 M KCl, +208 mV vs. a standard hydrogen electrode) and a Pt wire counter electrode. The potentiostat was an EG&G Princeton Applied Electronics M273A functioning in the potentiostatic mode. It was controlled manually from the front panel and the analog current and potential signals were routed into the measuring circuit of the ICP-OES spectrometer to ensure that spectrometer and electrochemical data were on the same time scale. The flow rate in the electrochemical cell was approximately 3.0 ml min⁻¹ and was measured for each series of experiments.

9.2.4. Analysis of the ICP-OES data

The total current density measured by the electrometer of the potentiostat is referred to as j_e , where e indicates the electrical nature. The partial elementary dissolution current density for element, M, j_M , is calculated from the downstream concentration of the element, C_M :

$$j_M = nFf C_M / A \quad (9-5)$$

where f is flow rate of electrolyte through the cell, F is the Faraday constant, A is the surface area, and n is number of electrons transferred in the oxidation step ($n = 2$ for Zn and $n = 3$ for Al). Note that all surface reaction rates are normalized to the geometrical surface of the sample exposed to the electrolyte (0.52 cm²). This is done for convenience and is not meant to imply that the specific reaction is actually uniform on the surface.

The total current is the sum of the anodic and cathodic partial currents, $j_e = j_a + j_c$. The anodic current may in turn be divided into soluble component for each element and an insoluble component, j_{ins} . The soluble components are measured by the ICP-OES (**Eqn. 9-5**).

We assume that the insoluble component remains on the surface of the sample (or within the porosity) in the form of a corrosion product or oxide film. Therefore, if the concentration and electrical transients have the same time resolution, the total current may be written as:

$$j_e = j_{ins} + \sum j_M + j_c \quad (9-6)$$

where j_c is the cathodic partial current and j_{ins} is the partial current corresponding to the instantaneous rate of formation of “insoluble” components of the anodic reaction. (Note that both Zn and Al dissolution pass through oxide/hydroxide intermediates. Although we use the term “insoluble”, in fact this only means that at a given time, the formation of solid intermediates is more rapid than their dissolution leading to an oxide growth on the surface). Under conditions in which $j_c = 0$, both Zn and Al dissolve from the alloy and j_{ins} may be determined by:

$$j_{ins} = j_e - j_{Zn} - j_{Al} \quad (9-7)$$

Under transient conditions, **eqn. 9-7** cannot be applied directly because of the temporal resolution difference between the electrochemical measurements (fast) and the spectrochemical measurements that are broadened by mixing in the hydraulic system. This may be corrected by performing a numerical convolution of j_e and $h(t)$ [4] such that:

$$j^*(t) = \int_0^t j_e(\tau) * h(t-\tau) d\tau \quad (9-8)$$

where $h(t)$ is the time constant distribution for the hydraulic system and τ is simply a variable of integration. Following this operation, the electrochemical data will be on the same time resolution as the concentration data. More precisely, **Eqn. 9-7** should be written as

$$j_{ins} = j_e^* - j_{Zn} - j_{Al} \quad (9-9)$$

During potential step experiments, it often happens that the Al dissolution rate is high prior to the imposition of the potential step due to the cathodic dissolution mechanism [5]. Therefore, following the potential step, the instantaneous partial Al dissolution rate will be the sum of two different components: (1) j_{Al}^t , which we define as the true Al dissolution rate, and (2) ψ_{Al} , the decreasing background from the Al concentration prior to the potential step. ψ_{Al} is a purely hydrodynamic phenomena and is only due to residual Al ions in the nebulization

chamber of the ICP-OES system. It is therefore, important to remove this contribution before attempting a kinetic analysis of Al dissolution rate versus time during these experiments.

$$j_{Al} = j_{Al}^t + \psi_{Al} \quad (9-10)$$

The later term is described in [5]:

$$\psi(t) = \int_{-\infty}^t j_{Al}(\tau) * h(t-\tau) d\tau \quad (9-11)$$

with $j_{Al}(t) = 0$ for $t > 0$.

Therefore, it is necessary to remove the decaying signal, ψ_{Al} , from the Al signal due to the corrosion of Al before the potential step is applied. **Eqn. 9-7** then becomes:

$$j_{ins} = j^* - (j_{Zn} + j_{Al} - \psi_{Al}) \quad (9-12)$$

The time constant distribution was determined as described in a previous publication [1] by measuring the concentration transient associated with a pulsed dissolution of copper in hydrochloric acid. The resulting transient was fit with a log-normal probability distribution. In this work, the time constant distribution parameters were found to be $\beta = 0.95$, $\tau = 13.5$ s and the offset due to transport in the capillaries was determined to be $\Delta t = 20$ s.

9.3. Results

9.3.1 Microstructure Analysis

Fig. 9-1a shows a scanning electron micrograph of the initial Galfan surface after polishing. The material consists of two phases: zinc-rich phase and the eutectic phase which an EDS analysis indicated 1.3 and 6.1 wt.% Al, respectively (**Fig. 9-1a**). A higher resolution image of the eutectic phase is shown in **Fig. 9-1b** where the β -Al appears as dark points of approximately 100 nm diameter surrounded by the η -Zn.

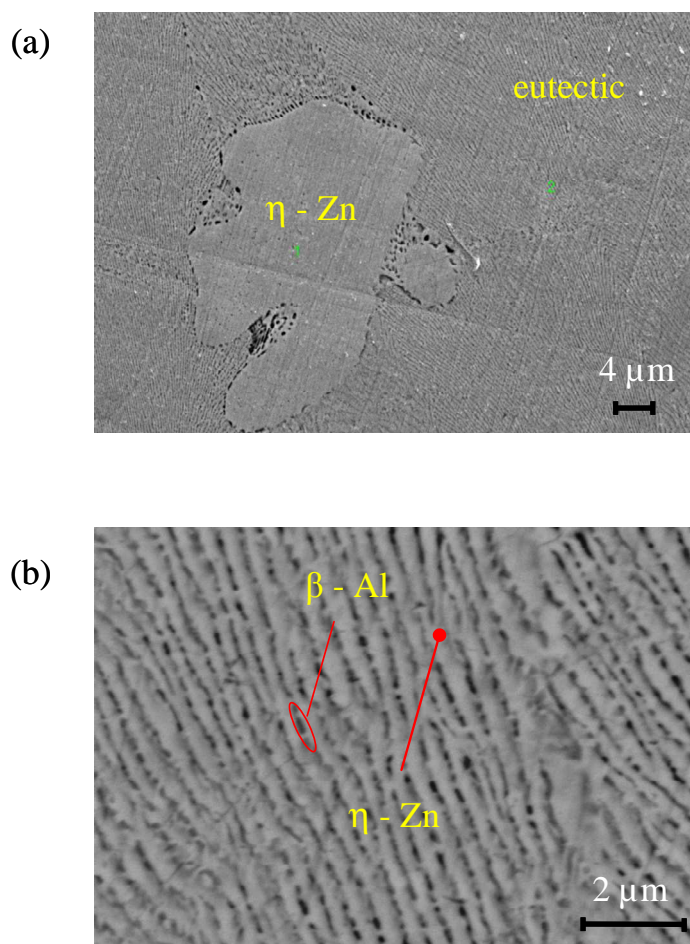


Figure 9-1: Microstructure of polished GalfanTM showing 2 phases: (a) secondary electron image showing the zinc-rich phase and the eutectic phase, (b) backscattered electron image showing the eutectic phase composed of Al rich lamellae surrounded by a zinc-rich phase.

9.3.2. Spontaneous reaction of 5% Al-Zn alloy with alkaline solutions

Fig. 9-2 gives (a) the open circuit potential and spontaneous elementary dissolution current densities j_{Al} and j_{Zn} , (b and c respectively) as a function of time for the reaction of 5% Al-Zn alloy coated steel with electrolytes of variable NaOH concentration as indicated. The 0.1 and 0.2 M reaction shows an initial open circuit potential of -0.96 V and -0.85 V vs. Ag/AgCl respectively consistent with an oxidized surface. After about 50 s, the potential drops through a second plateau of -1.35 and -1.43 V and then obtains a stable -1.48 V vs. Ag/AgCl for all three concentrations. The positive potential plateau during the early period is consistent with the dissolution of initial oxides from the surface. For 0.3 M NaOH, the potential dropped directly to the stable -1.48 V vs. Ag/AgCl indicative of a more rapid pickling of surface oxides. During the steady period, j_{Zn} was below the detection limit, as

shown in **Fig. 9-2c**, and the open circuit potential was stable at approximately -1.46 V vs. Ag/AgCl, consistent with the active dissolution of Al.

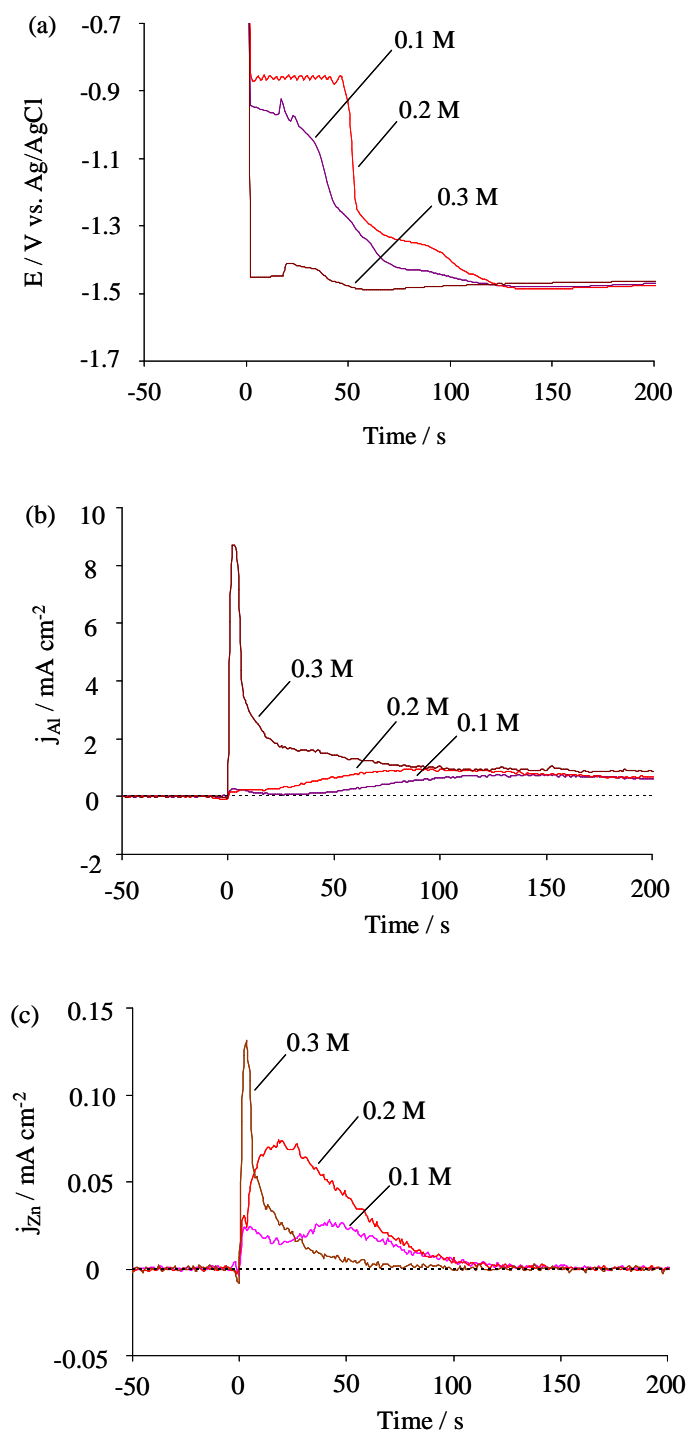


Figure 9-2: Spontaneous reaction profile for Galfan in contact with 0.1 M, 0.2 M, and 0.3 M NaOH solutions at open circuit potential. Shown as a function of time are the open circuit potential (E_{oc}) (a) and the instantaneous dissolution rates of (b) Al (j_{Al}) and (c) Zn (j_{Zn}).

The Al dissolution rate, j_{Al} , varied with hydroxide ion concentration. Average values for j_{Al} in the near steady state region (from 150 s to 200 s) (**Fig. 9-2b**) were 0.49, 0.67, and 0.88 mA cm⁻² for 0.1, 0.2 and 0.3 mol l⁻¹ OH⁻ respectively. The initial dissolution transients showed poor reproducibility, reflecting a varying state of oxide formation on the Galvanic surface.

9.3.3. Zn and Al dissolution in different potential domains

Fig. 9-3a shows a typical AESEC polarization curve of 5% Al-Zn alloy coated steel in 0.1 M NaOH solution. The total current, j_e , and the partial elementary currents, j_{Al} and j_{Zn} are shown. The experiment consisted of several time periods. First, the sample was exposed at open circuit potential (E_{oc}) until an approximately stable aluminum dissolution rate was obtained. Next, a potential step to -1.6 V vs. Ag/AgCl for 200 s (E_{ap}) was applied to the sample. This was followed by linear sweep voltammetry (lsv) from -1.6 V to -0.6 V vs. Ag/AgCl at a scan rate of 0.5 mV s⁻¹.

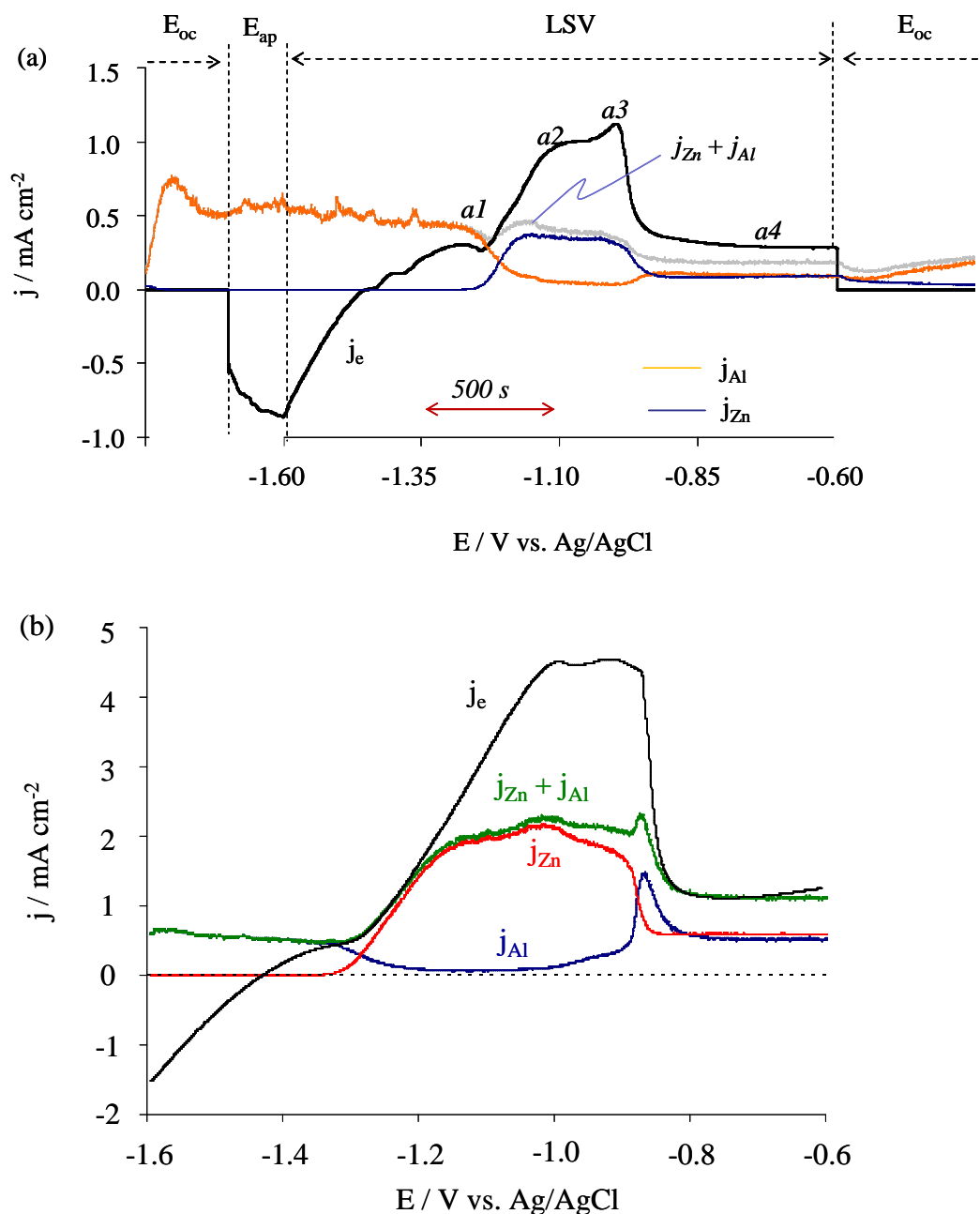


Figure 9-3: AESEC polarization experiment (LSV) showing the total current density (j_e) and dissolution rates of Zn (j_{Zn}) and Al (j_{Al}) as a function of potential when Galfan was polarized from -1.6 V to -0.6 V vs. Ag/AgCl with a sweep rate of 0.5 mV s^{-1} in (a) 0.1 M NaOH and (b) 0.25 M NaOH solution. Curve (a) also shows preliminary open circuit potential (E_{oc}) and the applied potential period (E_{ap}) at -1.6 V.

For the anodic polarization curve (LSV) in **Fig. 9-3a**, the total electrical current, j_e , shows several different anodic features labeled a1 – a4. This result illustrates the utility of the AESEC method as these features could not be interpreted unambiguously without knowledge

of the elementary dissolution rates. From -1.6 V to the potential labeled *a1* (referred to as the “Zn cathodic domain”) the interfacial kinetics are characterized by selective aluminum dissolution. The Al dissolution rate was essentially constant despite a very high cathodic current. In fact, Al dissolution did not seem to depend upon the applied potential at all and varied little when the potential was stepped from the open circuit potential (-1.46 V) to the initial sweep potential (-1.6 V). During the potential sweep, the magnitude of the total current j_e steadily approached zero, crossing zero at $E = -1.44$ V and rapidly approached j_{Al} . This gave rise to the feature labeled *a1* in **Fig. 9-3a**.

An anodic maximum, labeled *a2*, corresponds to an increase in j_{Zn} and a decrease in j_{Al} . In the potential domain between *a1* to *a2* (referred to as the “Zn Tafel domain”), the Zn dissolution rate increases exponentially with potential, with j_{Zn} reaching a maximum at *a2*. A second maximum in j_e , labeled *a3*, was observed at a slightly higher potential however this peak was less pronounced at higher hydroxide concentrations. In the potential domain from *a2* to *a3* (referred to as the “Zn maximum domain”) where the Zn dissolution rate is more or less independent of potential and curiously, the aluminum dissolution rate decreases to a minimum value.

Finally immediately following *a3* there is a rapid decrease in j_e and j_{Zn} to a steady state rate that is independent of potential (*a4*) (Zn passive domain). During this period, j_{Al} also increases to a steady state rate. At higher NaOH concentration, a peak of j_{Al} was observed immediately following *a3*. An example is shown in **Fig. 9-3b** where, for simplicity, only the linear scan voltammetry curve is shown. At higher potentials, the total current and the Al and Zn dissolution rates were relatively constant and dissolved at comparable rates. The j_{Zn} vs. E curve shown in **Fig. 9-3** is very similar to that observed for pure zinc and for electrogalvanized steel under similar conditions described in part I of this work [1].

9.3.4. SEM / EDS analysis after applied potential

In order to confirm the formation and the dissolution of the oxide in different potential domains after activating the surface at -1.6 V vs Ag/ AgCl, we have applied different constant potentials for 1 h and then observed the surface by scanning electron microscopy. **Fig. 9-4** gives the SEM images of the surface after various applied potentials. **Fig. 9-4a** shows the initial unpolished Galfan surface. As compared to **Fig. 9-1a** (polished surface), it is observed that the surface has a significant porosity. EDS analysis indicates that the more porous areas

have an Al content of 3.2 wt% while the less porous area has 5.2 wt%. After an applied potential of -1.2 V vs. Ag/AgCl for 1 hour (**Fig. 9-4b**), the presence of a precipitated corrosion products is visible. After an applied potential of -0.7 V, the precipitated product is no longer detected but a porous and non porous phase are clearly visible. The EDS elemental analysis of **Table 9-1** shows that Al is not detectable for either surface after polarization. This is consistent with the selective Al dissolution observed in **Fig. 9-3**.

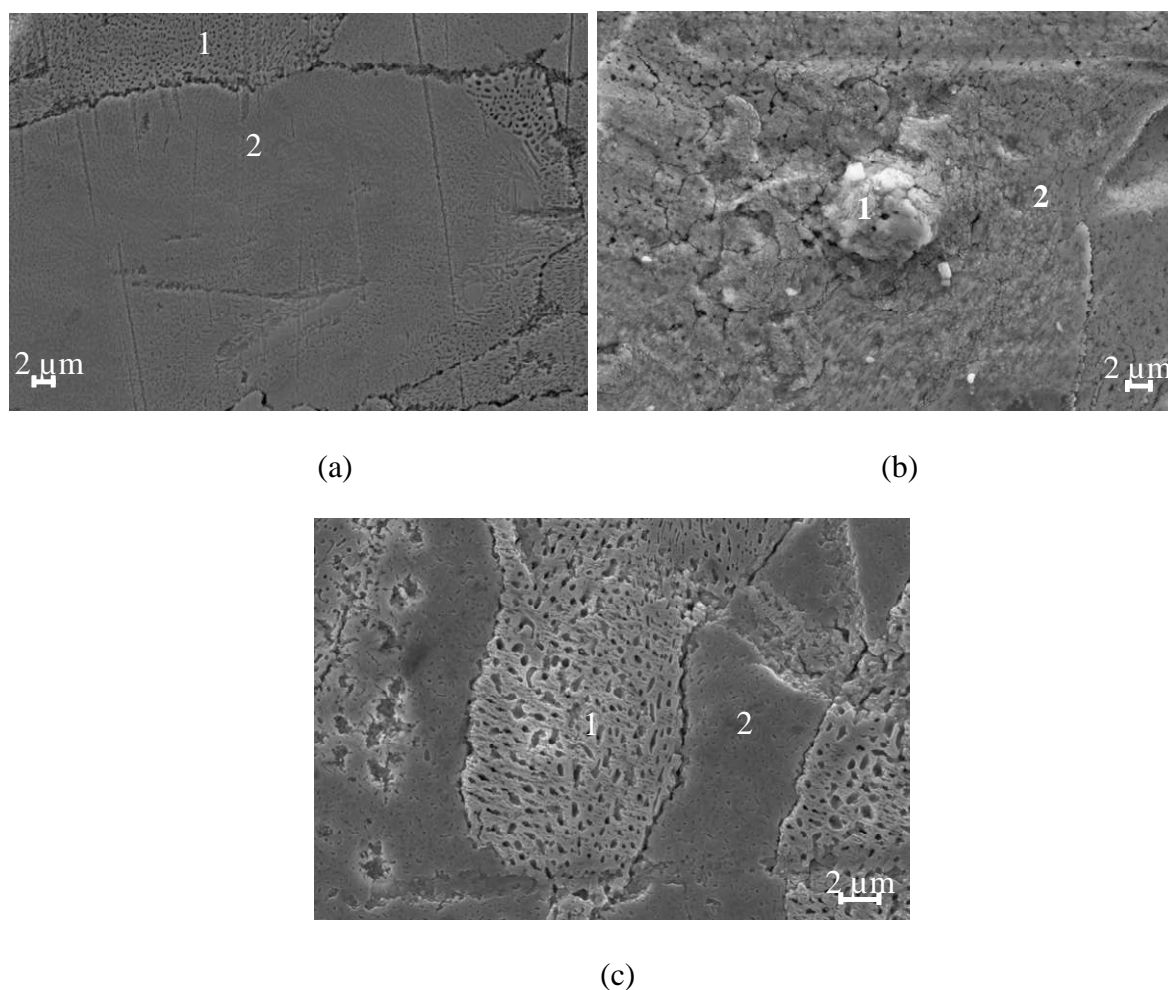


Figure 9-4: SEM images of the unpolished surface (a) before and (b & c) after applying potential at -1.2 V and -0.7 V vs. Ag/AgCl.

Table 9-1: EDS elemental analysis of surface in Fig. 9-4

Element		Zn	Al	O	Na	Fe	C
Fig. 9-4a	Zone 1	84.7	3.2	2.0	9.0	1.1	-
	Zone 2	84.2	5.2	1.5	8.4	0.7	-
Fig. 9-4b	Zone 1	55.6	1.1	23.2	9.6	-	10.5
	Zone 2	74.4	1.0	15.3	6.0	-	3.3
Fig. 9-4c	Zone 1	89.4	0.6	2.4	7.1	0.5	-
	Zone 2	89.8	0.1	2.0	7.4	0.7	-

9.3.5. Kinetic parameters

In **Fig. 9-5**, j_{Zn} and j_{Al} are shown as a function of the hydroxide ion concentration (0.1 to 0.5 M) in various potential domains of the polarization curve. In this domain where j_{Zn} is a maximum (-1.1 to -1.0 V vs. Ag/AgCl), a log-log plot of j_{Zn} vs. C_{NaOH} is linear with a slope, representing the reaction order, n , of approximately 1.5. j_{Al} is significantly lower than j_{Zn} in this domain and varies in a non linear fashion, increasing markedly at higher concentration. In the passive domain (-0.7 to -0.6 V vs. Ag/AgCl), a linear increase is observed in the log-log plot with $n = 1.3$ and 1.8 for Al and Zn respectively. By contrast, at lower potentials (not shown) from -1.5 V to -1.4 V, j_{Al} was essentially independent of hydroxide concentration with an apparent reaction order of only 0.3. Zinc dissolution was undetectable in this potential domain. These observed variations of the apparent reaction order for Al dissolution between the three potential domains may be associated with different dissolution mechanisms.

It was observed that j_{Al} increased during the second half of the activation peak. At high hydroxide ion concentrations, this is followed by a sharp peak in Al dissolution (**Fig. 9-3b**). This effect was not apparent at 0.1 M NaOH in **Fig. 9-3a**.

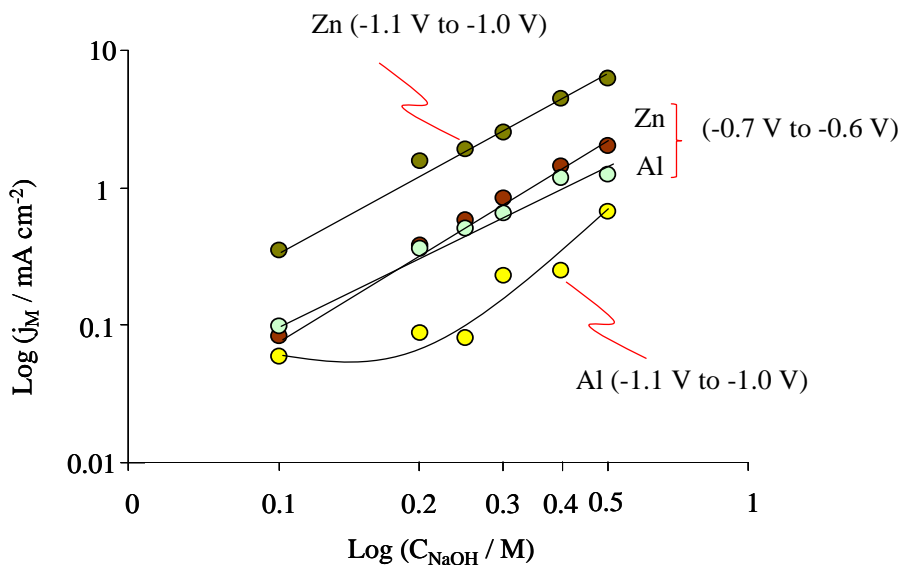


Figure 9-5: Reaction order analysis showing $\log(j_{Zn})$ and $\log(j_{Al})$ during polarization as a function of hydroxide ion concentration. The measurements were performed in the potential domains specified.

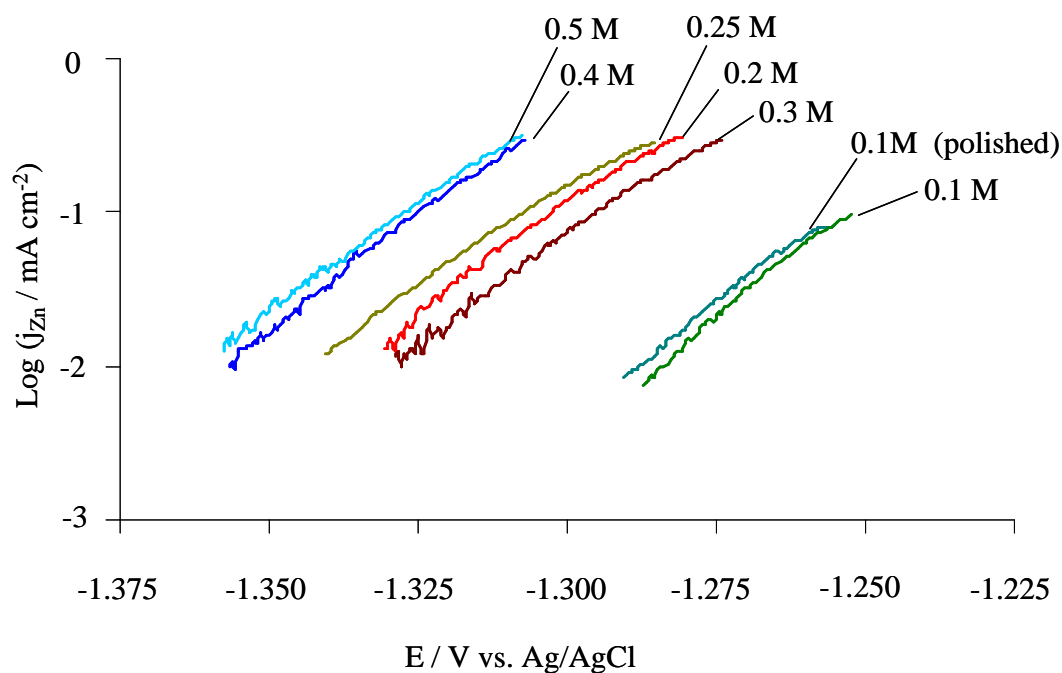


Figure 9-6: Tafel slope measurements for anodic Zn dissolution ($\log(j_{Zn})$ vs. E) at different hydroxide ion concentration from the linear potential sweep experiments. The Tafel slopes are given in **Table 9-2**.

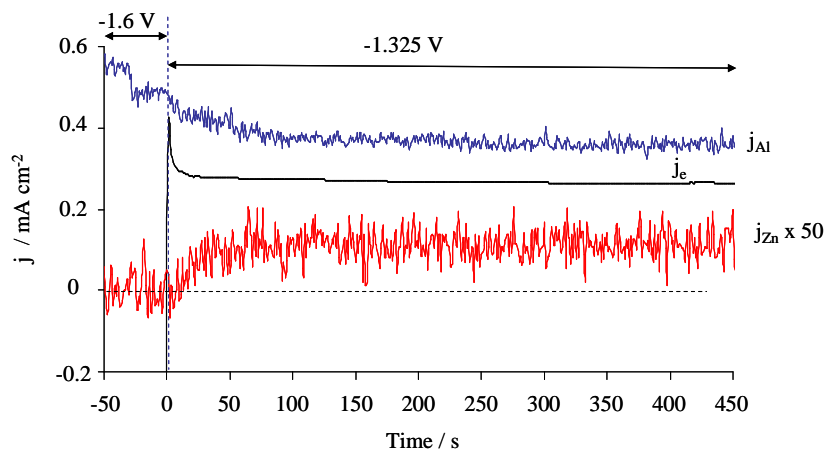
Table 9-2: Tafel slope of $\log(j_{Zn})$ vs. $\log(C_{NaOH})$ curves in **Fig. 9-6**

NaOH concentration (M)	Tafel slope (mV/decade)
0.1 (polished)	35
0.1	30
0.2	36
0.25	38
0.3	37
0.4	34
0.5	36

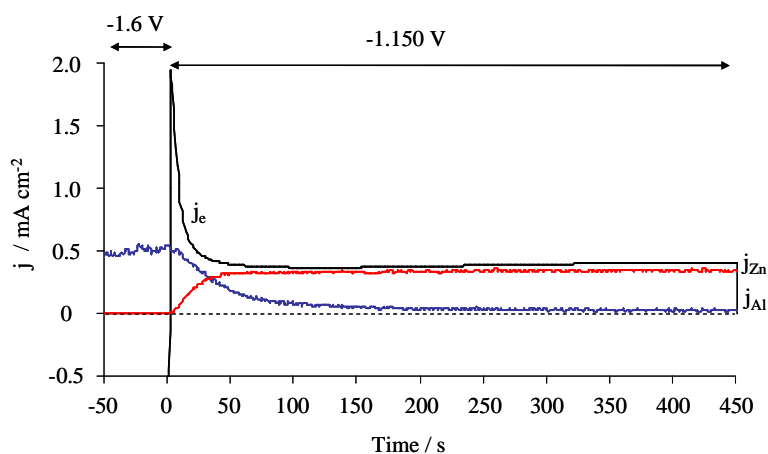
Fig. 9-6 gives the $\log j_{Zn}$ obtained at different hydroxide ion concentrations from the linear potential scan experiments. The Tafel slopes from these curves are summarized in **Table 9-2**. The results indicate that the Tafel slope for Zn dissolution in the active domain is approximately 35 mV/decade and is nearly independent of hydroxide ion concentration. This value is consistent with the dissolution of pure zinc obtained in Part I. We conclude from this result that the Al dissolution rate does not have a significant effect on the kinetics of zinc dissolution.

9.3.6. Potentiostatic Transient Experiments

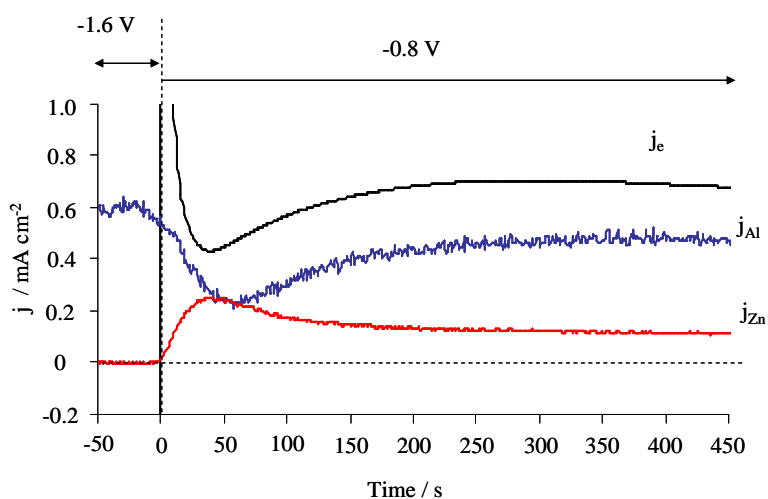
For the active region and beyond, during the linear scan voltammetry experiments, it was observed that the total current, j_e , was greater than the sum of the Al and Zn dissolution currents. This implies that a significant fraction of oxidized Al and/or Zn are insoluble and are therefore not detected by the ICP. It was therefore of interest to determine the steady state polarization curve, which in principle, should be less affected by film growth. Potential step experiments were performed by first polarizing the Galfan to -1.6 V (very close to the open circuit potential) for 300 seconds and then stepping the potential in the positive direction. **Fig. 9-7** gives the results of steps to different potential values in the different regions of the profile.



(a)

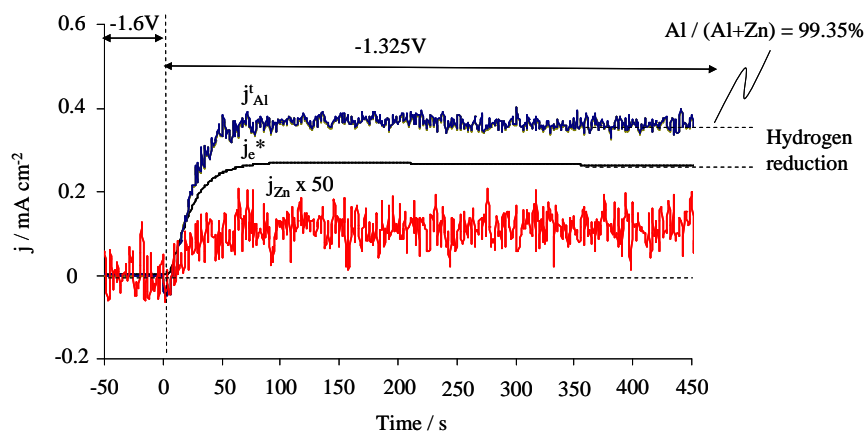


(b)

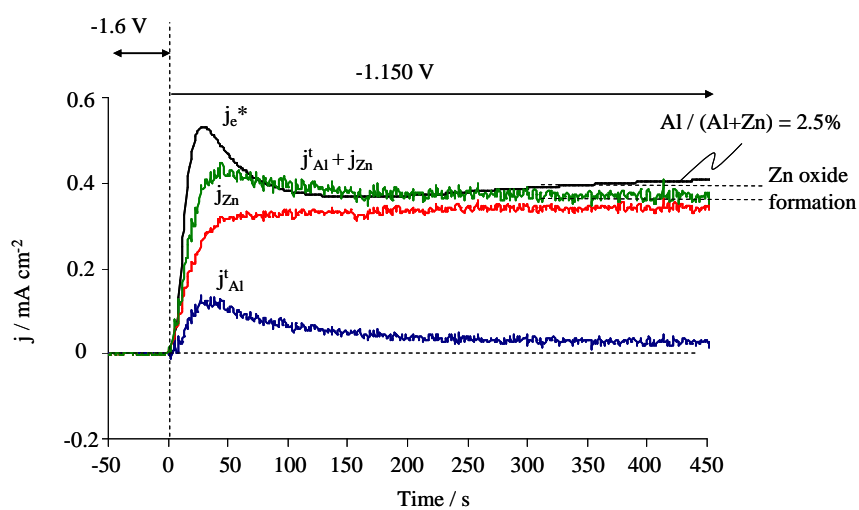


(c)

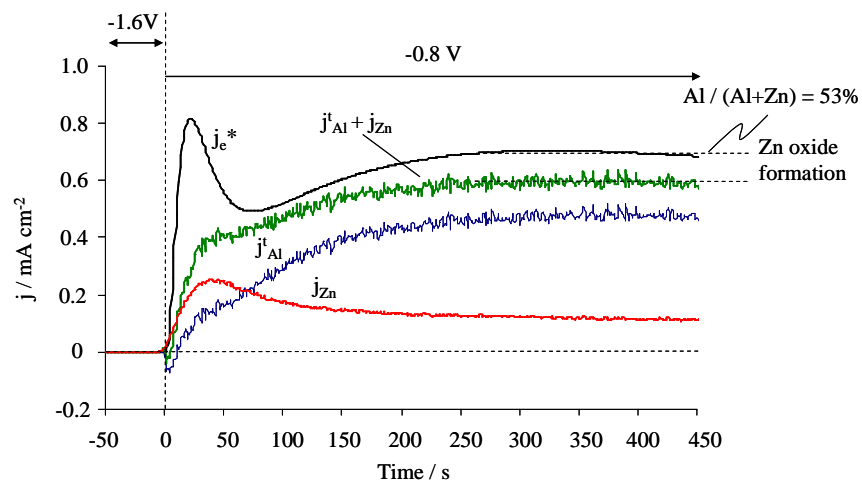
Figure 9-7: Transient analysis: j_e , j_{Al} and j_{Zn} from Galfan in 0.1 M NaOH as a function of time during a potential step from -1.6 V vs. Ag/AgCl to (a) -1.325 V , (b) -1.150 V , and (c) -0.8 V .



(a)



(b)



(c)

Figure 9-8: Transient analysis: j_e^* , j_{Al}^t and j_{Zn} in 0.1 M NaOH as a function of time during a potential step from -1.6 V vs. Ag/AgCl to (a) -1.325 V, (b) -1.150 V, and (c) -0.8 V.

Active domain potential step - An exploration of the active domain is shown in **Fig. 9-7a** with an applied potential of -1.325 V vs. Ag/AgCl. The increase in potential resulted in a stabilization of the Al dissolution rate at a slightly lower level than at -1.6 V vs. Ag/AgCl. The Zn dissolution rate rose only slightly above background to about $2 \mu\text{A cm}^{-2}$. Note that the Zn signal is multiplied by 50 in the figure. The total current, j_e , rose almost to the level of the Al dissolution rate. The difference may be attributed to the reduction of hydrogen occurring simultaneously with Al dissolution. The cathodic current density, j_{cat} was estimated at $80 \mu\text{A cm}^{-2}$. Selective dissolution of Al was clearly identified with Al cations comprising 99.35% of the dissolved species detected with ICP (**Fig. 9-8a**).

Maximum domain potential step - **Fig. 9-7b** presents a potential step into the active region. In this case, zinc dissolution increased markedly and Al dissolution decreased. At steady state, Al cations represented only 2.35% of the total dissolved cations (**Fig. 9-8b**), showing a preferential dissolution of zinc. We note that in the steady state period the insoluble component appears to be growing as indicated by the difference in the sum of Zn and Al dissolution rates and the total current. Nevertheless, the Al dissolution rate was relatively constant.

Passive domain potential step - **Fig. 9-7c** shows a dissolution profile for a potential step into the passive domain. This resulted in an increase in j_{Zn} which passed through a maximum and then decreased to a steady state rate. The j_{Al} signal passed through a minimum, shifted to slightly longer times, and then increased to obtain a steady state value. This result suggests that the early stage of the transient involves the formation of the type I and type II oxide that may have an initial inhibiting effect. However, as soon as the type III oxide was formed and the film was passive, Al dissolution became active once again.

It is of considerable interest to determine the rate of formation of insoluble oxidation products, j_{ins} as a function of time from the data in **Fig. 9-7**. This requires treating the data as described in the introduction. **Fig. 9-8** after treatment gives the convoluted total current, j_e^* , the zinc dissolution rate, j_{Zn} (unaltered), and $j_{\text{Al}}^t = j_{\text{Al}} - \psi_{\text{Al}}$ calculated from the data of **Fig. 9-7**. The rate of film growth may be determined as $j_{\text{ins}} = j_e^* - j_{\text{Al}}^t - j_{\text{Zn}}$ and can be apprehended visually by comparing j_e^* with $(j_{\text{Al}}^t + j_{\text{Zn}})$.

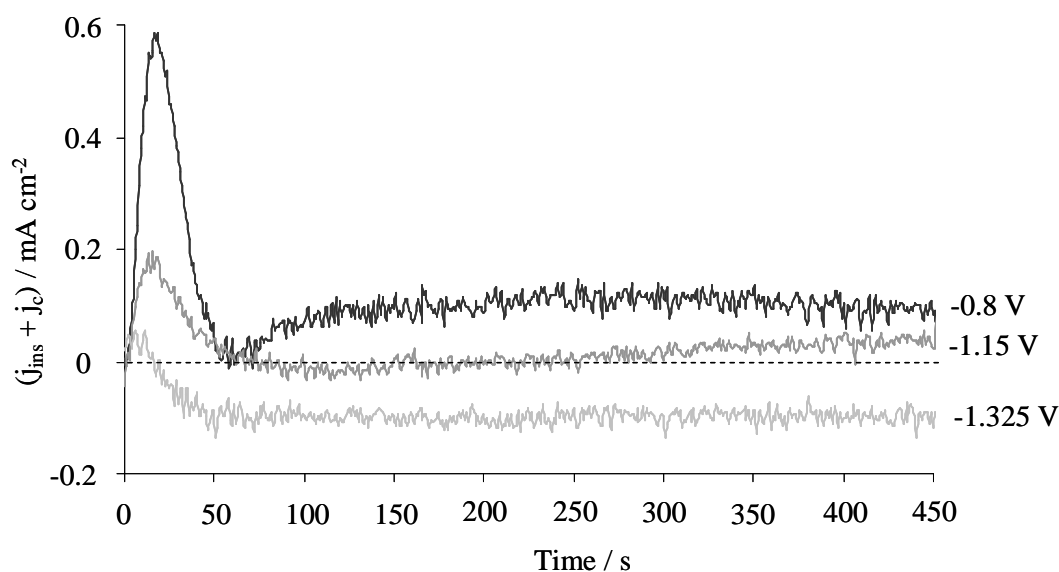


Figure 9-9: The total insoluble component formation rate and cathodic current ($j_{ins} + j_c$) in 0.1 M NaOH as a function of time for the potentials of -1.325 V, -1.15 V, and -0.8 V vs. Ag/AgCl.

Figure 9-9 shows $j_{ins} + j_c$ as a function of time for the three potentials of **Fig. 9-7** and **Fig. 9-8**. We attribute j_{ins} to the formation of insoluble or at least slowly dissolving oxides. The result in the cathodic domain is below zero indicating that the cathodic reaction is not negligible for this experiment and therefore oxide formation cannot be determined. Dissolution in the zinc active region shows a well defined peak during the first 40 s. Beyond this, j_{ins} ($j_c = 0$ in the anodic domain) is very close to zero suggesting that only the type I and II oxide forms in this domain. In the passive region, a very large Type I peak is observed followed by a slow rise to a steady state oxide formation rate. We attribute this slow rise to the formation of the zinc passive film which requires more time than the simple dissolution – precipitation mechanism of the type I, II.

9.3.7. Steady State Polarization curve

A steady state polarization curve in which j_e , j_{Al} and j_{Zn} were measured from the potential step experiments at steady state is shown in **Fig. 9-10**. Also shown in this curve is the sum of the elemental dissolution currents, $j_{Al} + j_{Zn}$. An inset in the upper part of the figure gives the current associated with the formation of insoluble elemental dissolution

components, (eqn. 9-7). Potentials below -1.25 V vs. Ag/AgCl, where $j_{\text{ins}} < 0$ were ignored for this calculation as this demonstrates a significant contribution of the cathodic current.

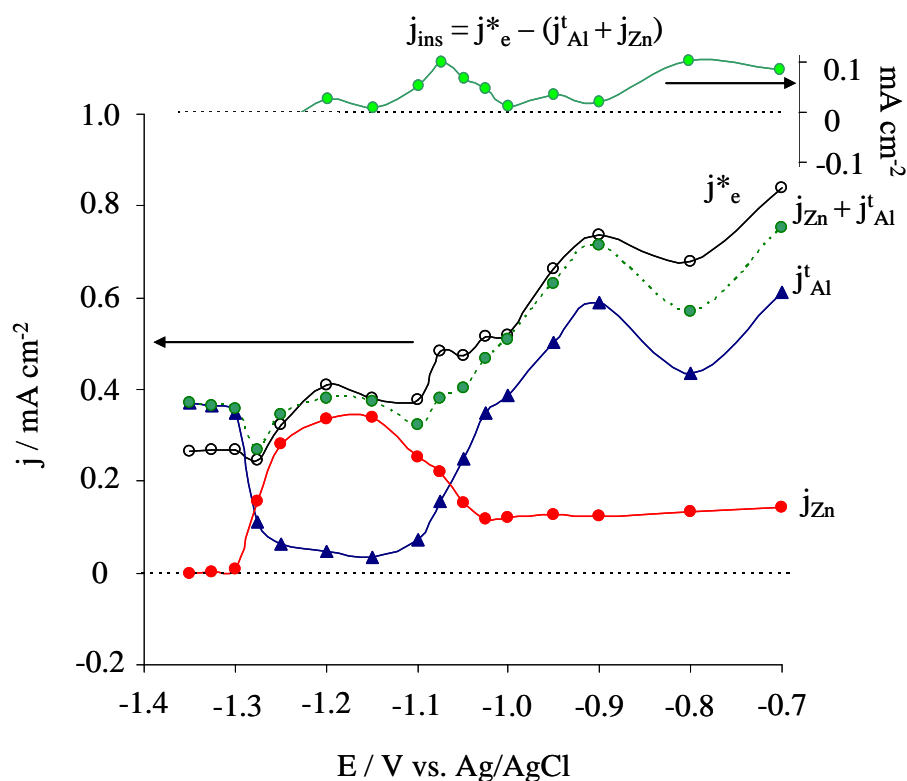


Figure 9-10: Steady state AESEC polarization curve showing j^*_e , j^t_{Al} , and j_{Zn} as a function of potential from -1.375 V to -0.7 V vs. Ag/AgCl in 0.1 M NaOH, calculated as the average values from 300 s to 400 s in Fig 7, 8 and 9. Also shown is the sum of the elemental dissolution current ($j^t_{Al} + j_{Zn}$) and the insoluble component of current, ($j_{\text{ins}} = j^*_e - j^t_{Al} - j_{Zn}$).

Several points are clear from the inspection of **Fig. 9-10**: Firstly, there is a good agreement between the sum of the elemental currents and the total current except in three potential regions – (1) the maximum of the active peak, (2) during the higher potentials of the passive domain, and of course (3) in the cathodic region which we do not consider. For (1) and (2), a measurable steady state oxide formation rate was observed. These results demonstrate that the anomalous oxidation observed in the previous section is only associated with the linear scan experiments; if sufficient time is given to the system, the total currents and the sum of the dissolution currents are in good agreement except in potential domains where oxide formation is expected.

Second, the potential corresponding to the zinc passivation was shifted approximately -100 mV relative to that obtained during the linear scan experiment. This suggests that nucleation phenomena do contribute to passivation; the linear scan experiment leads to the formation of an excess insoluble oxide that does not significantly contribute to passivation. During a transient step experiment, this oxide may form during the early stages and then dissolve at later stages.

Third, the inhibitive effect of Zn dissolution on Al dissolution is confirmed to not be associated with the linear scan experiment but was observed even at steady state. In **Fig. 9-7c** and **9-8c**, we see that a potential step into the passive domain leads to an initial decrease in j_{Al} followed by an increase. This implies that the state of the alloy / electrolyte interface obtained at the maximum in the zinc dissolution rate is a necessary passage for the system, even when the potential is stepped into the passive domain.

9.4. Discussion

In this section we propose a mechanistic interpretation of the kinetic results for Zn and Al dissolution, based on our understanding of the reactivity of pure zinc obtained in Part. I. **Fig. 9-11** shows a simplified schematic of the interfacial structure of the eutectic obtained in the different potential domains investigated in this work. We assume that Zn dissolution follows the mechanism proposed for pure zinc in our previous publication [1]. **Fig. 9-11a** shows the proposed structure when the sample is at open circuit or under the influence of a constant cathodic potential below the dissolution potential of zinc which in alkaline solution is $E^\circ \text{Zn}/\text{Zn}(\text{OH})_4^{2-} = -1.2 \text{ V vs. SHE}$ [16]. Under these circumstances, only Al dissolution will occur and the presence of Zn will have no effect on this reaction.

As the potential increases and active Zn dissolution begins, the surface will be covered with slightly soluble Zn oxide and hydroxide species that we previously described as type I and II oxides [1]. This is shown in **Fig. 9-11b**. Following the discussion of part 1, these oxides are probably formed by a dissolution-precipitation mechanism. Therefore the resulting film is not limited to the active zinc surface. The β -Al phase, which as shown in **Fig. 9-1** consists of spots of about 100 nm diameter, will also be covered with these corrosion products. We propose that it is these precipitated corrosion products that inhibit Al dissolution. The precise mechanism of inhibition may be due to the barrier effect of the products or may be due to a buffering of the interfacial pH due to the solubility of the

precipitated zinc oxides. Titration experiments [17] demonstrate that zinc oxide-hydroxide precipitation occurs at about pH 10. This lower pH would of course lead to a decreased solubility of the Al passive film (indicated in **Fig. 9-11** as AlOOH) and therefore a decreased dissolution rate.

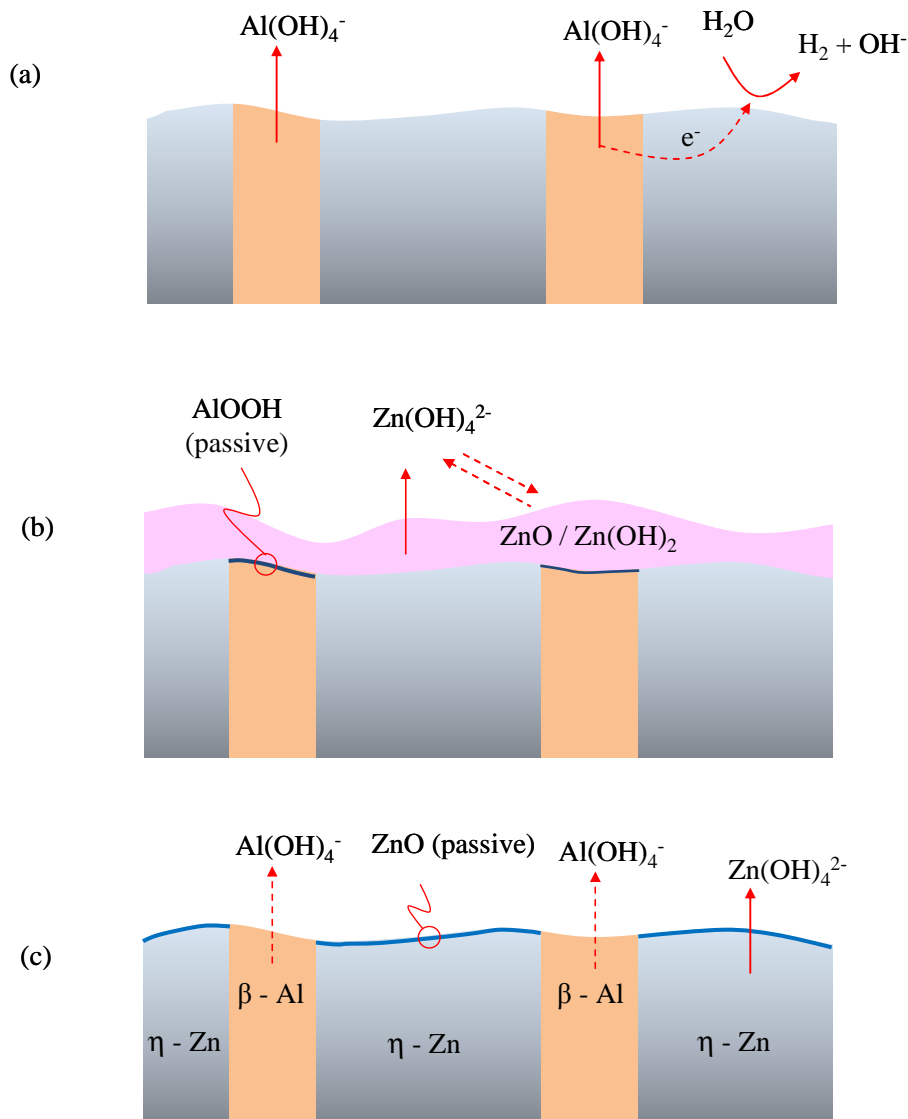


Figure 9-11: Schematic model showing the proposed interfacial structure of the eutectic phase during a polarization experiment. a) cathodic domain, b) active domain, c) passive domain. The zinc corrosion product film is formed by dissolution – precipitation mechanism in the active domain and by direct oxidation in the passive domain.

The passivation of the zinc requires a slow nucleation process to occur on the surface [1]. Once the passivation process is completed, the type I and II oxides will re-dissolve and

only a very thin zinc oxide passive film will remain. As this film is formed by a direct oxidation mechanism, the film will be localized on the Zn containing phases as illustrated in **Fig. 9-11c**. At this point, the Al will once again be exposed to alkaline electrolyte and Al dissolution will begin again. In fact, as the Al dissolution rate is limited by the solubility of the Al passive film [18], Al dissolution is nearly potential independent throughout the entire potential domain investigated in this work.

This simple model may also explain the sharp peak of Al dissolution observed in the linear scan polarization experiments at higher hydroxide concentrations (**Fig. 9-3**) and confirmed in the steady state polarization curve (**Fig. 9-10**). The dissolution of the zinc metal during the Zn active region with reduced Al dissolution may actually produce an enrichment of Al that immediately dissolves as soon as the surface is cleared of the type I and type II oxides.

This model could also be applied to an initially uniform alloy. During the early part of the experiment at open circuit and applied cathodic potential, there would be a strong selective dissolution of Al in the Zn-Al alloys. This would naturally lead to depletion of Al in the near surface region and form a thin porous film of zinc. Al dissolution would therefore occur across this film, consistent with the observed weak dependence on NaOH concentration in the passive domain. Not taking into account the porosity of the system, we can make a simple estimate of the depth of the depletion zone. Integration of several typical experiments yields an excess Al dissolution of approximately 2.9×10^{-5} g. Assuming 5% Al and a density of 7.14 g cm^{-3} (pure zinc) this would translate into a depletion of approximately 4 nm. Therefore, prior to the active dissolution domain, Al dissolution would occur across a porous phase of Al depleted zinc with an approximate thickness of 4 nm. During active dissolution, the porous phase would be blocked by the precipitated zinc oxide film. During the passive stage the zinc passive film would be significantly thinner and localized on the zinc surface and therefore have less effect on Al dissolution.

9.5. Conclusions

In this work, we have demonstrated that Zn dissolution from a Galfan alloy coating on steel behaved in a nearly identical fashion to the pure Zn. However, the Al dissolution rate was mostly potential independent as expected for pure Al in alkaline solution [6] but showed a substantial decrease during the Zn active domain. The Al dissolution rate returned to its

original value in the Zn passive domain. We interpret these results in terms of the three oxide model proposed for pure Zn in part I. Active zinc dissolution occurs through the formation of a relatively thick oxide film that blocks Al dissolution. After passivation, the excess oxide (type I and II) dissolves, allowing Al to dissolve once again.

Acknowledgement

We would like to thank the *European Union Research Fund for Coal and Steel* (AutoCorr project, grant agreement n° RFSR-CT-2009-00015 and the *Agence Nationale de Recherche* for partial funding of this work.

9.6. References

- ¹ K. Ogle, M. Mokaddem, P. Volovitch, *Electrochim. Acta.* 55 (2010) 7867-7875
- ² D. Hamm, K. Ogle, C. -O. A. Olsson, S. Weber, and D. Landolt, *Corros. Sci.* 44 (2002) 1443.
- ³ K. Ogle, A. Tomandl, N. Meddahi, *EFC 54 - Innovative pre-treatment techniques to prevent corrosion of metallic surfaces* (2007), edited by L. Fedrizzi, H. Terryn and A. Simões , p 158.
- ⁴ K. Ogle, J. Bayens, J. Swiatowska, P. Volovitch, *Electrochim. Acta.* 54 (2009) 5163.
- ⁵ K. Ogle, S. Weber, *J. Electrochem. Soc.* 147 (2000) 1770.
- ⁶ M. Mokaddem, P. Volovitch, F. Rechou, R. Oltra, K. Ogle, *Electrochim. Acta.* 55 (2010) 3779-3786.
- ⁷ J. Sullivan, C. Weirman, J. Kennedy, D. Penney, *Corros. Sci.* 52 (2010) 1853-1862.
- ⁸ S. Feliu Jr., V. Barranco, *Acta. Mater.* 51 (2003) 5413-5424.
- ⁹ F. Rosalbino, E. Angelini, D. Maccio, A. Saccone, S. Delfino, *Electrochim. Acta.* 52 (2007) 7107-7114.
- ¹⁰ A.R. Marder, *Prog. Mater. Sci.* 45 (2000) 191-271.
- ¹¹ G.A. Lopez, E.J. Mittemeijer, B.B. Straumal, *Acta. Mater.* 52 (2004) 4537-4545.
- ¹² J. O'M. Bockris, Z. Nagy, A. Damjanovic, *J. Electrochem. Soc.* 119 (1972) 285-295.

- ¹³ 13. Y.-C. Chang, *Electrochim. Acta.* 41 (1996) 2425-2432.
- ¹⁴ 14. S.-M. Moon, S.-I. Pyun, *Corros. Sci.* 39 (1997) 399-408.
- ¹⁵ H. Dafydd, D.A. Worsley, H.N. McMurray, *Corros. Sci.* 47 (2005) 3006-3018.
- ¹⁶ David R. Lide, *Handbook of Chemistry and Physics* (88th Ed.), Chemical Rubber Company, 2007.
- ¹⁷ P. Volovitch, C. Allely, K. Ogle, *Corros. Sci.* 51 (2009) 1251-1262.
- ¹⁸ K. Ogle, M. Serdechnova, M. Mokaddem, P. Volovitch, *Electrochim. Acta.* 56 (2011) 1711-1718.

Chapter X:

Inhibition mechanism of Al dissolution during polarization of Zn-Al alloys in alkaline solution

10. Inhibition mechanism of Al dissolution during polarization of Zn-Al alloys in alkaline solution

ABSTRACT: The inhibition mechanism of Al dissolution at the zinc active potential when Zn-Al alloys were polarized in 0.1 M NaOH (pH 12.8) was clarified using atomic emission spectroelectrochemistry (AESEC) and a specially designed bi-electrode with Zn and Al could either be polarized separately or in short circuit. The results demonstrated that the inhibition of Al dissolution was due to the presence of Zn^{2+} ion in solution. This is consistent with the mechanism developed previously concerning the effect of Zn-containing corrosion products formed by a dissolution precipitation mechanism.

Keywords: inhibition; Zn-Al alloys; polarization; alkaline; AESEC.

10.1. Introduction

The corrosion and polarization behaviors of Zn-Al alloys have been extensively studied in aqueous alkaline solution [1-5]. In our previous publication [6], we showed that when 5% Al-Zn alloy (GalfanTM) coating was polarized from cathodic to anodic potential in 0.1 M NaOH, the polarization behavior of Zn-Al alloys occurs in three different potential domains according to the partial dissolution rates of Zn and Al: (1) cathodic domain in which only Al dissolves from the alloy with a dissolution rate nearly independent of potential; (2) Zn active domain in which Zn starts dissolving and Al dissolution rate decreases significantly; and (3) Zn passive domain in which Al is re-active. Similar tendencies were observed for 55% Al-Zn (GalvalumeTM) alloy coating (Chapter 9). The behavior of Zn and Al in the Zn-Al alloy in the domains (1) and (3) are consistent with that of pure Zn and pure Al [7-14]. At cathodic potential in alkaline solution, a strong dissolution of pure Al is occurring due to hydroxide attack of the Al oxide film [7,8,15], while Zn is in-active [16]. Under anodic polarization, the Zn passive domain of Zn-Al alloy is similar to that of pure Zn for which the passivation mechanism is proposed to be concerning specific oxidation products of Zn referred to as type II oxide [6,10,16]. The passivating species of the passive film are assumed to be ZnO and/or Zn(OH)₂ [12-14].

Contrary to the domains (1) and (3), the domain (2) (Zn active domain) for Zn-Al alloys in which Zn is active but Al is inhibited can not be predicted from the polarization behavior of the pure metals. In the last chapter (Chapter 9), we proposed a mechanism in which zinc containing corrosion products formed during the zinc active potential inhibited the Al dissolution. However, this hypothesis should be experimentally confirmed and the role of different factors which may also affect the dissolution of aluminum in this domain, such as Zn-rich and Al-rich phase distribution, electrical coupling between Zn and Al, and the presence of Zn²⁺ in electrolyte should be understood. As proposed in [16], Zn²⁺ may precipitate when Zn becomes active, the type I and type II zinc oxides are formed over the entire surface. With the Zn-Al alloys, these kinds of Zn oxide in the zinc active domain are probably formed on the surface of the Al component and inhibit its dissolution. In addition, at the potentials during which Zn is active, the Zn rich phase of the Zn-Al alloys is oxidized to form Zn²⁺ ions whose hydrolysis would consume hydroxide ions and decrease the interfacial pH. This lower pH could lead to the formation of an Al passive film thereby decreasing the Al dissolution rate.

In Chapter 9, we suggested that the type I and II of zinc oxide inhibited the Al dissolution from Galvanic. In this chapter, we will verify this hypothesis in order to understand the mechanism of the inhibiting action of Zn on Al dissolution in alkaline solution (0.1 M NaOH). For this aim, model systems were designed in which we have attempted to separate the different effects mentioned above.

10.2. Experimental

10.2.1. Materials

The 1199 grade Al and Zn supplied by Goodfellow were used as pure Al (99.99% Al) and pure Zn (99.99% Zn). The role of Zn-rich and Al-rich phase distribution to the Al dissolution inhibition was studied using bi-electrode consisting of pure Zn and pure Al. This bi-electrode was prepared as follows: pieces of Zn and Al were welded to Cu wires. Both of them were then placed in epoxy resin (**Fig. 10-1**). Surfaces of the specimens were polished by metallographic paper up to 1 μm , and then cleaned in an ultrasonic bath (10 minutes) with ethanol followed by drying in flowing nitrogen.

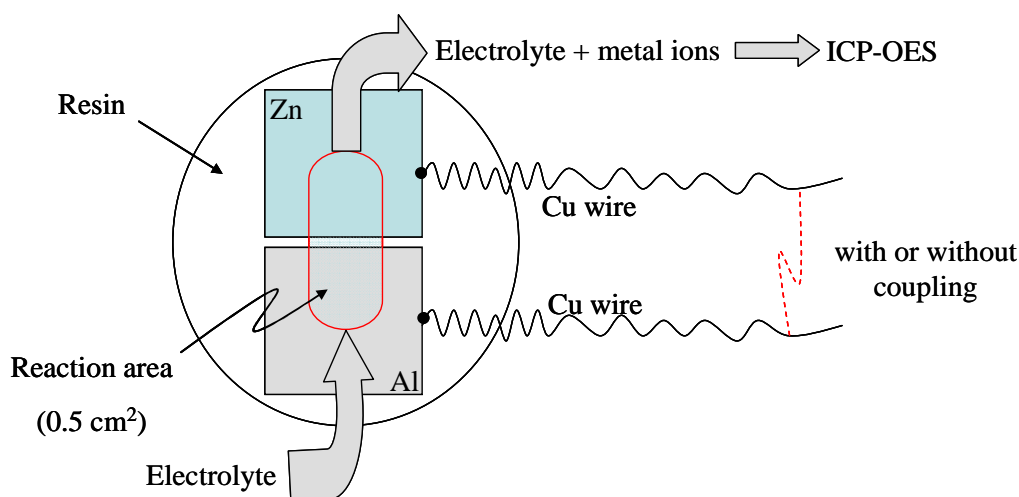


Figure 10-1: Schematic image of bi-electrode Zn/Al

Electrolytes were prepared from analytical grade NaOH (provided by Prolabo, S.A.) and deionized water (18.2 M Ω cm) prepared with a Millipore™ system. All solutions were deaerated for 10-15 minutes with flowing nitrogen prior to experiments to avoid the effect of cathodic oxygen reduction [1].

10.2.2. Atomic emission spectroelectrochemistry (AESEC) technique

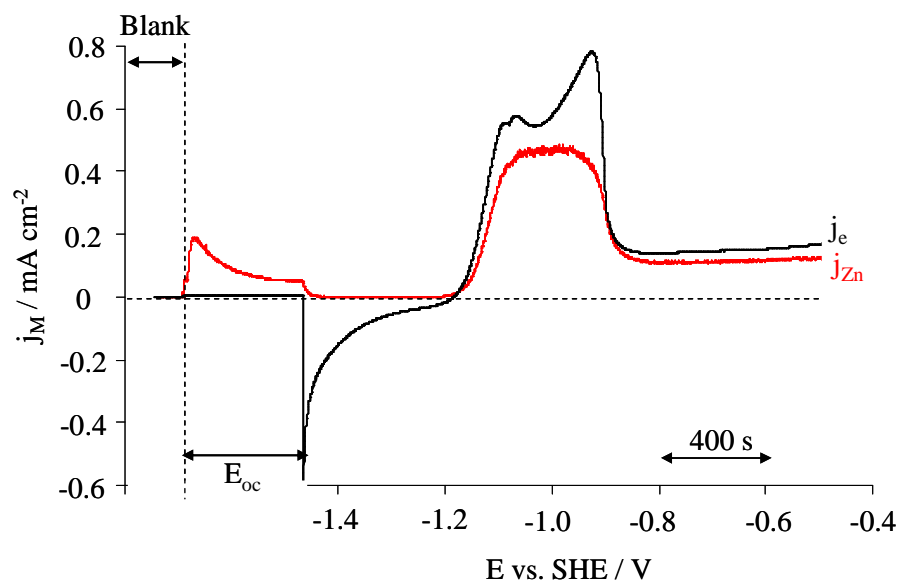
The atomic emission spectroelectrochemistry (AESEC) technique was described previously in chapter 5.

The electrochemical experiments were conducted in the AESEC electrochemical flow cell with a three electrode system. Two reference electrodes, saturated calomel electrode (SCE, 3 M KCl, +244 mV vs. a standard hydrogen electrode (SHE)) and Hg/HgO (1M KOH, +129 mV vs. a SHE), were used in this work. In the result section, potential is standardized to SHE for an easier comparison. The potentiostat was an EG&G Princeton Applied Electronics M273A functioning in the potentiostatic mode. It was controlled manually from the front panel and the analog current and potential signals were routed into the measuring circuit of the ICP-OES spectrometer to ensure that spectrometer and electrochemical data were on the same time scale. The flow rate in the electrochemical cell was approximately 3.0 ml min^{-1} and was measured for each series of experiments. In all experiments, the electrode is initially in contact with electrolyte for 400-500 s at open circuit potential (E_{oc}), followed by a linear scan voltammetry. The experiments were performed at 25°C and ambient pressure.

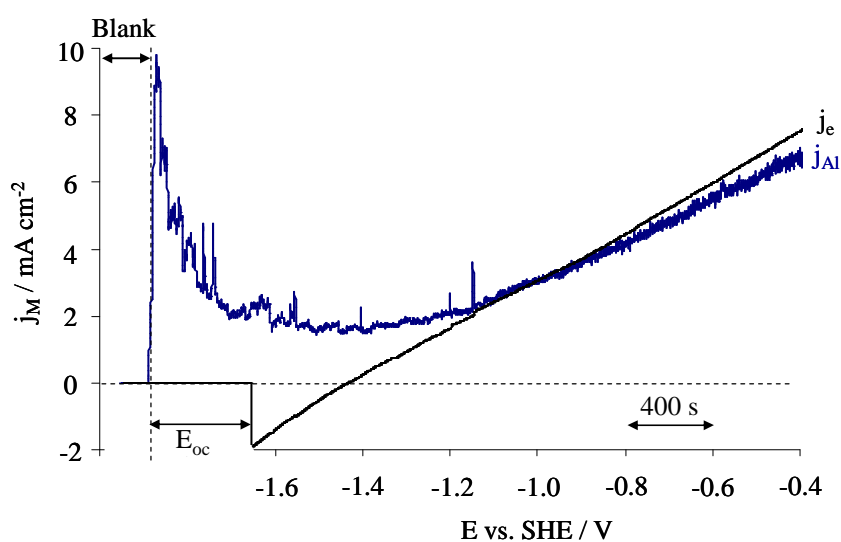
10.3. Results

10.3.1. Polarization curves for pure Zn, pure Al, and bi-electrode in 0.1 M NaOH

Fig. 10-2a shows an AESEC polarization curve giving the electrical current (j_e) and the dissolution current of pure Zn (j_{Zn}) in 0.1 M NaOH solutions (pH = 12.8). The experiment consisted of two time periods: At the beginning, the sample was exposed at open circuit potential ($E_{oc} = -1.16 \text{ V vs. SHE}$) for about 500 s during which the Zn dissolution rate was significant. After that, it decreased to almost zero when a linear scanning polarization started from cathodic potential (-1.47 V vs. SHE) at a scan rate of 0.5 mV s^{-1} to anodic potential where Zn was passive ($j_{Zn} = 0.12 \text{ mA cm}^{-2}$). At the potential domain from -1.1 V to -0.9 V , Zn was active with $j_{Zn(max)} = 0.48 \text{ mA cm}^{-2}$.



(a)



(b)

Figure 10-2: AESEC polarization experiment showing the total current density (j_e) and dissolution rates of Zn (j_{Zn}) and Al (j_{Al}) as a function of potential when (a) pure Zn and (b) pure Al were polarized with a sweep rate of 0.5 mV s^{-1} in 0.1 M NaOH followed by a preliminary open circuit potential (E_{oc}) dissolution.

Fig. 10-2b presents the electrical current (j_e) and the dissolution current of pure Al (j_{Al}) during the experiment including as before: an exposure to 0.1 M NaOH at E_{oc} (-1.66 V vs. SHE) followed by a linear scan polarization from -1.87 V to -0.60 V vs. SHE. Both j_e and

j_{Al} increase with the potential during the polarization. At the anodic potentials, j_e is slightly higher than j_{Al} .

Fig. 10-3 shows a typical AESEC polarization curve of the bi-electrode in 0.1 M NaOH solution. The electrical current, j_e , and the partial elementary currents, j_{Al} and j_{Zn} are shown. The first period is the spontaneous dissolution. We observed dissolution currents of both Zn and Al during first 70 s even though j_{Zn} is much smaller than j_{Al} . It is understandable from the point of view that Al is active and Zn is in-active in alkaline solution at open circuit potential [17] but the Zn surface may contain a smaller amount of zinc oxides which are formed during storage (after polishing) and easy to be dissolved in the alkaline solution. After that, the galvanic coupling between Zn and Al components is effective and the Zn dissolution is reduced to almost zero. The linear scanning polarization was then performed from -1.47 V to -0.47 V vs. SHE at a scan rate of 0.5 mV s^{-1} . At the cathodic domain from -1.47 V to -0.97 V, j_{Zn} is undetectable while j_{Al} is significant and increases with potential as seen with pure metals (**Fig. 10-2**). At the zinc active domain from -0.97 V to -0.67 V, j_{Zn} approaches the maximum value (0.51 mA cm^{-2}) but j_{Al} decreases from 5.53 mA cm^{-2} to 3.60 mA cm^{-2} (minimum value), which is not seen with pure Al. Although the effect is less pronounced than with Al-Zn alloys, this implies that Al is inhibited even when the Zn and Al are physically separated. This immediately rules out the possibility that the inhibitive effect may be attributed solely to the complex microstructure of the Zn-Al alloy. This cannot rule out the possibility that Zn ions coming from the Zn electrode during the spontaneous reaction may be deposited on Al by a displacement reaction:



However, the quantity of this electrodeposited Zn is very small because the amount of zinc oxide formed on the bi-electrode surface after polishing is insignificant.

In the Zn passive domain from -0.67 V to -0.47 V, j_{Zn} is rather stable at 0.12 mA cm^{-2} while j_{Al} increases again with the potential. During the entire polarization process, j_e is much lower than j_{Al} , therefore lower than $j_{Al} + j_{Zn}$, indicating a strong contribution of cathodic current which can be increased by the presence of Zn.

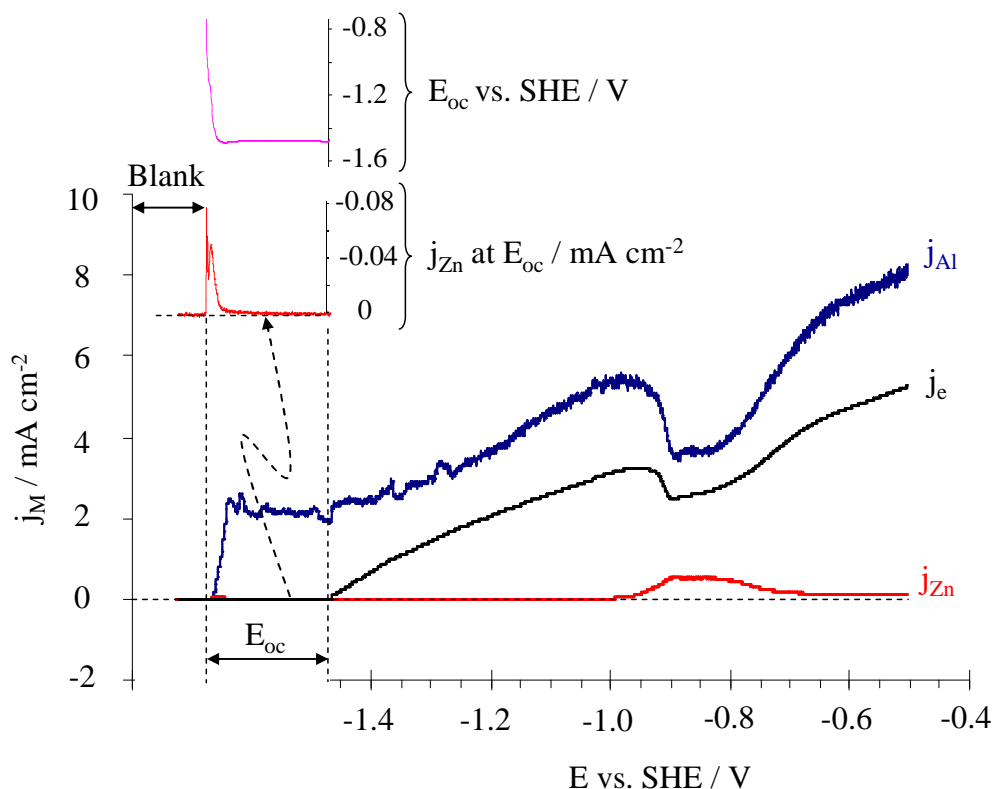


Figure 10-3: AESEC polarization curve for bi-electrode showing the total current density (j_e) and dissolution rates of Zn (j_{Zn}) and Al (j_{Al}) as a function of potential during polarization from -1.47 V to -0.47 V vs. SHE with a sweep rate of 0.5 mV s^{-1} in 0.1 M NaOH. The inset shows the open circuit potential (E_{oc}) as a function of time at open circuit period and j_{Zn} at E_{oc} at a small scale.

Table 10-1: Difference in dissolution rates of Al (Δj_{Al}) and Zn (Δj_{Zn}) at Zn active potential

$$\Delta j_M = j_M(\text{at } E_{active Zn}) - j_M(\text{before } E_{active Zn})$$

Experiment	Bi-electrode (Fig. 10-3)		Al (1 ppm Zn^{2+}) (Fig. 10-4a)	Al (5 ppm Zn^{2+}) (Fig. 10-4b)	Al (5 ppm Zn^{2+}) (Fig. 10-4c)
	Δj_{Al} (mA cm^{-2})	1.93	1.21	0.28	2.62
Δj_{Zn} (mA cm^{-2})	0.51	0.46	0.05	0.10	-

The experiment was repeated two times. The differences in Zn and Al dissolution rates (Δj_{Zn} and Δj_{Al} respectively) at Zn active potential and before Zn active potential are calculated

for both experiments (shown in **Table 10-1**). The experiment in which Δj_{Zn} is higher showed a stronger Al inhibition (higher Δj_{Al}). This observation demonstrates that the inhibition of the Al dissolution in the Zn active domain depends proportionally on the amount of Zn^{2+} released. In the next section, experiments with pure Al in the presence of Zn^{2+} are presented.

10.3.2. Polarization curves for pure Al in 0.1 M NaOH added Zn^{2+}

Fig. 10-4 shows the electrical current density (j_e) and the Al dissolution rate (j_{Al}) for pure Al during a potential scan in 0.1 M NaOH with an addition of Zn^{2+} standard solution (Titrosol™). The pH values of the alkaline solution before and after the addition were the same. Zn^{2+} concentration in the alkaline solution was converted into the equivalent current density in mA cm^{-2} (see Chapter 4) and shown as j_{Zn} in the figure. In **Fig. 10-4a**, Zn^{2+} was added before sample contact to the electrolyte ($C_{\text{Zn}^{2+}} \approx 1$ ppm). At the cathodic potential domain, j_e and j_{Al} still increase with potential as seen with pure Al in **Fig. 10-2b**, however j_e is much lower than j_{Al} . At around -0.73 V vs. SHE, j_{Al} suddenly decreases from 8.68 mA cm^{-2} to 8.40 mA cm^{-2} ($\Delta j_{\text{Al}} = 0.28 \text{ mA cm}^{-2}$), j_e also decreases simultaneously passing through a minimum and then returns to the original rate. A small increase of j_{Zn} at this potential is observed (from 0.62 to 0.67 mA cm^{-2} , i.e. $\Delta j_{\text{Zn}} = 0.05 \text{ mA cm}^{-2}$).

In **Fig. 10-4b**, a higher Zn^{2+} concentration was added in the electrolyte ($C_{\text{Zn}^{2+}} \approx 5$ ppm), a similar phenomenon was seen as compared to **Fig. 10-4a**. However, in **Fig. 10-4b** the potential at which j_{Al} starts decreasing is more negative (-0.9 V vs. SHE), Δj_{Al} and Δj_{Zn} are bigger (2.62 and 0.10 mA cm^{-2} respectively). In **Fig. 10-4c**, Zn^{2+} was just added into 0.1 M NaOH ($C_{\text{Zn}^{2+}} \approx 5$ ppm) during the polarization at -0.9 V vs. SHE. Before the Zn^{2+} addition, j_e is slightly lower than j_{Al} and both of them increase linearly with the potential. After the addition, j_e and j_{Al} are seen to decreased ($\Delta j_{\text{Al}} = 0.16 \text{ mA cm}^{-2}$). Even though this decrease is smaller than as observed in **Fig. 10-4b**, it is still significantly higher than the detection limit and can not be attributed to the experiment setup problem. The quantified results of the effect of Zn^{2+} ions on the Al dissolution in different experiments are summarized in **Table 10-1**.

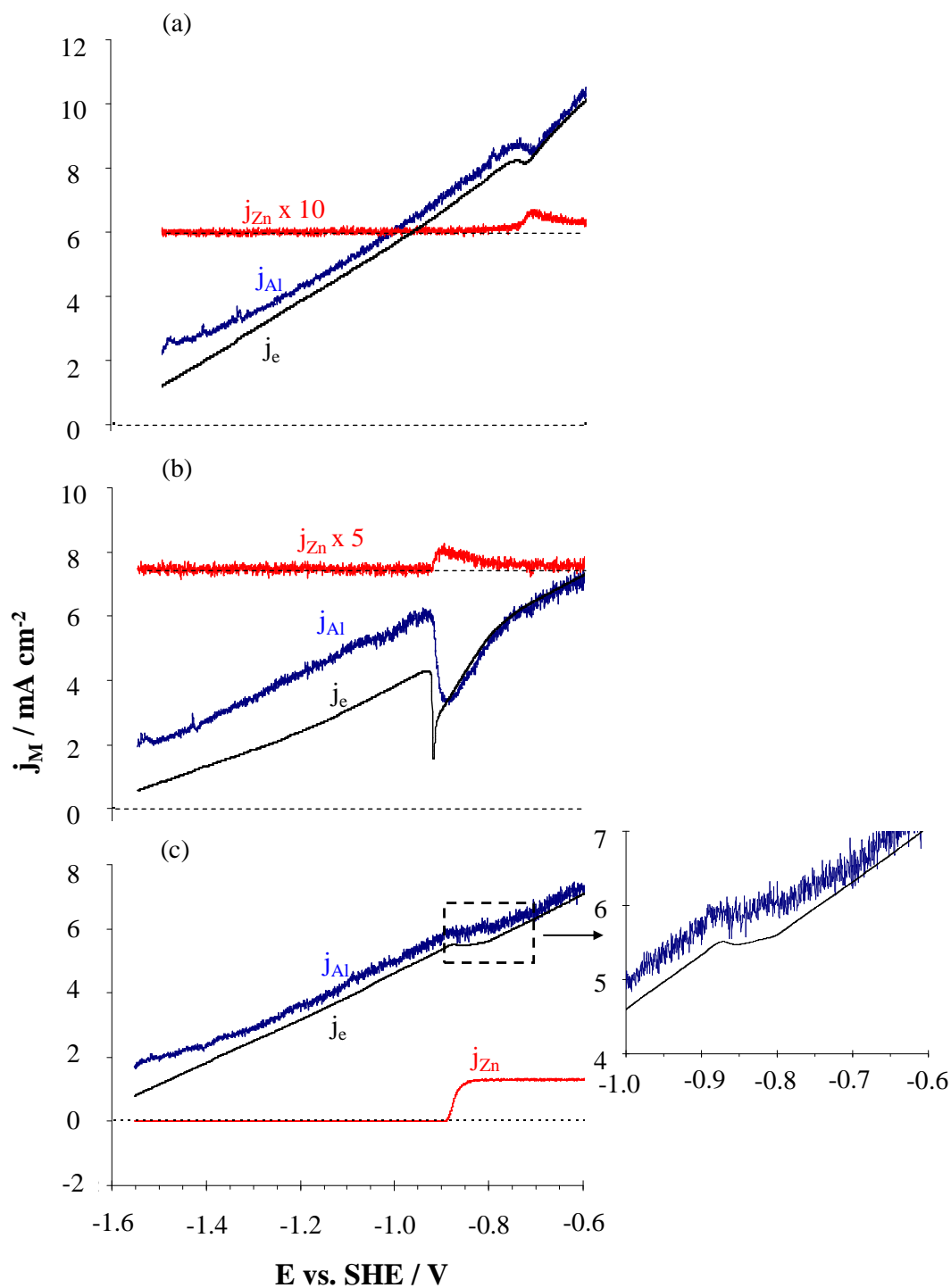


Figure 10-4: AESEC polarization curves for pure Al showing the total current density (j_e) and dissolution rates of Al (j_{Al}) as a function of potential in (a) 0.1 M NaOH added 1 ppm Zn^{2+} from the beginning, (b) 0.1 M NaOH added 5 ppm Zn^{2+} from the beginning, and (c) 0.1 M NaOH added 5 ppm Zn^{2+} at the zinc active potential. j_{Zn} corresponding to the zinc added concentration was also shown. The inset of Fig. 10-4c zooms in j_{Al} and j_e at Zn active potential at which Zn^{2+} is added.

10.4. Discussion

The result obtained from Zn-Al bi-electrode (**Fig. 10-3**) demonstrated that Zn component in the bi-electrode behaves similarly to pure Zn but Al component does not. Whenever the Zn component becomes active, Al dissolution is inhibited. The results demonstrate that the Al dissolution inhibition is not due to the complex microstructures (Zn-rich and Al-rich phase distribution) which do not exist in the bi-electrode consisting of pure Zn and pure Al.

However, with the addition of Zn^{2+} ions into the 0.1 M NaOH electrolyte, a sudden decrease of j_{Al} is observed at the active potentials of Zn (**Fig. 10-4a** and **10-4b**). A small increase of j_{Zn} is also seen in these figures because: when Zn ion was added from the beginning, a thin Zn metal layer would be electrodeposited on the Al surface (**Eqn. 10-1**). The deposited Zn metal would subsequently be oxidized to form a layer of zinc containing products right on the Al surface at the Zn active potential via the precipitation-dissolution mechanism [18] inhibiting Al dissolution. The more significant decrease of Al dissolution in **Fig. 10-4b** as compared to **Fig. 10-4a** at the Zn active potential demonstrates that a higher Zn^{2+} amount added into the electrolyte (before the potentiodynamic polarization) leads to a stronger inhibition of Al dissolution.

When Zn^{2+} is added into the electrolyte at the zinc active potential (**Fig. 10-4c**), a slight decrease of both j_{Al} and j_e is observed and followed by their continuous increase with potential. The decrease is probably due to the precipitation of the zinc based corrosion products with a subsequent buffering of the interfacial pH. As compared to the Δj_{Al} at the Zn active potential in **Fig. 10-4a** and **Table 10-1**, Δj_{Al} in this case is smaller (0.16 mA cm^{-2} vs. 0.28 mA cm^{-2}) even though more Zn^{2+} is added (5 ppm vs. 1ppm). This may be related to the “pre-concentration” effect due to Zn electrodeposition on Al surface and implies that Zn^{2+} directly formed at the interface of Zn-Al alloy is more concentrated and should play an important role in the inhibition of Al dissolution.

10.5. Conclusion

In this work, we demonstrated that Zn dissolution from Zn-Al coupling during linear scanning polarization was not affected by the presence of Al. However, aluminum dissolution was systematically inhibited at zinc active domain by the presence of Zn^{2+} ions in solution. The effect increasing with the amount of pre-deposited Zn on the Al surface which increases

the surface concentration of Zn^{2+} in active domain demonstrates that the Zn^{2+} surface concentration rather than Zn^{2+} bulk concentration is responsible for the inhibition. We interpret the effect of the presence of Zn^{2+} ions which result in either zinc containing corrosion products or interfacial pH buffering, was confirmed to be the main reason causing the aluminum dissolution inhibition. This is in agreement with our previous hypothesis as proposed in Chapter 9.

10.6. References

- ¹ H. Dafydd, D.A. Worsley, H.N. McMurray, The kinetics and mechanism of cathodic oxygen reduction on zinc and zinc–aluminium alloy galvanized coatings, *Corros. Sci.* 47 (2005) 3006-3018.
- ² W.J. Tomlinson, S.A. Brown, Corrosion of anodically polarized Zn-Al alloys in saturated $Ca(OH)_2$ containing Cl^- , *Surf. Coat. Tech.* 27 (1986) 95-100.
- ³ I.Odnevall Wallinder, W He, P-E Augustsson, C Leygraf, Characterization of black rust staining of unpassivated 55% Al–Zn alloy coatings. Effect of temperature, pH and wet storage, *Corros. Sci.* 41 (1999) 2229-2249.
- ⁴ N.R. Short, S. Zhou, J.K. Dennis, Electrochemical studies on the corrosion of a range of zinc alloy coated steel in alkaline solutions, *Surf. Coat. Tech.* 79 (1996) 218-224.
- ⁵ M.A. Arenas, L. Iglesias-Rubianes, Y. Liu, P. Skeldon, G.E. Thompson, H. Habazaki, K. Shimizu, P. Bailey, T.C.Q. Noakes, Behaviour of zinc in electropolished and etched Al-Zn alloy and effect on corrosion potential, *Corros. Sci.* 47 (2005) 2321-2331.
- ⁶ T.N. Vu, M. Mokaddem, P. Volovitch, K. Ogle, The anodic dissolution of zinc and zinc alloys in alkaline solution II. Al and Zn partial dissolution from 5% Al-Zn coatings, *Electrochim. Acta.* 74 (2012) 130-138.
- ⁷ K. Ogle, M. Serdechnova, M. Mokaddem, P. Volovitch, The cathodic dissolution of Al, Al_2Cu , and Al alloys, *Electrochim. Acta.* 56 (2011) 1711-1718.
- ⁸ A.R. Despić, J. Radošević, P. Dabić, M. Kliškić, Abnormal yields of hydrogen and the mechanism of its evolution during cathodic polarization of aluminium, *Electrochim. Acta.* 35 (1990) 1743-1746.

-
- ⁹ E.E. Abd El Aal, On the pitting corrosion currents of zinc by chloride anions, *Corros. Sci.* 46 (2004) 37-49.
- ¹⁰ J. Hendrikx, A. van der Putten, W. Visscher, E. Barendrech, The electrodeposition and dissolution of zinc and amalgamated zinc in alkaline solutions, *Electrochim. Acta.* 29 (1984) 81-89.
- ¹¹ S.B. Saidman, J.R. Vilche, A.J. Arvia, Voltammetric response of zinc in sodium hydroxide solutions containing sodium sulphide, *Electrochim. Acta.* 39 (1994) 1401-1407.
- ¹² M.A. Pech-Canul, R. Ramanauskas, L. Maldonado, An electrochemical investigation of passive layers formed on electrodeposited Zn and Zn-alloy coatings in alkaline solutions, *Electrochim. Acta.* 42 (1997) 255-260.
- ¹³ A.E Bohe, J.R Vilche, K Jüttner, W.J Lorenz, W Kautek, W Paatasch, An electrochemical impedance spectroscopy study of passive zinc and low alloyed zinc electrodes in alkaline and neutral aqueous solutions, *Corros. Sci.* 32 (1991) 621-633.
- ¹⁴ I.G. Murgulescu, O. Radovici, M. Borda, Studies of the mechanism of anodic dissolution of Al-Zn binary alloys in alkaline solutions by potentiodynamic and potentiostatic pulse methods, *Corros. Sci.* 5 (1965) 613-622.
- ¹⁵ S.-M. Moon, S.-I. Pyun, The corrosion of pure aluminium during cathodic polarization in aqueous solutions, *Corros. Sci.* 39 (1997) 399-408.
- ¹⁶ M. Mokaddem, P. Volovitch, K. Ogle, The anodic dissolution of zinc and zinc alloys in alkaline solution. I. Oxide formation on electrogalvanized steel, *Electrochim. Acta.* 55 (2010) 7867-7875.
- ¹⁷ T. N. Vu, P. Volovitch, K. Ogle, The effect of pH on the selective dissolution of Zn and Al from Zn-Al coatings on steel, *Corrosion Science* (2012) Submitted.
- ¹⁸ Y.-C. Chang, A kinetic model for the anodic dissolution of zinc in alkaline electrolyte with sodium metasilicate additions, *Electrochim. Acta.* 41 (1996) 2425-2432.

Chapter XI:

Conclusions and perspectives

11. Conclusions and perspectives

This dissertation work has mapped out the selective dissolution from binary Zn-Al alloys as a function of pH and of potential which are two important factors that determine the corrosion rate of materials during their outdoor applications. As we said, zinc and aluminum have similar activities and it is difficult to quantify the dissolution rates of each metal from Zn-Al alloys by classical electrochemical methods. This difficulty was overcome in this work by using the AESEC technique which allows us to measure *in situ* the elemental dissolution rates of Zn-Al alloys such as Galfan (5% Al-Zn) and Galvalume (55% Al-Zn) and to a lesser extent Zn-Mg-Al alloy at open circuit potential and applied potential in different environments. Other *ex situ* methods such as XRD, SEM / EDS, IR, and XPS were also used to characterize precipitated corrosion products and corroded surface composition.

These results yield a more complete picture of the kinetics of Zn-Al dissolution that may ultimately be extended to include the Zn-Al-Mg family of alloys and be incorporated into a numerical model. The results of my work may be summarized as follows:

1. The selective dissolution from Zn-Al alloys as a function of pH was mapped out

The selective dissolution of Zn and Al from Zn-Al alloys was investigated as a function of pH when 5% Al-Zn and 55% Al-Zn were exposed to a 30 mM NaCl electrolyte (chapter 7) and to more complex electrolytes – seawater / rainwater (chapter 6). It is demonstrated that the dissolution mechanism changed from selective zinc dissolution in the pH range of 2-4 (for Galfan) and 2-8 (for Galvalume) to selective aluminum dissolution at higher pH. The presence or absence of oxygen in the electrolyte did not change the selective dissolution behavior but influenced the dissolution rates (v_{Zn} and v_{Al}) which varied with time. Oxygen stabilized the oxide layer in aerated solution causing an anodic shift of the open circuit potential as compared to the results obtained in de-aerated solution. The galvanic coupling between Zn-rich and Al-rich phases of 5%Al-Zn was observed in the de-aerated solution at pH = 11.8 where Al dissolved quickly but Zn did not.

2. The selective dissolution from Zn-Al alloys as a function of potential was mapped out

The selective dissolution of Zn and Al from 5% Al-Zn and 55% Al-Zn was investigated as a function of potential in 0.1 M HCl (pH = 1.5), 0.1 M NaCl (pH = 6.7), and 0.1 M NaOH (pH = 12.8). During cathodic polarization, there was a strong selective dissolution of Al from both alloys in 0.1 M NaOH and 0.1 M NaCl, but selective dissolution of Zn was observed from Galvalume in 0.1 M HCl. During anodic polarization, a strong selective dissolution of Zn was seen in the acidic and neutral solutions. In the alkaline solutions, anodic branches of polarization curves for both Galfan and Galvalume are divided into 2 different domains: zinc active domain in which Zn selective dissolution occurs and zinc passive domain in which Al selective dissolution occurs.

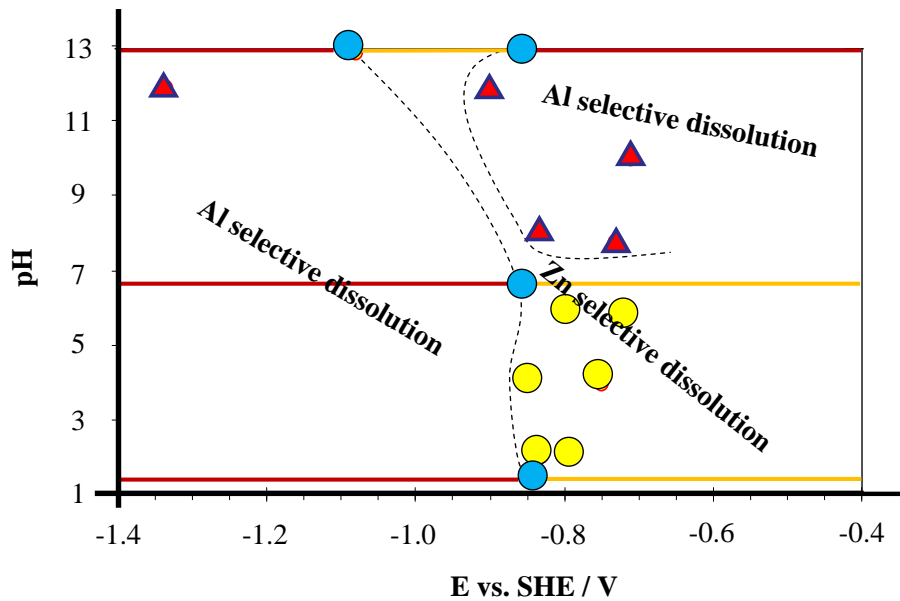
3. Aluminum dissolution is inhibited by Zn-containing corrosion products resulting from Zn selective dissolution

The inhibition of Al dissolution in the presence of dissolved Zn ions was mentioned in chapter 7 to chapter 10. In the investigation of selective dissolution as a function of pH (Chapter 7), the comparison of AESEC results and immersion test results demonstrates that the formation of a corrosion product layer of primarily Zn-containing products inhibited the Al release rate. It also demonstrates the complementarities of the short time AESEC corrosion rate measurements and the long term immersion exposures. During a long term exposure, the elementary corrosion reactions affect the pH of the electrolyte such that the pH approaches neutral. The AESEC experiments involve a constantly renewed electrolyte and thus the rate measurement more closely represents the "intrinsic" reactivity of the material with an electrolyte. In the investigation of selective dissolution as a function of potential in alkaline solution (chapter 8 and 9), AESEC polarization experiments indicate the inhibition of aluminum dissolution in the zinc active domain. The inhibition mechanism of Al dissolution in the alkaline solution at the zinc active potentials was proposed and verified (chapter 10) by performing further polarization experiments on special bi-electrode. It is demonstrated that Al dissolution during the Zn active domain where Zn selective dissolution occurs is inhibited by Zn-containing corrosion products and pH buffering which are attributed to the presence of Zn^{2+} in confined zone.

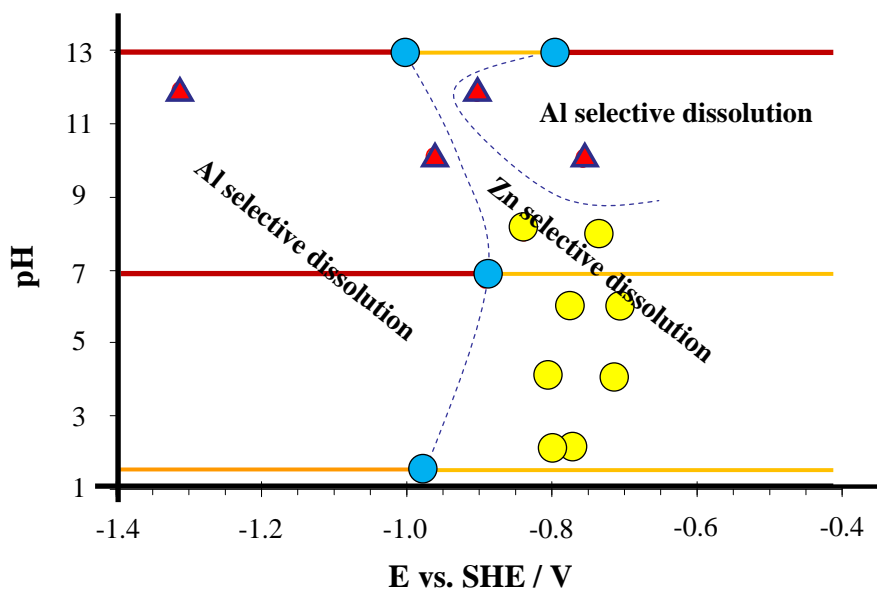
4. Aluminum dissolution does not have a significant effect on zinc dissolution

Polarization experiments in various alkaline solutions yields a Tafel slope of approximately 35 mV/decade for the Zn dissolution current - potential curve. This Tafel slope is nearly independent of hydroxide ion concentration. This value is consistent with the dissolution of pure zinc. It means that the Al dissolution rate does not have a significant effect on the kinetics of zinc dissolution.

In order to produce a numerical diagram based on the results in this work, the selective dissolution from Galfan and Galvalume was mapped out as a function of pH and potential as shown in **Fig. 11-1**. The details of the construction of this diagram are given in the figure caption. In principle, Zn selective dissolution occurs at anodic potentials and at low pH, while Al selective dissolution occurs at cathodic potentials or even at anodic potentials if the pH is high enough. The diagram in **Fig. 11-1** helps to predict the corrosion, the selective dissolution or de-alloying of Zn-Al alloys in different potentials and different environments, notably pH. However, it should be noted that the boundaries (dashed lines) between the different domains in this figure are approximate based on a small data set. In addition, the indicated pH is the initial solution pH and not the interfacial pH that may be altered due to the partial corrosion reactions. Bulk pH changes during the experiments were small, less than 0.3 as determined by downstream pH measurements. Further, the boundary points determined by linear scan voltammetry probably contain a junction potential due to the IR drop across the membrane.



(a) Galfan



(b) Galvalume

Figure 11-1: Diagram showing the different domains where Zn and Al selective dissolution occurs depending on pH and potential at 25°C. Yellow circles and red triangles represent open circuit potential measurements with Zn or Al selective dissolution respectively. The blue circles represent the point in the linear scan voltammetry curve where Zn and Al dissolve in proportion to their composition in the bulk alloy. The dashed lines are hypothetical boundaries between these different domains. The solid lines present the results of the potentiodynamic experiments in which yellow represents selective Zn dissolution and red represents selective Al dissolution.

5. Identification of the selective dissolution phenomenon during corrosion of Zn-Mg-Al alloy.

The dissolution behaviors of the different elements in Zn-Mg-Al alloys in the corrosion mechanism was identified by combining the AESEC technique, cyclic corrosion tests and surface characterization after the corrosion tests in chloride-containing and chloride-free environments. The important role of the Al rich phase in the microstructure of the Zn-Mg-Al alloy is to serve as a cathode at the initial stage of the corrosion process, while Zn and Mg are selectively dissolved at the anodic regions. The increased pH due to the cathodic reaction leads to Al dissolution via the cathodic dissolution mechanism. For Mg-containing alloys we propose that improved corrosion resistance is achieved by stabilization of more protective simonkolleite and zinc hydroxysulfate as compared with zinc oxide and hydrozincite. At later stages, for Zn-Al-Mg, the corrosion resistance is reinforced by the formation of layered double hydroxides (LDH). According to thermodynamic modeling, Mg^{2+} ions bind the excess of carbonate or sulfate anions buffering pH and preventing the formation of soluble or less-protective products. A preferential dissolution of Zn and Mg at initial stages of corrosion is confirmed by *in situ* dissolution experiment and seems to play an important role in the corrosion process.

Annex

Annex

New - Verband Der Automobilindustrie (New-VDA) test

New-VDA test is the accelerated corrosion test used in chapter 5 to study corrosion of coupled materials.

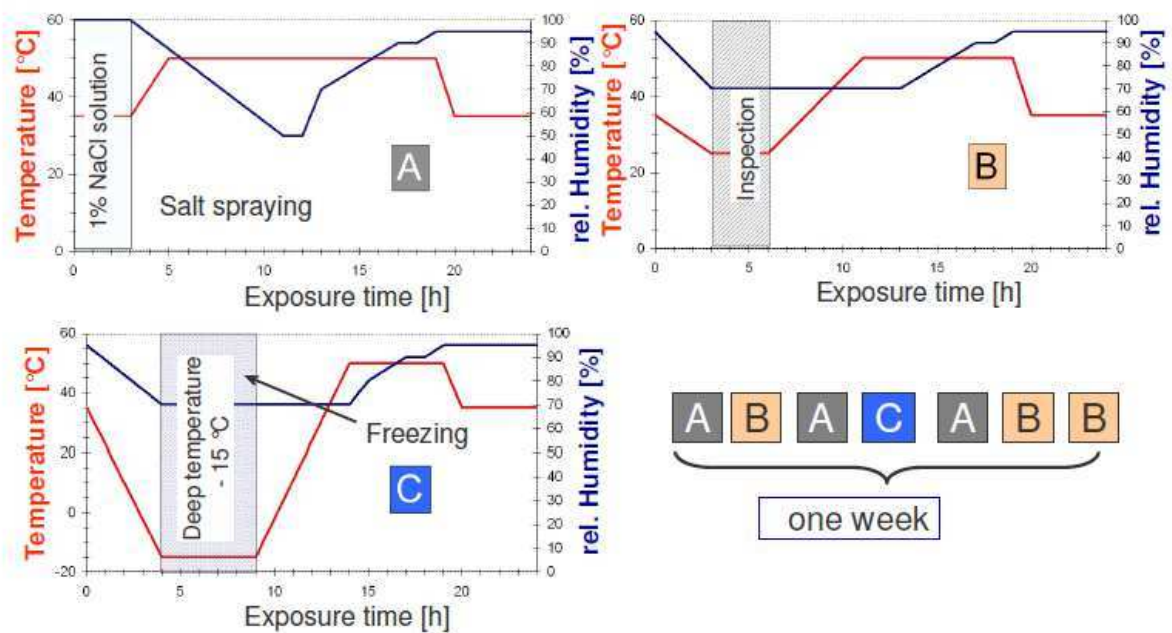


Figure 1: Definition of the new VDA test cycles including the freezing step that is absent in the old VDA test. The variation of humidity and temperature throughout the new-VDA test is also shown. Solution of 5% NaCl is often used in the salt spraying step.

X-ray diffraction

X-rays are electromagnetic radiation with typical photon energies in the range of 100 eV - 100 keV. For diffraction applications, only short wavelength x-rays (hard x-rays) in the range of a few angstroms to 0.1 angstrom (1 keV - 120 keV) are used. Because the wavelength of x-rays is comparable to the size of atoms, they are ideally suited for probing the structural arrangement of atoms and molecules in a wide range of materials. The energetic x-rays can penetrate deep into the materials and provide information about the bulk structure [1].

X-rays primarily interact with electrons in atoms. When x-ray photons collide with electrons, some photons from the incident beam will be deflected away from the direction where they originally travel, much like billiard balls bouncing off one another. If the wavelength of these scattered x-rays did not change (meaning that x-ray photons did not lose any energy), the process is called elastic scattering (Thompson Scattering) in that only momentum has been transferred in the scattering process. These are the x-rays that we measure in diffraction experiments, as the scattered x-rays carry information about the electron distribution in materials. On the other hand, in the inelastic scattering process (Compton Scattering), x-rays transfer some of their energy to the electrons and the scattered x-rays will have different wavelength than the incident x-rays.

Diffracted waves from different atoms can interfere with each other and the resultant intensity distribution is strongly modulated by this interaction. If the atoms are arranged in a periodic fashion, as in crystals, the diffracted waves will consist of sharp interference maxima (peaks) with the same symmetry as in the distribution of atoms. Measuring the diffraction pattern therefore allows us to deduce the distribution of atoms in a material.

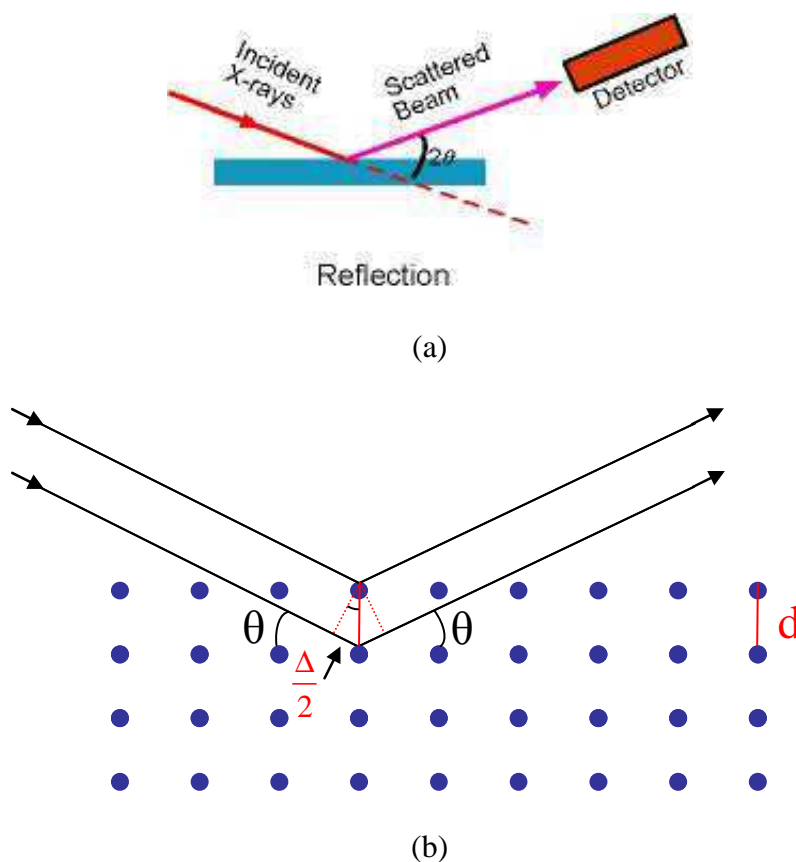


Figure 2: (a) collecting diffraction data using reflection geometry and (b) interaction between x-ray beam and the periodically arranged atoms

The peaks in an x-ray diffraction pattern are directly related to the atomic distances. Let consider an incident x-ray beam interacting with the atoms arranged in a periodic manner as shown in 2 dimensions in the **Fig. 2**. The atoms, represented as green spheres in the graph. Assume Δ is the pattern difference of 2 waves have the same wavelength interacting with 2 adjacent atoms, these x-ray forms a scattering angle of θ with the atomic plane. Based on the trigonometry, Δ can be calculated as follows:

$$\frac{\Delta}{2} = d \sin \theta$$
$$\Delta = 2d \sin \theta$$

in which d is the space between the atomic planes.

To obtain the interference, the pattern difference of 2 waves must be integer order of the wavelength, i.e. $\Delta = n\lambda$.

Therefore, we have

$$2d \sin \theta = n \lambda$$

which is known as the Bragg's law, after W.L. Bragg, who first proposed it. In the equation, λ is the wavelength of the x-ray, θ the scattering angle, and n is an integer representing the order of the diffraction peak. The Bragg's Law is one of most important laws used for interpreting x-ray diffraction data.

It is important to point out that although atoms have been used as scattering points in this example, Bragg's Law applies to scattering centers consisting of any periodic distribution of electron density. In other words, the law holds true if the atoms are replaced by molecules or collections of molecules, such as colloids, polymers, proteins and virus particles.

In this work, the XRD characterization was carried out by D5000 diffractometer and X'Pert PRO PANalytical system using Cu K_{α} radiation. Two types of spectra were studied. Firstly, the diffraction experiment was performed directly on the corroded surface. Then, the corrosion products were removed from the surface, grinded to powder, deposited on a glass support with a thin Vaseline layer for the fixation of the powder, and scanned from 5° to 70° (2theta) with a step size of 0.04° . Product identification was made using the PCPDFWIN software version 2.02 supporting the ICDD (International centre for diffraction data) database, and the X'Pert HighScore software which supports all types of reference databases, from actual to legacy, from premium-quality ICDD products over mid-priced solutions to free downloadable databases [2].

Scanning electron microscope (SEM) – Energy dispersive spectroscopy (EDS)

Scanning electron microscope is a type of electron microscope that images a sample by scanning it with a beam of electrons in a raster scan pattern. The electrons interact with the atoms that make up the sample producing signals that contain information about the sample's surface topography, composition, and other properties such as electrical conductivity [3].

When the primary electron beam having an energy ranging from 0.2 keV to 40 keV interacts with the sample, the electrons lose energy by repeated random scattering and absorption within a teardrop-shaped volume of the specimen known as the interaction volume, which extends from less than 100 nm to around 5 μm into the surface. The size of the interaction volume depends on the electron's landing energy, the atomic number of the specimen and the specimen's density.

Conventional SEM requires samples to be imaged under vacuum, because a gas atmosphere rapidly spreads and attenuates electron beams. Magnification in a SEM can be controlled over a range of up to 6 orders of magnitude from about 10 to 500,000 times.

The types of signals produced by a SEM include secondary electrons, back-scattered electrons, characteristic X-rays, etc.

- The secondary electron signals result from interactions of the electron beam with atoms at or near the surface of the sample. In the secondary electron imaging or SEI, the SEM can produce very high-resolution images of a sample surface, revealing details less than 1 nm in size and yielding a characteristic three-dimensional appearance useful for understanding the surface structure of a sample. The brightness of the signal depends on the number of secondary electrons reaching the detector. If the beam enters the sample perpendicular to the surface, then the activated region is uniform about the axis of the beam and a certain number of electrons "escape" from within the sample. As the angle of incidence increases, the "escape" distance of one side of the beam will decrease, and more secondary electrons will be emitted. Thus steep surfaces and edges tend to be brighter than flat surfaces, which results in images with a well-defined, three-dimensional appearance.

- The back scattered electrons (BSE) are beam electrons that are reflected or back-scattered out of the specimen interaction volume by elastic scattering interaction with specimen atoms. Since heavy elements (high atomic number) backscatter electrons more strongly than light elements (low atomic number), and thus appear brighter in the

image, BSE are used to detect contrast between areas with different chemical compositions [4]. In other words, BSE images can provide information about the distribution of different elements in the sample (from 5 to 10 nm in size) which would be difficult or impossible to detect in the secondary electron images. Backscattered electrons can also be used to form electron backscatter diffraction (EBSD) image that can be used to determine the crystallographic structure of the specimen.

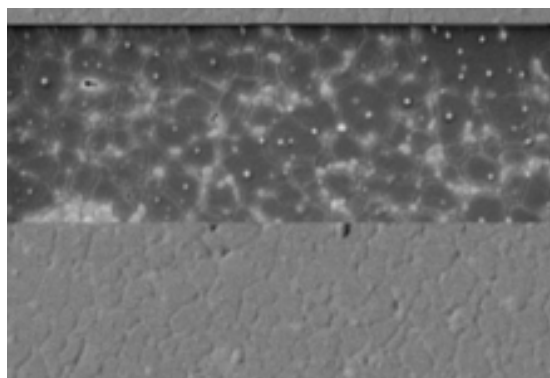


Figure 3: Comparison of SEM techniques:

Top: backscattered electron analysis - composition

Bottom: secondary electron analysis - topography

- The characteristic X-rays are emitted when the electron beam removes an inner shell electron from the sample, causing a higher-energy electron to fill the shell and release energy. These characteristic X-rays are used to identify the composition and measure the abundance of elements in the sample. The signals may be detected in an SEM equipped for energy-dispersive X-ray spectroscopy (EDS or EDXS). Specimens that undergo WDS or EDS analysis are often carbon coated.

In this work, surfaces characterization were performed by scanning electron microscopy (SEM) coupled with energy dispersive spectroscopy (EDS), using a Gemini 1530 microscope with field emission gun (FEG) source at 15 kV, Si(Li) detector for EDS and QUANTAX software (Bruker AXS).

Attenuated total reflectance (ATR) infrared

Infrared spectroscopy (IR spectroscopy) is the spectroscopy that deals with the infrared region of the electromagnetic spectrum, that is light with a longer wavelength and lower frequency than visible light. It exploits the fact that molecules absorb specific frequencies that are characteristic of their structure. These absorptions are resonant frequencies, i.e. the frequency of the absorbed radiation matches the frequency of the bond or group that vibrates. The energies are determined by the shape of the molecular potential energy surfaces, the masses of the atoms, and the associated vibronic coupling [5].

The infrared spectrum of a sample is recorded by passing a beam of infrared light through the sample. When the frequency of the IR is the same as the vibrational frequency of a bond, absorption occurs. Examination of the transmitted light reveals how much energy was absorbed at each frequency (or wavelength). This can be achieved by scanning the wavelength range using a monochromator.

Infrared spectroscopy is a simple and reliable technique widely used in both organic and inorganic chemistry, in research and industry. It is used in quality control, dynamic measurement, and monitoring applications such as the long-term unattended measurement of CO₂ concentrations in greenhouses and growth chambers by infrared gas analyzers. It is also used in forensic analysis in both criminal and civil cases, for example in identifying polymer degradation.

A useful way of analyzing solid samples without the need for cutting samples uses ATR or attenuated total reflectance spectroscopy. ATR is a sampling technique used in conjunction with infrared spectroscopy which enables samples to be examined directly in the solid, liquid or gas state without further preparation [6]. ATR-IR has the limited path length into the sample. This avoids the problem of strong attenuation of the IR signal in highly absorbing media, such as aqueous solutions.

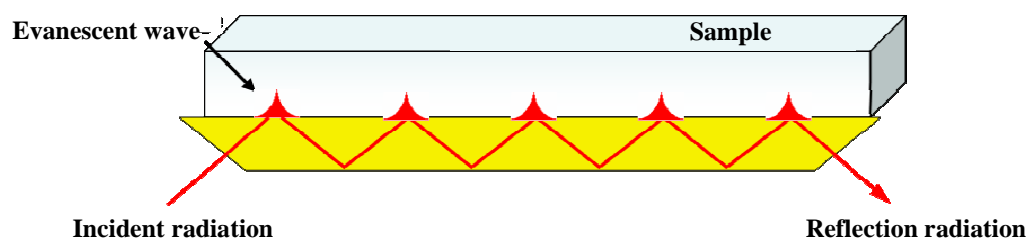


Figure 4: Light undergoes multiple internal reflections in the crystal of high refractive index, shown in yellow. The sample is in contact with the crystal.

ATR uses a property of total internal reflection resulting in an evanescent wave. A beam of infrared light is passed through the ATR crystal in such a way that it reflects at least once off the internal surface in contact with the sample. This reflection forms the evanescent wave which extends into the sample. The penetration depth into the sample is typically between 0.5 and 2 micrometers, with the exact value being determined by the wavelength of light, the angle of incidence and the indices of refraction for the ATR crystal and the medium being probed [7]. The number of reflections may be varied by varying the angle of incidence. The beam is then collected by a detector as it exits the crystal. Most modern infrared spectrometers can be converted to characterize samples via ATR by mounting the ATR accessory in the spectrometer's sample compartment.

The evanescent effect only works if the crystal is made of an optical material with a higher refractive index than the sample being studied. Otherwise light is lost to the sample. In the case of a solid sample, it is pressed into direct contact with the crystal. Because the evanescent wave into the solid sample is improved with a more intimate contact, solid samples are usually firmly clamped against the ATR crystal, so that trapped air is not the medium through which the evanescent wave travels, as that would distort the results. The signal to noise ratio obtained depends on the number of reflections but also on the total length of the optical light path which dampens the intensity. Therefore, a general claim that more reflections give better sensitivity cannot be made.

In this work, ATR-IR was obtained at the wavenumber range from 4000 cm^{-1} to 700 cm^{-1} with the resolution of 1 cm^{-1} . It was performed directly on the corroded sample surfaces using a Bruker Tensor 27, $\lambda_{\text{laser}} = 15799.76\text{ \AA}$ and OPUS 6.5 data treatment software. The results were then compared with reference spectra taken from the databases for minerals [8-11].

References

¹ <http://www.mrl.ucsb.edu/mrl/centralfacilities/xray/xray-basics/index.html#x0>

² <http://www.panalytical.com/index.cfm?sid=212>

³ http://en.wikipedia.org/wiki/Scanning_electron_microscope

⁴ G.I. Goldstein, D.E. Newbury, P. Echlin, D.C. Joy, C. Fiori, E. Lifshin, Scanning electron microscopy and x-ray microanalysis, New York: Plenum Press, 1981.

⁵ http://en.wikipedia.org/wiki/Infared_spectroscopy

⁶ http://shop.perkinelmer.com/content/TechnicalInfo/TCH_FTIRATR.pdf

⁷ F. M. Mirabella, Jr., Practical Spectroscopy Series; Internal reflection spectroscopy: Theory and applications, Marcel Dekker, Inc.; Marcel Dekker, Inc., 1993, 17-52

⁸ <http://www.mindat.org/>

⁹ <http://www.minerals.net/>

¹⁰ <http://webmineral.com/>

¹¹ <http://truff.info/>

Selective dissolution from Zn-Al alloy coatings on steel

The main objective of this work is to understand selective dissolution phenomena and map out the selective dissolution of Zn-Al alloys and to a lesser extent Zn-Mg-Al alloys as a function of pH and potential. This will help to build up a predictive model of galvanic coupling which is a major preoccupation of the automotive industry.

To approach the target, we utilize atomic emission spectroelectrochemistry (AESEC) technique which is a combination of electrochemical and analytical methods. This technique allows us to quantify in real time and separately dissolution rates of zinc and aluminum from Zn-Al alloys at open circuit potential and applied potential in different solutions. Selective dissolution of zinc and aluminum from Zn-Al alloys is then mapped out in the pH and potential ranges. The explanations for the selective dissolution and inhibition phenomena occurring during experiments are also given thanks to the complementary results from some other surface characterization methods (XRD, SEM/EDS, IR, and XPS).

Key words: atomic emission spectroelectrochemistry, zinc, aluminum, selective dissolution, pH, potential.

Dissolution sélective à partir des alliages Zn-Al sur l'acier

L'objectif principal de ce travail est de comprendre les phénomènes de dissolution sélective et de cartographier la dissolution sélective des alliages Zn-Al et des alliages Zn-Mg-Al dans une moindre mesure en fonction du pH et de potentiel. Cela aidera à construire un modèle prédictif de couplage galvanique qui est une préoccupation majeure de l'industrie automobile.

Pour s'approcher de la cible, nous utilisons la spectroélectrochimie d'émission atomique (AESEC) qui est une combinaison de méthodes électrochimiques et analytiques. Cette technique nous permet de quantifier en temps réel et séparément les taux de dissolution de zinc et d'aluminium à partir des alliages Zn-Al au potentiel de circuit ouvert et du potentiel appliqué dans différentes solutions. Dissolution sélective de zinc et d'aluminium à partir des alliages Zn-Al est ensuite tracée dans les gammes du pH et de potentiel. Les explications relatives à la dissolution sélective et les phénomènes d'inhibition survenant au cours d'expériences sont également donnés grâce à des résultats complémentaires de certains autres méthodes de caractérisation de surface (DRX, MEB / EDS, IR et XPS).

Mots-clés: spectroélectrochimie d'émission atomique, zinc, aluminum, dissolution sélective, pH, potentiel.